DEVELOPMENT OF A BROADBAND RADIO SPECTROPOLARIMETER FOR SOLAR OBSERVATIONS

A Thesis
Submitted for the Degree of

Doctor of Philosophy (Technology)

Submitted by

KISHORE PULAPALLI

Department of Applied Optics & Photonics
University College of Technology
University of Calcutta

August 2016

Dedicated to

My Family

Acknowledgements

At first, I would like to thank Dr. C. Kathiravan for letting me work independently. Due to his assistance in field tests, constant support throughout the project helped me to complete this thesis. I also like to thank Prof. R. Ramesh for teaching me the basics of Radio Astronomy techniques and introducing to the field of Solar radio astronomy. I would like to thank both of them for providing hospitality and taking utmost care during my stay at Gauribidanur Radio Observatory.

Here, I would like to thank all the Directors of Indian Institute of Astrophysics, the Dean and all the chairs of Board of Graduate Studies (B.G.S during 2009 - 2016) for giving me the opportunity to work in this institute and providing all the facilities required to carry out my research work. Also, I thank all the academic and administrative sections for letting me attend various schools and conferences during my tenure. I would like to thank all the working personnel in non-academic staff for clearing all the bills and arranging all the necessary arrangements with less administrative hurdles.

I like to thank all the professors of Department of Applied Optics and Photonics, Calcutta University, Prof. A. K. Chakraborty, Prof. L. N. Hazra, Prof. A. Ghosh, Dr. Kallol Bhattacharya, Dr. Samir Kumar Sarkar, Prof. A. Basu Ray and Dr. (Mrs.) Mina Ray, Mr. N. Chakraborthy and Mr. S. Bagchi. Due to above professionals, I learnt various aspects of optics and their applications.

Special thanks to Mr. Chandan, Prof. Ajoy Ghosh for taking care during our stay at Calcutta. I thank all my seniors for providing useful information at regular times. I also enjoyed the company of my classmates Mr. Narsi Reddy Anugu, Mr. Tarun Kumar Sharma, Mr. Jyotirmoy Paul, Ms. Soumi Paul and Ms. Amita Mohanty. They are very friendly and suggestive at many times. I appreciate PG Hall canteen staff for their timely service. I also enjoyed the company of my friends at PG Hall and in Applied Optics Department.

My first meeting with Prof. S. K. Saha (Ex-Chair, B.G.S), Mr. A. P. Monnappa and Mr. A. Narasimha Raju is still memorable. I would like to thank all of them for taking care of us both on the Campus and in the hostel during our temporary stay at Bengaluru. Special thanks to Mr. Shankaranarayanan, B.G.S, who is always helpful in forwarding official forms. I also thank all the B.G.S members for helping in resolving various administrative procedures during the course.

I am grateful to IIA teachers who introduced me to Astronomy. I would like to convey my thanks and regards to Prof. S. Annapurni, Assoc Prof. U. S. Kamath, Prof. S. K. Saha, Prof. K. E. Rangarajan, Prof. Arun Mangalam, Assoc Prof. Gajendra Pandey, Assoc Prof. Sivarani, Prof. A. Satyanarayanan, Prof. R. Ramesh, Dr. J. P. Lancelot, Prof. A. K. Saxena. Thanks to all B.G.S members for conducting the Internship Programme in the 3rd Semester. This help us to get ourselves introduced to IIA staff at various Labs and field stations. I am thankful to Assoc Prof. Muthu Mariappan, In-charge of VBO for his constant motivation during the stay at Kavalur. Special thanks to Mr. Mark, The University of Arizona for explaining the functionality of DIMM telescope. All Engineers at Kavalur are thanked for useful interactions. Thanks to Dr. J. P. Lancelot and Prof. A. K. Saxena for explaining various facilities at the Photonics Division within IIA Campus.

My heartfelt wishes and thanks to all workers at Gauribidanur Radio Astronomy field station; Mr. Siddaraju, Mr. H. S. Subramanyam, Mr. Jaya Shankara, Mr. H. S. Shivaji, Mr. Ramakrishna, Mr. R. Shivaji, Mr. R. Subramani, Mr. Narashima Murthy, Mr. Wazeed, Mr. H. N. Srinivasa Murthy, Mr. Siddappa, Mr. Chandra and Mr. Govinda. The installation of the spectrograph, as well as spectropolarimeter facilities, was successful because of their hard work and priceless effort. I enjoyed the company of my friends at Gauribidanur; I thank Mr. M. Rajalingam, Mr. Indrajith Barve, Mr. R. Rajesh, Mr. Santhosh, Mr. Nagendra Kumar, and Mr. Naveen Kumar for their Immense contributions in setting up the array as well. I would like to appreciate the efforts of all the cooks Mr. Paul Raj, Mr. Rame Gowda, Mr. Krishnamurthy (Late), Mr. Prakash, Mr. Anand and Mr. Venkatesh, who are dedicated

to delivering the food at Canteen as well as the guest house. I enjoyed the company of Mr. Sasi Kumar Raja, Mr. K. Hariharan and Mr. Gireesh G. V. S in the guest house. I would like to thank Mr. Gireesh G. V. S especially for his assistance in proofreading this manuscript. Loved the conversations with Mr. Nakkeran of BARC, enjoyed the company of all friends and buddies at the BARC guest house who are good companions at off work times. I also enjoyed the company of my junior friends especially Mr. Mayuresh Sarpotdar, Mr. Mugundan Vijayaraghavan, and Ms. Anshu Kumari. I also like to thank project student Ms. Sargam M. Mulay for assisting me in research work. Thanks to graduate intern Ms. Srimathi H. A, Ms. Anitha Ravishankar for helping in short term projects. It's hard to mention everyone with a name, but their contributions are never forgotten. I am indebted to one and all who helped me either directly or indirectly to complete my thesis work; I thank all of them.

I dedicate this thesis to my parents and sisters.

P. Kishore

Abstract

Energetic emission from the Sun can be divided into two broad categories, viz. gradual and impulsive. It is inferred from white-light observations that the first group is associated with mass ejections from the solar corona (i.e., coronal mass ejections or CMEs) whereas the second one is more likely related to flares. Near simultaneous spectral observations at low radio frequencies show that above white-light transients are associated with different types of radio bursts (viz. Type I, II, III, etc.). Since the latter are the signatures of shock waves, particle acceleration, etc. in the outer solar atmosphere, one can use radio spectral observations to study the properties of the coronal medium, the above transients, etc. over different phases of the solar cycle. Since the solar corona is a plasma medium which is at a temperature of about a million Kelvin, there is a significant amount of radiation at radio frequencies. Because of the gradual fall of density with increasing distance from the center of the Sun, the frequency of radio radiation also follows the same trend. The observed radio emission from these bursts is best detected in the frequency range of 440−40 MHz. These frequencies are of particular interest as they typically correspond to a radial height of ≈ 1.1 to 2 $R_\odot$ (density model dependent and $R_\odot$ is the photospheric radius) in the Solar atmosphere. This height range mostly remains as unexplored till date. Therefore, building a broadband low-frequency radio spectrograph is crucial; in this regard, we recently developed and commissioned a Low-frequency Solar Spectrograph at the Gauribidanur observatory called the Gauribidanur LOw-frequency Solar Spectrograph (GLOSS). This thesis work includes the design, and development of a broadband antenna (Log−Periodic Dipole Antenna) which is the primary or the front-end receiver of the GLOSS. Various tests such as tuning of the antenna (matching the antenna impedance throughout the band), characterization of front-end amplifiers, coaxial cables, delay systems used are discussed elaborately. Also, programming the data

acquisition modules, testing and calibration methodology are described.

The coronal magnetic field plays a very crucial role in triggering the aforementioned coronal transients; therefore, it becomes necessary to estimate the strength of the associated coronal magnetic field (**B**) towards predicting the location and time of onset of such events in the context of space weather. The sudden, unpredictable changes in the latter can lead to ground base communication disruption, long-duration power outages, space-borne system failures, etc. There are only a few direct measurements of **B** available so far, that too only over the inner corona ($r \leq 1.2$ $R_\odot$). Faraday rotation measurements are used in the outer corona ($r > 3$ $R_\odot$). Similar estimates are not available in the middle corona (1.2 $R_\odot < r < 3$ $R_\odot$) due to a variety of reasons. Towards addressing this, a new spectro-polarimeter called the Gauribidanur RAdio Spectro-Polarimeter (GRASP) has been newly installed at the Gauribidanur observatory. Making use of the newly developed LPDAs (40−440 MHz) a traditional adding interferometer has been set-up with two identical antennas orthogonal to each other. The signals from them are combined using a quadrature power combiner in order to detect the circular polarization (classical method). In this way, the weakly polarized radio emission from the solar corona are detected over a broad frequency regime, i.e., 40−400 MHz, which will cover almost the middle corona. The description of the front-end, back-end receiver systems, data acquisition modules, calibration methodology is presented.

Using the above facilities, viz. GLOSS and GRASP new results are obtained. For example, the salient features of various types of radio bursts and their emission mechanism, estimation of the coronal magnetic field **B**, etc. The radiation mechanism of slowly drifting radio bursts called moving Type IV (or Type IVm) bursts was studied carefully, and we believe that our suggestions would highly be useful to contemporary researchers. Also, systematic statistical studies were carried out on Type III, Type IV & Type V by supplementing the data obtained with on-board instruments like i) the Solar

& Heliospheric Observatory (SOHO), Large Angle and Spectrometric Coronagraph Experiment (LASCO), ii) CME positional information from Solar TErrestrial RElations Observatory (STEREO), iii) Soft X-ray flux from Geostationary Operational Environmental Satellite system (GOES) and iv) Soft X-ray imaging from Reuven Ramaty High Energy Solar Spectroscopic Imager (RHESSI). Estimation of magnetic field strengths at the location of Type II radio bursts is made using appropriate density values. Therefore, the results will be less biased to the selection of density model. By combining radio imaging observations from Gauribidanur RAdioheliograPH (GRAPH) and white-light imaging observations with LASCO-C2 one can understand the CME associated non-thermal emission in a better manner is highlighted. The spectral class and polarization strength determination using GLOSS and GRASP may extensively be used to study various kinds of coronal radio emission in detail is suggested finally.

List of Publications

Published/Accepted in refereed journals (till date)

1. *Constraining the solar coronal magnetic field strength using split-band Type II radio burst observations*, **P. Kishore**, R. Ramesh, K. Hariharan and C. Kathiravan *Manuscript submitted to Astrophysical Journal*.

2. *Spectropolarimeter observations of the low-frequency Type V solar radio bursts*, **P. Kishore**, R. Ramesh, C. Kathiravan, E. Ebenezer, H. A. Srimathi, Anitha Ravishankar *Manuscript submitted to AGU, Space Weather Journal: SI*.

3. *A Low-Frequency Radio Spectropolarimeter for Observations of the Solar Corona*, **P. Kishore**, R. Ramesh, C. Kathiravan C, M. Rajalingam M, *Solar Physics*, 2015 Sep 1;290(9):2409-22.

4. *An Estimate of The Coronal Magnetic Field Near a Solar Coronal Mass Ejection From Low -Frequency Radio Observations*, K. Hariharan, R. Ramesh, **P. Kishore**, C. Kathiravan, and N. Gopalswamy, 2014, *The Astrophysical Journal*, 2014 Oct 9;795(1):14.

5. *Gauribidanur Low−Frequency Solar Spectrograph*, **P. Kishore**, C. Kathiravan, R. Ramesh, M. Rajalingam, and Indrajit V. Barve, *Solar Physics*, 2014 Oct 1;289(10):3995-4005.

6. *Low−Frequency Observations of Drifting, Non-Thermal Continuum Radio Emission Associated With The Solar Coronal Mass Ejections*, Ramesh, R., **P. Kishore**, Sargam M. Mulay, Indrajit V. Barve, C. Kathiravan, and T. J. Wang, 2013, *The Astrophysical Journal*, 2013 Oct 31;778(1):30.

Conference Proceedings

1. *Gauribidanur Radio Spectropolarimeter*, **P. Kishore**, R. Ramesh, C. Kathiravan, and M. Rajalingam, *MetreWave sky conference series*, February 20–22, 2013.

2. *A preliminary scheme to modify the reception characteristics of a log-periodic antenna within its operating bandwidth*, **P. Kishore**, C. Kathiravan, *Astronomical Society of India Conference Series*, December 9–13, 2013.

Table of Contents

List of Figures

List of Tables

Chapter 1

Introduction

SUN is the nearest star to us, and hence it is relatively easy to study and to understand different kinds of astrophysical processes that take place therein as compared to other celestial objects. Plasma processes dominate in all radiative astrophysical objects including the Sun. Since we cannot mimic most of those processes on the Earth, the Sun serves as an excellent natural plasma laboratory. The plasma processes act as drivers of various transient energy releases that take place in the inner/lower corona ($r \lesssim 1.2$ $R_\odot$, where $R_\odot \approx 6.95 \times 10^5$ km is the photospheric radius) of the Sun. The energy release is observed to be present in almost all wavelengths of the electromagnetic (EM) spectrum. Examples of such activities are Solar Flares, Solar Energetic Particles (SEPs include Solar Wind), Jets and Coronal Mass Ejections (CMEs); these events release several tons of charged particles, radiation, etc. into the interplanetary medium. Apart from plasma processes, thermal bremsstrahlung, gyro-magnetic processes, etc. can also generate a broad range of emission in EM spectrum. It is, therefore, important to study and predict these transients to understand their geophysical consequences. An overview of all these processes and their impacts are discussed in the following sections.

1.1 Overview of the Solar activities

Figure 1.1 shows the cross section of different layers/zones inside the Sun, large-scale features on the solar surface, and the associated EM emissions. Most of the Sun's energy is generated in the interior layer [known as the *Core*] mainly by thermonuclear reactions. In each reaction, the Hydrogen (71 % of the Sun's composition) atoms fuse to form Helium and a little amount of energy released in the form of EM radiation. Such reactions keep the core to be at a temperature of $\approx 15 \times 10^6$ K and pressure of $\approx$ 340 billion atmospheres [Christensen-Dalsgaard et al. (1996)]. The energy thus generated will be transported to the outer layers by means of conduction, radiation, and convection.

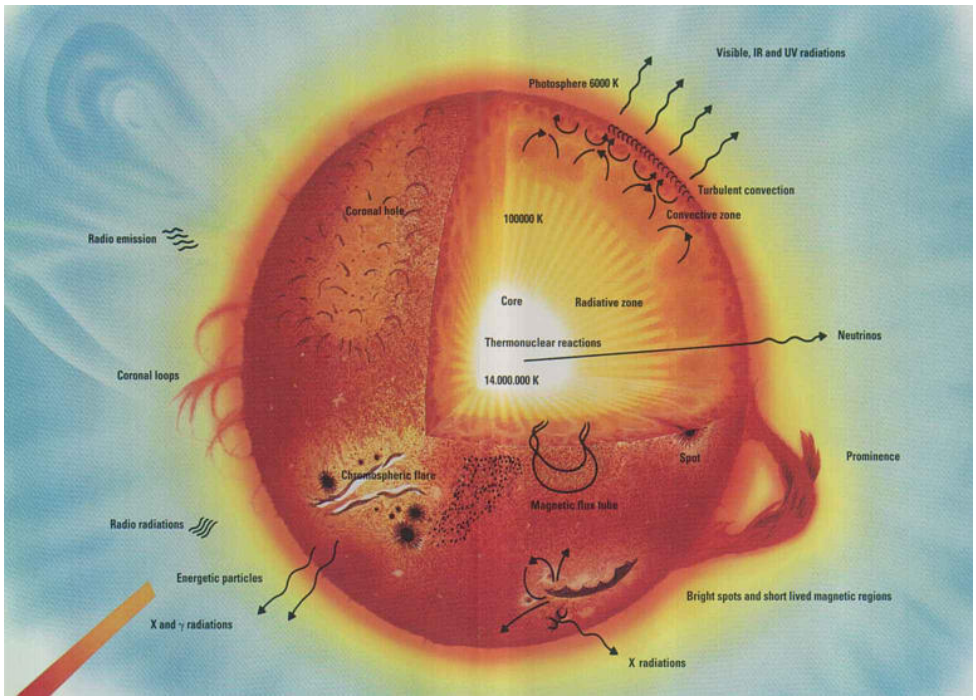

Figure 1.1: Graphical representation of different layers of the Sun and various features present there. The associated emissions observable in different parts of the electromagnetic spectrum are illustrated. Image Source: `http://solarviews.com/cap/sun/sundiag.htm`
(Courtesy NASA/ESA)

The *Core*, which is super-hot and dense radiates high energy $\gamma-$rays and spews out neutrinos, the by-products of the nuclear reactions. At the core, the temperature and radiation follow the laws of black-body radiation. The energy is transported outwards

by radiation (i.e., by photons). The temperature and pressure gradually decrease to a spherical region of a shell whose radius is $\approx \frac{1}{4}^{\text{th}}$ of the visible photospheric radius. The annular region between $\approx \frac{1}{4}^{\text{th}}$ to $\approx \frac{3}{4}^{\text{th}}$ of radius is known to be the *Radiative region* where the transport of energy is mainly due to radiation. The spherical zone above the radiative zone and extends its boundary to visible photosphere is said to be the *Convection Region*. As the plasma density and pressure decreases radially outwards, so as the temperature change across the region. Over the edge of the radiative zone, the temperature drops to $\approx$ 2 million Kelvin; at this temperature partially ionized heavier atoms such as carbon, nitrogen, oxygen, calcium, and iron make the surface opaque to the radiation. The heated plasma in this region is being brought to the top by *Convection*. The material thus cools down by radiating the energy into space. Therefore, over the outer edge of the convective zone to the boundary of visible photosphere the electron temperature drops significantly to $\approx$ 5700 K [Fludra et al. (1999)]. This spherical boundary over which the visible photons start to escape defines the *Photosphere*. The edge of the photosphere appears to be fainter when compared to the disk brightness at visible wavelengths due to *limb darkening* effect [Pierce and Slaughter (1977)]. This is nothing but the boundary at which the *optical depth*, a ratio of photons which are not being scattered or absorbed during their course of travel from the core, falls to a proportion of $\frac{2}{3}$. White-light observations of the photosphere confirm a variety of features such as *granules, super-granules, sunspots & faculae*. Due to the convective motion in the photosphere, the rising and sinking boiling plasma forms *granular* network. They resemble the cell-like structures with a typical size of $\approx$ 1000 km. *Supergranules* ($\approx$ 35,000 km) are the large scale version of granules; they form much above the granular network and spread all over the Sun. *Sunspots* are the dark features seen on the visible surface as they are at a relatively low temperature (non-convecting regions) compared to ambient medium. They are the regions of intense magnetic field on the Sun. The magnetic field originates as a result of the flow

of charged particles and ionized gasses in the medium that constitute electric currents which in turn generate the magnetic field [Parker (1955); Babcock (1961); Gough and McIntyre (1998)]. Also, the non-uniform rotational motion of the photosphere from its equator to poles forms densely packed regions of plasma known as *active regions*. Therefore, the active regions/sunspots are the regions on which the powerful magnetic fields are anchored to the photosphere. Their population increase/decrease over a period of 11 years, with a peak in between. This phenomenon is known as the *magnetic cycle*. The active regions reconfigure among themselves or with nearby regions in a sidereal rotation period of $\approx$ 26 days. The *faculae* are the less dense magnetic field regions which appear bright in white-light images. All these features appear differently at other wavelengths. The thermal black-body radiation from the photosphere also lies in near infra-red (NIR) range. The magnetic field loops in the active regions are best observed at Extreme Ultra Violet (EUV) and X-ray wavelengths. Above the photosphere, there is a thin overlying layer of the atmosphere (spreads over few hundreds of kilometers of radius) known as the *chromosphere*. The temperature in the chromospheric region rises to 20,000 K (due to unknown reasons). At this temperature, the chromosphere emits in H-alpha (6562.8 Å) wavelength.

1.1.1 The Solar Corona

Further above the chromosphere, the transition region exists which is a thin layer between the chromosphere and the inner corona. Again, because of unknown reasons the temperature rises abruptly to 10^6 K in the corona. The corona is faint by several orders of magnitude as compared to the photosphere. Only during eclipses, it is partially visible when the moon occults the bright photospheric disk. The scattered photospheric light is classified into three principal components. They are i) *K-corona* or the electron/continuum emission corona which is due to the scattering of photospheric

light by high energy electrons; ii) *Fraunhofer Corona*, which is mainly due to the scattering by dust particles in the ecliptic plane; iii) *Thermal Corona*, which is due to the emission of the thermal energetic particles in the corona. Since Eclipses are rare phenomena, artificial coronal occulters in the form of coronagraphs are deployed in space [for example, the LASCO coronagraph on-board the Solar & Heliospheric Observatory (SOHO), the STEREO-A and STEREO-B coronagraphs on-board the Solar TErrestrial RElations Observatory (STEREO), etc]. Both space based, and eclipse observations of these components reveal different coronal structures such as *streamers, coronal loops* above the active regions of sunspots and *coronal holes* of the quiet Sun region. Normally the Coronal holes are regions of less electron density associated with areas of open magnetic field lines. The Coronal holes appear dark in contrast to the magnetic field loops at X-ray wavelengths. The extension of coronal plasma into interplanetary space is said to be *Solar wind*. Most of the acceleration of solar wind takes place in coronal holes.

As mentioned earlier the *Corona* is a tenuous plasma (an ionic medium with no net charge) medium that extends its boundary till the *heliopause*, i.e., the spherical outer boundary of the solar system. The electron number density decreases radially outward from the center of the Sun so as the plasma frequency [based on equation (1.1)]. Figure 1.2 shows the electron density and plasma frequency as a function of heliocentric distance since both are related to each other [Tonks and Langmuir (1929)] by the following equation:

$$f_p \approx 9 \times 10^3 \sqrt{N_e} \tag{1.1}$$

where N_e is the electron number density (cm^{-3}), f_p is the plasma frequency in Hz. There are various plasma density models [Baumback (1937); Allen (1947)] which are empirically derived using eclipse observations to determine the radial dependence of

N_e and f_p. As per equation (1.1) the high-frequency radio emission originates from the inner regions of the corona whereas the low-frequency emission emanates from the outer regions.

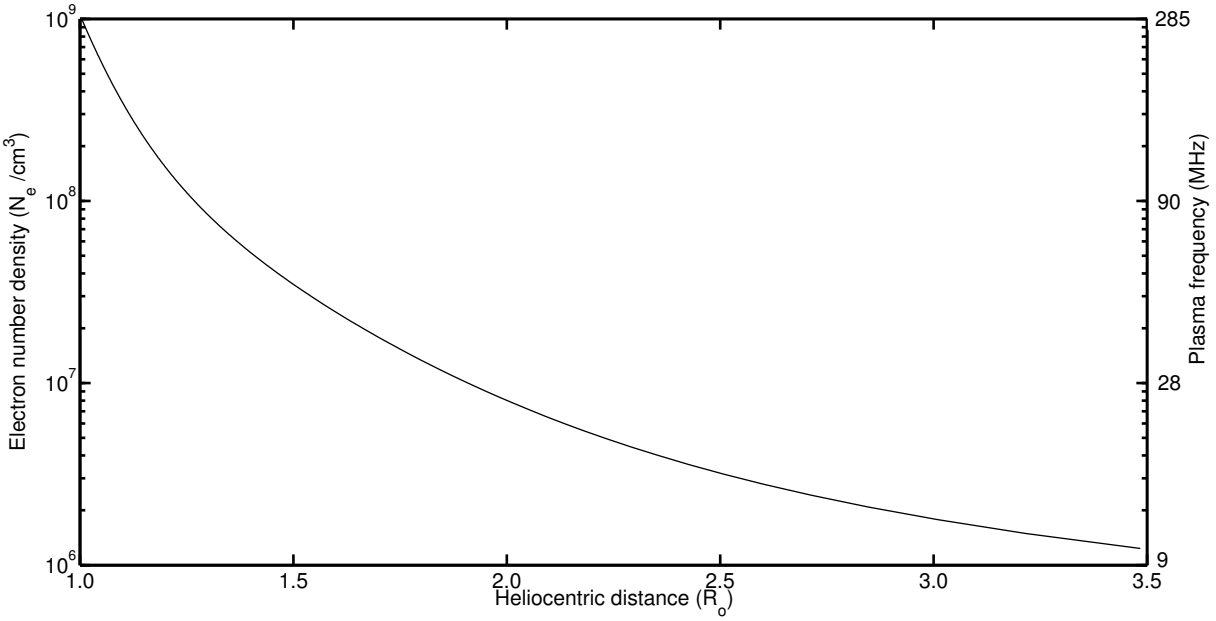

Figure 1.2: Electron number density and the corresponding plasma frequency as a function of heliocentric heights for a ten-fold Baumbach-Allen [Baumback (1937); Allen (1947)] density model.

The strength of the radio frequency emission from the corona is closely associated with the dynamic evolution of active coronal structures such as coronal *helmet streamers, prominences, plumes, Coronal mass ejections*, etc. (refer Section 1.2.1). The magnetic field confines most of plasma material in these structures. Observed transient energy releases like *jets, flares, Coronal Mass Ejections (CMEs)* are triggered as a result of magnetic reconnection (the reorganization of the magnetic field after getting twisted and reunited with the neighboring field) activities in the proximity of interacting active regions.

1.2 Motivation

During the progression of the above-mentioned transient processes, high energy particles from the corona (in addition to *the Solar Wind*) are expelled into the interplanetary space. If the latter is directed towards the Earth, severe threats to the technological systems deployed in space are more likely since their effects are rather harmful. So it is important to study these transient activities in the context of *Space Weather* which is defined according to the U.S. National Space Weather Plan as *the conditions on the Sun and in the solar wind, magnetosphere, ionosphere and thermosphere that can influence performance and reliability of space−borne and ground−based technological systems and that can affect human life and health* [Schwenn (2006)]. Therefore forecasting the space weather becomes an important task towards safeguarding the technological systems. As drivers of many of these events mainly originate in the corona, studying their associated radio emission would be of great help in realizing the above goal.

1.2.1 CMEs & geomagnetic storms

The CMEs are large-scale transient explosions that occur in the outer atmosphere of the Sun. They contain huge mass [$\approx 10^{15}$ g; Jackson and Howard (1993)] of magnetically confined coronal material (including radiation), which eventually get detached from the solar surface and enter into the interplanetary space. They propagate outward through the ambient corona at speeds ranging from $\approx$ 100 to 2500 km/s [Gopalswamy et al. (2000)].

The ejected plasma consists primarily of electrons and protons, with small quantities of heavier elements such as Helium, Oxygen, and Iron. Magnetic reconnection (as described earlier) is primarily responsible for the high amount of mass and energy release during these ejections. Coronal Mass Ejections disrupt the flow of the solar wind

and produce disturbances in the Earth's atmosphere when an ejection is directed towards the Earth. Since the CME plasma enters into the Earth's medium with high speed and density, it causes ionospheric disturbances which ultimately lead to shock wave generation, etc.; This is defined as the onset of a geomagnetic storm. The latter can disrupt radio transmissions and cause damage to space communication and electrical transmission systems, resulting in long-lasting power outages and other socio-economic losses (exposure of humans in space or at high altitudes, in air-crafts, etc.; to this intense radiation). Auroras around Earth's polar regions is also an effect of this phenomenon. Therefore, forecasting the onset of CMEs and other coronal transients (different types of radio bursts) at their early stage becomes inevitable to get rid of the above catastrophic effects.

Therefore, continuous monitoring of conditions of solar wind, charged particle emissions around the clock is necessary to predict the conditions of Geo-Space weather or Space weather. The X-ray telescope (XRT) on-board Hinode [Golub et al. (2007)] and the X-ray spectropmeter on-board RHESSI [The Reuven Ramaty High-energy Solar Spectroscopic Imager mission; Lin et al. (2004b)] are a few dedicated instruments to study the high-energy X-ray emissions of lower corona. Coronagraphs (artificial occulters that block the photospheric light to see the corona alone) are used to study the coronal structures in white-light. Studying the radio radiation from the corona is advantageous as one can simultaneously observe the features both on the disk as well as off the limb. Also, one can have high temporal and spectral resolution with radio observations, which are crucial to study solar transients. Therefore, the primary objective of this thesis is i) to develop new instruments to observe the solar corona with high spectral and temporal resolution both in total and polarized intensity; and ii) to bring out interesting results by combining the new radio data with those obtained at other wavelengths.

1.3 Radio emission from the Sun

Most of the metre-wave radiation originates from the middle corona (1.2 $R_\odot < r <$ 3 $R_\odot$) whereas the longer wavelength radiation comes mainly from the outer corona ($r >$ 3 $R_\odot$). The high-frequency emission observed at decimeter wavelengths comes from the inner corona ($r \leq$ 1.2 $R_\odot$). The radio emission is primarily due to *plasma emission* which involves the conversion of plasma/electrostatic waves into escaping electromagnetic radiation either at the fundamental or harmonic frequencies [McLean and Labrum (1985)]. Radio emission from the Sun can be broadly classified into two types: 1) Gradual and 2) Impulsive.

1.3.1 Gradual

This component is due to thermal processes, and therefore the emission (as a function of frequency) follows the black body spectra (Rayleigh-Jeans Law). This type of radiation is expected at the non-flaring time from active regions, or the constant background emission of the Sun whose peak brightness temperature is $\approx 10^6$ K. Example of such a process is the thermal *bremsstrahlung* which is a free-free emission due to incoherent plasma processes. This gradual component is usually periodic with the sidereal period of the Sun. Most of the quiet Sun observations were extensively studied by Smerd (1950). There is also a slowly varying component (*S-Component*) of radiation mainly observed in the mm range wavelength which is primarily attributed to emission from the active regions.

1.3.2 Impulsive

This type of radiation is purely transient in nature (also called radio outbursts) and is observed mainly at metre wavelengths. The estimated equivalent brightness temperature

lies in the range $10^{12}-10^{14}$ K. These transients are observed over a broad frequency range (few MHz−few GHz). Depending upon the temporal and spectral occupancies, they are further divided into five types [Wild et al. (1963)].

1.3.2.1 Classification Radio out-bursts

Type I: These are spiky, narrow band, and short-lived (1s) bursts; but the spread in frequency is very large, and they appear like a continuum. These bursts last for hours and are not associated with flares. Most of them are circularly polarized ($\approx$ 100%) in Ordinary mode [refer magneto-ionic theory by McLean and Labrum (1985)].

Type II: This type shows a slow drift rate from high frequency to low-frequency. Both fundamental and harmonic emission can be seen clearly in some cases. These are associated with mass motion and shock waves inside the coronal plasma.

Type III: These are most frequently occurring bursts which last for a few seconds (high drift rate) and tend to occur in isolation or groups. Electrons that move relativistically along the open magnetic field lines are responsible for this type of burst.

Type IV: a) Stationary Type IV (or Type IVs): A storm that follows a major flare is responsible for this continuum emission; it develops into Type I storm later on.

b) Moving Type IV (or Type IVm): It also belongs to continuum storm but fades away as it progresses into the interplanetary medium.

Type V: This is a combination of continuum followed by a series of Type III bursts that last for few minutes.

There is another form of radio emission process called *gyro-magnetic* process. It is due to the gyration of electrons along the open magnetic field lines. Depending upon the relativistic speed of the spiraling electrons the emission can be *gyro-synchrotron* (mildly relativistic 100 keV−300 keV) or *synchrotron* (highly relativistic $>$ 300 keV). The

optically thin gyro-emission is also expected at its harmonics and are mostly circularly polarized.

Radio imaging observations of the Sun may be limited by angular resolution, but are highly rich in temporal and spectral resolutions. Probing different layers of the Sun with high spectral and temporal resolutions may enable us to understand the characteristics of the highly transient activities take place there. Since, magnetic field plays a crucial role in all sort of energy release processes its measurement is considered to be one of the important holy grails in solar physics.

1.4 Sun and Galactic background

There is significant non-thermal emission from the Center of our Galaxy (GC). This emission is believed to be due to synchrotron mechanism and has a spectral index of -2. Therefore, obviously the Sun and the Galactic background are the strongest radio sources in the electromagnetic spectrum. Also, from Figure 1.3 the emission from the active Sun is higher in several orders of magnitude as compared to GC. These measurements are obtained from in-situ instruments on-board space missions as well as from several ground-based observatories. The low-frequency cut-off is attributed to the ionospheric electron content and its plasma frequency. Also, the observations of high-frequency counterparts are limited by the absorption by water vapor and other molecules. Observations of GC on a long-term basis can be helpful to calibrate the radio spectral and spectro-polarimetic observations. The detailed methodologies and their application to particular bursts are covered in this thesis.

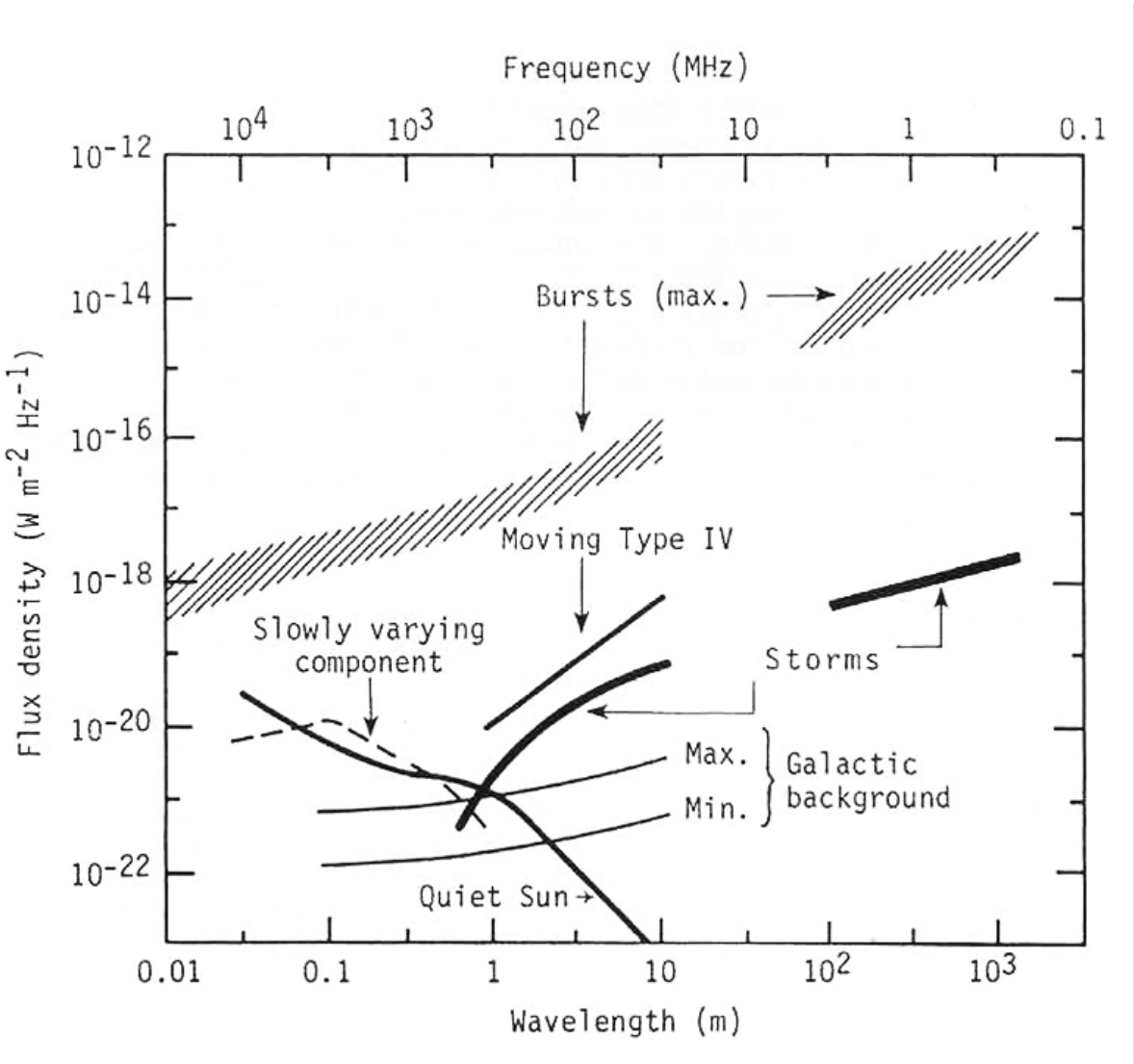

Figure 1.3: Schematic showing different types of radio bursts, their wavelength extent, and the flux densities as compared to the galactic background emission. Image Source: `https://web.njit.edu/~gary/728/Lecture10.html`

1.5 Flares in X-ray and White-Light Versus Radio bursts

Solar flares are one of the important activities in which sudden [fraction of seconds(s)] release of energy ($\approx 10^{27}$ ergs/s) almost over the entire EM spectrum takes place. In white-light data, a flare can be seen as an intense patch of emission over the photospheric disc. Sometimes flares may also occur in isolation (i.e., without any association with CMEs or radio out-bursts). Flares can be studied better with X-rays; the latter mainly originates in the corona. Depending on the energy the X-ray flares are classified into different categories viz B, C, M & X class in ascending order of energy[1]. During these flares, high energy particles are accelerated to near relativistic speeds which can trigger all the transient processes. For example, the high energy X-class flares can create radio block-outs (failure of HF communication) as they trigger broadband radio continuum and particle emission. It is due to the increase of total electron content in the ionosphere because of additional particle injection by flares.

1.6 Thesis Outline

This thesis is intended to develop radio observing facilities with which the solar coronal transients can be observed with high sensitive, spectral and temporal resolution. This is inevitable to study the salient features of different kinds of radio bursts that originate in the lower and middle solar corona in greater detail. Therefore, the thesis covers the design and development aspects of the front-end and back-end receiver systems for dedicated solar facilities and the analysis of the radio data observed with them followed by the respective scientific results.

Chapter 2 describes the method of developing a broadband antenna especially a Log-periodic Dipole Antenna (LPDA). It includes design aspects, field tests, and other

[1]http://spaceweather.com/glossary/flareclasses.html

relevant results. It also discusses the RFI mitigation technique by slightly modifying the configuration of a usual LPDA to reduce the contribution of RFI at the earliest possible stage of a radio antenna setup. Commissioning of a broadband spectrograph at the Gauribidanur observatory called *Gauribidanur LOw-frequency Solar Spectrograph (GLOSS)* using the above LPDA is described in the latter part along with details of the front-end and back-end instrumentation, control software and calibration techniques developed to characterize the entire system. One of the observed split-band type-II radio burst spectrum was chosen as a sample to demonstrate how the data can be used to determine the associated magnetic field strength by combining the radio spectrum with white-light and radio imaging observations and a suitable electron density model for the coronal medium. It should be noted that estimating the magnetic field strength in the lower and middle corona using observations other than radio wavelengths is highly difficult because of various technical reasons. Therefore, as mentioned earlier, developing such solar-dedicated radio facilities and determining coronal parameters using the observed data assume significance in the above context.

In **Chapter 3**, the observations of 4 split-band Type II bursts are elaborated. Since they were believed to be due to CME related shocks, they were used to determine the strength of the associated CME magnetic field. Estimates of them were verified by constraining the density model chosen and therefore, the estimates are less likely biased on the density model.

Chapter 4 covers observations, analysis and results of three slowing drifting Type IVm bursts, observed with the GLOSS. The emission mechanism for them was suggested by combining radio, White-light, EUV and X-ray observations. Magnetic field estimates of these bursts were obtained, and conclusions were drawn about the emission mechanism responsible for Type-IVm bursts.

Chapter 5 discusses the need for a broadband spectro-polarimeter to complement spectrograph observations. The details of the spectro-polarimeter, its various front-end

and back-end receiver modules, and commissioning of the array are described. A novel method of calibrating the ground-based spectro-polarimeter is also discussed with examples. Furthermore, the procedure of identifying the sense of circular polarization is explained.

Chapter 6 describes 4 Type V radio bursts, the determination of their lifetimes, the associated magnetic-field strength(s), etc., using their polarization spectra and their relationship with X-ray flares. Results obtained are used to model the radial dependence of the magnetic field especially in the middle corona. These results also assume significance in the context of coronal magnetic field estimation, as mentioned earlier.

Chapter 7 concludes the thesis with remarks, summary and future scope of improving the existing facilities at the Gauribidanur Radio Observatory especially GLOSS and GRASP.

Chapter 2

Antenna Design, Development & Characterization

The contents presented in this chapter are based on the following publications

1. *Gauribidanur Low−Frequency Solar Spectrograph*

   P. Kishore, C. Kathiravan, R. Ramesh, M. Rajalingam, and Indrajit V. Barve, *Solar Physics*, 2014 Oct 1;289(10):3995-4005.

2. *A preliminary scheme to modify the reception characteristics of a log-periodic antenna within its operating bandwidth*

   P. Kishore, C. Kathiravan, *Astronomical Society of India Conference Series*, 2013, vol 9, pp 140.

3. *Design of a Broad Band Antenna System (40 to 500 MHz) for the Spectral Observations of Solar Corona*

   P. Kishore, Masters Thesis, 2011, IIA.

2.1 Introduction

ANTENNA is a device used to transmit, receive or transceive electromagnetic (EM) radiation, especially in the radio and microwave frequency regime. They are widely used in telecommunication industry, navigation systems, space-based systems,

military, and other innumerable number of applications. In this chapter, the principles of radiation from an antenna and the associated parameters are discussed (test and measurements of various parameters). *Antenna is a structure associated with the region of transition between a guided wave and a free-space wave, or vice versa* [Kraus and Marhefka (2001)]. It also does the action of a transducer. That is, it converts electrical energy to EM energy in the case of transmission, and vice versa during the reception. It can also be viewed as an impedance matching device between the free space and the transmitter/receiver or vice-versa. Moreover, it is used to boost/suppress the RF energy in desired/undesired directions.

2.1.1 Working principle

2.1.1.1 Transmission lines & Antennas

A transmission line is nothing but a medium to guide the electromagnetic/RF energy. Co-axial cable, wires, waveguides and optical fibers are examples of transmission lines. The electrical properties of a transmission line changes drastically with length and operating frequencies [refer distributive networks in Jordan and Balmain (1968)]. The characteristic impedance (Z_o) of a transmission line is the ratio of an infinite line voltage to the line current. Also, the power from a source to load is maximally transferred if the latter is terminated with the line's characteristic impedance. An antenna is nothing but an open-ended transmission line through which the guided RF energy is released into free space. The characteristic impedance of any antenna has to match with the source impedance ($|Z_s|$) as well as the free space impedance to efficiently transceive the EM radiation.

2.1.1.2 Antenna radiation

Generally, any piece of conducting wire/structure acts as an antenna, but the radiation characteristics greatly vary according to the dimensions of the structure involved. Basically an alternating current element (of vector electric and magnetic potential) is responsible for electro-magnetic radiation which is obvious from the famous Maxwell's equations. The time varying current produces alternating electric and magnetic fields in its vicinity. The space and time rate of change of such fields lead to propagation of EM radiation. In order to have an idea of radiated E and H fields, knowing the current distribution in the associated structure becomes important; also, it gives an indirect estimate of the impedance of the structure which is an important parameter to understand the antenna performance. It is difficult to find the current distributions in complex geometric structures with complicated boundary conditions. Also, not all structures radiate as efficiently as they are designed for; one has to account for various other losses to make it highly radiative. Therefore, identifying an appropriate structure/antenna that transmits/receives efficiently in the desired direction and bandwidth is one of the important tasks in designing a radio receiver system.

2.2 Antenna Bandwidth

Antenna bandwidth is defined as the range of frequencies over which the antenna characteristics (transmission/reception) are optimal. These include the structure characteristic impedance, radiation parameters like beam widths, effective collecting area, etc. These characteristics are frequency dependent and should not vary with time. This is very crucial, especially for astronomical observations.

Based on the transmission/reception characteristics, antennas can be categorized into many types. If the antenna radiates/receives the maximum power fed to/incident

upon over a broad frequency range (as compared to the operating frequency range of a simple dipole antenna), then it is said to be a broad-band antenna. The maximum power deliverance/reception is achieved only when the impedance of the antenna matches well with that of the feeder/receiver. Practically the impedance of an antenna system is determined with an instrument that can measure the Voltage Standing Wave Ratio (VSWR). Antennas are fed with alternating voltage sources that force the electrons to flow through them. When the current sees the terminal ends, it gets reflected back to feed point. Therefore, the incident and reflected current superimpose and gives rise to Standing wave pattern. The ratio of V_{min} to V_{max} of the standing wave is called as the VSWR, which is an an indirect measure of impedance. This is because the VSWR and the impedance are related to each other, i.e., the VSWR $= \frac{1+\Gamma}{1-\Gamma}$ where Γ is the reflection coefficient of the transmission line and the latter is related to the line (Z_L) and source (Z_S) impedances as $\Gamma = \frac{Z_L - Z_S}{Z_L + Z_S}$; here Z_S is the input impedance of the antenna. The level of reflected current is high in case of larger mismatch. In many conventional antennas such as monopoles, dipoles, Yagi-Uda, etc. the impedance match is found to be over a narrow range of frequencies; therefore they are called as narrow-band antennas. The magnitude of reflected current is not only due to ends, but also depends on the conductor edges and other dimensions.

2.2.1 Broad-band (BB) antennas

If the resultant current (incident+reflected) at the feed terminals is constant and lower in magnitude to that of incident, irrespective of the frequency, the broad−band performance is said to be achieved. Such type of structures has almost identical input impedance, radiation characteristics, etc. throughout the band. According to Babinet's principle [Balanis (2005)] on EM waves, the impedance of any radiating antenna combined with its self-complementary structure becomes frequency independent. One should not

get confused with self-complementary and self-similar structures, as both contradict each other. Some examples of Planar, Non-Planar, Self-complimentary and Self-similar structures are reported briefly in Antenna Theory [Balanis (2005); Jordan and Balmain (1968)]. Although there are many types of BB antennas available one has to choose a convenient type according to the physical and operational constraints one faces at the installation site.

2.3 Log-Periodic Dipole Antenna (LPDA)

There are numerous antennas with distinct radiative properties. Conventional antennas like Dipole, Yagi-Uda fails to work over a broad bandwidth as the impedance falls off on either side of the center frequency as described earlier. V. H. Rumsey developed a theory behind the broadband antennas [Rumsey (1957)]; according to him the geometry of a structure specified entirely by angles will be ideal for broad-bands. The combined principle of angle-only-specified-geometry and self-complimentary structures lead to the development of Log Periodic Structures (LPS). Some examples of LPS are Toothed structure, planar structures, spiral structures, etc. Such structures are designed and developed by DuHamel and Isbell (1966). Initially, LPS were planar structures; later D. E. Isbell modified this structure viz. the two planar structures are folded to obtain a non-planar Log Periodic Dipole Antenna (LPDA) structure. This structure doubled the impedance $(60\pi)^2$ [Kraus et al. (2006)] compared to those earlier structures and also improved the directional property of that antenna. Later R. L. Carrel presented an elaborate mathematical treatment on designing an LPDA [Carrell (1961)]. The response characteristics such as input impedance, VSWR, Radiation pattern of the antenna is a periodic function of logarithm of frequency hence the name LPDA.

2.4 Design of LPDA

An LPDA as shown in Figure 2.1 is nothing but a series of dipoles stacked together to a transmission line systematically such that

$$\frac{L_n}{L_{n+1}} = \frac{S_n}{S_{n+1}} = \tau \tag{2.1}$$

Where τ is the design constant, L_n, L_{n+1} are the length of the adjacent dipole elements, and S_n, S_{n+1} are the successive inter-element spacings.

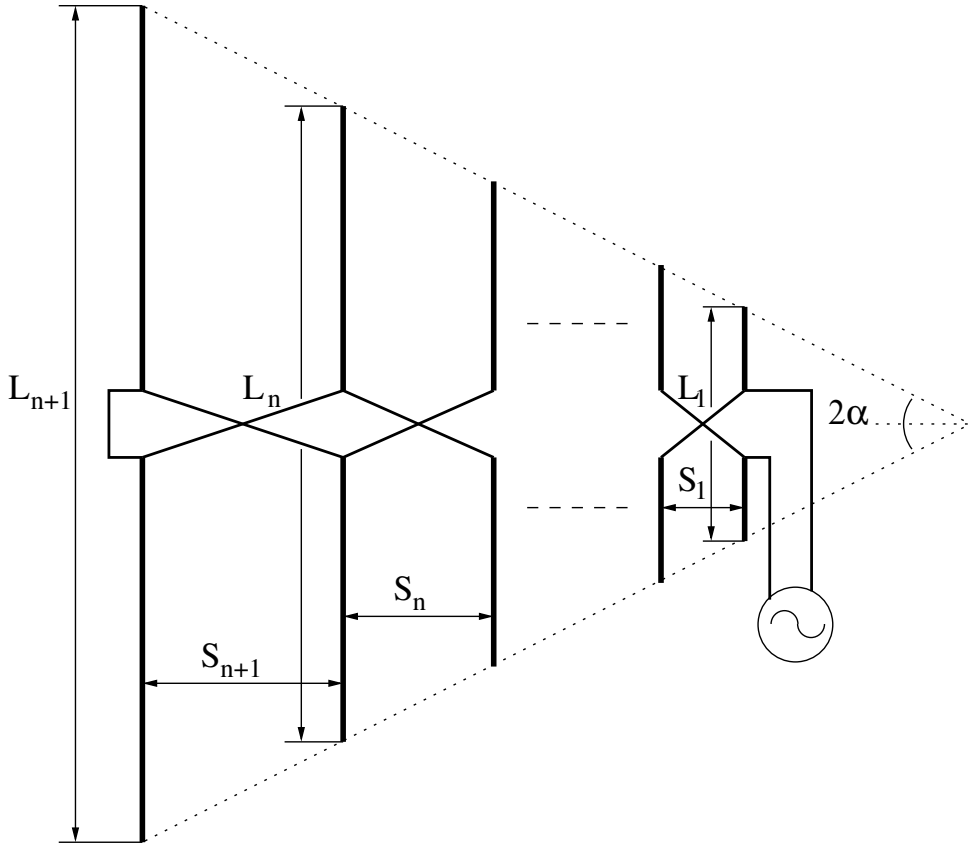

Figure 2.1: Schematic of the Log Periodic Dipole Antenna (LPDA) with an apex angle 2α. The adjacent half wave dipoles are combined in 'Criss-Cross' fashion in order to ensure a phase difference of 180° between the voltage and the current in the adjacent dipoles. As a result, the overall antenna response will be free from cross-talks and interference between adjacent elements.

From the geometry of the structure, one can notice that a triangle can be drawn by

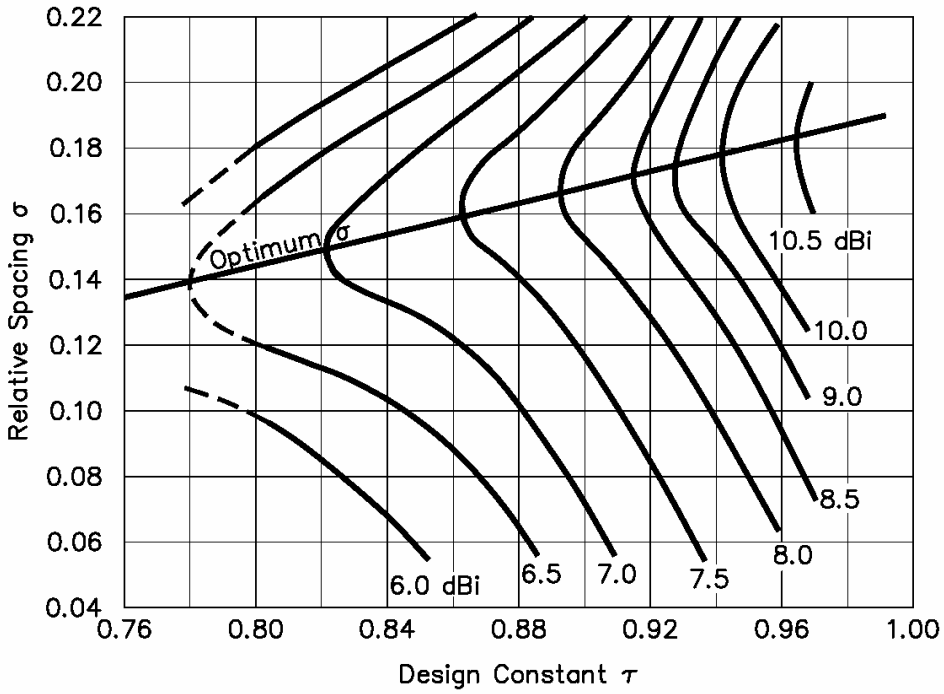

Figure 2.2: Set of design curves obtained by R. L. Carrel. The optimum design corresponds to the one that has a minimum number of dipoles to cover the maximum bandwidth. Such a design is obtained by choosing the parameters from the straight line [$\sigma = 0.243\ \tau - 0.051$].

joining the tips of the dipole elements. If 2α is the semi-apex angle of the triangle then

$$tan(\alpha) = \frac{L_{n+1} - L_n}{4\sigma} \tag{2.2}$$

The half apex angle α and τ (design constant) determines the length and number of arms in the LPDA. Figure 2.2 shows various combinations of τ, σ (spacing factor infraction of the wavelength) plotted against gain values [Carrell (1966); Hutira et al. (2004)].

As shown in Figure 2.1 the successive dipoles ($\frac{\lambda}{2}$ length) are phased 180° with respect to the previous dipole. This is known as Criss-Cross phasing that helps in minimizing the cross talk between adjacent elements. The output is taken from the apex whereas the transmission lines are shorted at the bottom.

2.4.1 Design Methodology

We followed the design methodology as described in Kraus and Marhefka (2001). The steps are:

1. First choose the bandwidth ratio **F** = $\frac{f_{max}}{f_{min}}$. In our case f_{max} = 440 MHz, f_{min} = 40 MHz; $\therefore$ **F** = 14

2. Select the right combination of τ and σ from Figure 2.2 for the required gain of LPDA. For a moderate gain of $\approx$ 7 dBi, one would obtain τ = 0.88, σ = 0.077. One can even choose still lower value of σ for large **F** ratios.

3. Calculate the number of arms as n = $\frac{ln(\mathbf{F})}{ln(\frac{1}{\tau})}$. We got n $\approx$ 19. Further, we added 4 more extra elements to take care for lower and higher frequency cut-off of LPDA. With above values, we obtained $\alpha = 22^{\circ}$

4. Begin with the lower frequency 40 MHz, calculate its $\frac{\lambda}{4}$ length, proceed to next spacing and $\frac{\lambda}{4}$ length by making use of either equation (2.1) or equation (2.2)

5. Finally, tabulate the lengths, spacings, and their resonant frequencies of all arms of LPDA.

2.4.2 Fabrication

The lengths and spacings of dipole arms and their resonant frequencies are given in Table 2.1. The designed antenna is 4.6 m long. The dipoles/arms of the LPDA are made of hollow aluminium tubes whose outer, and inner diameter are 13 mm and 8 mm respectively. A pair of hollow aluminium rectangular booms (of $1'' \times 1''$ cross-section and 4.6 m long with a thickness of 3 mm) acts as the transmission line. The separation (D) between the booms (transmission lines) are chosen such that the feed line characteristic impedance will be 50 Ω using the equation (2.3) of Jordan and Balmain (1968), i.e.,

$$D = d\ Cosh(\pi \frac{Z\sqrt{\epsilon_r}}{Z_o}) \tag{2.3}$$

where d is the diameter of boom = $1^{''}$, Z is the desired characteristic impedance to feed line (= 50 Ω), Z_o is the impedance of free space = 377 Ω & ϵ_r is the permittivity of medium ($\approx$ 1 for air). Plugging the above values, we get the boom separation $D \approx 1^{''}$. The $\frac{\lambda}{4}$ length arms are attached to each boom by M8 screws (Figure 2.3).

The bottom of the transmission line is shorted by U-type short with 10 cm spacing from the longest arm. To achieve better Front to back ratio, the short should be placed at a distance of $\frac{L}{4}$, where L is the length of longest arm [Hutira et al. (2004)]. At 10 cm above the shortest arm, a TNC female connector is fastened to the boom. RG58/U (50 ohms) coaxial cable of length 5 m is inserted in one of the booms. The ends of it are fitted with TNC male connectors. Its one end is connected to TNC male at apex, and the other end is used to connect the test and measuring equipment. The cable ground is connected to the boom in which the cable is running through, and the center conductor of the cable is connected to the other boom for better feed point impedance [Ramesh et al. (1998)]. A good electrical contact with the booms and connector is essential for better VSWR at high frequencies. The two booms are separated by $1^{''}$ spacing (as mentioned above) and are held together by Nylon spacers. Figure 2.4 shows the image of an installed LPDA in field. The arms of the LPDA are supported with the non-metallic arrangement to avoid sagging. The apex is also covered with a nylon cover to protect the feed point from environmental changes.

Table 2.1: Specification of 40-440 MHz LPDA

Dipole no.	Half of the Dipole length ($\frac{\lambda}{4}$ cm)	Spacing (cm)	Freq (MHz)
1	187.5		40.0
		57.7	
2	164.4		45.6
		50.6	
3	144.1		52.0
		44.3	
4	126.3		59.3
		38.9	
5	110.7		67.7
		34.1	
6	97.0		77.3
		29.8	
7	85.0		88.2
		26.1	
8	74.5		100.6
		22.9	
9	65.3		114.8
		20.1	
10	57.2		131.1
		17.6	
11	50.1		149.7
		15.4	
12	43.9		170.8
		13.5	
13	38.4		195.3
		11.8	
14	33.6		223.2
		10.3	
15	29.4		255.1
		9.0	
16	25.7		291.8
		7.9	
17	22.5		333.3
		6.9	
18	19.7		380.7
		6.0	
19	17.2		436
		5.3	
20	15.0		500
		4.6	
21	13.1		572.5
		4.0	
22	11.4		657.8
		3.5	
23	9.9		757.5

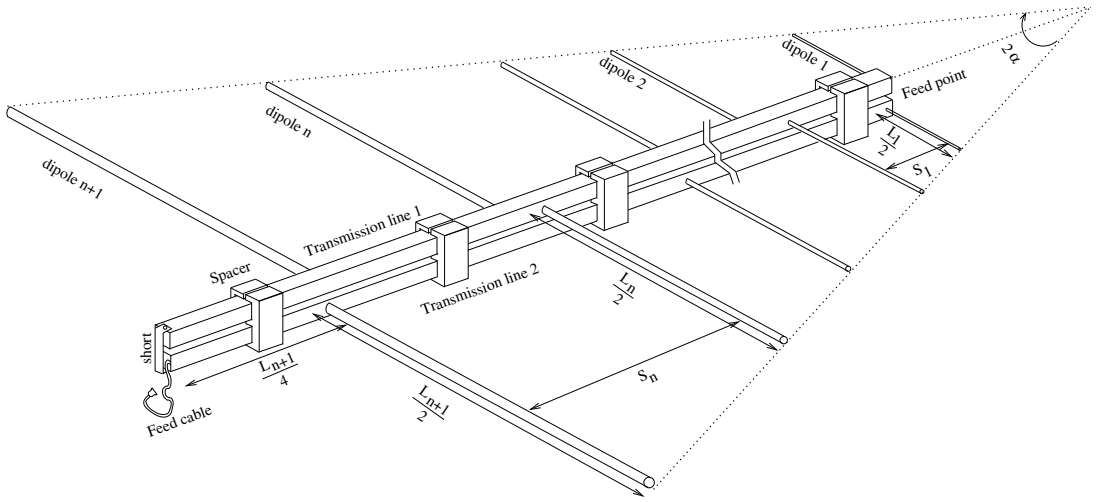

Figure 2.3: Design schematic of LPDA

2.5 Tests and Results

2.5.1 Voltage Standing Wave Ratio (VSWR) Measurement

For measuring the VSWR, Agilent Vector Network Analyzer (VNA) E5061A is used. As it requires, 1-port measurement only single S-parameter S_{11} in terms of Return Loss or Reflection Coefficient or VSWR is measured with the instrument. For a properly balanced transmission line, the line impedance should equal to characteristic impedance Z_o (here $Z_o = 50\ \Omega$; refer Section 2.4.2). To achieve it, VSWR values preferably < 2 is essential. Otherwise, signal will be lost and hence maximum power will not be delivered to load. The same principle applies to any antenna since it may be considered as an open ended transmission line (refer Section 2.1.1.1). In our case, the VSWR < 2 throughout the band is achieved (refer top-right panel of Figure 2.4). The plot in right-middle panel of Figure 2.4 shows the magnitude of input impedance ($|Z_{in}(l)|$) of the antenna measured with respect to 50-ohm load. Antenna efficiency ($\eta = 1 - |\Gamma|^2$) is also plotted (refer the plot in bottom-right panel in Figure 2.4) as a function of frequency indicates that the antenna will respond effectively in the 40-440 MHz bandwidth. The VSWR response of

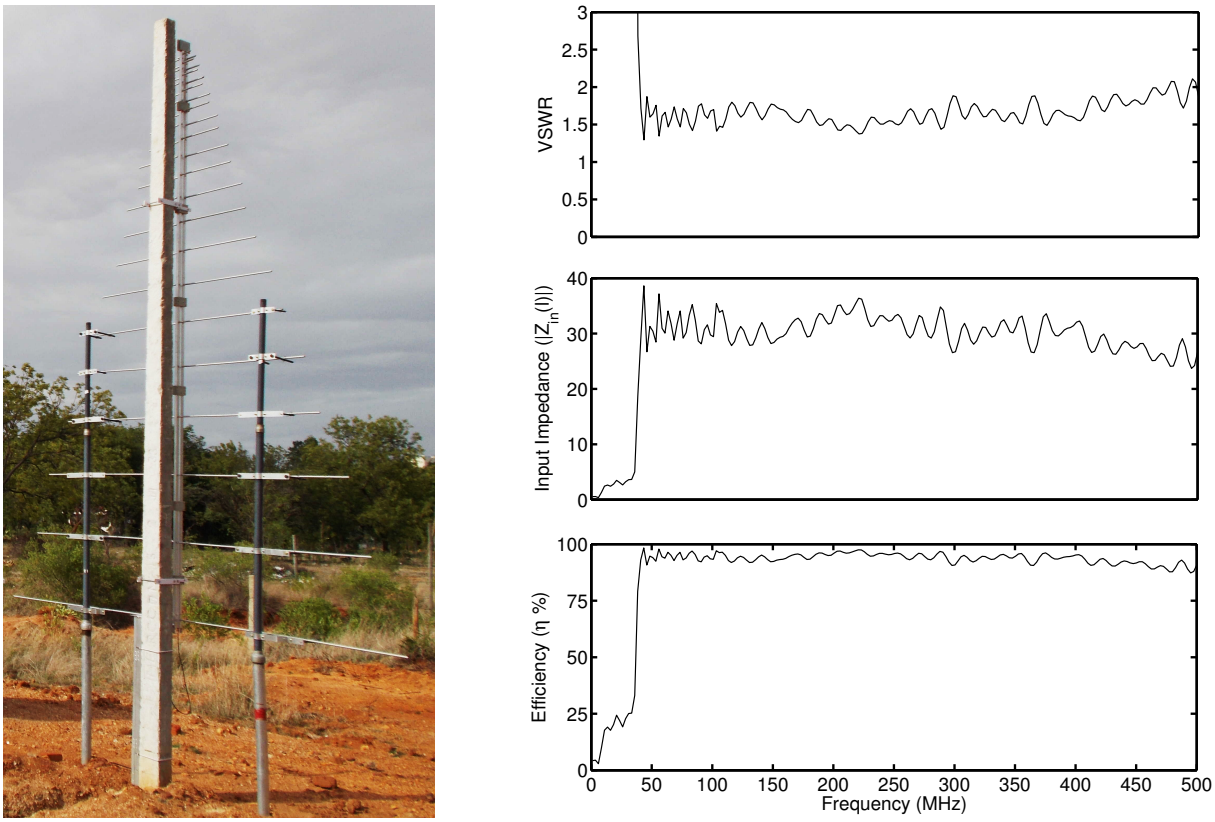

Figure 2.4: Left inset: Photograph showing the newly designed LPDA mounted on a cement pole with PVC supporting poles (for holding the dipoles) on both sides of it. The top-right panel: the VSWR response of the LPDA; Right-middle panel: the Impedance ($|Z_{in}(l)|$) of the LPDA; Bottom-right panel: the equivalent transmission line efficiency of antenna (efficiency; $\eta = 1 - |\Gamma|^2$).

an LPDA can be improved further by carefully adjusting the length and spacing given in Table 2.1. The general form of line impedance ($Z_{in}(l)$) of a transmission line with Z_L and Z_o as load and characteristic impedance respectively, is given by the relation:

$$Z_{in}(l) = Z_o \frac{Z_L + jZ_o tan(\beta l)}{Z_o + jZ_L tan(\beta l)} \tag{2.4}$$

where l and β are the given length and phase constant (rad/s) of a transmission line. As the antenna is similar to an open load transmission line, plugging $Z_L = \infty$ in equation (2.4) we get Z_{in}(l) = -j$Z_o$cot(βl). This implies that for any differential length of transmission line the impedance is purely reactive (i.e., either capacitive or inductive).

The transmission line input impedance ($Z_{in}(l)$) is also related to the load (Z_L) and characteristic impedances (Z_o) as follows

$$Z_o^2 = Z_{in}(l) \times Z_L \tag{2.5}$$

Using equation (2.5), antenna impedances (input: $Z_{in}(l)$, load: Z_L & characteristic impedance Z_o respectively) mentioned in Section 2.2 are calculated. Also the reflection co-efficient, antenna transmission/reception efficiency are tabulated in Appendix A (Table 1.1).

2.5.2 Far-field Pattern and 4nec2 Simulation Results

Radiation measurements are made in open space due to non-availability of anechoic chamber. The test set-up consists of 2 antennas. First one is the designed LPDA used as transmitter. It is excited with RF signal generated by a broadband noise source (1-500 MHz), and amplified by a power amplifier up to 0 dBm throughout the band. The second LPDA has kept 90 m apart from transmitter and is used as the receiver. It is connected to an analyzer to record the received RF signal level. Both transmitter and receiver antennas were fixed at a height of 1.5 m above the ground with the help of wooden poles (Figure 2.5). Their E and H-planes are also aligned along the line-of-sight. The transmitter is rotated over the entire 360° azimuth angle, and readings were noted down for every 10° intervals.

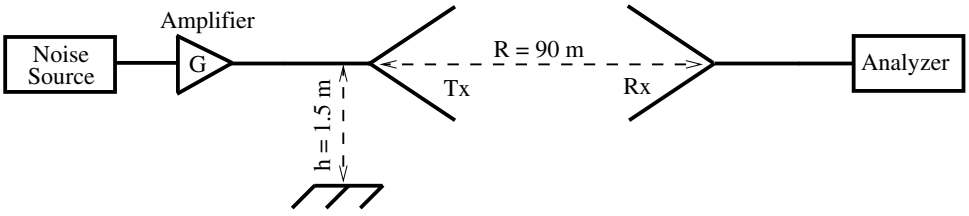

Figure 2.5: Setup to measure the Radiation pattern. Both antennas are supported by wooden poles (height = 1.5 m) and are separated by far-field distance (90 m).

To compare the characteristics of the designed antenna with the ideal one (i.e., theoretical) a similar prototype model is implemented on 4nec2 (Numeric Electro-magnetic Code2 & 4) simulation software. Here the antenna is represented by a wire model of line segments with current and voltage in linear variation across them. This code can be used to simulate any wire or mesh type structure for finding the response under various ground conditions and material options (`http://www.qsl.net/4nec2/`). The simulation gives the solution to integral equations for induced currents with excitation by a plane wave or a voltage source. The output parameters include the gain, beam-width over E and H planes, structure impedance, reflection coefficient, front to back ratio, etc. at far-field and near-field regions.

Obtained simulation results of the far-field pattern (also called beam pattern) are plotted over the band (refer Figure 2.6). The beam patterns over E & H planes at two different frequencies are shown in Figure 2.7. Also, Figures 2.8 & 2.9 show the beam patterns pseudo coloured with directional gain values. The measured Half-Power beam width (HPBW) over E-plane at 80 MHz is $\approx 80^\circ$ whereas it is 70° in the simulated pattern. The same for H-plane is $\approx 110^\circ$ and 100°, respectively.

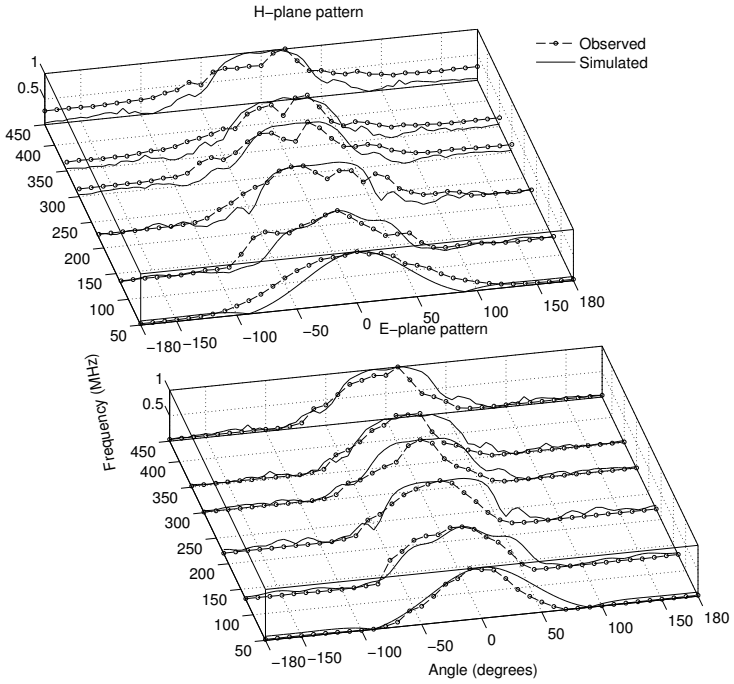

Figure 2.6: Over-plot of the measured radiation pattern over H & E-plane and the corresponding simulated profile using 4nec2.

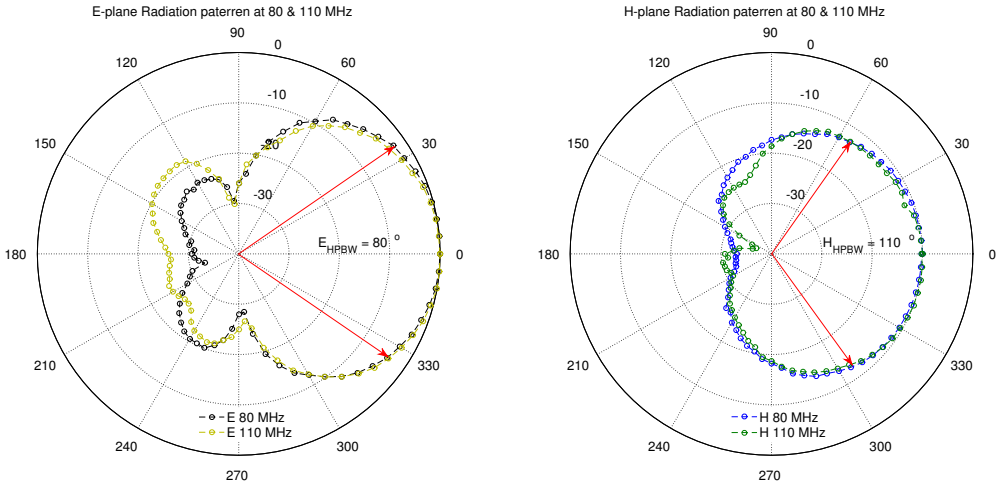

Figure 2.7: Measured radiation pattern (polar plot) over E and H planes at two frequencies viz. 80 & 110 MHz. The concentric circles represent the grid to mark the received power levels with the receiving antenna. The red arrow lines indicate the Half power (-3 dB down from maximum) points on both planes. The cone angle subtended by these points is the measure of Half Power Beamwidth (HPBW). The measured HPBW of the designed antenna throughout the band does not vary much is an indication that the antenna belongs to a frequency independent antenna category as mentioned in the Section 2.2.

2.5.2.1 Few other antenna parameters

The HPBWs along the E & H-planes were used to determine the following additional parameters:

1. **Gain:** The directive gain is the ratio of radiation intensity in a given direction of the antenna under test to that of an isotropic radiator (Omnidirectional antenna). Often the *Directivity*, i.e., the maximum directive gain is referred to by engineers, and is related to HPBWs along E & H-planes as

$$Directivity(D) = \frac{4\pi}{\Omega_A} \tag{2.6}$$

   For our antenna, the directivity is 6.5 dBi. Here Ω_A = HPBW$_E\times$ HPBW$_H$ is the beam solid angle. The gain of an antenna is always expressed with respect to an isotropic antenna.

2. **Beam Efficiency:** Beam efficiency is the ratio of beam solid angle (Ω_A) to the main beam solid angle (Ω_M). Ideally, it is unity for a directive antenna, i.e., the one with no side lobes. It is 0.9 in our case.

3. **Front to Back Ratio (F2B):** Ratio of the gains in forward to the rear side of an antenna. It is $\approx$ 23 dB for our antenna.

4. **Effective Aperture:** This describes how effectively an antenna can receive the radiation. It is expressed as

$$A_e = \frac{\lambda^2}{4\pi} G_d \approx 0.4\lambda^2 \tag{2.7}$$

   where G$_d$ is the directive gain of the antenna.

5. **Sensitivity:** The sensitivity of any radio telescope is given by the relation

$$\Delta S_{min} = \frac{2k\ T_{sys}}{A_e\ \sqrt{\beta\ \tau}} \tag{2.8}$$

where ΔS_{min} is the minimum detectable flux density (W m^{-2} Hz $^{-1}$) of the receiver, T_{sys} is the system temperature (K) which is a sum of sky noise as well as receiver noise temperatures, β is the observing bandwidth and τ is the integration time. At a typical frequency of 80 MHz and for time bandwidth product of 1, considering the sky temperature from NRAO[1], and receiver noise of 300 K, the sensitivity of a single antenna system would be $\approx$ 47670 Jy.

The directivity of LPDA was calculated to be $\approx$ 6.5 dBi which is almost same as the expected design value (6.6 dBi) while the simulated value is 7.4 dBi. The F2B ratios are also consistent with that of the simulated results in 4nec2. Table 2.2 gives the comparison of simulated and experimental results.

Table 2.2: 4nec2 versus Experimental results

Parameter	Experimental	4nec2
Directivity	6.5 dBi	7.4 dBi
Front to Back Ratio	26.3 dB	23 dB
VSWR (40-440 MHz)	< 2	< 2
HPBW E-Plane	80°	70°
HPBW H-Plane	110°	100°
Effective Aperture	0.36 λ^2	0.44 λ^2
Beam Efficiency	0.93	0.99

[1] `https://www.cv.nrao.edu/~demerson/radiosky/rsky_p3.htm`

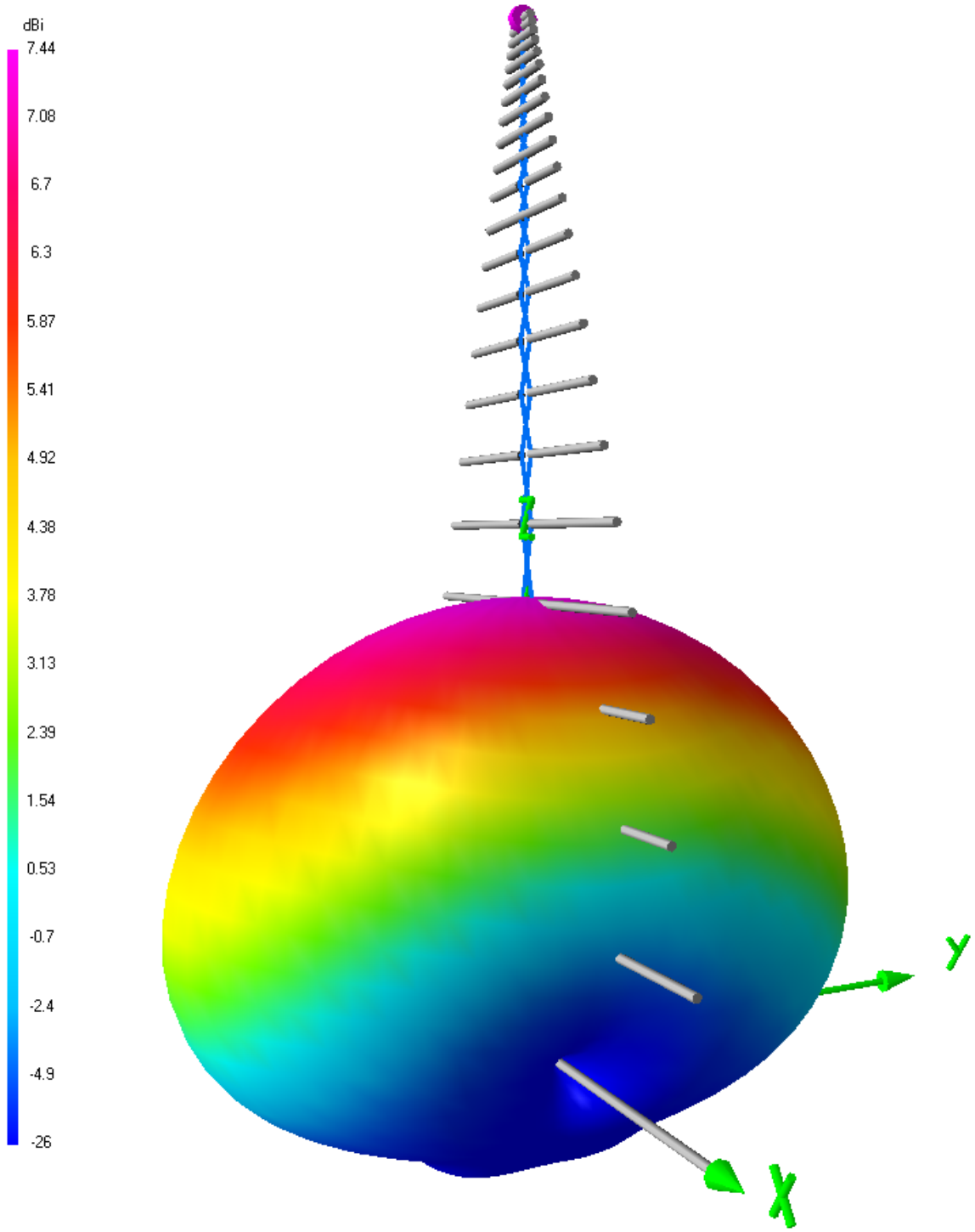

Figure 2.8: Simulated surface (3D) plot of the far-field pattern at 80 MHz. Directional gain values are indicated by different colors (refer to the scale shown to the left side of the surface plot for a specific color). A minor back lobe with low gain can also be seen at the bottom.

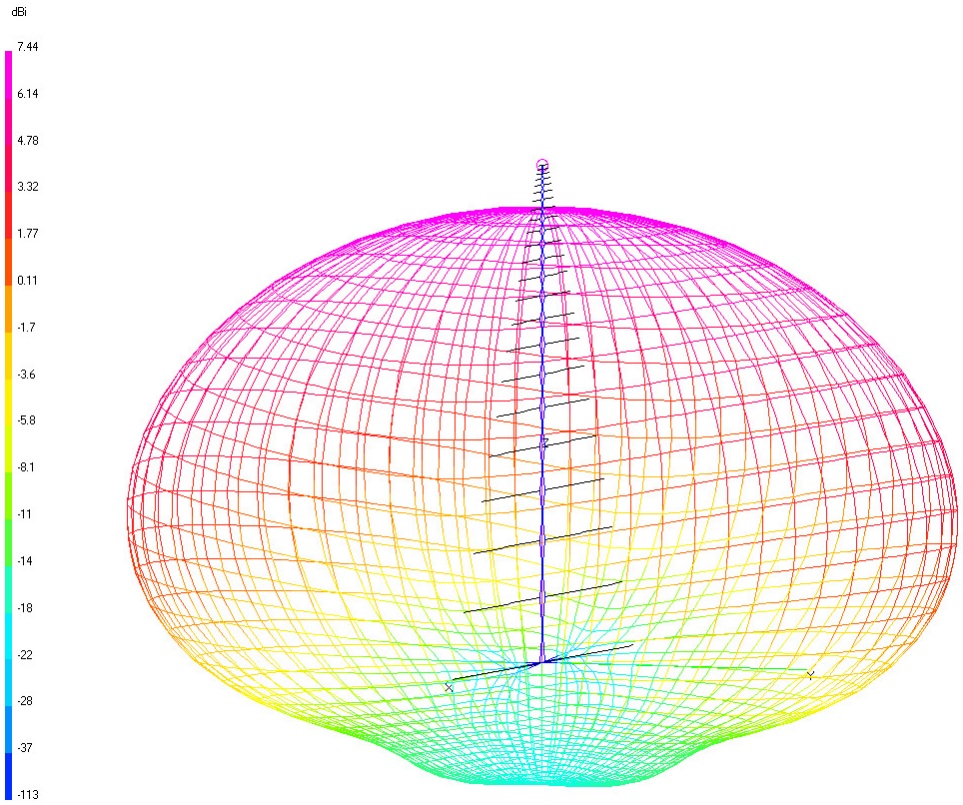

Figure 2.9: Contour representation of Figure 2.8.

All parameters and properties of designed LPDA are listed in Table 2.3. Additional parameters obtained with far-field measurements are also presented in Appendix A (Table 1.1).

Table 2.3: Measured antenna parameters at 80 MHz

Parameter	Value
Directivity	6.5 dBi
Front to Back Ratio	26.3 dB
VSWR (40-440 MHz)	< 2
Relative Spacing (σ)	0.077
Design Constant (τ)	0.88
Antenna Length	460 cm
Longest Arm Length	187.5 cm
Shortest Arm Length	9.9 cm
HPBW E-Plane	80°
HPBW H-Plane	110°
Effective Aperture	0.36 λ^2
Beam Efficiency	0.93

2.5.3 New method to reject selective RF band of an LPDA

The strength of the radio signal from the astronomical source is generally very weak ($\approx$ -100 dBm) at low-frequencies. Also, it is corrupted by man-made Radio Frequency Interference (RFI) such as FM (88-108 MHz), Airport traffic control, TV and Satellite Communications, etc. A Narrow Band stop Filter, or a Notch filter is generally used to filter out RFI. It is also possible to attenuate the signal with the help of the antenna itself. A new method is developed to mitigate the RFI over a selective band within the operating bandwidth of an LPDA [Kishore and Kathiravan (2013)].

D. E. Isbell elaborated two methods of exciting the LPDA [Isbell (1960)]. They are (i) feeding all dipoles in a Criss-Cross manner (leading to a phase reversal of 180° between adjacent dipoles) and (ii) in equi-phase as feeder [refer Figure 2.10(b)]. The latter arrangement makes the LPDA antenna to attenuate selective frequencies because the impedance of the system over those frequencies differ from the characteristic impedance of the system.

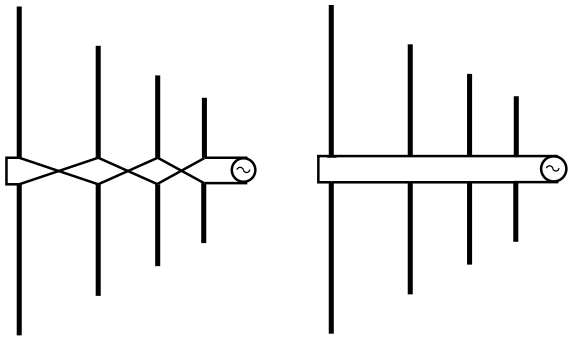

Figure 2.10: The methods of feeding an LPDA: (a) Criss-Cross feeding (b) Equi-phase feeding

The above strategy is chosen to reject the RFI over selected bandwidth. For example, in the designed LPDA 16^{th} & 15^{th} arms (from top) correspond to 88.2 MHz & 100.6 MHz frequencies. These two arms are fed with equi-phase, the rest of the elements are maintained in Criss-Cross fashion. As expected from theory, an over shoot of

VSWR/drastic fall of impedance in FM band is noticed. VSWR of LPDA obtained with and without rejection over certain bands are shown in Figure 2.11.

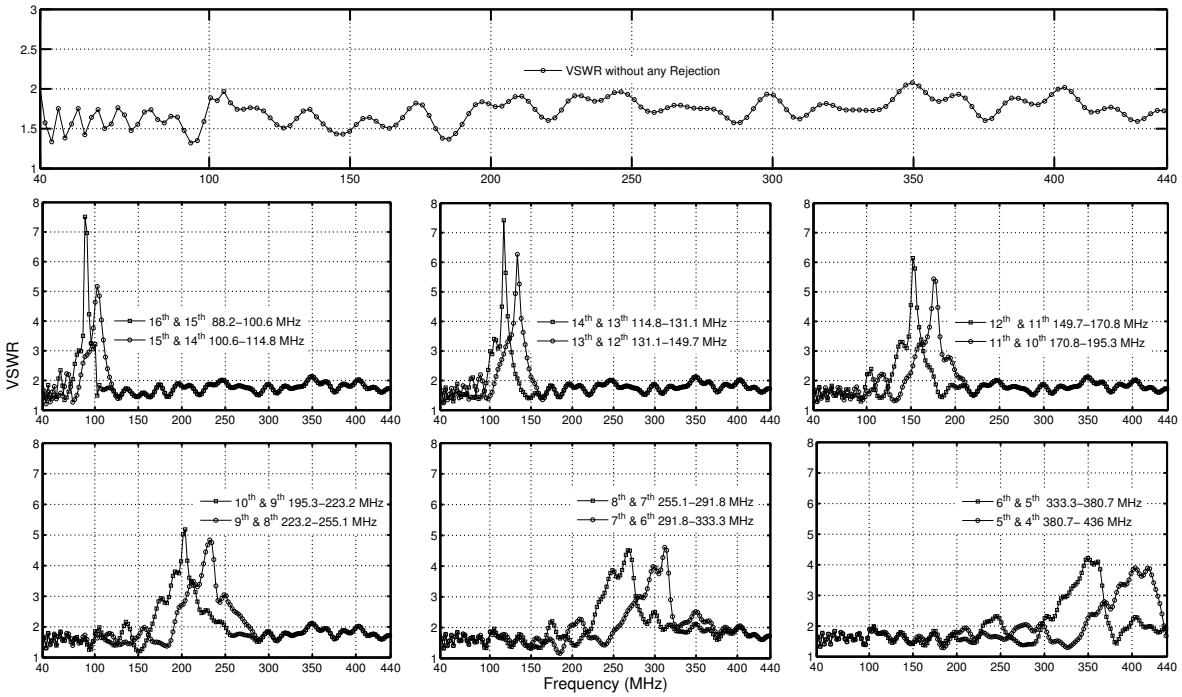

Figure 2.11: First row: VSWR of antenna without any rejection. Second & Third row: VSWR obtained after keeping the adjacent arms along the same direction. One can clearly notice the shift in rejection (VSWR > 2) band as the successive arms are fed without changing the signal phase. The above frequency bands may be used to reduce the RFI due to FM radio transmission, TV broadcast, Airport Traffic control, and Satellite Communications.

2.5.3.1 Method of altering the performance of LPDA over a selective bandwidth

The following methodology is suggested to alter the performance of an LPDA over a selective Radio frequency bandwidth.

1. Choose the frequency band to be rejected and calculate its bandwidth ratio. For example, we have chosen 88-108 MHz. Therefore, the rejection Frequency ratio $F_r = \frac{108}{88} \approx 1.23$.

2. Calculate the number of elements(n_r) in the rejection band using $n_r = \frac{ln(F_r)}{ln(\frac{1}{\tau})} \approx 2$ (rounded to the nearest integer).

3. Find the dipole that corresponds to 88 MHz using the following equation.

$$f_n = \frac{f_1}{\tau^{n-1}} \tag{2.9}$$

here f_n is frequency of n^{th} dipole = 88 MHz, f_1 is frequency of first dipole (40 MHz). From equation (2.9) the absolute value of n = 16. So the 16^{th} & 15^{th} arms have to be oriented in the same direction so that the test signal does not have a phase difference between adjacent dipoles.

4. Calculate the lengths and spacing of 16^{th} & 15^{th} arms making use of equation (2.1) or equation (2.2). The rest of the arms are to be oriented in Criss-Cross fashion.

2.5.3.2 Simulation results of Rejection using 4nec2

4nec2 is used again to simulate the performance of the LPDA designed to reject the frequencies between 88–108 MHz. The VSWR, Gain, Front to Back ratio (F2B) with and without the rejection are compared in Figure 2.12.

This is a preliminary method to limit the RFI over a specific bandwidth of frequencies using the LPDA itself. In this way, most of the RFI may be eliminated at the earliest stage of an RF receiver chain. The results are as expected over small bandwidths whereas we need to understand further to increase the bandwidth further. Elaborate tests are being carried out to improve the methodology, and the results remain inconclusive at this stage.

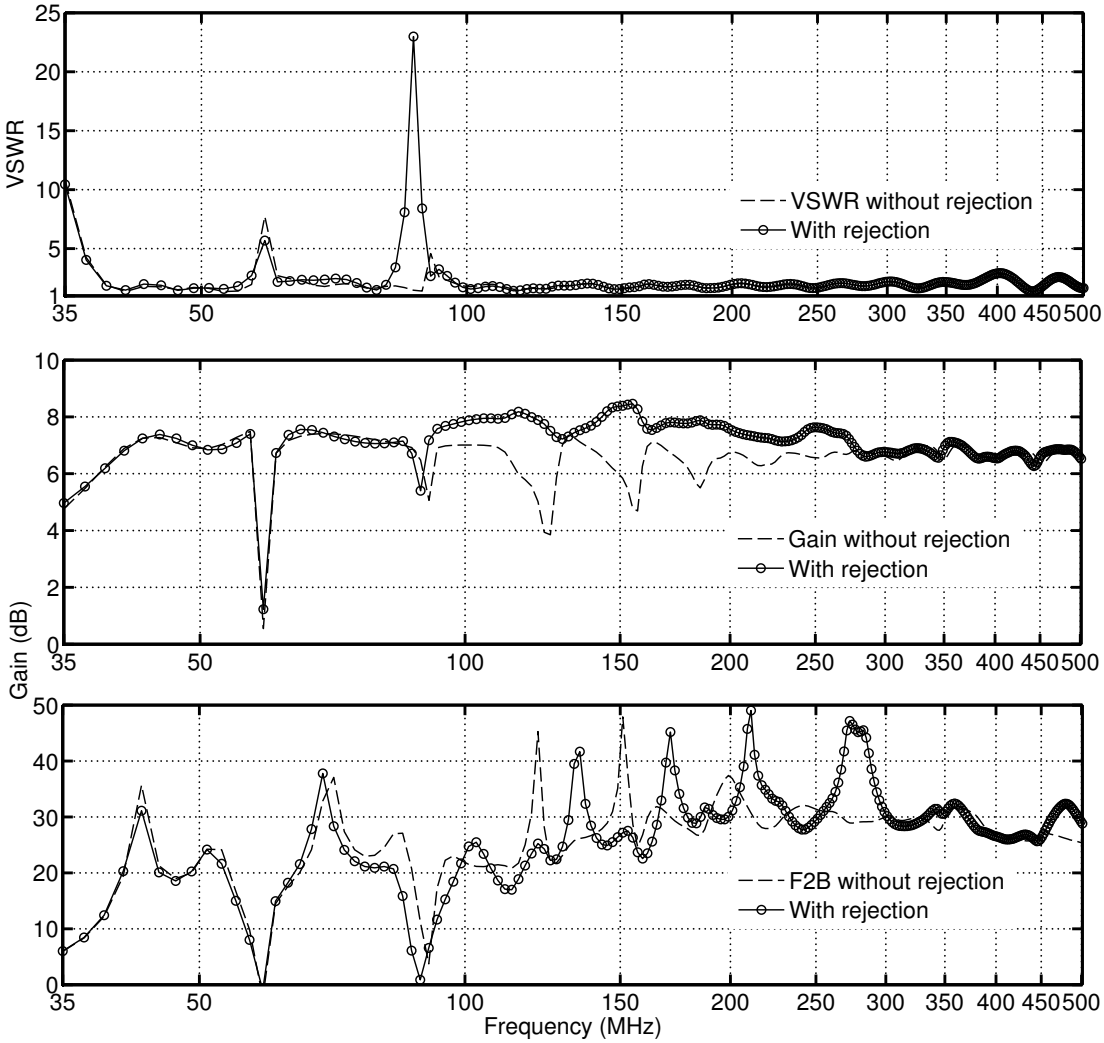

Figure 2.12: Comparision of simulation results of LPDA using 4nec2: ideal operation mode (dashed line) vs rejection operation mode (continuous line with circles); the frequency bandwidth is chosen to study the rejection properties is 88-108 MHz. Top panel: Superposition of VSWR profiles; Middle panel: Superposition of directive gains; Bottom panel: Superposition of front-to-back ratios. All profiles are plotted against frequency over the entire operating bandwidth of the LPDA designed.

2.6 Gauribidanur LOw-frequency Solar Spectrograph (GLOSS)

As mentioned in the Section 2.5.2.1, the sensitivity, and effective aperture are low for a single antenna. Therefore, a broad-band decameter spectrograph array was

commissioned to improve the sensitivity in order to record the salient features of radio emission associated with wide variety of weak transient out-bursts mentioned in Section 1.3.

2.6.1 Array set-up & Front-end receiver system

Figure 2.13 shows the schematic of the GLOSS array. Eight identical LPDAs (the one described in the Section 2.4.1) with their E-plane orientation along the East-West direction, are combined to form an adding interferometer with baseline along the North-South direction. The antennas are mounted on to RCC poles using electrically non-conducting clamps and solid PVC rod supports with an inter-antenna separation of 5 m. The received signal from each antenna is passed through a high pass filter (PHP-50+ of M/s. Mini-Circuits, Inc.) with a 3 dB cut-off frequency around 40 MHz. High pass filtering helps to eliminate the spurious low-frequency signals and their inter-modulation products, which would reduce the dynamic range of receiver otherwise. The signal is then amplified by a low noise amplifier (MAN-1LN of M/s. Mini Circuits Inc.) of gain $\approx$ 28 dB and having $\approx$ 8 dBm power output at 1 dB compression point. The amplifier has a flat response over 0.5-500 MHz with Noise Figure $\approx$ 3 dB. Later the signal from all the antennas are combined using a 2-way-0° power combiner (PSC-2-1+ of M/s. Mini-Circuits, Inc.) via a declination control system (nothing but analog delay shifters; marked as DSB I, II and III in Figure 2.14). Due to array geometry and the relative location of the celestial source, the signal from the latter reach the individual antenna at different instances of time. One has to compensate this delay between different antennas in order to add the signals correctly or cohesively. This is done by passing signal through a low loss cable of length corresponding to the required amount of delay. To achieve this an electronically controlled Delay Shifter system (DSB) is designed using RF diodes, low-loss co-axial cables, etc. All the 8 antennas of the

system are combined using DSBs at 3 stages (i.e Ist, IInd & IIIrd as shown in the schematic Figure 2.13)

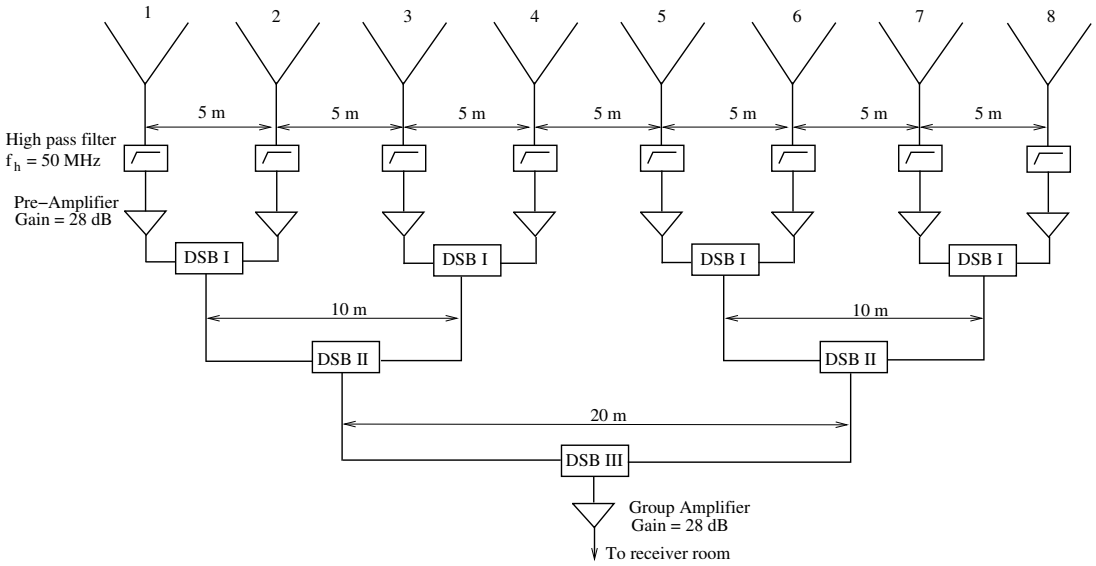

Figure 2.13: GLOSS front-end receiver system; refer Section 2.6.1 for the explanation of the setup and the components used.

Figure 2.14: Photograph showing the front-end receiver system of Gauribidanur LOw-frequency Solar Spectrograph (GLOSS). Delay Shifter Boxes are protected inside the RCC box (a small cement housing seen at array center).

Figure 2.15: The left photograph shows the pre-amplifier connection. It is kept in a rectangular casing to protect from pests. The right photograph shows the RF modules (the group amplifier, filters, DSB boxes, their control signal units and the AC mains power supply) inside the RCC box. Individual signals from the antennas are brought to the RCC box through low-loss coaxial cables before being added using DSB modules at various stages (I, II and III).

This is equivalent to an antenna having the collecting area of 6.6 m^2, sensitivity of 2560 Jy (5σ level) along with high directionality ($\approx$ 19.2 dBi) at 80 MHz. Note that the above values are calculated by assuming the signals from all the antennas are added up coherently. In practice, the gain varies $\pm$ 0.5 dB with respect to the above mean value.

These DSBs are in-house fabricated and characterized for various parameters like VSWR, Isolation and Insertion loss throughout the band. As inter- antenna spacing increases in successive stages so as the delay by a factor cvf (cable velocity factor). The delay for each stage would be cvf$\times$d$\times$Sin(θ)/c where d is inter-antenna spacing, c is speed of light and θ is the angle subtended by the source with the normal to the array baseline. The signal output from the third stage is again amplified by 30 dB using MAN-1LN of M/s. Mini-Circuits. The resultant group beam has an HPBW of 80° in E-W direction and $\approx$ 6° in N-S direction at 80 MHz. Considering the local latitude 13° N the group beam has to be steered to either a maximum declination of +36.5° N or a minimum of -10.5° S in order to track the Sun. This total angular extent is covered by means of 4 cable delay sections of the DSB. In this way, the RF co-axial cables provide

the instrumental phase ϕ_i to compensate for the geometric phase ϕ_g (due to the celestial position of the source with respect to the antenna system). The lengths and phase of RF co-axial cables should be chosen in such a way that the residual phase error $\Delta\phi = \phi_g - \phi_i$ should be as small as possible (for fine tilting angles). The final amplified output is transmitted to the lab through a low-loss cable of 200 m length.

2.6.2 Grating Lobes of GLOSS

The spacing of 5 m between the adjacent LPDAs in the GLOSS is greater than the observation wavelengths at frequencies $\geq$ 60 MHz. Then, the array has grating lobes in the corresponding frequency range, *i.e.,* 60-440 MHz [Kraus et al. (2006)]. The grating lobes are symmetrical on either side of the main lobe and are modulated by the single antenna response on the respective combining direction (refer Appendix 1.3 for more details). The separation between the main lobe and grating lobe is given by

$$\theta_g = sin^{-1}\Big(\frac{n\lambda}{d}\Big) \tag{2.10}$$

where θ_g is the angular separation between the main lobe and grating lobe, λ is the wavelength, d is the separation between the antennas, and n is the grating lobe number. Here the grating lobe angles are $\approx 8^\circ$ at 440 MHz and $\approx 90^\circ$ at 60 MHz (from equation (2.10)). However, any contribution to the GLOSS output from the possible presence of strong radio-wave emitting solar/cosmic sources present simultaneously at the location of the grating lobes as well as the main lobe in the sky is expected to be small because: i) The size of the Sun in the radio range increases with decreasing frequency. The average sizes are $\approx 0.6^\circ$ and $\approx 0.8^\circ$ at 440 and 60 MHz, respectively [Sheridan and McLean (1985); Avignon et al. (1975)]. Compared to this the grating lobes at the corresponding frequencies are far away. So, there will not be multiple lobes present at the same time while observing the Sun. ii) The flux densities of most radio bursts from the Sun are

larger than those of radio emission from cosmic radio sources [McLean and Labrum (1985)]. Also, iii) their temporal and spectral characteristics are different (refer Section 1.3.2.1).

2.6.3 Back-end Receiver

At Lab side, the signal is passed through an amplifier (MAN-1LN of M/s. Mini Circuits Inc.), slope filter (to reduce the differential loss across the band) and finally fed to a spectrum analyzer (SA). Commercially available Agilent E4401B (9 kHz-1.5 GHz) Spectrum Analyzer acts as the back-end receiver system (Figure 2.16). The amplified RF is fed to the mixer (inside the SA) where the incoming RF signal is mixed with the internal Local Oscillator (LO) signal. The LO is swept by a voltage controlled oscillator across the band. The basic functionality of an analyzer resembles the Super heterodyne receiver (SHD). In SHD receivers the tuning is done manually, but here it is done electronically. Generally, the LO signal is chosen above the range of RF frequency to avoid the null response (DC) in the Intermediate Frequency (IF) band. If f_{RF} be the incoming frequency of RF signal and f_{LO} be the Local Oscillator frequency, then the output is expressed as

$$Sin(2\pi f_{RF})Sin(2\pi f_{LO}) = -Cos(2\pi f_{LO} + 2\pi f_{RF}) + Cos(2\pi f_{LO} - 2\pi f_{RF}) \qquad (2.11)$$

Both terms in equation (2.11) represent the intermediate frequencies which contain the original RF signal. The high-frequency product (and other harmonics) is left out as the receiver electronics cannot perform such high-speed operations, therefore, the lower IF product (f_{LO}-f_{RF}) is chosen for smooth operation. The LO is swept at different frequencies with the help of sweep generator. One can get better RBW by choosing

less span or high sweep time. The IF filter section cuts out the higher IF product. Then lower IF product is passed through an envelope detector which gives the change in the envelope of IF signal. This means that it indirectly demodulates the IF signal from LO carrier giving out the spectral information of input RF signal. The video output of the absolute power spectrum is displayed with the help of an internal sweep generator (using any of Normal, Positive or Negative peak detection methods).

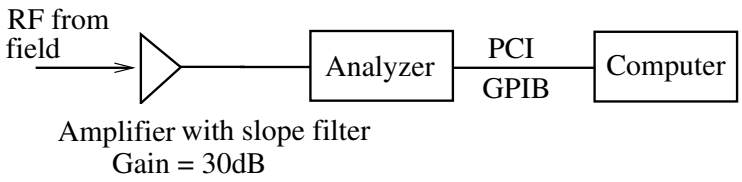

Figure 2.16: GLOSS Back-end receiver system; it comprises of a LPF, and Spectrum Analyzer connected to PC via GPIB interface.

The analyzer is interfaced to local computer via GPIB-PCI card (Agilent 82350B; see Figures 2.16 & 2.17). The controller will be the computer, and the analyzer is a listener/talker on the GPIB network.

Instrument control and data acquisition code is written in C++ under Microsoft Visual C++ idle. The code includes checking/clearing the status of the analyzer and setting up the observation parameters. After the instrument is ready the observation parameters (like sweep time, bandwidth, frequency limits) are initialized by the program. The idle compiles and executes the code to produce a batch file. Later this batch file is executed to run the data acquisition with the observational constraints. The controller PC initiates the sweep, queries the data from the instrument, etc. Each swept data has 401 amplitude points along with system time in UT (synchronized by GPS disciplined time server), observing band, sweep time, etc. Later they are written as a 32-bit binary file by the controller PC. The Data writing speed is around 50 ms. The instrument is operated in continuous sweep mode. Data for a total of 2000 sweeps acquired over 7.8 min is written with extension Data'A', where A stand for sample number. Every day the spectrograph is operated between 2.5 UT to 11.5 UT. Therefore, for an observation

duration of 9 hours, we would get 70 raw data files which are compressed and archived on a CD for later processing using MATLAB or IDL.

Figure 2.17: Left: The E4411B spectrum analyzer from M/s. Agilent Technologies that is used as the backend for GLOSS. Right: host PC with a PCI-GPIB interface that controls and stores the observed data with the spectrum analyzer.

2.7 Array Measurements

VSWR of a single antenna is used to characterize the impedance of the antenna alone. When many such antennas are combined in-phase, the resultant impedance of the entire system is altered by the adjacent elements of the array. Two different parameters are used to characterize the impedance of arrays they are i) Self-Impedance and ii) Mutual-Impedance

2.7.1 Self-Impedance

Self-impedance of an antenna in an array is defined as the impedance of that antenna when the other antennas are kept in open circuit condition. It tells how the impedance of a single antenna is altered by inter-elements in that array. Ideally, the self-impedance of an antenna should be equal to its input impedance (null contributions from rest). Table 2.4 gives the self impedance of 8 antennas that constitute the GLOSS spectrograph array. For this measurement, the antenna under test is connected to a 2-port Vector Network Analyzer (to know S-parameters). As the antenna is a single port

transmission line, directly the reflection co-efficient is displayed on the instrument. Actually, the VNA generates an internal RF signal, transmits to the port connected to 50 Ω load (calibration). The reflection over this load is noted, and the instrument computes the complex reflection co-efficient. Later the load is replaced by the Test antenna to determine the reflection co-efficient which is an indirect measurement of antenna impedance. In this way, the self-impedance measurement is done on all eight antennas of the array. The complex number under the heading ANT-1, ANT-2 . . . ANT-8 correspond to the self-impedance of the respective antenna as a function of frequency. The obtained self-impedance values indicate minimal inter-element contributions of GLOSS.

Table 2.4: Table showing measured self-impedance values of individual antennas in GLOSS. For this measurement, the impedance is measured by a network analyzer for each antenna numbered ANT-1, ANT-2 . . . ANT-8 in North-South direction. The analyzer is set to measure the reflection co-efficient which is latter converted to complex impedance with respect to a matched load of 50 + j 0 Ω impedance.

f (MHz)	ANT-1	ANT-2	ANT-3	ANT-4	ANT-5	ANT-6	ANT-7	ANT-8
50	70-j13	65+j8	63+j15	73+j4	64+j4	63+j7	59+j3	69-j17
100	73+j79	58+j75	47-j71	67-j73	50+j78	53+j66	57+j34	46+j69
150	43-j36	46-j42	53-j34	43-j33	50-j34	43-j33	41-j41	44-j30
200	58-j7	56-j13	58-j7	53-j8	59-j12	58-j41	54-j14	57-j14
250	63-j48	70-j43	59-j20	71-j41	70-j39	60-j45	57-j20	57-j44
300	43-j32	57-j29	69-j49	58-j36	67-j31	61-j38	67-j32	53-j39
350	38-j17	57-j38	48-j20	44-j24	45-j26	50-j26	42-j19	37-j21
400	47-j27	44-j29	50-j31	45-j16	52-j23	42-j15	55-j17	38-j17
450	40-j15	39-j17	41-j27	44-j16	48-j26	43-j20	49-j24	34-j18
500	28-j18	37-j17	34-j14	35-j21	33-j21	26-j15	41-j23	30-j3

2.7.2 Mutual-Impedance

Consider two antennas in an array. The mutual impedance between them is defined as the ratio of ANT-1 voltage to Current in ANT-2 under the condition that ANT-2 is shorted leaving all other antennas in open circuit condition. It is denoted as Z_{12}. The converse of the above is also true and is denoted as Z_{21}. However, these values are not the same

as transfer impedance values in a 2-port network analyzer. The definition of transfer impedance says that ratio of the voltage impressed (not induced) in one close circuit to the current produced in another closed circuit with other antennas under open condition. Ideally, the mutual impedance between two antennas should be as low as possible to have a high degree of isolation between them.

Consider any two antennas in an array. Let Z_s be the self-impedance of antenna 1 or antenna 2. Z_1 is the measured terminal impedance of antenna 1, when antenna 2 is shorted, and rest of the antennas are in open condition. The mutual impedance Z_m between the antennas is given as

$$Z_m = \sqrt{Z_s(Z_s - Z_1)} \tag{2.12}$$

The mutual impedance measurements of GLOSS are tabulated in Table 2.5. Values obtained thus indicate the mutual coupling effects in the GLOSS array also minimal.

Table 2.5: Table for mutual impedance. It is calculated by using the relation (2.12) & values taken from Table 2.4. Here M.I ANT$_{XY}$ (XY are antenna numbers) indicates the Mutual impedance of Antennas X & Y under the conditions X is connected to VNA, Y connected by a short, keeping rest of elements in the open condition.

f(MHz)	M.I.ANT$_{12}$	M.I.ANT$_{13}$	M.I.ANT$_{14}$	M.I.ANT$_{15}$	M.I.ANT$_{16}$	M.I.ANT$_{17}$	M.I.ANT$_{18}$
50	23-23j	18-20j	23-16j	23-16j	27-26j	12+1j	23-11j
100	38+16j	50+123j	52+119j	33+17j	27+10j	55+118j	27+10j
150	19+10j	4-14j	9-3j	14-14j	15+7j	14+2j	17-39j
200	26+18j	18+8j	23+6j	11+7j	18+12j	19+12j	23+8j
250	19-24j	16-36j	13-24j	23-11j	11-27j	27+6j	24-26j
300	5-19j	13+6j	11+5j	5-14j	8+7j	17+3j	8+0j
350	1-7j	14-1j	12-5j	11-10j	1-10j	10+1j	15-8j
400	8-14j	4-19j	3-16j	9+16j	2-17j	1-12j	0-22j
450	11-7j	15-9j	1+9j	12+13j	5+3j	3+10j	10-3j
500	5-1j	8-9j	1-11j	7-6j	9+1j	7+9j	7-2j

2.8 GLOSS receiver Noise, and minimum detectable Temperature measurements

2.8.1 Receiver Noise, Antenna Temperature

In order to evaluate the performance of any radio receiver its equivalent noise figure has to be determined at first. Therefore, the newly commissioned spectrograph array GLOSS have been characterized to know its noise figure. Generally, the receiver noise of any system is specified by its equivalent noise temperature. Both the Noise figure (N in dB) and Noise temperature (T in K) are related as

$$T = 290 \times (10^{N/10} - 1)K \ [Friis\ (1944)] \tag{2.13}$$

The noise power measured across a resistor at room temperature is proportional to the bandwidth of the signal and the ambient temperature. This noise is known as thermal noise or Johnson Noise [Friis (1944)], which is due to the random motion of charge carriers over temperatures above absolute zero. There are other kinds of Noise which are less prominent here. A well-matched antenna (VSWR $<$ 2 or Impedance $\approx$ 50 Ω) can be considered as a passive resistor. Therefore, the available noise power across the antenna terminals is an indicator of temperature which is an estimate of equivalent temperature (from Kirchhoff and black-body radiation laws in Kraus (1966)).

An antenna looking at the plane of the sky directly gives an estimate of the equivalent brightness temperature which can be determined from its received noise power. This is called the antenna temperature (T_A). However, the following factors may introduce inaccuracies in the measured values.

1. A perfectly matched antenna: Since antenna's impedance should be perfectly matched with the characteristic impedance of transmission line, the antenna itself

may re-radiate.

2. Side lobes: The antenna may receive through side lobes if it is not highly directional.

3. Spurious pick-ups: The noise picked up by the antenna from the surrounding such as ground reflections or any man made or terrestrial interference.

4. Pointing errors: Errors in pointing the beam.

2.8.1.1 GLOSS Noise Figure

GLOSS receiver chain containing all the active (amplifiers)/passive (cables, connectors, power combiners, etc.) elements is shown in Figure 2.18. All these blocks are provided with the equivalent Noise Figure values (refer Table 2.6). It contains 14 block elements comprising of various signal conditioning and transportation blocks. These include amplifiers, Filters (High-pass & Band-pass), coaxial cables and delay shifters. The Noise figure for the active elements such as amplifiers is taken from the device manufacturer's manual. The noise figure of the passive devices such as lossy or attenuator networks is determined from their attenuation factors (inverse gain) as mentioned in Kraus et al. (2006).

An equivalent noise figure of the receiver chain comprising of various gain factors (gain/attenuation) is given as [Friis (1944)]

$$F_e = F_1 + \frac{F_2 - 1}{G_1} + \frac{F_3 - 1}{G_1 G_2} + \ \ldots \ + \frac{F_n - 1}{G_1 \ldots G_{n-1}} \tag{2.14}$$

Here F_1, $F_1 \ldots F_n$ are the noise figures of individual blocks and G_1, $G_1 \ldots G_n$ are the Gain/Attenuation of the respective element.

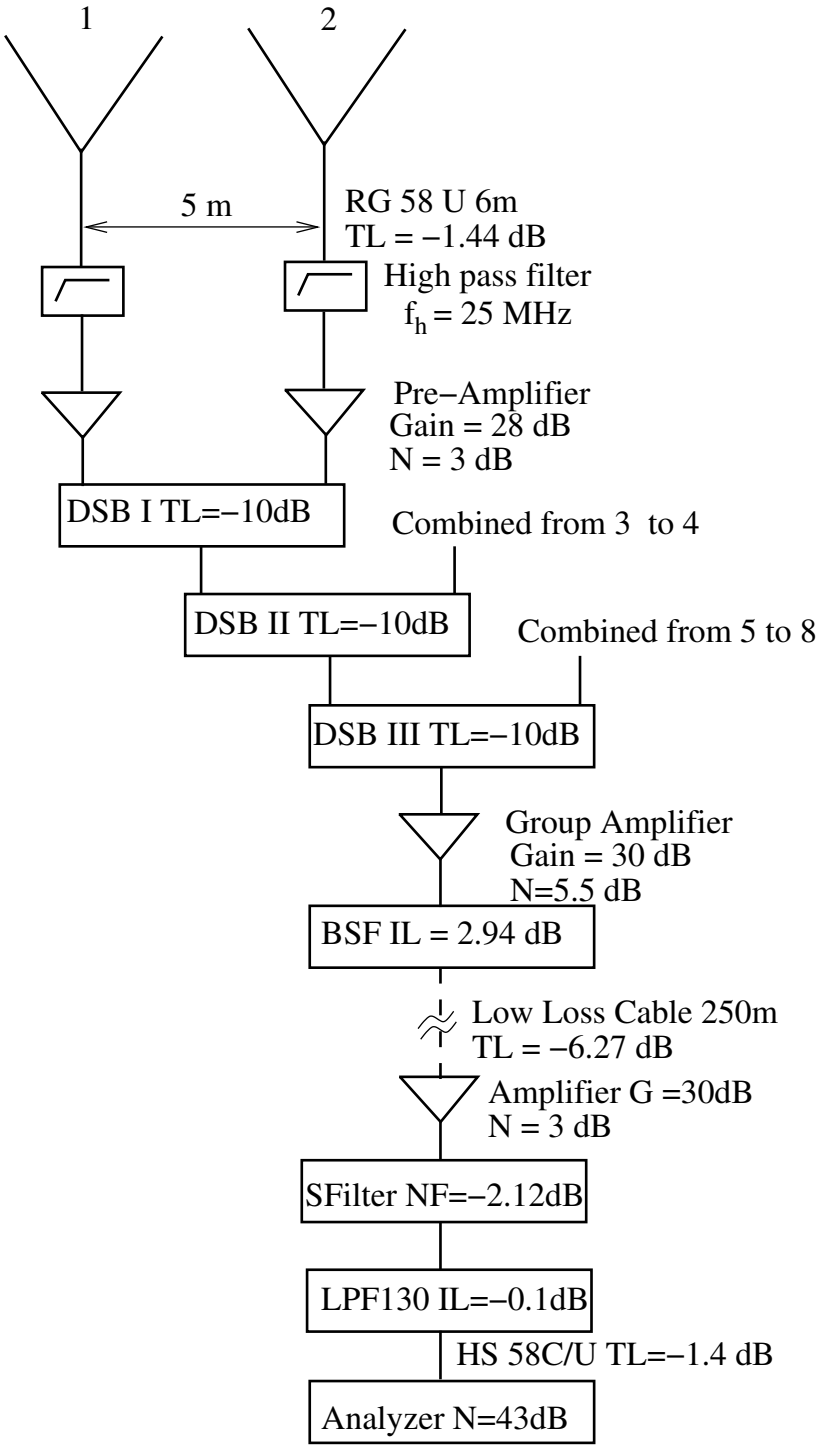

Figure 2.18: GLOSS receiver chain block diagram showing antennas, amplifiers, Delay Shifter Box (DSBs), co-axial cables with Gain/Attenuation values and their corresponding equivalent noise figure values (denoted as N). Here TL stands for Transmission Loss, NF for Noise figure, IL for Insertion Loss, SFilter for Slope filter. The numbers 1-8 represent GLOSS antennas.

Table 2.6: Top: Table showing equivalent Noise Figure values of the individual amplifiers, DSBs, co-axial cable systems, etc. for a single antenna system. Bottom: same as the top table but for all eight antennas included in the receiver chain.

For single antenna system														
Block Number	1	2	3	4	5	6	7	8	9	10	11	12	13	14
Gain (dB)	-1.44	30	-2.25	-10	-10	-10	30	-2.94	-6.27	30	-2.12	-0.1	-1.4	
Noise Figure F(dB)	1.44	3	2.25	10	10	10	5.5	2.94	6.27	3	2.12	0.1	1.4	43
Gain in Linear	0.72	1000.00	0.60	0.10	0.10	0.10	1000.00	0.51	0.24	1000.00	0.61	0.98	0.72	
$\prod_{i=1}^{n-1} G(i)$	0.72	717.79	427.56	42.76	4.28	0.43	427.56	217.27	51.29	51286.14	31477.48	30760.97	22284.35	
F Ratio Linear	1.39	2.00	1.68	10.00	10.00	10.00	3.55	1.97	4.24	2.00	1.63	1.02	1.38	19952.62
F-1		1.00	0.68	9.00	9.00	9.00	2.55	0.97	3.24	1.00	0.63	0.02	0.38	19951.62
F (Equivalent)	1.39	1.39	0.00	0.02	0.21	2.10	5.96	0.00	0.01	0.02	0.00	0.00	0.00	0.90
F (Equivalent)	**12.01**													
F (Equivalent dB)	**10.79**													

Total Gain (dB)	43.48	**For entire receiver chain**												
					Friss Equivalent (F)									
					Up to First Stage		Equivalent linear (3dB) better							
F (Equivalent)	1.39	1.39	0.00	0.02	2.80		0.81							
					Up to Second Stage									
F (Equivalent)	0.81	10.00			1.02		-0.98							
					Up to Third Stage									
F (Equivalent)	-0.98	10			1.13		-0.87							
Gain (dB)	Combined	30	-2.94	-6.27	30	-2.12	-0.1	-1.4						
Noise Figure F(dB)		5.5	2.94	6.27	3	2.12	0.1	1.4	43					
Gain in Linear		1000.00	0.51	0.24	1000.00	0.61	0.98	0.72						
$\prod_{i=1}^{n-1} G(i)$	0.43	427.56	217.27	51.29	51286.14	31477.48	30760.97	22284.35						
F Ratio Linear		3.55	1.97	4.24	2.00	1.63	1.02	1.38	19952.62					
F-1		2.55	0.97	3.24	1.00	0.63	0.02	0.38	19951.62					
F (Equivalent)	-0.87	5.96	0.00	0.01	0.02	0.00	0.00	0.00	0.90					
	6.02	**Sum of rest**												
F (overall)	**6.02**													
F (Equivalent dB)	**7.80**													

The attenuation values of the co-axial cables used in the receiver chain has been measured at a typical frequency of 80 MHz. Also, the insertion and transmission losses in the cables are related to their noise figure as mentioned above. All the values are tabulated in Table 2.6 and the equivalent receiver noise figure was estimated by making use of the relation (2.14). It is $\approx$ 8 dB for the entire receiver chain.

2.8.1.2 Analyzer Calibration & Sensitivity

The back-end instrument for GLOSS is a commercially available M/s. Agilent Technologies E4401B analyzer. Before starting a continuous spectral run, the analyzer was properly pre-set with observing parameters. The latter are taken care of by the instrument control software which runs on the data acquisition PC. Described below are the steps carried out on the analyzer to know its equivalent noise figure.

- The observing pre-set conditions were set in the analyzer.
- The input of the analyzer was terminated with a characteristic impedance of 50 Ω.
- Using the relationship between the receiver noise and noise figure for a real receiver [Friis (1944)] i.e., N = F k T B (where k is Boltzmann constant, T is room temperature (290 K), B being the observing bandwidth) the typical Noise Figure of the analyzer was determined, and the value is $\approx$ 40 dB.

Using the relationship for sensitivity given in equation (2.8), with all parameters obtained from the field tests, sensitivity of GLOSS was calculated. The sky noise temperature values were taken from NRAO[2]. The minimum detectable flux is around $\approx$ 0.5 sfu[3] at 40 MHz and 3 sfu at 440 MHz with 5 σ confidence. GLOSS system characteristics are tabulated in Table 2.7.

[2] `https://www.cv.nrao.edu/~demerson/radiosky/rsky_p3.htm`
[3] 1 sfu=10,000 Jansky

Table 2.7: GLOSS receiver Characteristics

Parameter	Value
Frequency range	$\approx$ 40-440 MHz
Number of frequency points	= 401
Frequency resolution	$\approx$ 1 MHz
Sweep time ($40 - 440$ MHz)	$\approx$ 250 ms
Total observation duration	$\approx$ 9 hrs
Local meridian	$\approx$ 06:30 UT
Effective Collecting Area	$\approx 3\lambda^2$
Minimum detectable flux density (5σ level)	$\approx$ 0.5 sfu (40 MHz) $\approx$ 3 sfu (440 MHz)
Location	$\approx$ 77°E 14°N

2.9 Calibration of dynamic spectral data of GLOSS using Galactic Center Observations

Dynamic spectral data obtained with GLOSS contains the raw intensities over the observing band. These intensities have to be properly converted to solar flux units in order to use them in scientific analyses. One such method was developed by Dulk et al. (2001) which can be applied to all ground based radio spectrographs working in the frequency $<$ 100 MHz. At these frequencies, the overall system temperature is mainly limited by the sky temperature as the receiver noise temperature is significantly lower than the former [Kraus and Moffet (1967)]. It shows a steep fall from low to high frequencies. Also, the solid angle subtended by Galactic Centre (GC) is comparable to that of GLOSS beam solid angle. Therefore, the obtained antenna temperature will be from GC alone. This methodology is primarily adopted for flux calibration of Solar radio bursts which are often comparable to the flux estimates of GC (refer Section 1.4). At local meridian (14° North) the declination of GC is about -30° South. To compensate this, the GLOSS primary beam is steered in the direction of GC using the delay shifter boards as described in Section 2.6.1.

Cane (1977), Cane and Whitham (1977) and Cane (1978) combined several other results of low-frequency observations of Galactic Center and derived an empirical

relationship for specific intensity (W/m^2/Hz/sr) as a function of frequency; it is written as

$$I_\nu = I_g \nu^{0.52} \frac{1 - e^{\tau(\nu)}}{\tau(\nu)} + I_{eg} \nu^{0.52} \tau(\nu) \tag{2.15}$$

where I_ν(ν in MHz) is the specific intensity (a function of frequency) which has contributions from galactic (I_g) and extra galactic (I_{eg}) components. $\tau(\nu)$ is the optical depth along the line of sight. According to Dulk et al. (2001), I_g = 2.48 $\times$ 10^{20} W/m^2/Hz/sr, I_{eg} = 1.06 $\times$ 10^{20} W/m^2/Hz/sr and $\tau(\nu)$ = 5.0$\times$ ν^{20}.

Figure 2.19 shows the extrapolation (up to 100 MHz, using equation (2.15)) of galactic flux density as well as the average specific intensity weighted by antenna response (S^{gal}_{beam}). Also, the latter is related to the isotropic component (I^{iso}_ν) of equation (2.15) as $S^{iso}_{beam} = I^{iso}_\nu \times \Omega_{beam}$, where Ω_{beam} is the antenna beam area. For our LPDA S^{iso}_{beam} = 3.38 $\times I^{iso}_\nu$

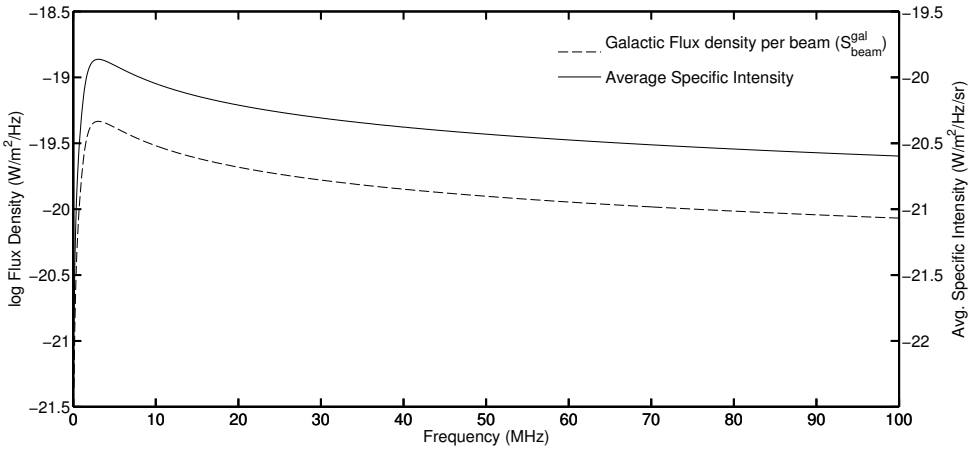

Figure 2.19: Simulated Galactic flux density as a function of frequency using equation (2.15) and the average specific intensity weighted by LPDA beam (S^{gal}_{beam}). These values are useful to estimate the flux density of target source at multiple frequencies.

2.9.1 Calibration Methodology

This method involves the observation of Galactic Center at night and target source at day. First, the calibrator is observed in transit mode. Around the transit time (17:45

LST) the peak power recorded in the spectrum is used to calibrate the raw spectral data. On next day, target source is observed around the transit time. This contains the burst, receiver as well as galactic spectral powers ($P_{BRG}(\nu)$). The earlier observation contains both the receiver as well as galactic spectral power ($P_{rec}(\nu)$+$P_{gal}(\nu)$). This has to be subtracted from the following day observation to get the true spectral power ($P_B(\nu)$) of any transient solar radio burst. The receiver noise power $P_{rec}(\nu)$ of GLOSS is estimated from the equivalent noise figure as described in Section 2.8.1.1. Using these estimates the target source (solar burst), flux density was calibrated as

$$S_B(\nu) = S_{beam}^{gal} \frac{P_B(\nu)}{P_{gal}(\nu)} \tag{2.16}$$

where $S_B(\nu)$ (W/m^2/Hz) is the calibrated target flux density and S_{beam}^{gal} is Galactic specific flux density (refer Figure 2.19).

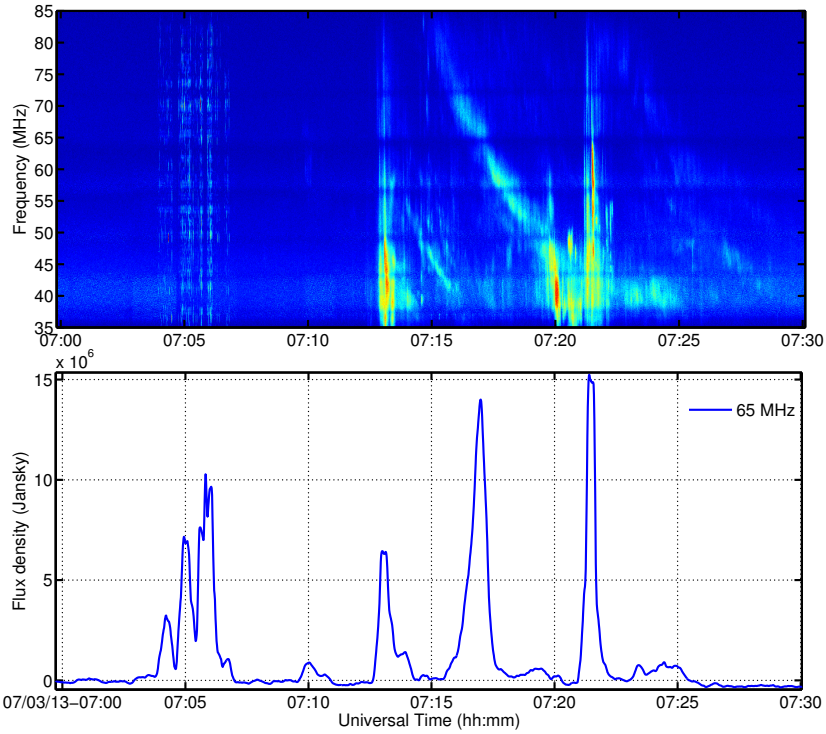

Figure 2.20: Top panel: GLOSS dynamic spectrum of a Type II burst observed on 3rd July 2013. Bottom panel: A crosscut at a typical frequency of 65 MHz. The calibration scheme is applied to this frequency profile to determine the absolute amplitude level.

However, the estimated flux density values are subject to errors due to i) beam pointing errors, ii) gain variations and various other factors. This method estimates the flux density with an error margin of $\approx$ 2 orders of magnitude. The same method is applied to GLOSS data to calibrate the true flux density of a Type II radio burst observed on 3^{rd} July 2013 (Figure 2.20). The estimated peak flux is $\approx 15\times10^6$ Jansky[4] indicates that the emission mechanism is predominantly non-thermal.

2.10 Other Observing Facilities

In addition to GLOSS, there are other observing facilities at Gauribidanur radio observatory. They are i) a dual frequency radioheliograph and ii) a dual channel radio interferometric polarimeter. Their details are given briefly as the data from them are also used (wherever required) in the scientific analyses along with GLOSS data.

2.10.1 Gauribidanur RAdio heliographPH (GRAPH)

Gauribidanur RAdio heliographPH [GRAPH, Ramesh et al. (1998); Ramesh et al. (1999); Ramesh et al. (2006b)] is a dedicated two-dimensional imaging instrument to get the snap shot images of the Solar Corona in the frequency range 40-150 MHz. The co-ordinates of the array are: Longitude = $77^\circ27'07"$ East, and Latitude = $13^\circ36'12"$ North. The antennas of GRAPH are also fixed vertically pointing toward the zenith. The tilting/steering of the antenna response ('beam') is achieved electronically through the use of diode switches, and cable delays in the radio frequency signal path from the antennas as like the GLOSS system [refer Section 2.6.1]. While the GRAPH has a provision to steer the 'beam' in both hour angle and declination, it is only in declination for GLOSS. It is a '+' (plus) shaped interferometric array consisting a total of 384

[4] 1 Janky = 10^{-26} W/m^2/Hz

antennas (LPDAs) grouped in East−West (32 groups; 8 antennas per group) and North−South (32 groups; 4 antennas per group) directions respectively. The principles of synthesis imaging [Thompson et al. (2004)] is followed to image the Sun using GRAPH visibilities on all baselines. The sensitivity and angular resolution are approximately 0.01 sfu (solar flux unit) and $5' \times 10'$ (R.A. $\times$ decl.), respectively at a typical frequency of operation at 80 MHz. A 4096 channel digital receiver helps to obtain solar images in transit mode with a maximum dynamic range of about $\approx$ 20 dB.

2.10.2 Gauribidanur Radio Interference Polarimeter (GRIP)

Two groups of LPDAs (16 antennas are combined in phase in each group) with their arms oriented in East−West & North−South form the Gauribidanur Radio Interference Polarimeter (GRIP) [Ramesh et al. (2008)]. The multiplication of the above two groups are carried out with a dedicated dual channel digital correlator similar to GRAPH produce interferometric intensity profiles of the Sun (in Stokes I & V) at two frequencies. The minimum detectable flux density of GRIP is $\approx$ 0.02 sfu.

2.11 GLOSS Observations

The GLOSS has been operated regularly between 2 and 11 UT. Several interesting radio bursts have been observed since after commissioning. The HPBW of the GLOSS in the East−West direction [$\approx 80^{\circ}$, refer Section 2.6.1] and the primary beam is pointing to the local zenith at Gauribidanur. The above width corresponds to $\approx$ 5.5 hrs in time. But in practice, we carry out observations for longer periods ($\approx$ 9 hrs) since the solar radio bursts, particularly at low-frequencies, are usually very intense [Nelson and Melrose (1985)]. Figure 2.21 shows the background subtracted GLOSS dynamic spectrum of a Type III burst followed by a F-H Type II radio burst observed on 17 November 2011

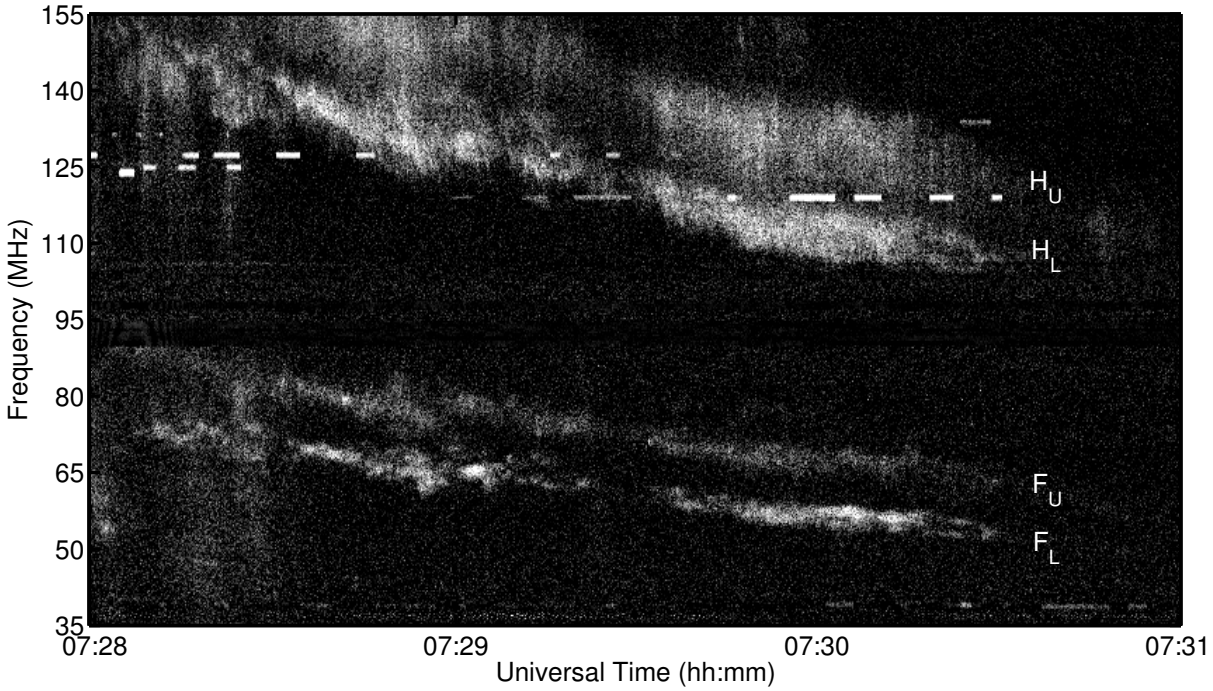

Figure 2.21: GLOSS observations of Type III radio bursts followed by a F-H split-band Type II burst on 17 November 2011. The horizontal dashed lines of intense emission near 125 MHz are due to local radio frequency interference (RFI).

during the interval ≈ 07:28–07:31 UT. The frequency range corresponding to the F and H components of the Type II burst in Figure 2.21 are ≈ $55-85$ MHz, and ≈ $110-155$ MHz. Both the components show a split-band structure with distinguishable upper and lower bands, *i.e.,* $\mathrm{F_U}, \mathrm{F_L}, \mathrm{H_U}$ and $\mathrm{H_L}$ [Nelson and Melrose (1985)]. To verify observationally the effect of the comparatively larger A_e and hence lower ΔS_{min} of GLOSS as compared to a single LPDA, we carried out simultaneous observations with the GLOSS and a single LPDA. The signal transmission and data acquisition in these two cases were similar. Figure 2.22 shows the observations of the same radio bursts in Figure 2.21, but with a single LPDA. The enhanced contrast of the spectral features in GLOSS observations are clearly evident.

Figure 2.23 shows the spectral profile of the Type II burst in Figure 2.21 at ≈ 07:30 UT. The ratio of the total bandwidth of the F and H components, peak frequencies of $\mathrm{F_L}$ and $\mathrm{H_L}$ and $\mathrm{F_U}$ and $\mathrm{H_U}$ are $\approx 1:2$. The intensity of the harmonic component is

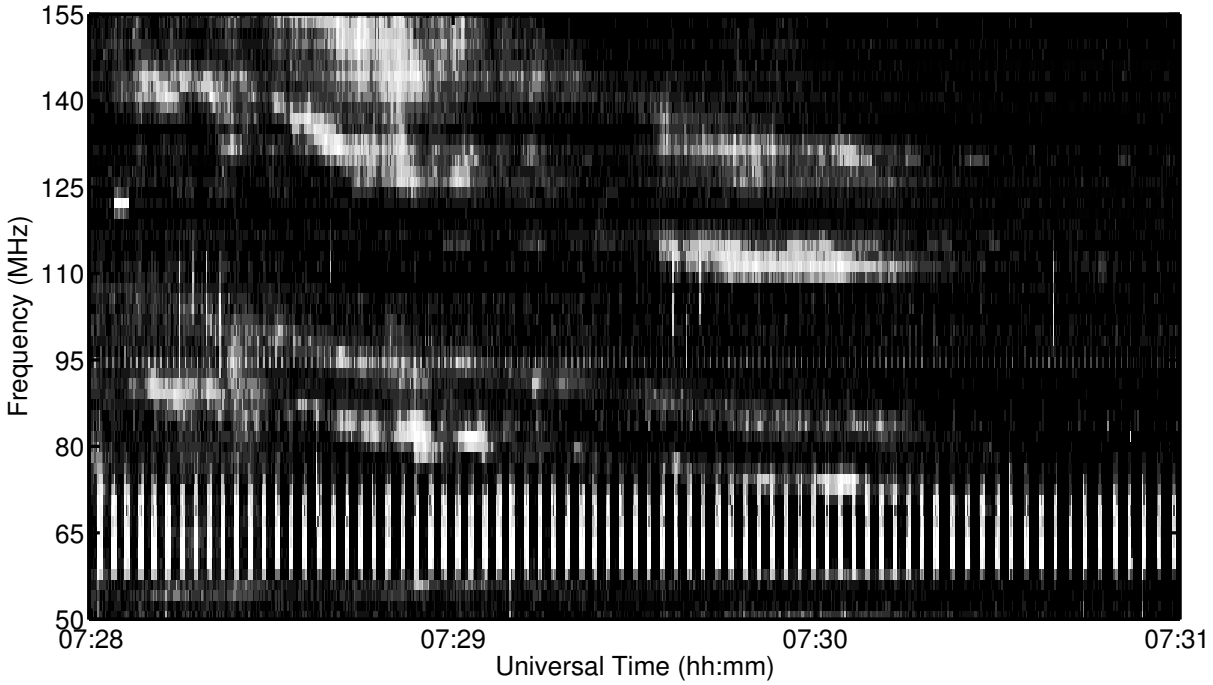

Figure 2.22: Same observations as in Figure 2.21, but with a single LPDA. The vertical stripes centered around 65 MHz are instrumental artifacts.

greater than that of the fundamental component [Wild et al. (1954); Roberts (1959)]. The event was associated with a C 6.0 class soft X-ray flare (07:16–07:30 UT) with peak at ≈ 07:27 UT and a SF class Hα flare (07:19- 07:29 UT) with peak at ≈ 07:22 UT from AR 11346 located at S19E08[5]. The *Large Angle and Spectrometric Coronagraph* C2 [LASCO C2; Brueckner et al. (1995)] on-board the orbiting *Solar and Heliospheric Observatory* (SOHO) observed a CME around the same time as the flare and the radio burst mentioned above. The CME was first noticed in the coronagraph field of view at ≈ 07:48 UT when its leading edge was at a radial distance r ≈ 2.6 $R_\odot$. Its central position angle and angular width were ≈ 81° and 97°, respectively[6]. The projected speed of the CME in the plane of the sky was ≈ 458 km s^{-1}. It was a decelerating event (≈ $-38\ \mathrm{m\ s^{-2}}$). The speed between the initial two height-time measurements was ≈ 580 km s^{-1}.

Figure 2.24 shows the location of the fundamental component of the above Type II

[5]www.swpc.noaa.gov/ftpmenu/warehouse/2011.html
[6]cdaw.gsfc.nasa.gov

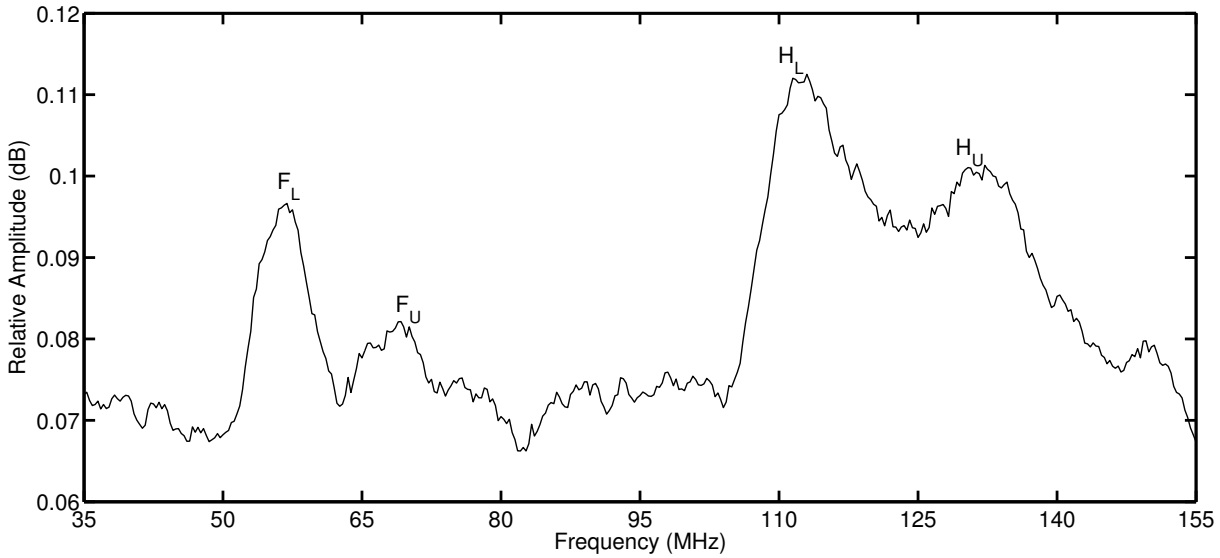

Figure 2.23: Spectral profile of Type II burst in Figure 2.21 at ≈ 07:30 UT. The ratio of the split in Fundamental and Hamonic bands are approximately 1:2.

burst at 80 MHz, observed with the Gauribidanur Radio Heliograph [GRAPH - Ramesh et al. (1998); Ramesh et al. (1999); Ramesh et al. (2006b); Ramesh et al. (2011)] around ≈ 07:28:30 UT. An inspection of Figures 2.22 and 2.24 indicate that GRAPH observations correspond most likely to the upper frequency $\mathrm{F_U}$ of the split-band structure in the fundamental component of the burst shown in Figure 2.22. The radial distance of the burst is ≈ 1.4 $\mathrm{R_\odot}$, nearly the same as the extrapolated location of the leading edge of the CME (backward towards the Sun) around the same time, obtained using a quadratic fit to the height-time measurements[7]. This spatio-temporal association between the Type II burst and the CME is consistent with the statistical results reported recently by Ramesh et al. (2012).

We followed the methodology described in Cho et al. (2007) to calculate the magnetic field strength (B) associated with the Type II burst. Assuming the hybrid coronal electron-density model of Vršnak et al. (2004), we find that B ≈ 2.8-1.9 G (refer Table 2.8) in the radial distance range r ≈ 1.4 - 1.6 $\mathrm{R_\odot}$, nearly corresponding to the fundamental component in Figure 2.22. The above density model gives a drift speed

[7]cdaw.gsfc.nasa.gov/CME_list/UNIVERSAL/2011_11/

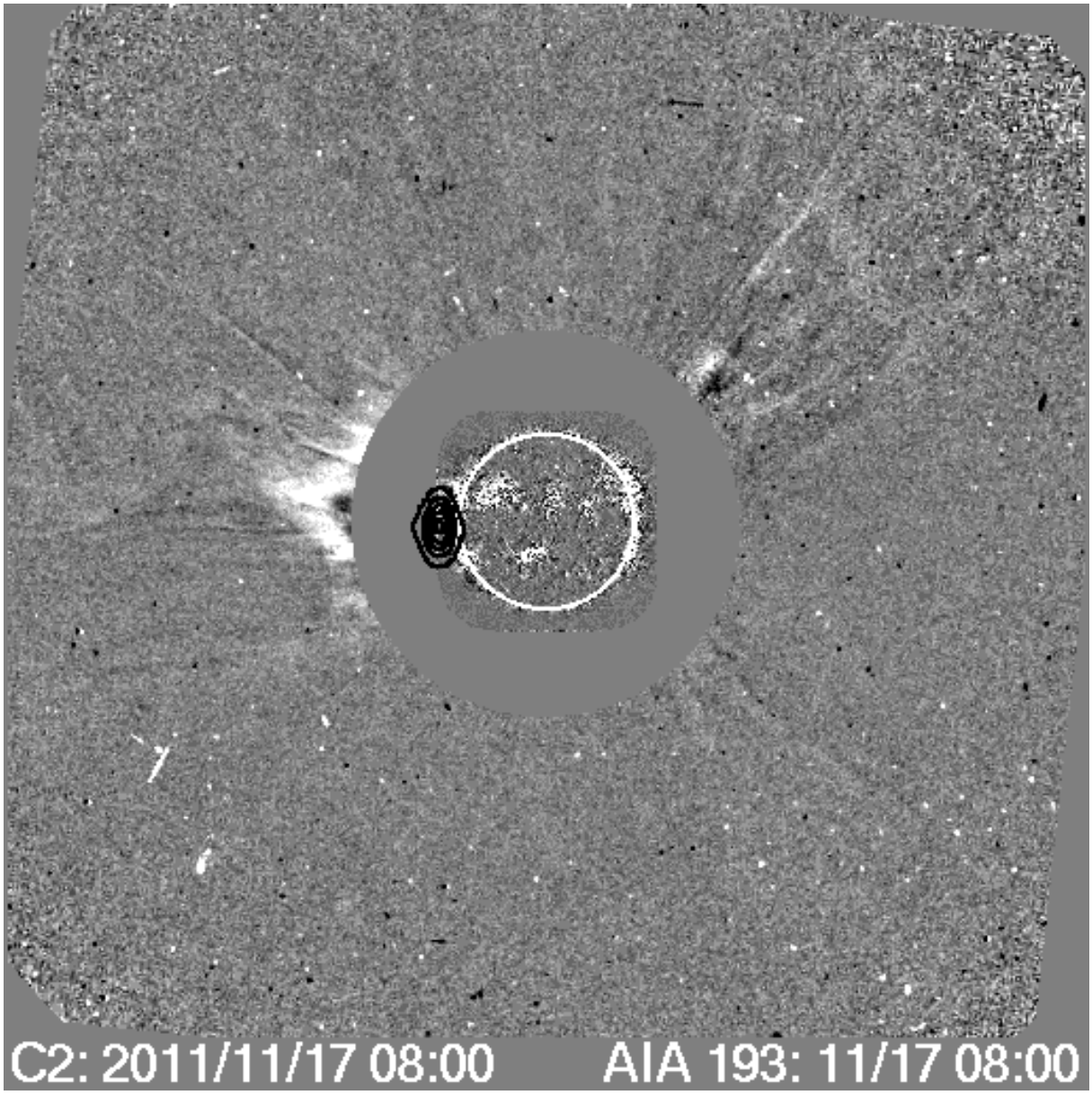

Figure 2.24: Composite of the radioheliogram (black colour contours) of the Type II burst observed with the GRAPH at 80 MHz on 17 November 2011 around ≈ 07:28:30 UT and the SOHO/LASCO C2, SDO-AIA (193 Å) images obtained around ≈ 08:00 UT on the same day. The peak brightness temperature (T_b) of the burst is $\approx 2.7 \times 10^8$ K.

Table 2.8: Split-band Type 2 characteristics

Time (Hours)	f_u (MHz)	f_l (MHz)	BDW[a]	X[b]	M_A[c]	F_L H ($R_\odot$)[d]	V_A[e] (km/s)	$B(r)$[f](G)
7.48	80.60	70.40	0.14	1.31	1.24	1.45	804.56	2.89
7.48	76.10	65.30	0.17	1.36	1.28	1.49	780.49	2.60
7.49	71.00	59.00	0.20	1.45	1.35	1.54	737.65	2.22
7.50	67.10	56.30	0.19	1.42	1.33	1.57	750.45	2.15
7.51	63.20	52.10	0.21	1.47	1.37	1.61	727.11	1.93
	Drift rate	**Shock speed**	**= 997.78 km/s**					
	= 0.14(MHz/s)	**Mean**	**= 0.18**	**1.40**	**1.31**			

[a]Instantaneous bandwidth BDW = (f_u-f_l)/f_l, where f_l and f_u are the frequencies in the F_L and F_U bands of the Type II burst, respectively.

[b]Density jump across the shock X = (BDW+1)^2.

[c]Alfvénic Mach number $M_A = \sqrt{X(X+5)/2(4-X)}$.

[d]Radial Heights (in $R_\odot$) corresponding to f_l for Hybrid density model

[e]Alfvén speed $v_A = v_{cme}/M_A$.

[f]$B(r) = 5.1 \times 10^{-5}\ f_l\ v_A$.

of $\approx$ 1000 km s^{-1} for the Type II burst which agrees reasonably well with the estimated speed of the CME close to the Sun using its height-time measurements and deceleration mentioned above. We remark that the B values are: 1) about a factor of three higher than the estimates of the magnetic field in the 'undisturbed' corona in the similar height range [Ramesh et al. (2011)]; 2) consistent with similar estimates for the 'disturbed' corona using other types of radio bursts as tracers in the same height range [Dulk and McLean (1978); Ramesh et al. (2003a); Raja and Ramesh (2013)].

Chapter 3

Near-source coronal magnetic field estimates using split-band Type II bursts

The contents presented in this chapter are based on the following publication

Constraining the solar coronal magnetic field strength using split-band Type II radio burst observations

P. Kishore, R. Ramesh, K. Hariharan, and C. Kathiravan

Manuscript submitted to Astrophysical Journal.

3.1 Introduction

TYPE II radio bursts from the Sun are caused due to Langmuir waves generated by non-thermal electrons in magnetohydrodynamic (MHD) shocks propagating outward in the solar atmosphere. Later the Langmuir waves set the local electron concentration into oscillations in the successive plasma outer layers during its course of travel. The Langmuir wave interactions involve different stages [McLean and Labrum (1985)] of plasma process and in the end, escapes as radio waves at the fundamental or at second harmonic plasma frequencies. The characteristics and description of the solar

Type II bursts can be found in the review by Nelson and Melrose (1985). They are observed as narrow-band emission features drifting from higher to lower frequencies in spectral observations. They frequently occur as two relatively slow drifting emission bands [fundamental (F) and harmonic (H)] with a frequency ratio of $\approx$ 1:2. The frequency drift [typically $\sim$ 0.1 MHz/s, see Mann et al. (1996); Gopalswamy et al. (2009)] results from the decrease of the coronal electron density (N_e) and hence the plasma frequency, with increasing distance (r) in the solar corona. The observed drift rate can be converted into the speed of the associated MHD shock if N_e(r) is known. At times, Type II bursts exhibit split-band structure: either or both the F and H components of the burst are split into two sub-bands (the upper band U and the lower band L) with a separation in frequency, usually small compared to the frequency separation between the F and H components themselves. The L and U bands in a split-band Type II burst are considered to be due to emission generated ahead of and behind the associated MHD shock front, i.e., at the upstream and downstream regions or the pre-shock and post-shock regions or the 'undisturbed' and 'disturbed' corona, respectively [Tidman et al. (1966); Vršnak et al. (2001) and Hariharan et al. (2014)].

It was first shown by Smerd et al. (1974, 1975) that Type II solar radio bursts that exhibit split-band structure can be used to determine the magnetic field strength ($B(r)$) along the paths of the propagating MHD shocks. Magnetic field strength is routinely measured only in the photosphere at present. The magnetic field strength of the 'undisturbed' corona is obtained from such measurements using extrapolation techniques [Schatten et al. (1969); Schrijver and DeRosa (2003)]. Although estimates of coronal magnetic field strength ($B(r)$) from observations in infrared, microwave, and EUV wavelength bands [Lin et al. (2000); Lee (2007) and West et al. (2011)] are possible, they are limited mostly to the 'inner' corona ($r \lesssim 1.2$ $R_\odot$). But phenomena like the acceleration of energetic particles by coronal mass ejection (CME) driven shocks, acceleration of fast solar wind, etc. occur typically in the 'middle' corona, i.e.,

$1.2\ \mathrm{R}_\odot \lesssim r \lesssim 3.0\ \mathrm{R}_\odot$ [Gopalswamy et al. (2011); Mancuso and Garzelli (2013)]. There are estimates of $B(r)$ in the above heliocentric distance range from the spectral observations of split-band Type II solar radio bursts [Smerd et al. (1974, 1975); Vršnak et al. (2002); Cho et al. (2007); Zimovets et al. (2012); Mancuso and Garzelli (2013); Hariharan et al. (2014); Vasanth et al. (2014); Hariharan et al. (2015)]. But the locations of the bursts at different frequencies, and hence the B at the corresponding values of r, were derived independently without referring to the deprojected height-time details of the associated shock driver. Considering that there is close spatio-temporal association between the Type II bursts and the CMEs [Stewart et al. (1974); Stewart (1974); Gopalswamy and Kundu (1992); Mancuso and Raymond (2004); Gopalswamy et al. (2005); Lin et al. (2006); Cho et al. (2008); Gopalswamy et al. (2009); Liu et al. (2009); Ramesh et al. (2010, 2012); Ma et al. (2011); Cho et al. (2013); Kouloumvakos et al. (2014); Hariharan et al. (2014); Hariharan et al. (2015)], we have shown, in this chapter, the method of estimating $B(r)$ by constraining the choice of $N_e(r)$ and consequently the locations of the bursts based on the observed parameters of the Type II bursts and the accompanying CMEs together. There is considerable evidence for this method because the starting frequency of the Type II bursts has a power-law relationship with the leading edge (LE) of the associated CMEs as was shown by Gopalswamy et al. (2013).

3.2 Observations

The radio spectral data were obtained during the period October 2013 - February 2014 with the GLOSS (refer Section 2.6) We specifically chose the above period for the present work since the Sun was closer to the Galactic Center (GC) in both R.A. and decl., and hence it was possible to calibrate the GLOSS antennas and the receiver system through observations of the galactic background emission in the direction of GC

[Dulk et al. (2001); Ramesh et al. (2013a); Kishore et al. (2015)]; refer Section 2.9 for more details. We used images obtained with the COR1 coronagraph of the Sun-Earth Connection Coronal and Heliospheric Investigation [Howard et al. (2008)] on-board the Solar TErrestrial RElations Observatory (STEREO), and the Large Angle and Spectrometric Coronagraph [Brueckner et al. (1995)] on-board the Solar and Heliospheric Observatory (SOHO) for information on the associated CMEs. For flare information, we used soft X-ray data obtained with the Geostationary Operational Environmental Satellite (GOES).

Figure 3.1 shows the dynamic spectrum of a typical split-band Type II burst observed with the GLOSS on 2013 November 8 during the interval 04:27-04:42 UT in the frequency range 85-35 MHz. The splitting of the F component into lower (L) and upper (U) bands, i.e., F_L and F_U, can be clearly noticed. In the H component, only the H_L band could be seen. The H_U band is close to the detection limit of GLOSS and hence unnoticeable in the dynamic spectrum (see Figure 3.2).

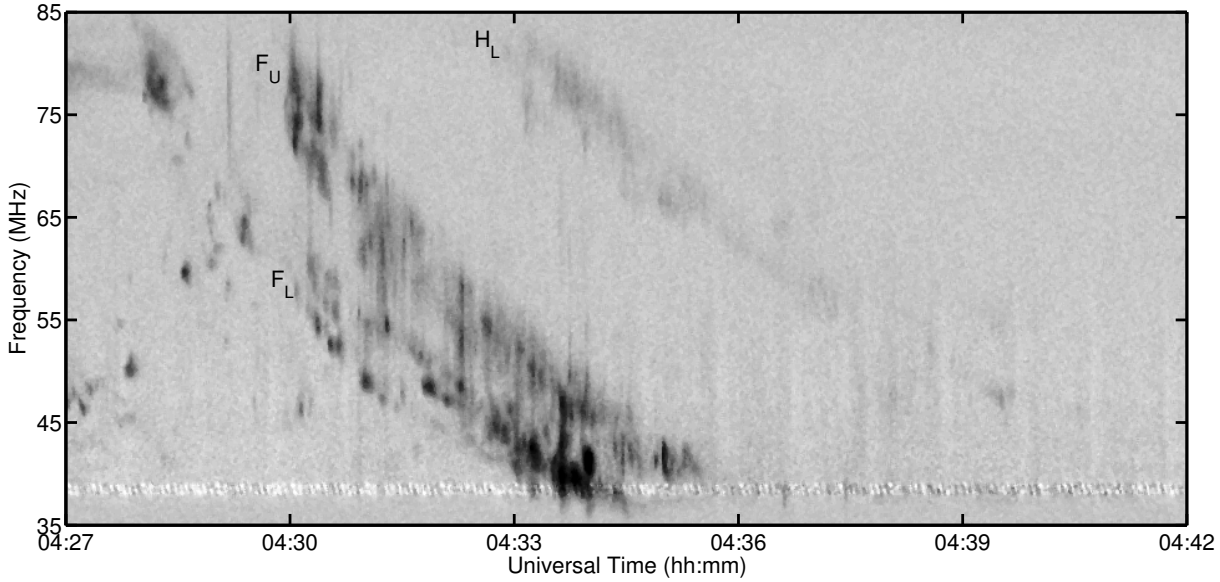

Figure 3.1: Dynamic spectrum (85-35 MHz) of the Type II radio burst from the solar corona obtained with the GLOSS on 2013 November 8 during 04:27-04:42 UT. The F and H components of the Type II burst with band splitting (in the F component) are clearly noticeable. The labels F_L and F_U represent the lower and upper bands in the F component of Type II burst. The white horizontal line close to 35 MHz is due to local radio frequency interference (RFI).

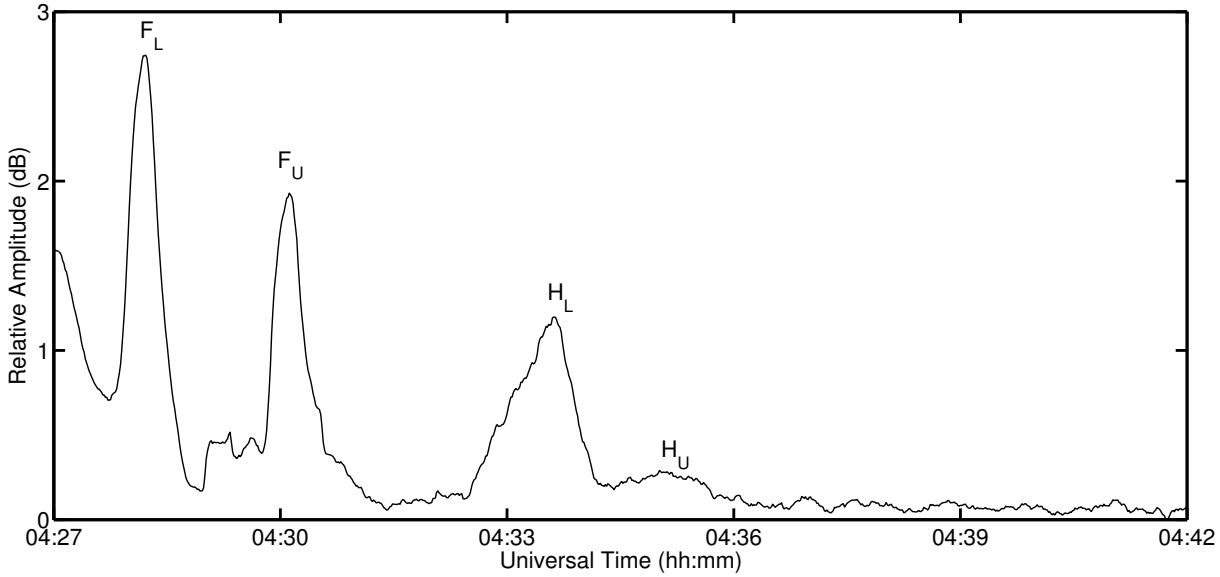

Figure 3.2: Temporal profile of the Type II burst shown in Figure 3.1 at 80 MHz showing emission corresponding to the F_L, F_U, H_L and H_U bands.

The onset time of the F_L and F_U bands at a typical frequency like 80 MHz are $\approx$ 04:28 UT and $\approx$ 04:30 UT, respectively. They are last noticed at $\approx$ 40 MHz at $\approx$ 04:34 UT and $\approx$ 04:35 UT, respectively. The duration of the F_L, F_U, H_L and H_U bands estimated from their temporal profile at 80 MHz are t_{fl}: $\mathrm{t}_{fu} \approx$ 1:2 and $t_{hl} : \mathrm{t}_{\mathrm{hu}} \approx$ 1:1.7 (see Figure 3.2). The frequency ratio of the F_L and H_L bands estimated from the respective maximum amplitudes (f_l and h_l) in the spectral profile at $\approx$ 04:33 UT are f_l: $h_l \approx$ 1:2 (see Figure 3.3).

Ratio of the corresponding instantaneous bandwidths H_L: H_L is $\approx$ 1:1. These values are consistent with those reported in the literature for split-band Type II radio bursts [see for example Hariharan et al. (2014)]. An inspection of the e-CALLISTO solar radio spectrometer [Monstein et al. (2007); Benz et al. (2009)] observations at the Gauribidanur observatory in the frequency range 45-440 MHz revealed that the above Type II burst was limited to frequencies $\lesssim$ 150 MHz.

Figure 3.4 shows the STEREO-B COR1 difference image obtained on 2013 November 8 at $\approx$ 04:45 UT. The faint white-light emission above the occulting disk in the lower

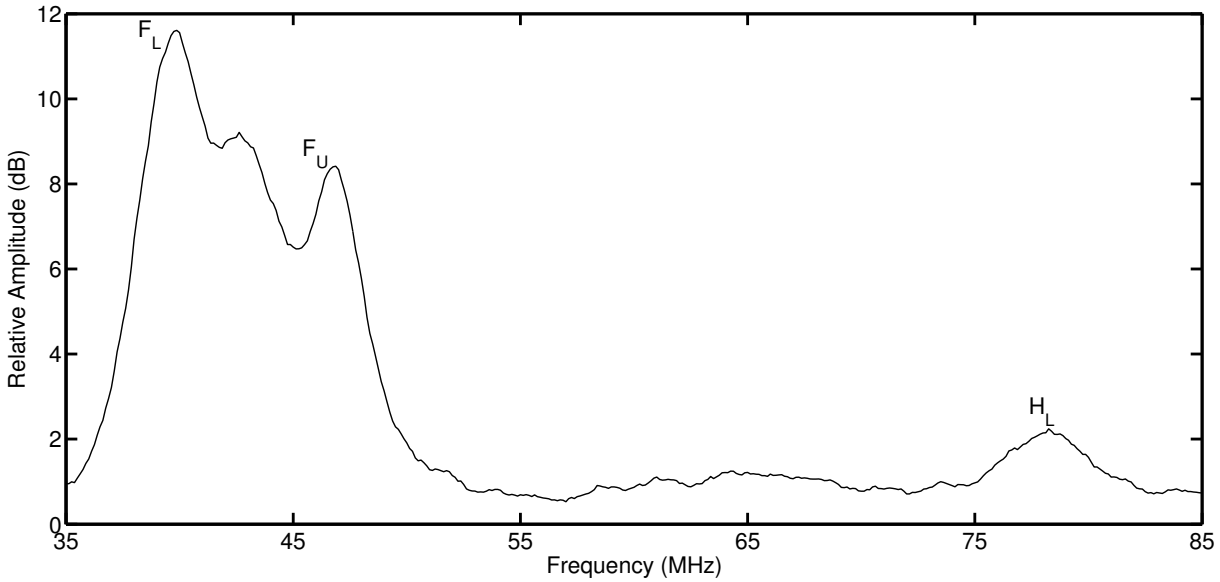

Figure 3.3: Spectral profile of Type II burst in Figure 3.1 at ≈ 04:33 UT. The emission corresponding to the F_L, F_U, H_L bands are noticeable. The H_U was not observable during the above time (refer Figure 3.1.)

right quadrant corresponds to a CME.

It was first observed in the STEREO-B field of view (FOV) at the above epoch. The angular width of the CME is ≈ 24°, and its LE is at ≈ 1.8 $R_\odot$. It was associated with a X1.1 class GOES soft X-ray flare from the NOAA active region AR11890[1] located at S13E13[2]. Note that STEREO-B was behind the Earth at ≈ E144 in the above epoch[3]. This implies that AR11890 was at ≈ W131 (i.e., ≈ 41° behind the limb) for STEREO-B view. Assuming that projection effects vary as 1/cos(ϕ), where ϕ is the angle from the plane of the sky (POS), we calculated the de-projected location of the CME LE (r_{CME}) in Figure 3.4 at ≈ 04:45 UT to be ≈ 2.33 $R_\odot$. The corresponding location at ≈ 04:50 UT is ≈ 2.64 $R_\odot$. The speed of the CME LE (v_{CME}) calculated from the above values is ≈ 719 km/s. Though the above values of r_{CME} and v_{CME} correspond to the LE of the CME, in the present case they can be considered to be nearly the same for the flank of the CME also since the angular width of the CME is small (≈ 24°) in the STEREO-B

[1]ftp://ftp.swpc.noaa.gov/pub/warehouse
[2]http://www.lmsal.com/solarsoft/latest_events/
[3]stereo-ssc.nascom.nasa.gov/cgi-bin/make_where_gif

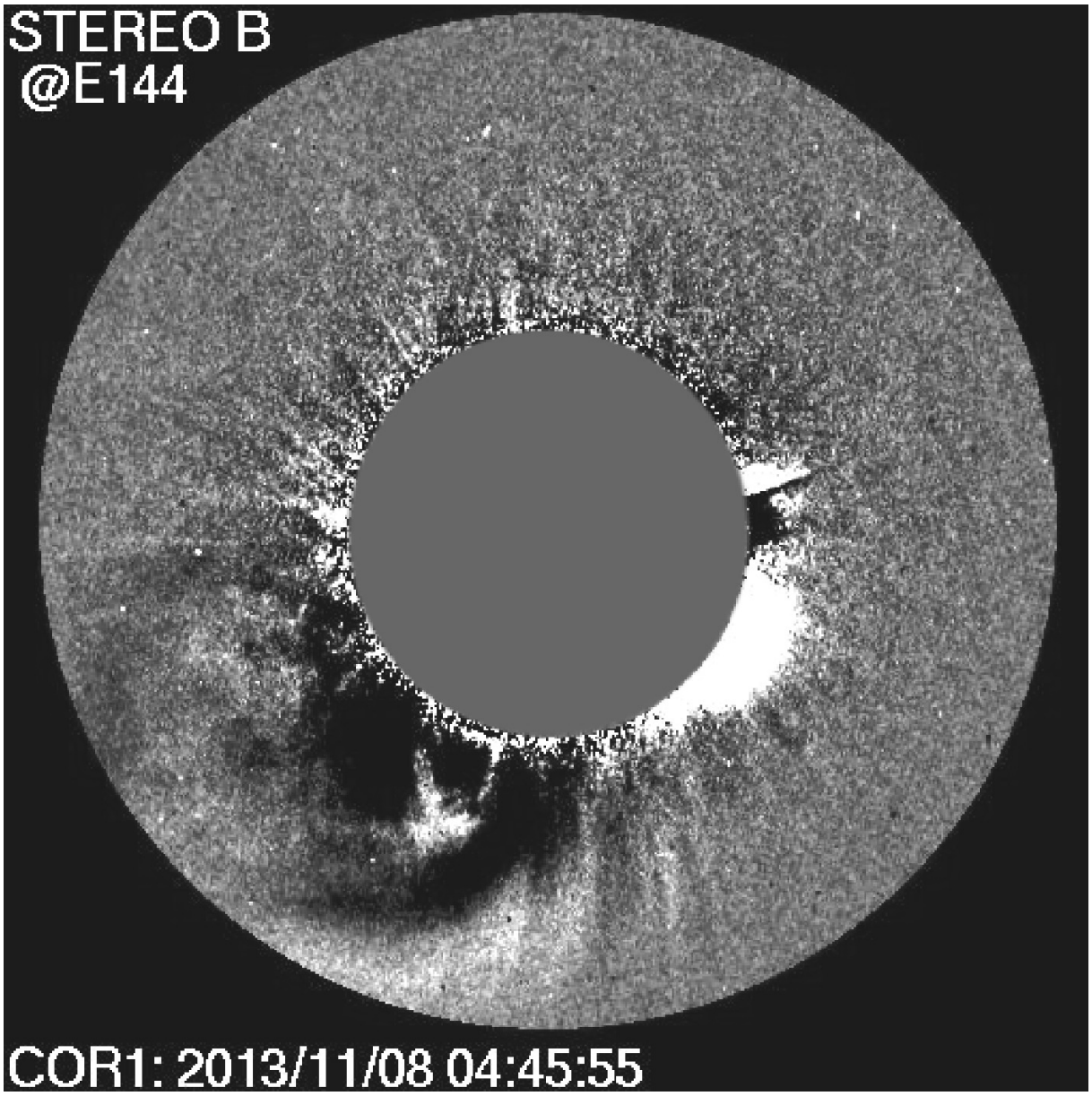

Figure 3.4: STEREO B-COR1 image obtained on 2013 November 8 at $\approx$ 04:45 UT. The 'gray' circle represents the occulting disk of the COR1 coronagraph. Its radius is $\approx$ 1.4 $R_{\odot}$. The enhanced emission above the coronagraph occulting disk in the lower right quadrant corresponds to the white light CME discussed in Section 3.2.

COR1 FOV. Note that Type II burst in Figure 3.1 was observed before the CME appeared in the STEREO-B COR1 FOV at ≈ 04:45 UT. This implies that the angular width of the CME could have been $\lesssim 24^{\circ}$ during the Type II burst period. So the above assumption regarding r_{CME} and v_{CME} is justified. The details related to the Type II bursts, flares, CMEs, and the coronal electron density distribution are listed in Table 3.1.

3.3 Results and Analysis

An inspection of Figure 3.1 indicates that the earliest time at which the Type II burst can be noticed simultaneously in both the F_L and F_U bands is ≈ 04:30 UT. The burst was present at frequency (f_s) ≈ 60 MHz in the F_L band at the above epoch. An extrapolation of the h-t locations of the associated CME mentioned in Section 3.2 indicates that r_{CME} ≈ 1.65 $R_{\odot}$ at ≈ 04:30 UT. We adopted different coronal electron density models [Baumback (1937); Allen (1947); Newkirk Jr (1961); Saito et al. (1977); Vršnak et al. (2004)] with the aim to identify the particular model(s) that satisfies the following criteria for the Type II bursts caused by CME-driven shock: 1) the location of the plasma level (r_{radio}) corresponding to f_s should be consistent with r_{CME} at the same time as the occurrence of f_s; 2) the drift speed (v_{TypeII}) of the Type II bursts based on such a model for $N_e(r)$ should agree closely with the v_{CME} of the corresponding CMEs. Note that all the above density models are applicable in the 'middle' corona where the density falls off typically as r^{-6} [Leblanc et al. (1998)]. After various trials, finally we found that both the aforementioned criteria can be closely satisfied for all the four Type II bursts and the associated CMEs by adopting Saito model with suitable density enhancement factor (D) for each burst. For example in the case of the Type II burst of 2013 November 8 (Figure 3.1), we find that 6×Saito model gives the best results. The estimated r_{TypeII} ≈ 1.61 $R_{\odot}$ corresponding to f_s = 68 MHz at ≈ 04:40 UT (see columns 3, 4 and 11 in Table 3.1) agrees closely with the r_{CME} ≈

1.67 $R_\odot$ at the above epoch. The estimated $v_{TypeII} \approx$ 843 km/s, obtained after satisfactorily addressing the first criteria mentioned above, is reasonably close to $v_{CME} \approx$ 719 km/s. The drift rate of the above Type II burst is $\approx$ 0.1 MHz/s. The density scale height in the 6$\times$Saito model is $\approx 2.3\times10^5$ km. This is nearly the same as the typical density scale height for the coronal streamers at $r \gtrsim 1.5$ $R_\odot$ [Aschwanden and Acton (2001)]. Considering that the CMEs are also density enhancements like the streamers, the similarity is possible. We also used the correspondence between the starting frequency (f) of the Type II bursts and the distance (r) of the associated CME LE, i.e., f(r)=307.87$r^{-3.78}$-0.14, to estimate v_{TypeII} [Gopalswamy et al. (2013)]. Note that the above power-law relationship should be converted to a 'model' (from now on it is referred to as Gopalswamy model) for $N_e(r)$ to calculate v_{TypeII}. We used the equality $N_e(r)=9\times10^{-3}\sqrt{f(r)}$, where $f(r)$ and $N_e(r)$ are in units of MHz and cm^{-3} respectively, for this. The density was enhanced by a factor of two (i.e., 2$\times$Gopalswamy model) to meet the criteria 1 and 2 listed above for the CME-Type II burst association in the case of the 2013 November 8 event. The estimated $v_{TypeII} \approx$ 635 km/s agrees closely with the aforementioned v_{CME}.

We calculated the associated coronal magnetic field strength ($B(r)$) from the split-band characteristics of the Type II burst of 2013 November 8 following the methodology described in Vršnak et al. (2002) and Cho et al. (2007). The results indicate that $B(r) \approx$ 1.8-1.3 G in the range $r \approx$ 1.67-1.97 $R_\odot$ in the case of 6$\times$Saito model. For 2$\times$Gopalswamy model, $B(r) \approx$ 1.35-0.97 G in the range $r \approx$ 1.68-1.91 $R_\odot$. Note that the above distance range corresponds to the frequency interval of 60-37 MHz over which both the F_L and F_U bands in the 2013 November 8 Type II burst were observed with the GLOSS (see Figure 3.1). Based on similar CME associated Type II burst observations and independent electron density estimates, Zucca et al. (2014) recently reported $B \approx$ 1 G at $r \approx$ 1.6 $R_\odot$. The corresponding plasma frequency was 70 MHz. These numbers are in good agreement with our above results. We carried out

similar analysis for the other Type II bursts reported in the present work using both Saito and Gopalswamy models. The results are listed in columns 11-13 of Table 3.1. The associated shock parameters are listed in Table 3.2.

Note that the CME associated with one of the split-band Type II bursts (19 November 2013) evolved into a 'halo' CME in the SOHO-LASCO C2 FOV during the post Type II burst period (see column 9 in Table 3.1). A comparison of r_{TypeII} (corresponding to f_s) with deprojected r_{CME} (see columns 7 and 11 in Table 3.1), and v_{TypeII} with deprojected v_{CME} (see columns 8 and 12 in Table 3.1) for each event indicates that there is closer agreement between the respective values in $D\times$Saito model (see particularly v_{TypeII} and deprojected v_{CME} for 19 November 2013 and 10 February 2014 events). In this regard we would like to mention that the D values used in the $N_e(r)$ model for each event (see column 10 of Table 3.1) are consistent with: 1) those reported earlier for radio observations associated with large scale density enhancements like the CMEs and coronal streamers in the solar atmosphere [Sastry et al. (1981, 1983); Lantos et al. (1987); Schmahl et al. (1994); Ramesh et al. (2001); Kathiravan et al. (2002); Kathiravan and Ramesh (2004); Kathiravan and Ramesh (2005); Subramanian (2004)]; 2) recent observations by Morosan et al. (2014) which indicate that plasma levels corresponding to $\approx$ 60-30 MHz as in the present case (see column 3 in Table 3.1) can occur at heliocentric distances as large as $r \approx$ 2.5-4.0 $R_\odot$ when there is a CME. We found that for this to happen, the value of D as per Saito model used should be $\gtrsim$ 35; 3) white-light coronagraph observations of CME associated MHD shock indicate that even the POS density ahead of the propagating CME front is enhanced by a factor of $\gtrsim$ 10 for 'halo' CMEs at $r \approx 6$ $R_\odot$ [Vourlidas et al. (2003); Ontiveros and Vourlidas (2009)]. This implies that the enhancement could be larger when the CMEs are located comparatively closer to the Sun where the Type II bursts in the present case occur since the size of the CMEs increase as they propagate [Gopalswamy et al. (2012)].

Table 3.1: Details related to Type II bursts, flares, CMEs, $N_e(r)$, and $B(r)$

S.No.	Date	Type II burst		X-ray flare	Spacecraft[a]/	CME LE[b]		CME	Ne(r)	r_{TypeII}	v_{TypeII}	$B(r)$
		freq. range[c]	onset time	class/location	location	proj./ de proj.	proj./de proj.	width[b]	Model [d]	range ($R_\odot$)	(km/s)	range (G)
		(MHz)	(UT)			r_{CME}[e]($R_\odot$)	v_{CME}(km/s)	(deg.)				
1	2013/10/08	68-51	04:50	B6.9/S13E63	S-B/E140	1.58/1.37	411/435	29	6S	1.67-1.97	555	1.73-1.32
									2G	1.63-1.76	431	1.34-1.02
2	2013/11/08	60-37	04:30	X1.1/S13E13	S-B/E144	1.25/1.65	549/719	24	6S	1.67-1.97	843	1.80-1.30
									2G	1.68-1.91	635	1.35-0.97
3	2013/11/19	61-36	10:29	X1.0/S13W69	S-A/W149	1.96/2.00	878/894	40[f]	17S	2.00-2.40	711	1.50-1.11
									8G	2.01-2.30	503	1.00-0.80
4	2014/02/10	43-38	05:16	C3.0/S12E29	S-B/E158	1.56/2.02	696/900	14	9S	2.01-2.12	847	1.17-1.04
									4G	2.01-2.09	620	0.86-0.76

[a] S-A and S-B stand for STEREO-A and STEREO-B, respectively.

[b] STEREO-COR1 measurements during/close to the Type II burst period.

[c] Correspond to the F_L band.

[d] S and G indicate Saito and Gopalswamy model respectively. The prefixed numbers specify the density enhancement factor (D× S/G).

[e] At the time of first appearance.

[f] Evolved into a 'halo' CME in the SOHO-LASCO C2 FOV, after the Type II burst observations.

Table 3.2: Shock parameters estimated from the band-split of the Type II bursts listed in 3.1

S.No.	Date	freq. range (MHz)	Ne(r) model [a]	r_{TypeII} ($R_\odot$)	BDW[b]	X[c]	M_A[d]	v_A[e] (km/s)	$B(r)$[f](G)
1	2013/10/08	68-51	6S	1.61-1.77	0.06	1.13	1.1	508-498	1.73-1.32
2	2013/11/08	60-37	6S	1.67-1.97	0.21	1.45	1.36	681-585	1.80-1.30
3	2013/11/19	61-36	17S	2.00-2.40	0.22	1.5	1.4	598-495	1.50-1.11
4	2014/02/10	43-38	9S	2.01.2.12	0.3	1.69	1.56	638-631	1.17-1.04

[a] S indicates Saito model. The prefixed numbers specify the density enhancement factor.

[b] Instantaneous bandwidth BDW = $(f_u\text{-}f_l)/f_l$, where f_l and f_u are the frequencies in the F_L and F_U bands of the Type II burst, respectively.

[c] Density jump across the shock X = (BDW+1)^2.

[d] Alfvénic Mach number $M_A = \sqrt{X(X+5)/2(4-X)}$.

[e] Alfvén speed $v_A = v_{cme}/M_A$.

[f] $B(r) = 5.1 \times 10^{-5}\ f_l\ v_A$.

Figure 3.5 shows the estimates of $B(r)$ for the split-band Type II bursts reported in the present work using $D\times$Saito model. The radial variation follows a power-law of the form $B(r) = 1.26 \times (r-1)^{-0.58}$ in the range $r \approx$ 1.6-2.4 $R_\odot$ where the radio emission corresponding to the frequencies 68-36 MHz originated in the present case (see columns 3 and 11 in Table 3.1). The estimated $B(r)$ values agree reasonably well with those reported in the literature based on observations of Type II bursts at different epochs. The best fit to the estimates from different Type II bursts gives $B(r) = 0.88 \times (r-1)^{-0.39}$ in the range $r \approx$ 1.2 - 2.4 $R_\odot$, i.e., the 'middle' corona (see Figure 3.6).

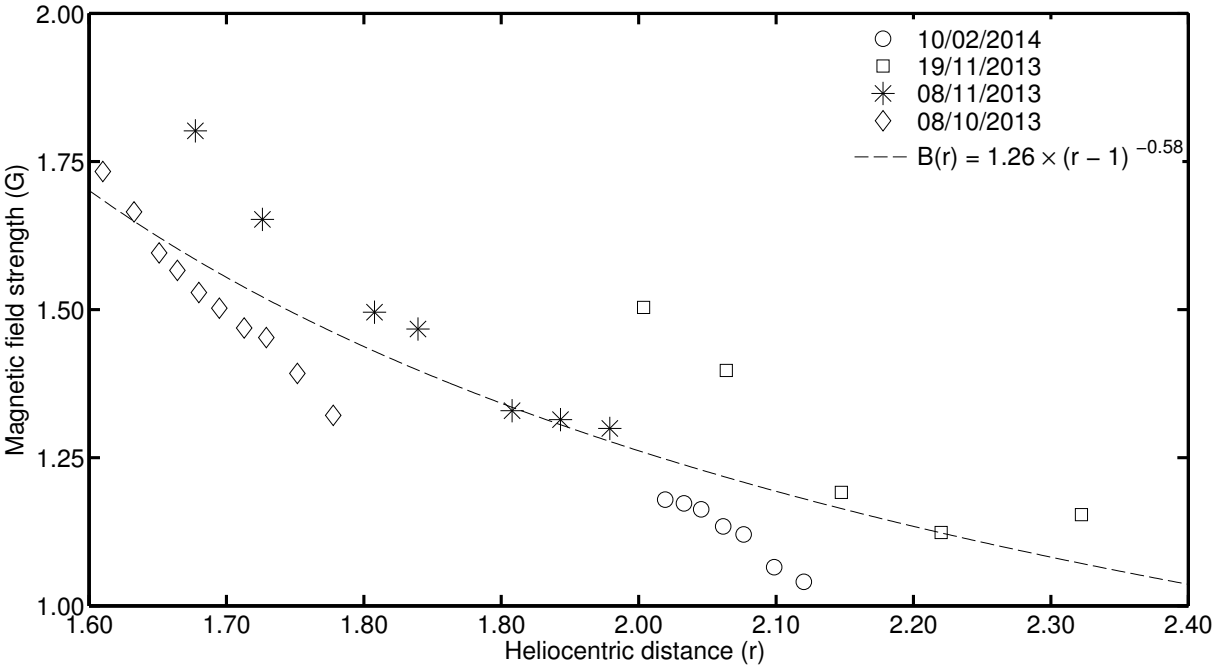

Figure 3.5: $B(r)$ obtained from the split-band Type II bursts using $D\times$Saito model (see Table 3.1). The 'dashed' line is the best fit to the estimates.

We would like to add that the field strengths in Figure 3.6 agree reasonably with those reported in the literature from observations of other CME associated phenomena also [Bastian et al. (2001); Ramesh et al. (2003a,b, 2013a); Gopalswamy et al. (2011); Kwon et al. (2013); Sasikumar Raja et al. (2014); Susino et al. (2015); Hariharan et al. (2016)]. A comparison with the $B(r)$ values for the non-flaring corona indicates that the present estimates are approximately two times larger [Gopalswamy et al. (1986);

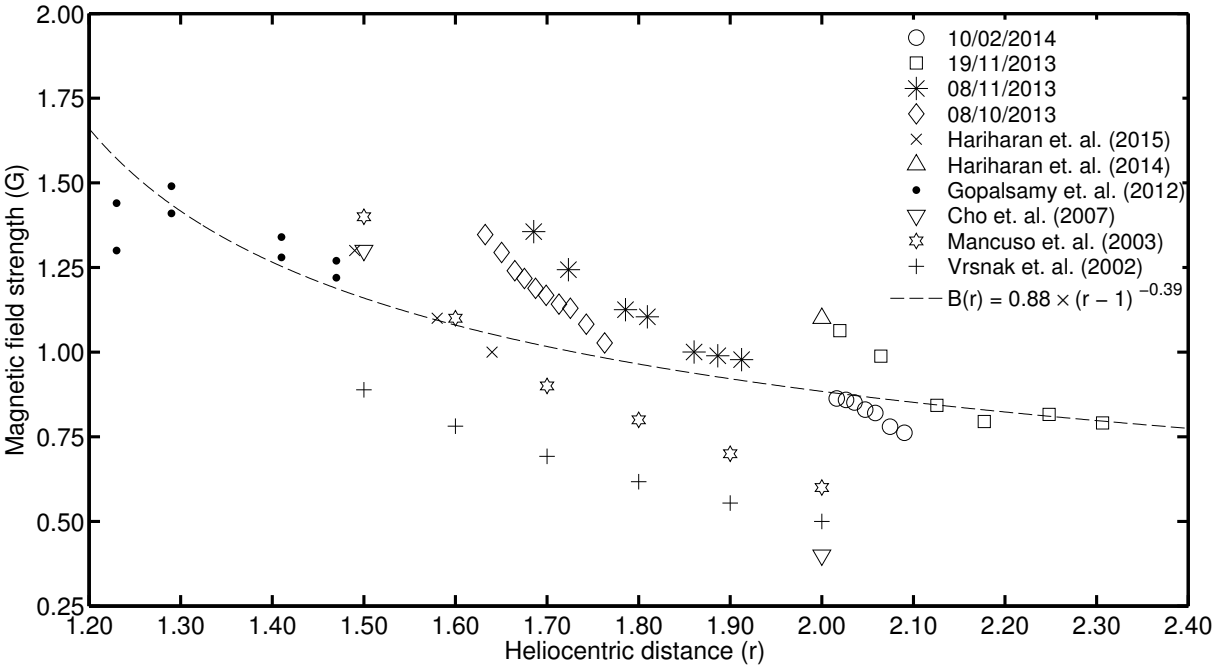

Figure 3.6: $B(r)$ obtained from the split-band Type II bursts presented (see Table 3.1 and Figure 3.5), and measurements reported in the literature based on Type II burst observations. The 'dashed' line is the best fit to the estimates.

Ramesh et al. (2011)]. This is consistent with the results obtained by Bemporad and Mancuso (2010) that the coronal magnetic field strength associated with a CME is twice enhanced compared to the pre-CME corona.

Chapter 4

On the emission mechanism & magnetic field estimates of moving Type IVm radio bursts

The contents presented in this chapter are based on the following publication

Low−Frequency Observations of Drifting, Non-Thermal Continuum Radio Emission Associated With The Solar Coronal Mass Ejections

Ramesh, R., **P. Kishore**, Sargam M. Mulay, Indrajit V. Barve, C. Kathiravan, and T. J. Wang, 2013, *The Astrophysical Journal*, 2013 Oct 31;778(1):30.

4.1 Introduction

AMONGST the different types of transient low-frequency non-thermal radio emission from the solar corona, the moving Type IV bursts are considered useful to understand the CMEs because of their close spatio-temporal association with the latter and the possibility to estimate the strength of the CME magnetic field using them. The bursts last for tens of minutes at each observing frequency and have the character of smooth continuum. Their spectrum is often featureless, and recognition requires

directional observations. A majority of the reported observations of the moving Type IV bursts are limited to frequencies $<$ 200 MHz. The burst source has been observed to steadily move outward in the solar atmosphere at speeds in the range $\approx$ 100-1600 km/s [Stewart (1985); Gopalswamy and Kundu (1989a)]. Statistically the drift speeds of the moving Type IV bursts associated with the CME frontal structure has been found to be faster than the speed of the bursts located behind the CME. The latter category of bursts are associated with either prominence eruptions or slower moving CME features [Stewart (1985); Gopalswamy and Kundu (1995)]. Note that while the frequency-time drift rates of moving Type IV bursts can be very similar to that of typical Type II bursts, the durations of Type II bursts at a given frequency ($\sim$ 1 m) are much shorter than for IVm bursts, producing much sharper features in a dynamic spectrum. Second harmonic plasma radiation from non-thermal electrons trapped in the plasmoids associated with the CMEs [Duncan (1981); Stewart et al. (1982); Gary et al. (1985); Gopalswamy and Kundu (1989b); Kundu et al. (1989)] or optically thin non-thermal gyro-synchrotron emission from mildly relativistic electrons spiralling in the magnetic field transported by the aforementioned plasmoids [Gopalswamy and Kundu (1989a); Bastian and Gary (1997); Tun and Vourlidas (2013)] are the mechanisms invoked to explain the moving Type IV bursts. The latter is usually invoked only if the density in the plasmoid were too low. It has also been suggested that second harmonic plasma emission followed by gyro-synchrotron emission could plausibly explain all the observed features of the bursts [Melrose (1985)]. The non-thermal electrons are considered to be produced through either flare or filament-eruption related reconnection process. Smerd and Dulk (1971) sub-classified the moving Type IV bursts into three categories based on phenomenological differences. They are: (1) isolated source, (2) expanding arch, and (3) advancing front. Their locations with respect to the CME are also different. The faster moving Type IV bursts are of the advancing variety, and they are associated with the CME frontal structure as mentioned earlier. More details are presented in the review

by Stewart (1985). It is more than half a century since the discovery of the moving Type IV bursts [Boischot (1957)], but simultaneous white-light, radioheliograph and radio spectrograph observations (the latter particularly almost till the Low-frequency cut-off for ground-based radio observations) of the bursts have rarely been reported. While the heliograph and white light coronagraph observations help to establish the spatial correspondence between the location of the radio burst and the CME, the spectrograph observations are required to identify the spectral nature of the observed emission from the presence/absence of drift in the emission frequency of the bursts as a function of time and also constrain the electron density. This chapter deals with low-frequency ($<$ 100 MHz) radio imaging and spectral observations of three moving Type IV bursts along with the coronagraph observations of the associated white light features. The bursts were observed on three different days from the same active region during the transit of the latter across the solar disk. Arguments for the probable emission mechanism and also for constraining the associated magnetic field are presented in this chapter.

4.2 Observations

The radio data reported in this chapter were obtained on 2012 January 16, 2012 January 23 and 2012 January 26 at 80 MHz with the GRAPH in the imaging mode, and over the 85-35 MHz band with the GLOSS in the spectral mode. The optical data were obtained with the Large Angle and Spectrometric Coronagraph [Brueckner et al. (1995)] on-board the Solar and Heliospheric Observatory (SOHO), COR1 coronagraph and 195 Å Extreme-UltraViolet Imager (EUVI) of the Sun-Earth Connection Coronal and Heliospheric Investigation [Howard et al. (2008)] on-board the Solar TErrestrial RElations Observatory (STEREO), and in 193 Å with the Atmospheric Imaging Assembly [Lemen et al. (2012)] onboard the Solar Dynamics Observatory (SDO).

4.2.1 The event of 2012 January 16

Figure 4.1 shows the moving Type IV radio burst observed with the GLOSS on 2012 January 16 during ≈ 03:18-04:48 UT in the frequency range 85-35 MHz. The average duration (τ) of the bursts was ≈ 78 m. Assuming 10 × Baumbach-Allen model [Baumback (1937); Allen (1947)] for the electron density distribution in the solar corona under 'disturbed' conditions we calculated the drift speed of the burst to be ≈ 162 km/s. Figure 4.2 shows the location of the above moving Type IV burst at 80 MHz around ≈ 03:30 UT and ≈ 04:00 UT on the SOHO-LASCO C2, SDO-AIA 193 Å images, both obtained around ≈ 03:24 UT on the same day.

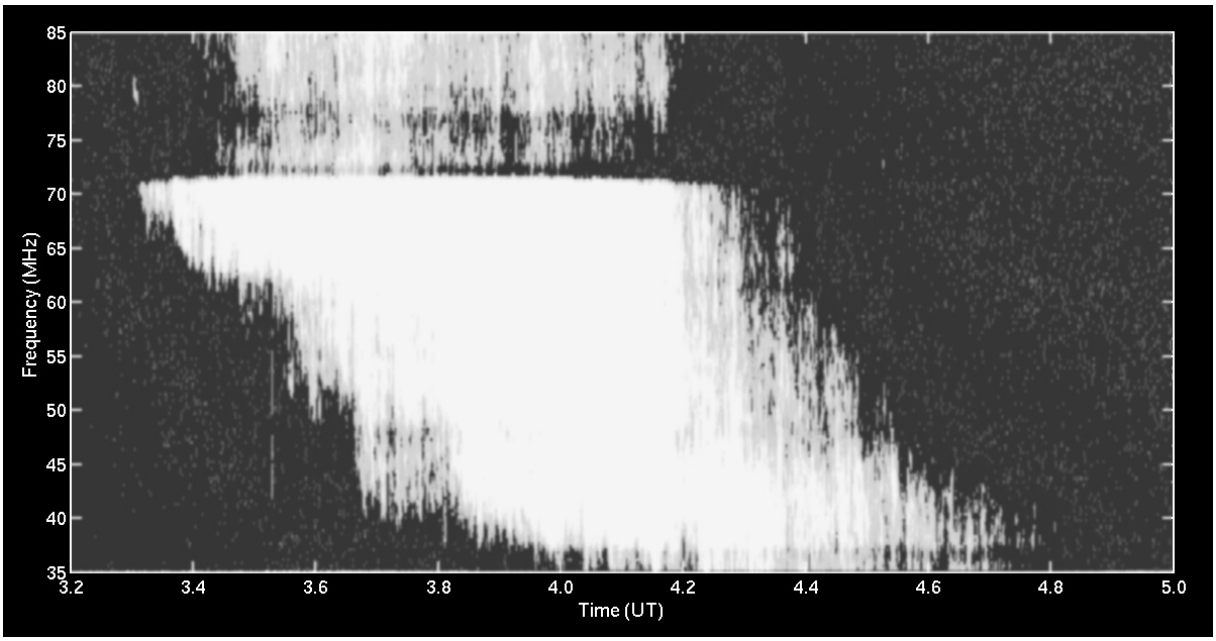

Figure 4.1: Dynamic spectrum of the moving Type IV radio burst observed with the GLOSS on 16 January 2012 during ≈ 03:18-04:48 UT in the frequency range 85-35 MHz. The drift speed of the burst is ≈ 162 km/s by using 10 times Baumbach-Alen density model. The discontinuity in the spectrum near 70 MHz is due to the use of a 'notch' filter to suppress the strong radio frequency interference at that frequency.

The centroids of the burst are at $r \approx 1.4$ $R_\odot$ (03:30 UT) and $r \approx 1.8$ $R_\odot$ (04:00 UT). This gives a projected speed of ≈ 155 km/s for the burst which is nearly equal to that obtained using its dynamic spectrum mentioned above. The peak T_b of the bursts at

the above two locations and epochs are $\approx 6.2 \times 10^7$ K and $\approx 7.4 \times 10^7$ K, respectively. The enhanced white-light emission in Figure 4.2 at a position angle (PA, measured counter-clockwise from the solar north) of $\approx 50^\circ$ in the coronagraph field of view (FOV) corresponds to a CME.

It was associated with a C6.2 class GOES soft X-ray flare ($\approx$ 02:28-04:20 UT) and C6.5 class GOES soft X-ray flare ($\approx$ 02:36-06:46 UT) from the sunspot region AR 11402 at the heliographic location $\approx$ N34E86[1]. The projected speed[2] of the CME leading edge (CME LE) in the plane of the sky was $\approx$ 1060 km/s. Note that according to the height-time data of the CME, its LE was at $r \gtrsim 3.47$ $R_\odot$ as early as $\approx$ 03:12 UT itself. This indicates that the aforementioned moving Type IV burst was not associated with the CME LE. A comparison of the positions of the burst and the white-light CME indicates that the centroid of the burst was most likely co-spatial with the southern leg of the CME beneath the occulting disk of the coronagraph.

4.2.2 The event of 2012 January 23

Figure 4.3 shows the moving Type IV radio burst observed with the GLOSS on 2012 January 23 during $\approx$ 04:00-04:42 UT in the frequency range 85-35 MHz.

The average duration of the bursts is $\approx$ 40 m and their drift speed estimated as mentioned in Section 2.1 is $\approx$ 179 km/s. The Type IV bursts were preceded by a group of Type III bursts during $\approx$ 03:39-03:50 UT. Figure 4.4 shows the location of the above moving Type IV burst at 80 MHz around $\approx$ 04:05 UT and $\approx$ 04:40 UT on the SOHO-LASCO C2, SDO-AIA 193 Å images, both obtained around $\approx$ 04:00 UT on the same day. The centroids of the burst are at $r \approx 1.5$ $R_\odot$ (04:05 UT) and $r \approx 2.0$ $R_\odot$ (04:40 UT). This gives a projected speed of ≈ 166 km/s for the burst which is nearly equal to that obtained using its dynamic spectrum mentioned above. The peak T_b of the bursts at the

[1]www.lmsal.com/solarsoft/latest_events_archive.html
[2]http://cdaw.gsfc.nasa.gov/CME_list

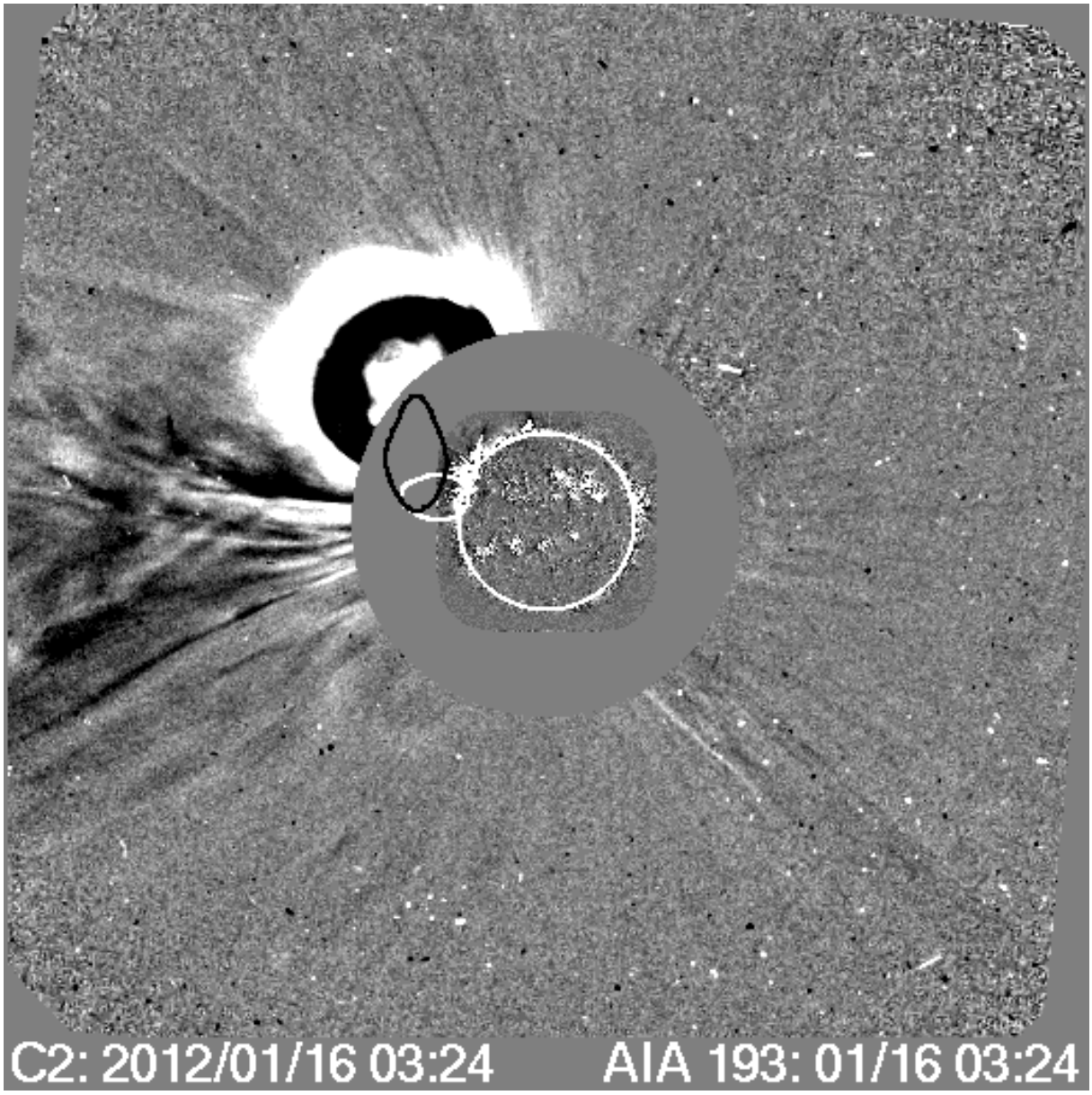

Figure 4.2: A composite of the half-power contour of the moving Type IV bursts observed with the GRAPH on 16 January 2012 at 80 MHz around ≈ 03:30 UT (white colour), ≈ 04:00 UT (black colour) and the SOHO-LASCO C2, SDO-AIA (193 Å) images obtained at ≈ 03:24 UT on the same day. The peak T_b of the bursts are ≈ 6.2 $\times$ 10^7 K and 7.4 $\times 10^7$ K, respectively.

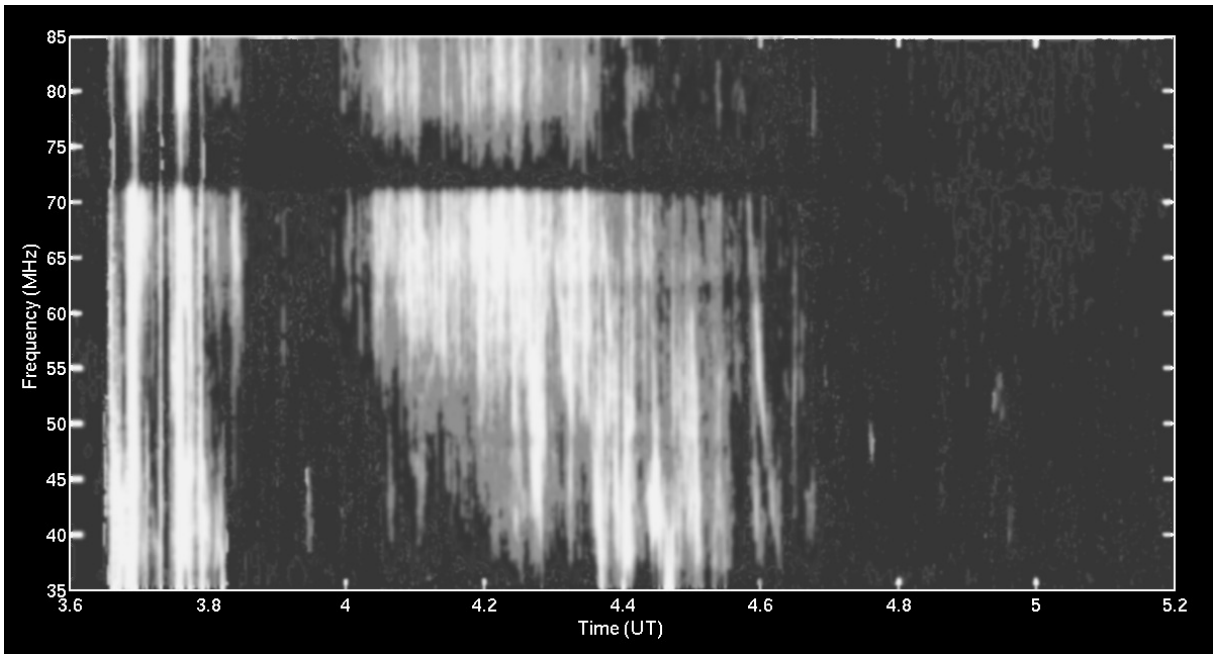

Figure 4.3: Same as Figure 4.1 but observed on 23 January 2012 during $\approx$ 04:00-04:42 UT. The drift speed of the burst is $\approx$ 179 km/s. The fast drifting emission during $\approx$ 03:36-03:48 UT corresponds to a group of Type III bursts.

above two locations and epochs are $\approx 7.4 \times 10^7$ K and $\approx 6.2 \times 10^7$ K, respectively. The enhanced white-light emission in Figure 4.4 at PA $\approx 332^\circ$ in the coronagraph field of view (FOV) corresponds to a CME. It was associated with an M8.7 class GOES soft X-ray flare ($\approx$ 03:38-04:34 UT) and a SF class Hα flare ($\approx$ 03:25-03:30) from the sunspot region AR 11402 at the heliographic location $\approx$ N33W21. The projected speed of the CME LE in the plane of the sky was $\approx$ 2175 km/s. Note that according to the height-time data of the CME, its LE was at $r \gtrsim 3.38$ R$_\odot$ as early as $\approx$ 04:00 UT itself. This indicates that the aforementioned moving Type IV burst was not associated with the CME LE. A comparison of the positions of the burst and the white-light CME indicates that the centroid of the burst was most likely co-spatial with the southern leg of the CME beneath the occulting disk of the coronagraph.

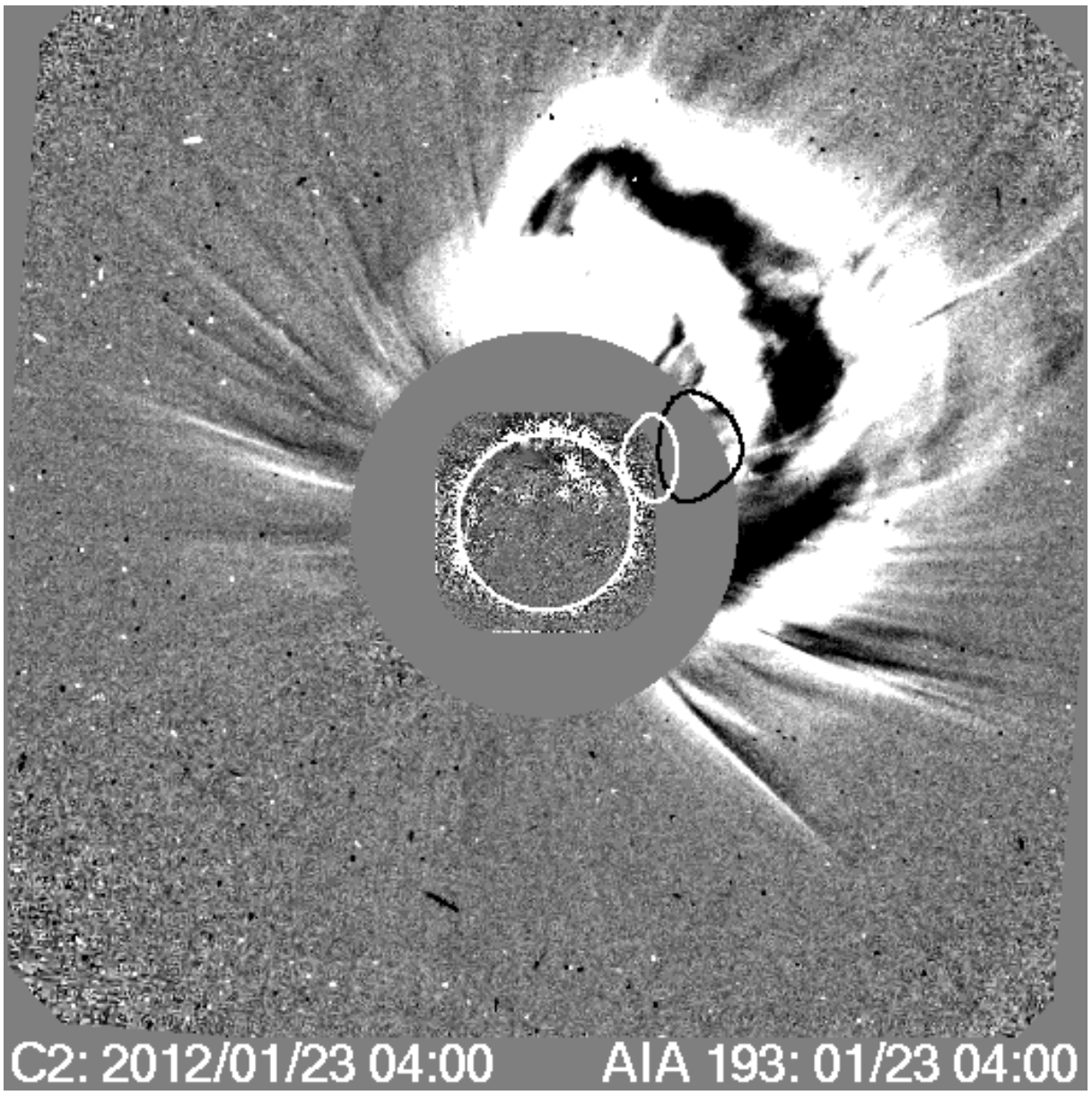

Figure 4.4: A composite of the half-power contour of the moving Type IV bursts observed with the GRAPH on 23 January 2012 at 80 MHz around ≈ 04:05 UT (white colour), ≈ 04:40 UT (black colour) and the SOHO-LASCO C2, SDO-AIA (193 Å) images obtained at ≈ 04:00 UT on the same day. The peak T_b of the bursts are ≈ 7.4×10^7 K and 6.2×10^7 K, respectively.

4.2.3 The event of 2012 January 26

Figure 4.5 shows the moving Type IV radio burst observed with the GLOSS on 2012 January 26 during ≈ 04:30-05:18 UT in the frequency range 85-35 MHz.

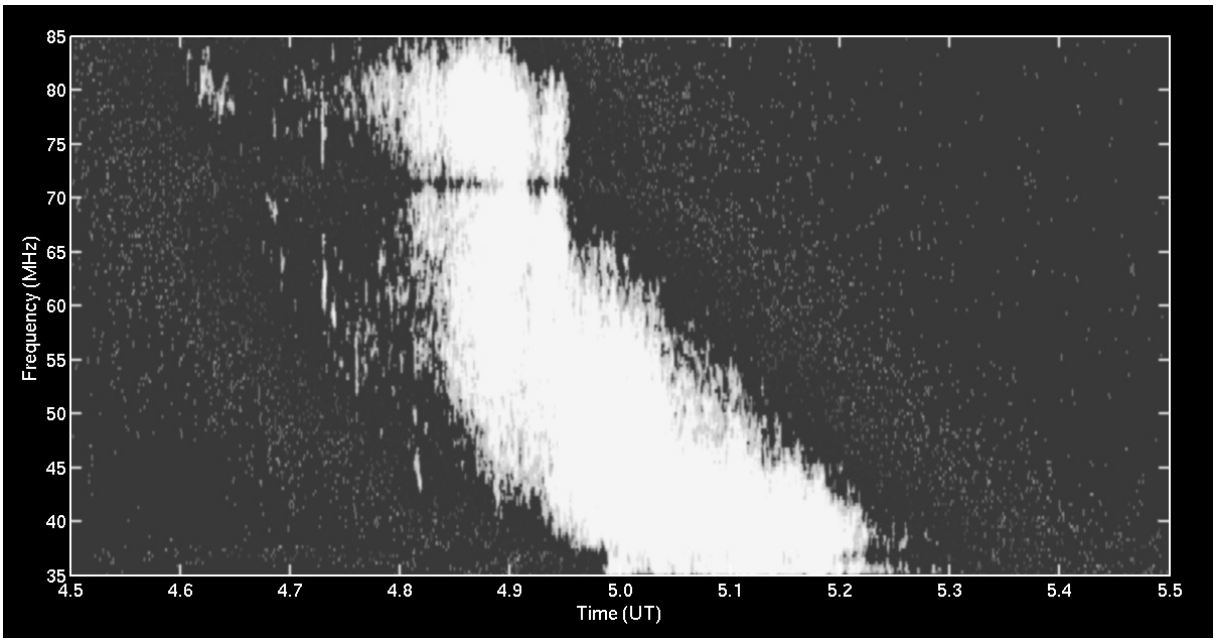

Figure 4.5: Same as Figure 4.1 and 4.3, but observed on 26 January 2012 during 04:30-05:18 UT. The drift speed of the burst is ≈ 284 km/s.

The average duration of the bursts is ≈ 36 m and their drift speed estimated as mentioned in Section 2.1 is ≈ 284 km/s. Figure 4.6 shows the location of the above moving Type IV burst at 80 MHz around ≈ 04:40 UT and ≈ 04:55 UT on the SOHO-LASCO C2, SDO-AIA 193 Å images, both obtained around ≈ 05:00 UT on the same day. The centroids of the burst are at $r \approx 1$ $R_\odot$ (04:40 UT) and $r \approx 1.6$ $R_\odot$ (04:55 UT). This gives a projected speed of ≈ 464 km/s for the burst which is about a factor of two higher than that obtained using its dynamic spectrum mentioned above. The peak T_b of the bursts at the above two locations and epochs are ≈ 7.9 × 10^7 K and ≈ 8.4 × 10^7 K, respectively. The enhanced white-light emission in Figure 4.6 at PA ≈ 324° in the coronagraph field of view (FOV) corresponds to a CME. Details of all three bursts are tabulated in Table 4.1

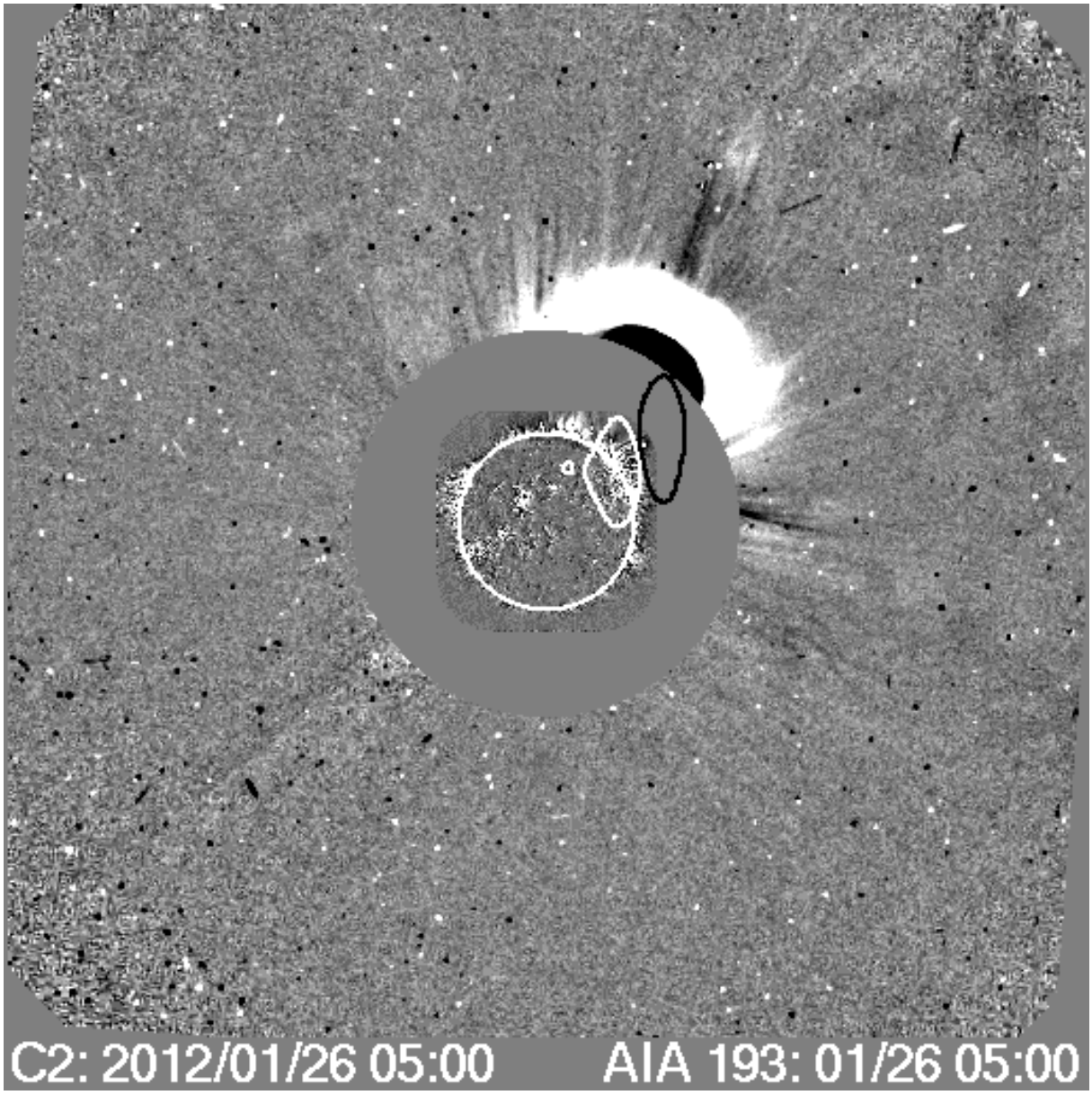

Figure 4.6: A composite of the half-power contours of the moving Type IV burst observed with the GRAPH on 26 January 2012 at 80 MHz around $\approx$ 04:40 UT (white colour), $\approx$ 04:55 UT (black colour), and the SOHO-LASCO C2, SDO-AIA (193 Å) images obtained at $\approx$ 05:00 UT on the same day. The peak T_b of the bursts are $\approx 7.9 \times 10^7$ K and 8.4×10^7 K, respectively.

Table 4.1: Details of all three moving Type IV bursts

	16 Jan		23 Jan		26 Jan	
Epoch of bursts	03:30	04:00	04:05	04:40	04:40	04:45
Peak Brightness Temperature (T_b K) at 80 MHz	6.2×10^7	7.4×10^7	7.4×10^7	6.2×10^7	7.9×10^7	8.4×10^7
Bursts centeriods ($R_\odot$, GRAPH)	1.4	1.8	1.5	2	1	1.6
Burst Duration (in minutes)	78		40		36	
v_{TypeIV} (km/s)	162		179		284	
De-projected Speed (km/s)	155		166		464	
Position Angle (Degrees)	50		332		342	
Projected Speed (km/s)	1060		2175		1020	
Associated Soft X-ray Flare (GOES)	C6.2		M8.7		C6.4	
Heliographic Location	N34E86		N33W21		N41W84	
Average radio flux spectral index (α_o)	-3.4		-2.5		-2.7	
Power-Law spectral index (α_t)	-2		-4		-4.2	

4.3 About GRAPH observations

A comparison of the above three moving Type IV bursts reveal that the same sunspot region (AR 11402) was associated with all of them. No Hα filament/prominence eruption was associated with the bursts[3]. Note that any error in the position/size of the moving Type IV bursts in Figures 4.2, 4.4 and 4.6 and due to ionospheric effects and/or scattering (irregular refraction due to density inhomogeneities in the solar corona) is expected to be small ($\approx \pm$ 0.1 $R_\odot$) because: 1) positional shifts due to ionospheric effects are expected to be $\lesssim$ 0.1 $R_\odot$ at 80 MHz in the hour angle range $\pm$ 2h [Stewart and McLean (1982)]. The local noon at Gauribidanur occurs around $\approx$ 06:30 UT and the GRAPH observations described above are close to the above hour angle range; 2) the effects of scattering are considered to be small at 80 MHz compared to lower frequencies [Aubier et al. (1971); Bastian (2004); Ramesh et al. (2006a)]. The positional shift of discrete solar radio sources due to scattering is expected to be $\lesssim$ 0.1 $R_\odot$ at 80 MHz [Riddle (1974)]. Ray tracing calculations employing realistic coronal

[3]www.swpc.noaa.gov/warehouse/2012.html

electron density models and density fluctuations show that the turning points of the rays that undergo irregular refraction almost coincide with the location of the plasma ('critical') layer in the non-scattering case even at 73.8 MHz [Thejappa and MacDowall (2008)]. Obviously, the situation should be still better at 80 MHz. The aforementioned issues related to scattering indicates that its effects on the T_b of the bursts in the present case may also be minimal. Similarly, projection effects on the position of the bursts are also expected to be minimal since the latter are located near the solar limb. However, the effect of the limited angular resolution of the GRAPH ($\approx 10^{'} \times 15^{'}$) on the T_b cannot be ruled out. The 'true' T_b of the bursts could be higher ($\sim 10^9$ K) since moving Type IV bursts of comparatively smaller angular dimensions at 80 MHz have been reported in the literature. The average size itself is smaller, $\approx 8^{'}$ with no spatial structure [Robinson (1978)]. Note that high angular resolution observations of the solar corona indicate that discrete radio sources of angular size $\approx 1^{'}$-$3^{'}$ are present in the solar atmosphere from where low-frequency radio radiation originates [Kerdraon (1979); Lang and Willson (1987); Willson et al. (1998); Ramesh et al. (1999); Ramesh and Sastry (2000); Ramesh and Ebenezer (2001); Mercier et al. (2006); Kathiravan et al. (2011); Ramesh et al. (2012)]. We would like to add here that the moving Type IV bursts in Figures 4.1, 4.3 and 4.5 were observed elsewhere also and that too at frequencies < 35 MHz. An inspection of the dynamic spectrum obtained with the Bruny Island Radio Spectrometer [Erickson (1997)] on 2012 January 16, 2012 January 23 and 2012 January 26 revealed that the moving Type IV bursts were noticeable $\lesssim 20$ MHz on all the aforementioned three days[4]. We also found that all the three bursts were limited to frequencies $\lesssim 100$ MHz. Observations with the e-CALLISTO solar radio spectrometer receiver [Benz et al. (2009)] at the Gauribidanur Radio Observatory in the frequency range 45-440 MHz range was used for this purpose.

[4]http://www.astro.umd.edu/∼white/gb/Html/2012/TypeIV_ims.html

4.4 Results and Analysis

4.4.1 Emission mechanism

As mentioned earlier both optically thin gyro-synchrotron emission from mildly relativistic electrons and second harmonic plasma emission have been suggested as possible mechanisms for the moving Type IV radio bursts. All the three bursts reported in the present work (2012 January 16, 2012 January 23 and 2012 January 26) are most likely due to the second harmonic plasma emission because of the following reasons: 1) in the presence of a medium, the gyro-synchrotron emission is strongly suppressed at frequencies $< 2f_p$, where f_p is the plasma frequency [Wild and Smerd (1972); Dulk (1973); Melrose (1985)]. To verify this, we used the pB measurements obtained with STEREO-COR1 to estimate the coronal electron density, particularly for the 2012 January 26 event where the ambiguities were less. The electron density in the CME at $r \approx 1.8$ $R_\odot$ around $\approx$ 04:55 UT, the closest distance and the earliest time at which the measurements could be obtained, is $\approx 0.5 \times 10^7$ cm^{-3} (see Figure 4.7). The background electron density of the pre-CME corona obtained at $\approx$ 03:20 UT is $\approx 0.3 \times 10^7$ cm^{-3}. So the total electron density at $r \approx 1.8$ $R_\odot$ around $\approx$ 04:55 UT is $\approx 0.8 \times 10^7$ cm^{-3}. This implies that if the moving Type IV burst of 2012 January 26 had been due to gyro-synchrotron emission, it should have been suppressed over frequencies $\lesssim$ 50 MHz.

But this is not the case since all the three moving Type IV bursts reported in the present work were noticed $\lesssim$ 20 MHz as mentioned in Section 4.2.3. This explains second harmonic plasma emission for the moving Type IV bursts which requires an electron density of $\approx 2 \times 10^7$ cm^{-3} at 80 MHz. Such values close to the Sun have been reported in the literature from CME observations [Sheridan et al. (1978); Stewart and McLean (1982); Gary et al. (1985); Gopalswamy and Kundu (1992); Akmal et al.

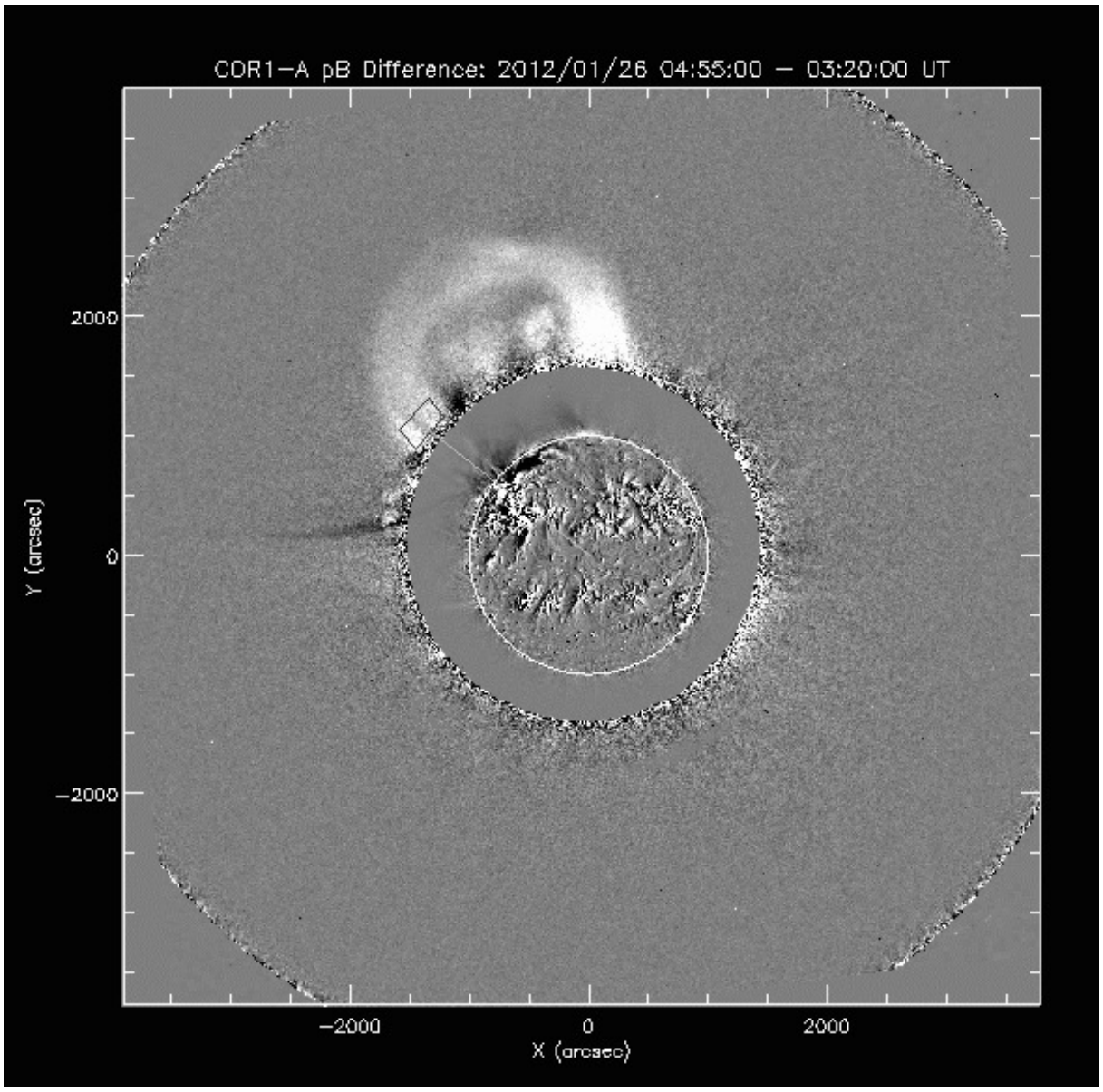

Figure 4.7: A composite of the difference images (04:55-03:20 UT) obtained with STEREO-COR1 A and STEREO-EUVI obtained on 2012 January 26. The enhanced white light emission at PA $\approx$ 30° above the occulting disk of the coronagraph corresponds to the CME mentioned in Section 2.3. The boxed region over the leg of the CME around PA $\approx$ 51° at $r \approx 1.8$ $R_\odot$ indicates the location at which the CME density mentioned in Section 3.1 was estimated.

(2001); Ciaravella et al. (2001); Kathiravan et al. (2002); Ramesh et al. (2003b); Kathiravan and Ramesh (2005); Bemporad et al. (2007)]; 2) past observations indicate that the moving Type IV bursts (belonging to the expanding arch category mentioned in Section 4.1 of this chapter) associated with the 'legs' of the CME are likely due to plasma emission [Wild (1969); Smerd and Dulk (1971)]; 3) calibration of the GLOSS dynamic spectrum (refer Section 2.19) of the moving Type IV bursts reported in the present work using the galactic background emission as described in Dulk et al. (2001) indicates that the spectral index of the bursts in the frequency range 85-35 MHz are $\alpha_o \approx$ -3.4, -2.5 and -2.7, respectively for the events observed on 2012 January 16, 2012 January 23 and 2012 January 26. Compared to this the spectral indices for the fundamental plasma emission, second harmonic plasma emission and the optically thin gyro-synchrotron emission as predicted by the theory are α_t = -2, -4 and -4.2, respectively [Melrose (1975); Dulk (1985)]. The estimated values are lower than that expected for the gyro-synchrotron mechanism. They are in between the corresponding values for the fundamental and second harmonic plasma emission. We may rule out the former because of the typical electron densities ($\approx 10^7$ cm^{-3}) of the CME frontal structure mentioned above. For fundamental plasma emission at 80 MHz, one needs almost an order of magnitude higher density, $\approx 7.9 \times 10^7\ cm^{-3}$. We would like to add here that the spectral index calculations over different frequency bins in the range 85-35 MHz for each of the three moving Type IV bursts described here remained nearly constant; 4) according to the plasma emission model, the source (plasmoid) expands with time. This results in a decrease in the plasma density and so the peak emission shifts to lower frequencies (see for eg. Figure 4.8). The extent in frequency over which the emission is observed depends on the range of densities within the source. At any given time, emission at high frequencies would be from the center where larger densities are expected, and emission at lower frequencies would be produced near the edge [Robinson (1978)]. The frequency drift and the range of frequencies over which the emission is observed for the

bursts reported is consistent with this scenario.

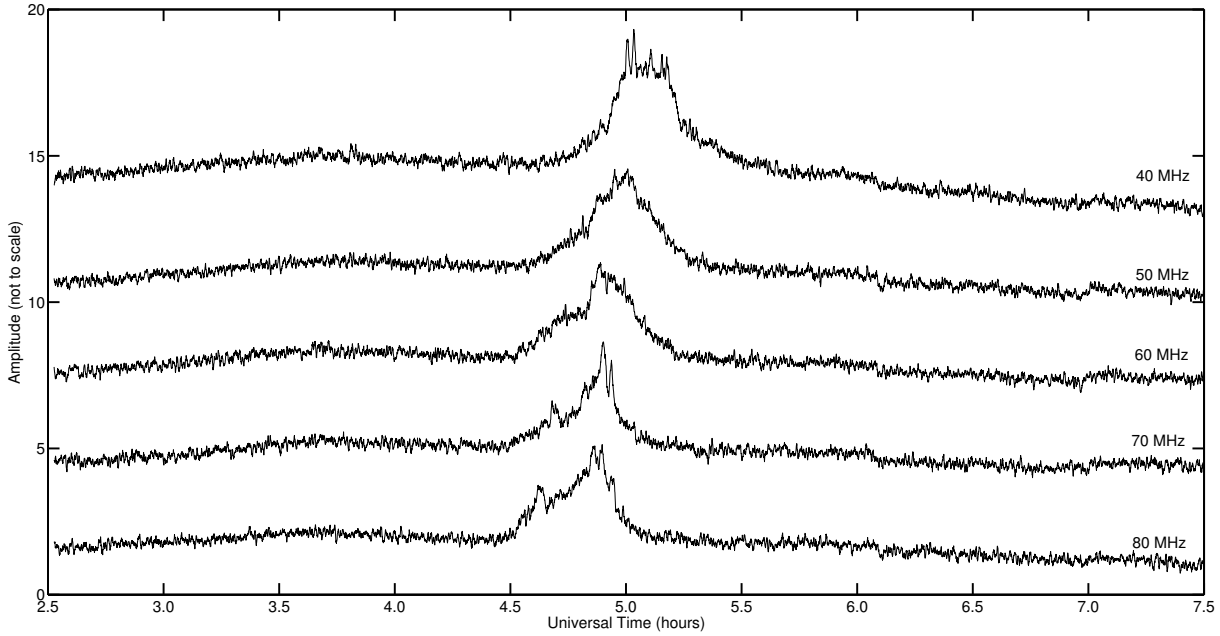

Figure 4.8: Time profiles of the moving Type IV burst observed with the GLOSS on 26 January 2012 (refer Figure 4.5).

We would like to add here that multi-frequency two-dimensional imaging observations of moving Type IV bursts reported in the literature have shown dispersion in the source position as a function of frequency, at any given time. The source sizes at lower frequencies were also correspondingly larger [Nelson (1977); Duncan (1978); Kundu et al. (1989)]; However, the dispersion has been found to be less in the moving Type IV bursts as compared to Type II and III bursts [Stewart (1985)]; 5) fine structures in the spectrum of the moving Type IV bursts (see for e.g., Figure 4.3) and the fact that the average bandwidth of the observed radio emission at any given time is limited to $\approx$ 50-60% (see for, e.g., Figure 4.8) indicates that it may be difficult to explain the bursts based on gyro-synchrotron emission [Benz (1993); Aurass et al. (2005)].

4.4.2 Determination of the magnetic field

In the present case the moving Type IV burst is observed up to a maximum frequency of $\approx$ 80 MHz. Assuming second harmonic plasma emission as the cause for the bursts as mentioned above, we find that the maximum plasma frequency (f_p) in the source region of all the three bursts should be $\approx$ 40 MHz. This corresponds to an electron density $N_e = 2 \times 10^7$ cm^{-3}. Note that according to the theory of moving Type IV bursts based on second harmonic plasma emission by Stepanov (1974), energetic electrons trapped in the magnetic loop has a loss-cone distribution which excites plasma waves near the upper hybrid frequency $f_{uh}^2 = f_p^2 + f_c^2$, where f_p and $f_c = 2.8B$ are the electron plasma and gyrofrequencies, respectively and B is the magnetic field. An estimate of the magnetic field in the source region of the burst can be made if its polarization is known. But we do not have polarization information in the present case. If we assume that the polarization associated with second harmonic plasma emission is in general weak and all the more weaker for the structureless bursts [Dulk and Suzuki (1980); Stewart (1985)], then the largest magnetic field required is for the case where the upper hybrid frequency resonates with the fourth harmonic of the gyrofrequency [Stepanov (1974); Gopalswamy and Kundu (1989b)]. We find then $f_p^2 = 15 f_c^2$. Substituting for the different parameters, we get $B \lesssim 4$ G. Although the above limiting value of B has been obtained for the specific case of energetic electrons with loss-cone distribution and the related second harmonic plasma emission, the following reports seem to strengthen the case: (1) moving Type IV bursts occur predominantly at frequencies < 100 MHz [White (2007)] which limits the maximum value of f_p mentioned above, and (2) all Type IV emissions are consistent with coherent radiation of loss-cone instabilities [Benz (1993)]. It is expected that polarization observations of moving Type IV radio bursts in the future for, e.g., with instruments like the Gauribidanur Radio Interference Polarimeter [Ramesh et al. (2008)], might be useful in this regard.

Chapter 5

Development of a new radio Spectropolarimeter for low-frequency radio observations

The results presented in this chapter are based on the following publication

A Low-Frequency Radio Spectropolarimeter for Observations of the Solar Corona

P. Kishore, R. Ramesh, C. Kathiravan C, M. Rajalingam M, *Solar Physics*, 2015 Sep 1;290(9):2409-22.

5.1 Introduction

DIRECT estimates of the magnetic-field strength [B] in the solar atmosphere are presently limited to the "inner" corona, *i.e.,* radial distance $r \lesssim 1.2$ $R_\odot$ [Kuhn (1995); Lin et al. (2004a); Gelfreikh (2004); White (2005)]. In the "outer" corona, *i.e.,* $r \gtrsim 3$ $R_\odot$, Faraday rotation observations of microwave signals emitted by transmitters on-board artificial satellites and/or distant background cosmic sources that pass through the solar corona are used to derive the magnetic field strength [Patzold et al. (1987); Spangler (2005)]. Compared to the above, polarization measurements in the range 1.2 $R_\odot \lesssim r \lesssim 3$ $R_\odot$ (*i.e.,* "middle" corona) are rare due to lack of observational

facilities. As the photosphere, chromosphere, and corona are coupled by the solar magnetic field, the magnetic-field strength in the above distance range is obtained by mathematical extrapolation of the observed line-of-sight component of the photospheric magnetic field assuming a potential or force-free model [Schatten et al. (1969); Schrijver and DeRosa (2003)]. Most of the low-frequency solar radio bursts originate in the “middle" corona and their emission mechanism is due to plasma processes [McLean (1985)]. Plasma emission in the presence of a magnetic field is split into ordinary [O] and the extraordinary [X] modes. Due to the differential absorption of these two modes in the medium, a net degree of circular polarization (dcp) can be observed [Melrose and Sy (1972)]. The latter is related to the strength of the magnetic field in the source. Therefore, it is possible to estimate the coronal magnetic-field strength using observations of polarized radio bursts [Dulk and McLean (1978); Mercier (1990); Ramesh et al. (2003a); Ramesh et al. (2011); Sasikumar Raja and Ramesh (2013); Hariharan et al. (2014)]. Note that due to the decrease in the coronal electron density [$N_{\rm e}$] and hence the associated plasma frequency [$f_{\rm p}$] with increasing radial height in the solar atmosphere, the lower the frequency of observation the larger will be the corresponding radial distance. So observations with a broadband radio spectropolarimeter are useful since the field strength can be obtained over a range of r for the same event in a near-simultaneous manner. Keeping these views in mind, a broad-band radio spectropolarimeter has been commissioned recently for dedicated observations of the solar corona in the frequency range 85 – 35 MHz. Radio emission in the above frequency range originates typically in the range 1.2 $R_\odot \lesssim r \lesssim$ 2 $R_\odot$ in the solar atmosphere as mentioned earlier. This chapter describes the observational set-up, calibration scheme and the initial results on the estimates of the coronal magnetic field strength in the above distance range.

5.2 Gauribidanur RAdio SpectroPolarimeter (GRASP)

The front-end of the radio spectropolarimeter (Gauribidanur RAdio SpectroPolarimeter, GRASP) consists of two log-periodic dipole antennas [LPDAs: Carrel (1961); Ramesh et al. (1998); Kishore et al. (2014)] designed and fabricated at the Gauribidanur Observatory for observations in the frequency range of 85 – 35 MHz with VSWR $\lesssim 2$ and directional gain of $\approx$ 7 dBi. The effective collecting area [$A_{\rm e}$] of each LPDA is $\approx 0.4\lambda^2$, where λ is the wavelength of observation (refer Sections 2.4.1, 2.4.2 for more details). Figure 5.1 shows the block diagram of GRASP set-up. The LPDAs have been mounted vertically with a spacing [d] of 10 m between them in the North−South direction. While the orientation of the "arms" of one of the LPDAs is in the East−West direction, they are in the North−South direction for the other, *i.e.,* the two LPDAs are mutually perpendicular (Figure 5.2). Grating lobes will appear in GRASP above 30 MHz; refer Sections 2.6.2 & Appendix 1.3 for the details regarding the angular separation and half-power widths of grating lobes in GRASP. The LPDAs respond to linearly polarized signal in the direction of the orientation of their "arms". The half-power width of the response pattern ("beam") of the above two LPDAs is $\approx 80^\circ$ in the E-plane and $\approx 110^\circ$ in the H-plane, throughout the operating bandwidth (refer 2.5.2.1). This enables us to carry out observations for longer time duration ($\gtrsim$ six hours) and over a wide range of declination. Note that though the North−South oriented baseline between the two LPDAs facilitate observations without the need for steering the "beam" of the LPDAs along the hour angle, there will be a delay $d\sin\theta$, where θ is the zenith angle, between the RF signal incident on the two LPDAs depending on the declination of the radio source. This will lead to the phase difference, a function of frequency, between the two signals. We have provision to include coaxial cable of appropriate length in the signal path from either of the two LPDAs to compensate for the above delay. Note that the latter is nearly constant over a $\approx \pm$ three

hours observing period in hour angle for a particular declination. Also since the change per day in the declination of the Sun is minimal ($\approx 0.1^{\circ}$), inclusion of a co-axial cable of specific length will provide the required delay for about one month. The residual phase difference is $\lesssim \pm 5^{\circ}$ over the 85 – 35 MHz band.

5.2.1 Front-end & Back-end receiver configuration

The radio frequency (RF) signals from individual LPDAs are high-pass filtered and amplified by $\approx$ 28 dB in the first-stage amplifier. After transmission over a distance of $\approx$ 20 m via a coaxial cable, the signals are again amplified by $\approx$ 30 dB in a second-stage amplifier. The signal amplitude after the above two stages of amplification is ≈ -40 dBm in each path and is nearly constant over the entire RF band (85 – 35 MHz) to within ± 1 dB. The amplified RF signal from the two antennas are independently converted to an optical signal by modulating with a low-power laser (+4.5 dBm at 1310 $\pm$ 10 nm) in two separate RF-to-optical converters. Maximum RF input power that can be connected to the latter is $\approx$ 15 dBm. As the background RF signal amplitude after the second-stage amplification is ≈ -40 dBm, this indicates that an increase in the signal level by $\approx$ 50 dB can be comfortably accommodated using the above RF-to-optical converter. Note that this is nearly the same as the typical dynamic range ($\approx$ 40 dB) required for the solar radio receivers due to the wide range of fluxes encountered between the “undisturbed" Sun and the “active" Sun [Nelson et al. (1985)]. The output from the RF-to-optical converters are transmitted to the receiver room through two separate single mode step index optical fiber cables (OFC) of length $\approx$ 500 meters. The OFCs are drawn inside plastic tubes (“conduits") buried $\approx$ 2 meters below the ground. Signal attenuation in the OFC splicing and connectors is ≈ 0.5 dB/splicing and ≈ 1 dB/connector, respectively.

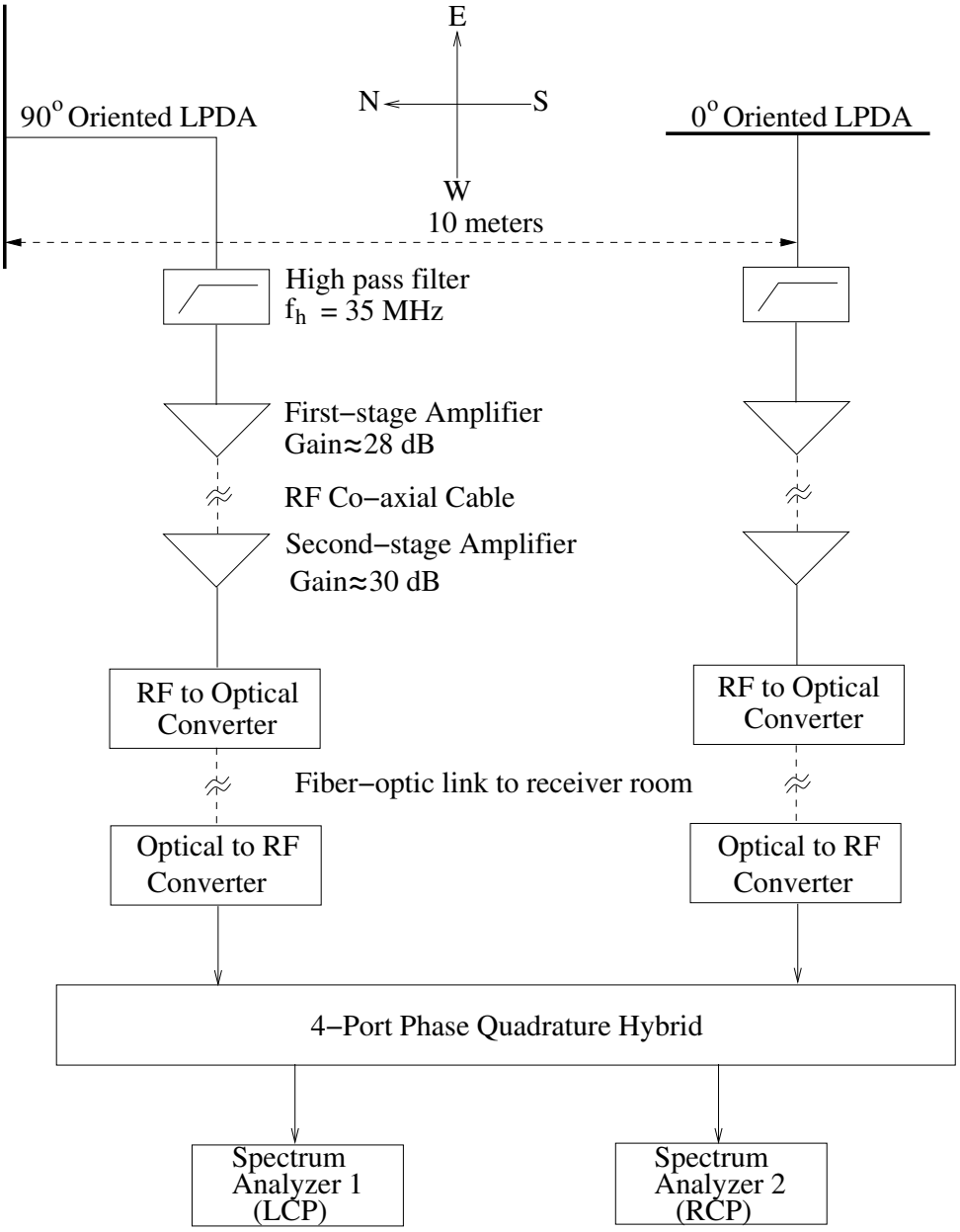

Figure 5.1: Block diagram of the GRASP.

Figure 5.2: A view of the GRASP. The first and last LPDAs are in mutually orthogonal orientation, and they are part of the GRASP, the third antenna (middle) belongs to the e-CALLISTO set-up at the observatory [Benz et al. (2009)]. The “white" enclosures near each antenna house the respective RF-to-optical converter.

Figure 5.3: The left inset picture shows the RCC protective casing for RF & RF to Otical conversion modules. Here the main/second stage amplifier is also protected by lightening arrester (not in picture). The rolled orange cable is the optical fibre ($\approx$ 500 m) which transport the modulated wideband RF from the converter to lab. Similar optical to RF modules at lab side demodulates the optical to wideband RF and later connected to the 4-port phase quadrature and finally to two independent spectrum analyzers that are connected to independent PCs via PCI-GPIB interface (refer Section 2.6.3).

The output from the two OFCs are converted back to RF signals in two separate optical-to-RF converters in the receiver room. A PIN photo diode with a spectral response of 1100 nm to 1650 nm is utilized for this purpose. It has an RF frequency range of $\approx$ 2 – 3000 MHz. We found that the signal flatness over the above frequency band is $\approx \pm 1$ dB. The overall loss in the signal strength during the conversion from RF to optical domain and back to RF domain, including that of the OFC splicing joints and the connectors, is $\approx$ 20 dB. This loss is compensated by adjusting the gain of the built-in amplifiers in the converters appropriately so that the amplitude of the RF signal corresponding to the two LPDAs are the same ($\approx$ - 40 dBm).

5.2.1.1 4-port phase Quadrature Hybrid (QH)

The transducer (optical to RF) outputs (for both East-West & North-South) are connected to a commercial broadband ($\approx$ 30 – 88 MHz) four-port 90° (phase quadrature) network [`www.innovativepp.com`].

The following are the properties of a 4-port phase quadrature hybrid:

- It is a bi-directional device, i.e., functions irrespective of either side ports. It is a quadrature (90°) hybrid because it provides 90° phase shift between signals at the coupled ports.
- This can be used in applications where the power at one port has to divide/combine equally with 90° phase difference.
- The input ports are labelled as Input (IN) and Isolation (ISO) respectively. The output will be 3 dBm down from input which means the hybrid will divide/combine the power equally at the ports on the other side (CP1 & CP2).
- **Power Divider:** A continuous wave (CW) signal from either of IN/ISO ports will divide the power equally but with a phase difference of 90° at the ports on the

other side.

- **Power Combiner:** Similarly a (cw) signal fed at both ports (IN & ISO) simultaneously combines the power at either of the port at the output. In our case the QH is used as a passive power combiner; it accepts inputs from two orthogonal LPDAs. As a result, the coupled signal at one of the output port will be LCP (left circularly polarized)/RCP (right circularly polarized) and vice versa. This condition is explained in detail in the next section.

The block diagram of the hybrid is shown in the left panel of Figure 5.4. The outputs from the East−West and the North−South oriented LPDAs (90° and 0° orientation, respectively), after-this referred to as E−W LPDA and N−S LPDA, are connected to the Coupled Port 1 (CP1) and Coupled Port 2 (CP2) of the hybrid. Outputs are labelled as Input (IN) and Isolation (ISO) ports. At the IN/ISO port, the power from the E−W LPDA and the N−S LPDA are combined with $0^\circ/90^\circ$ and $90^\circ/0^\circ$ phase lag, respectively (see left panel in Figure 5.4). Depending on the sense of rotation of the electric field vector along the direction of propagation of the incident radiation, *i.e.,* clockwise (right circular polarization: RCP) or counter-clockwise (left circular polarization: LCP) as per the IAU definition [Thompson et al. (2004)], the signals may add or subtract at the CP1/CP2 ports.

5.2.1.2 Detection of circularly polarized signal using QH

Assume a circularly polarized (of unknown rotation) wave is falling on both North-South and East-West oriented LPDAs at the same time. The direction of arrival of the wave from the sky will be taken as +Z-axis, X (E−W LPDA) and Y (N−S LPDA) are the antenna orientations on the ground. Such a wave can be best described as

$$\vec{\mathbf{E}}(z,t) = E_o\, Cos(\omega t - \beta z)\hat{\mathbf{x}} \pm E_o\, Sin(\omega t - \beta z)\hat{\mathbf{y}} \tag{5.1}$$

where $\vec{\mathbf{E}}(z,t)$ is equation of circularly polarized wave as a function of distance and time, E_o is amplitude of electric field, ω is the angular frequency (rad/s), t is time (s), β=$\frac{2\pi}{\lambda}$ is wavenumber, $\hat{\mathbf{x}}$, $\hat{\mathbf{y}}$ are the unit vectors in the direction of horizontal (X) and vertical (Y) axes. The -ve sign indicates for RCP and +ve sign for LCP wave (IAU Convention). Let us examine the ports condition if an LCP wave is incident on GRASP antennas. Equation (5.1) has two components of the wave i) the parallel ($\parallel$) component (E_oCos(ω t- β z)) and the second ii) perpendicular ($\perp$) component (E_oSin(ω t- β z)). The $\parallel$ component falling on N−S LPDA is fed to CP2 and the $\perp$ component falling on E−W LPDA is fed to CP1 (see right panel in Figure 5.4) of QH. According to the properties of QH Section 5.2.1.1, the power combined at IN port is given as

$$
\begin{aligned}
IN_p &= \frac{1}{\sqrt{2}}90^\circ \parallel + \frac{1}{\sqrt{2}}0^\circ \perp && \text{0°, 90° rotations introduced by QH} \\
&= \frac{1}{\sqrt{2}}E_oCos(\omega t - \beta z - 90^\circ) + \frac{1}{\sqrt{2}}E_oSin(\omega t - \beta z - 0^\circ) && \tfrac{1}{\sqrt{2}} \text{ for equal power condition} \\
&= \frac{1}{\sqrt{2}}E_oSin(\omega t - \beta z) + \frac{1}{\sqrt{2}}E_oSin(\omega t - \beta z) \\
&= \sqrt{2}E_oSin(\omega t - \beta z) && \text{maximum coupled power for LCP}
\end{aligned}
$$

Similarly, the power combined at ISO port is given as:

$$
\begin{aligned}
ISO_p &= \frac{1}{\sqrt{2}}0^\circ \parallel + \frac{1}{\sqrt{2}}90^\circ \perp \\
&= \frac{1}{\sqrt{2}}E_oCos(\omega t - \beta z - 0^\circ) + \frac{1}{\sqrt{2}}E_oSin(\omega t - \beta z - 90^\circ) \\
&= \frac{1}{\sqrt{2}}E_oCos(\omega t - \beta z) - \frac{1}{\sqrt{2}}E_oCos(\omega t - \beta z) \\
&= 0 && \text{minimum coupled power for LCP}
\end{aligned}
$$

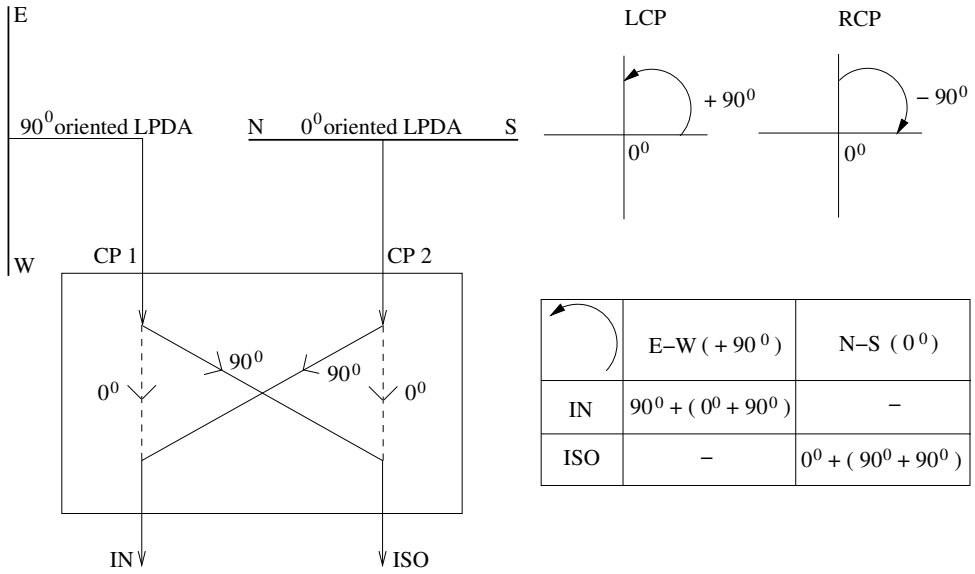

	E–W (+ 90 ⁰)	N–S (0 ⁰)
IN	90⁰ + (0⁰ + 90⁰)	–
ISO	–	0⁰ + (90⁰ + 90⁰)

Figure 5.4: Left: Block diagram of the phase quadrature hybrid used in the GRASP. Right: An example illustrating the detection of LCP signal with GRASP.

In this way, the case for RCP polarization can be proved for which the maximum deflection will be at ISO$_p$. The results for other polarization of incidence can be found from the truth table Table (5.1).

Table 5.1: Truth table for a QH for various incident polarization

Input Signal	Input Port	Output Ports ISO	Output Ports IN	Polarization
E_oCos(ωt - βz)	CP1	$\frac{1}{\sqrt{2}}$ E_oCos(ωt - βz - $\frac{\delta}{2}$ - 45°[a])	$\frac{1}{\sqrt{2}}$ E_oCos(ωt - β z - $\frac{\delta}{2}$ + 45°[a])	General state for a given phase angle δ
E_oCos(ωt - βz + δ)	CP2			
E_oCos(ωt - βz)	CP1	0	$\sqrt{2}$ E_oSin(ωt - βz)	Left Circular Polarization
E_oSin(ωt - βz)	CP2			
E_oSin(ωt - βz)	CP1	$\sqrt{2}$ E_oCos(ωt - βz)	0	Right Circular Polarization
E_oCos(ωt - βz)	CP2			

[a]Here the phase angles +45°, -45° in the ISO and IN ports differ by 90° for an arbitrary phase of δ.

Note that in addition to the above circularly polarized component, the randomly polarized components of the incident signal (for cases where the incident signal is not 100 % circularly polarized) whose electrical field vectors are parallel to the orientation

of the “arms" of the LPDAs will also be present at the inputs of the hybrid. So one of the outputs of the hybrid will be the sum of the polarized (LCP or RCP) and randomly polarized components of the incident signal, and the other will be the randomly polarized component alone.

The outputs of the hybrid are connected to two independent, identical commercial spectrum analyzers 1 and 2 (Agilent Technologies model E4411B) to obtain the respective dynamic spectra. The sweep time and the instantaneous observing bandwidth are $\approx$ 100 ms and $\approx$ 125 kHz, respectively. Minimum detectable flux density with the GRASP considering the above parameters and $A_{\rm e} \approx 0.4\lambda^2$ for the LPDAs, is $\lesssim$ 3 sfu at 35 MHz and $\lesssim$ 4 sfu at 85 MHz (1 sfu = 10^{-22} $\mathrm{Wm^{-2}Hz^{-1}}$). Note that the peak system temperature $T_{\rm sys}$, dominated by the temperature of the background sky at low frequencies, for the calculations was assumed to be $\approx 1 \times 10^4$ K and $\approx 5 \times 10^4$ K at 85 and 35 MHz, respectively[1]. The spectrum analyzers are connected to two personal computers (PCs) through PCI-GPIB hardware and data acquisition is carried out using specialized Microsoft Visual C++ software (refer Section 2.6.3). The computers are synchronized with a common GPS clock. This helps to achieve temporal coherence between the data acquired with the two systems [Ebenezer et al. (2007); Kishore et al. (2014)]. The total intensity (Stokes-I) corresponding to each frequency in the range 85 – 35 MHz is estimated offline by adding the corresponding observed amplitudes. The difference between the two amplitudes is the Stokes-V intensity [Iwai and Shibasaki (2013)]. Possible contribution of the randomly polarized component to the latter is subtracted out since they are expected to be of nearly equal strength in both the outputs of the hybrid. This is one of the advantages in the measurement of circular polarization with linearly polarized antennas [Thompson et al. (2004)]. Note that linear polarization, if present at the coronal source region, tends to be obliterated at low radio frequencies because of the differential Faraday rotation of the plane of

[1] `https://www.cv.nrao.edu/~demerson/radiosky/rsky_p3.htm`

polarization (during transmission through solar corona and the Earth's ionosphere) over the usual observing bandwidths of a few kHz or more [Grognard and McLean (1973)]. The above method of observing circularly polarized emission with two linearly polarized LPDAs arranged in orthogonal orientations with a spacing between them also, helps to minimize both mutual coupling effects and polarization cross-talk [Morris et al. (1964); Suzuki (1974); Weiler and Raimond (1976); Thompson et al. (2004); Ramesh et al. (2008)].

5.3 Calibration

The various measurement parameters such as the frequency span, video bandwidth (VBW), resolution bandwidth (RBW), attenuation, and sweep time were set identical in the two spectrum analyzers. Broadband noise source that can work over the frequency range 35 – 85 MHz was connected simultaneously to both the units using a calibrated power splitter. The difference in the signal level in the two analyzers was adjusted offline. We also corrected for the difference in the signal attenuation in the two paths by transmitting a continuous-wave (CW) signal to the input of the first stage amplifier, and appropriately adjusting the gain of the built-in amplifiers in the converters. The difference between the gain of the two LPDAs is minimal ($\pm$ 1 dB) in the above frequency range.

5.3.1 Quadrature Hybrid Calibration with a Cross Log-periodic dipole antenna (CLPDA)

The quadrature hybrid was characterized as follows: A CW signal at a frequency of 80 MHz was given to the IN port of a phase-quadrature hybrid. The ISO port of the hybrid was terminated with a 50 Ω load. Outputs from the ports CP1 and CP2 of the hybrid were connected as inputs to a dual polarized CLPDA ($\approx$ 77 – 88 MHz) [Raja

et al. (2013)]. Circularly polarized signal transmitted by the latter was received by the LPDAs in the GRASP. The CLPDA (“transmitting" antenna) and the GRASP (“receiving" antennas) were separated by $\approx$ 100 meters. In the receiver room, the signal strengths were recorded. Later the %dcp (at 80 MHz) for both inputs of QH of the transmitter side was estimated to be 100%. This indicates that the GRASP can be used effectively to observe circularly polarized radio emission. This test was repeated by disconnecting one of the inputs to CLPDA, and the remaining port was terminated with a $50\ \Omega$ load. Later the ports were interchanged, and test observations were carried out few minutes with GRASP antennas. From the output of QH it was verified that the CLPDA transmits linearly polarized signal in this case. If such polarization is incident on GRASP antennas the signal is expected to peak in one port which is clearly evident from Table 5.2. The measured small % of dcp could be due to i) the uncertainty in the angle of linear polarization ii) polarization leakage and so on. Nevertheless, the signal power of a single channel output is predominantly due to the linearly polarized component.

Table 5.2: Table showing the results of the experiments carried out with a CLPD, QH and GRASP antennas. 0° & 90° corresponds to horizontal and vertical arms (ON=signal connected; OFF= signal disconnected states) of the CLPD. IN, ISO represent the transmitter side QH input ports. LCP (CP1), RCP (CP2) are the outputs obtained at the other side of the QH. %dcp is estimated by converting the logarithmic values to linear values using the formula $\frac{RCP-LCP}{RCP+LCP}$. Negative values indicate that the sense of rotation is dominant in right-handedness (IAU Convention)

Input Port:	IN			ISO		
Output (dBm):	LCP	RCP	%dcp	LCP	RCP	%dcp
0° & 90° ON (Circular Polarization)	-23.61	-41.95	-0.97	-22.66	-39.79	-0.96
0° ON 90° OFF (Horizontal Polarization)	-28	-41.8	-0.92	-29.85	-43.21	-0.91
90° ON 0° OFF (Vertical Polarization)	-32	-41.14	-0.78	-31.16	-40.45	-0.79

5.3.2 Calibration of QH with Type I Noise storm observations

The above section explains the procedure of identifying LCP and RCP ports. Another way is to use radio observations of Noise storms or Type I continuum. As mentioned in the Section 1.3 and also majority of noise storms show high degree of circular polarization [Kai et al. (1985); Krüger (2012)]. Almost most of them are left circularly polarized (% dcp $\approx$ 100%) in 'O' mode [McLean and Labrum (1985)] .

Therefore, we used GRASP observation of Type I bursts to cross check the results in Section 5.3.1. Figure 5.5 shows the time profiles of LCP and RCP of the noise storm event observed for $\approx$ 1 hr on 16 April 2013. The estimated % dcp indicates a high level of circular polarization in LCP mode.

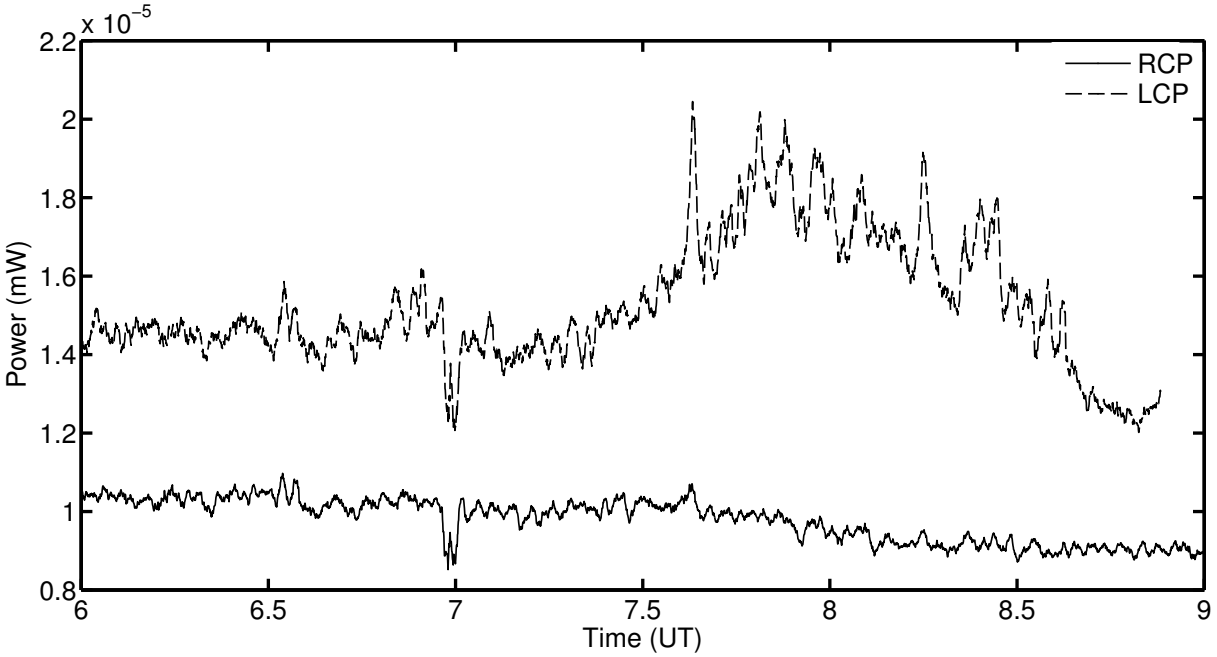

Figure 5.5: Plot showing Noise storm (Type I) observed with GRASP on 16 April 2013. The two line profiles are 1 MHz band averaged intensities at 65 MHz. The continuum lasted for $\approx$ 1 hr in LCP channel whereas it is not that intense in RCP channel. The majority of the noise storms are reported to be highly left circularly polarized in the literature [Kai et al. (1985); Krüger (2012)].

5.3.3 Calibration of Spectropolarimeter data with Galactic Center observations

As a final step in the calibration of GRASP, we carried out observations of the Galactic Center (GC) during the period March–July 2012 (refer Table 5.3). We specifically chose the above period since the Sun was away from the Galactic plane. Data were recorded in both the LCP and RCP channels for $\pm$ four hours around the transit time ($\approx$ 17:42 Local Sidereal Time: LST) of the GC across the local meridian at Gauribidanur. We assume the radio emission from the direction of the GC to be randomly polarized in our case since circularly polarized emission, if present, may be below the sensitivity limit of GRASP [Weiler and De Pater (1983); Bower et al. (1999)] and it is difficult to observe linearly polarized emission with the GRASP due to propagation effects (refer Section 5.2). So the average signal amplitude in the LCP and RCP channels over the frequency range 85 – 35 MHz should be nearly equal. Any difference if present is most likely due to instrumental and other errors (Figure 5.6). We would like to remark here that this is a novel and efficient scheme to calibrate the solar radio spectropolarimeter data, particularly at low frequencies, since radio emission from the direction of the GC is non-thermal in nature and hence intense at low frequencies.

Once the offset between the LCP and RCP channels are corrected, frequencies are calibrated, the degree of circular polarization [$dcp = V/I$] of the incident radiation is estimated using the relation

$$\%dcp = \frac{A_{\rm RCP} - A_{\rm LCP}}{A_{\rm RCP} + A_{\rm LCP}} \tag{5.2}$$

where A is the signal amplitude (refer Section 5.2).

Figure 5.7 shows the results of the above calibration scheme obtained from GC observations with the GRASP at a typical frequency of 65 MHz on June 18, 2014. The peak deflection in the LCP and RCP channels (top panel) corresponds to the transit of GC over the local meridian at Gauribidanur. The dcp of the observed emission at 65

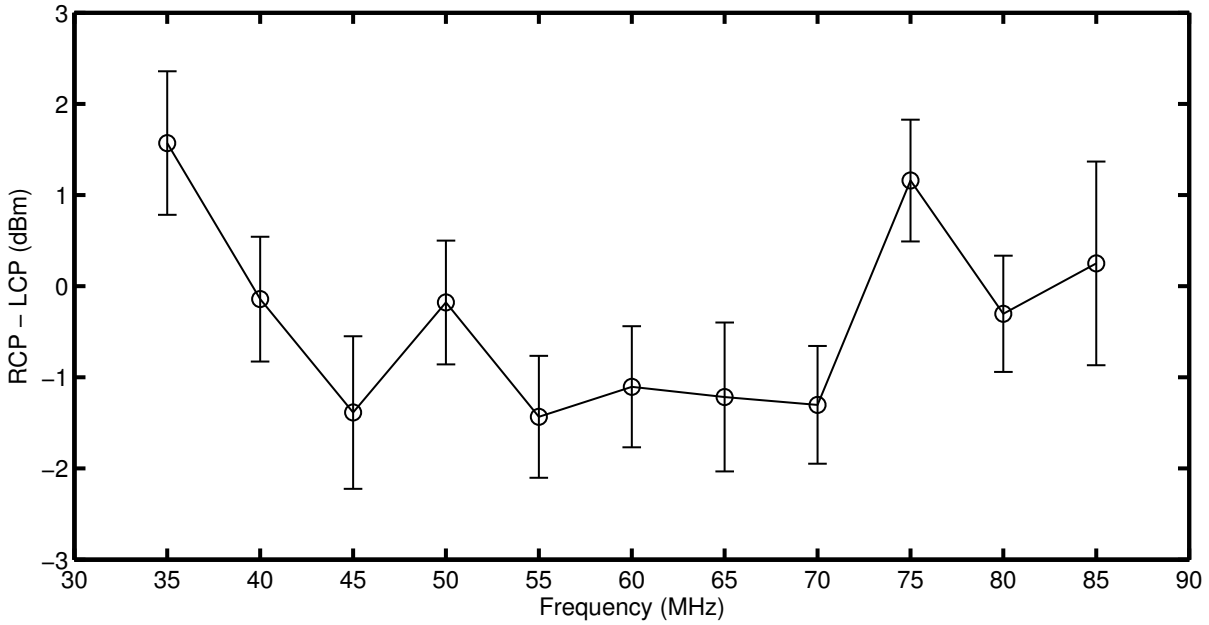

Figure 5.6: Offset between the LCP and RCP channels of GRASP at different frequencies as estimated from Galactic Center observations.

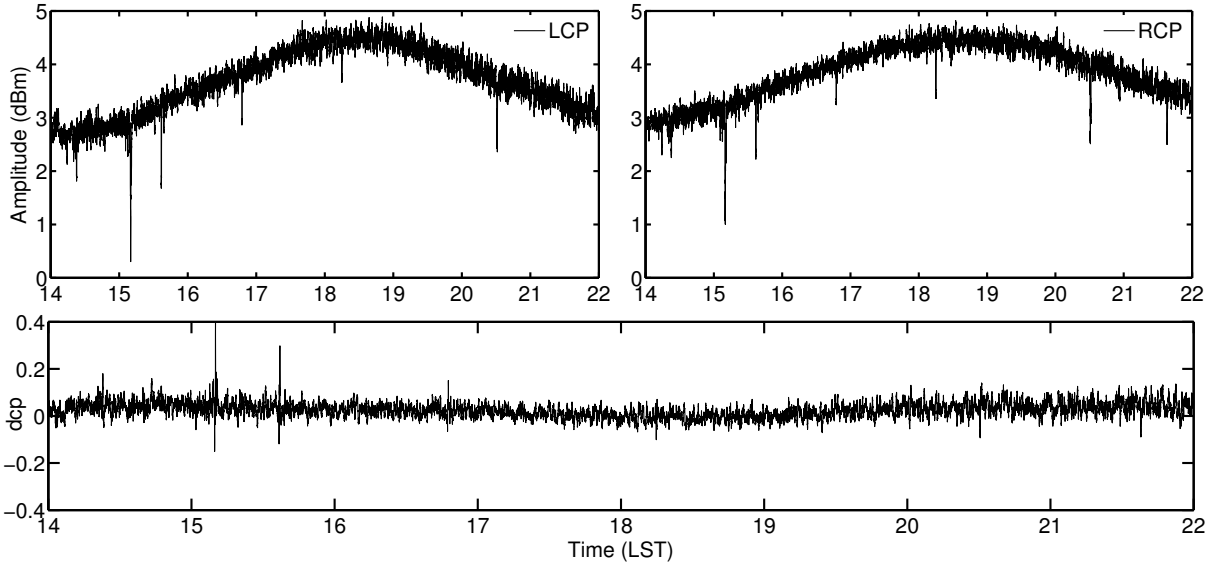

Figure 5.7: Observations of the Galactic Center with the GRASP at a typical frequency of 65 MHz. Top left panel: output of the LCP channel. Top right panel: output of the RCP channel. Lower panel: Degree of circular polarization [dcp].

Table 5.3: Table showing the measured power difference between LCP and RCP channels of GRASP using Galactic Center (GC) observations. The peak power during the transit of GC at local time (17:45 LST) is noted in the both channels for 11 spot frequencies in the observation band (35-85 MHz) and the absolute difference between the channels is estimated. The average estimates are used to produce Figure 5.6 and also applied to the target source to remove instrumental polarization effects.

	LCP and RCP Power difference across different frequency (MHz) bands										
Date	35	40	45	50	55	60	65	70	75	80	85
20140513	-1.44	-0.28	1.43	0.51	1.22	1.31	1.46	1.32	-1.08	0.40	-0.93
20140516	-1.53	-0.22	1.04	0.51	1.12	1.10	1.18	1.28	-1.29	0.42	-1.05
20140613	-2.03	-0.33	1.20	-0.23	0.96	0.64	0.82	0.84	-1.53	0.05	-0.72
20140614	-1.26	0.52	1.69	0.21	1.67	1.38	1.46	1.57	-0.83	0.58	0.00
20140615	-2.55	-0.93	0.46	-0.79	0.47	-0.05	0.45	0.29	-2.11	-0.57	-1.47
20140618	-2.21	-0.35	0.88	-0.42	0.91	0.55	0.82	0.88	-1.70	-0.28	-1.10
20140620	-1.93	-0.12	1.30	-0.15	1.17	0.75	1.13	1.05	-1.52	0.00	-0.75
20140621	-2.35	-0.36	0.91	-0.40	0.74	0.50	0.79	0.70	-1.61	-0.21	-1.02
20140623	-2.12	-0.25	1.07	-0.19	1.09	0.60	1.05	0.90	-1.51	-0.16	-1.04
20140624	-1.60	0.18	1.63	0.25	1.47	1.12	1.46	1.49	-1.11	0.25	-0.43
20140625	-1.24	0.70	1.88	0.66	1.81	1.49	1.77	1.84	-0.71	0.62	0.00
20140626	-1.34	0.78	1.98	0.85	2.04	1.62	1.91	1.73	-0.60	0.82	0.00
20140627	-1.07	0.63	2.07	0.85	1.86	1.36	1.77	1.86	-0.67	0.73	0.00
20140628	-1.03	0.60	1.97	0.74	1.82	1.55	1.85	1.83	-0.71	0.70	0.00
20140701	-1.83	-0.30	1.20	-0.08	1.10	0.73	1.10	1.09	-1.33	0.17	-0.64
20140702	1.30	0.68	2.08	0.67	2.39	1.70	1.94	1.68	-0.57	0.80	0.00
20140703	-1.10	0.98	2.01	1.07	1.92	1.97	1.87	2.28	-0.64	1.01	0.00
20140706	-1.04	0.69	2.00	0.60	1.89	1.52	1.85	1.81	-0.75	0.81	0.00
20140707	-1.92	-0.32	1.13	-0.38	1.06	0.64	0.79	0.88	-1.51	-0.07	5.14
20140709	-1.76	-0.15	1.20	-0.20	1.08	0.92	1.13	1.02	-1.42	0.00	-0.75
20140710	-2.51	-0.48	0.72	-0.77	0.71	0.30	0.60	0.60	-2.02	-0.58	-1.24
20140711	-1.95	-0.30	0.99	-0.27	1.90	0.73	0.83	0.99	-1.60	-0.16	-1.02
20140712	-2.20	-0.47	0.98	-0.46	0.87	0.57	0.81	0.73	-1.76	-0.28	-1.07
20140713	-1.33	0.65	2.01	0.56	2.03	1.63	1.96	1.72	-0.73	0.86	0.00
20140714	-1.56	0.24	1.54	0.23	1.44	1.07	1.37	1.22	-1.09	0.29	-0.37
20140715	-1.08	0.78	2.12	0.78	1.97	1.75	0.94	1.88	-0.67	0.87	0.00
20140716	-1.42	0.49	1.61	0.48	1.68	1.45	1.60	1.66	-1.06	0.62	0.00
20140717	-0.98	0.88	2.17	0.80	2.18	1.85	2.13	2.00	-0.43	1.06	0.00
20140718	-1.03	0.83	2.17	0.80	2.00	1.80	-1.94	1.85	-0.58	0.98	0.00
20140720	-2.78	-0.94	0.52	-0.95	0.38	0.12	0.28	0.22	-2.24	-0.75	-1.26
20140721	-2.90	-1.21	0.23	-1.30	0.21	-0.18	0.00	-0.07	-2.45	-0.97	1.91
20140722	-2.83	-1.18	0.00	-1.08	0.00	-0.21	0.00	0.04	-2.52	-0.98	-1.60
20140723	-2.91	-1.22	0.00	-1.13	0.00	-0.17	0.00	-0.03	-2.61	-0.99	-1.68
20140725	-0.67	1.28	2.67	1.13	2.64	2.27	2.35	2.25	0.00	1.39	0.69
20140726	-0.92	0.91	2.24	0.78	2.18	1.70	2.15	1.92	-0.11	1.14	0.00
20140727	-1.48	0.51	1.88	0.52	1.73	1.40	1.68	1.60	-0.83	0.57	0.00
20140728	-1.24	0.52	1.79	0.66	1.81	1.51	1.71	1.55	-0.84	0.58	0.00
20140729	-1.52	0.40	-1.73	0.45	1.59	1.46	1.49	1.56	-1.00	0.52	0.00
20140730	-0.81	0.90	2.29	0.80	2.20	1.76	2.02	1.88	-0.37	0.94	0.11
20140731	-0.64	0.93	2.12	1.05	2.05	1.95	2.06	2.21	-0.25	0.95	0.32
Mean	**-1.61**	**0.10**	**1.34**	**0.14**	**1.40**	**1.06**	**1.17**	**1.26**	**-1.20**	**0.27**	**-0.27**

MHz is shown in the lower panel. It remains constant at zero (as expected) over $\approx$ eight-hour period, indicating the robustness of the calibration. The variation in the dcp due to noise fluctuations is $\approx \pm 0.01$. This indicates that GRASP can detect circularly polarized flux density to a minimum of 1 % of the total flux density. Routine observations in the direction of the GC indicate that the system is reasonably stable. Note that the offset errors in Figure 5.6 obtained from observations towards the direction of the GC are expected to be the maximum since the declination of the GC ($\approx -30^{\circ}$ S) is almost at the half-power limit for the LPDAs used in the GRASP (refer Section 5.2). The latitude of Gauribidanur is $\approx 14^{\circ}$ N. So the zenith angle of the GC for GRASP is $\approx -44^{\circ}$. This is less than the range of zenith angles (-37° to $+9^{\circ}$) for the Sun in a year, as seen from Gauribidanur.

5.4 Survey of Type III radio bursts with GRASP

Figure 5.8 shows the Stokes-I and Stokes-V dynamic spectra obtained from GRASP observations on 4 February 2013 during the interval 08:07:00 – 08:11:00 UT. One can notice patches of intense emission drifting rapidly in frequency as a function of time in both the spectra. These are the characteristic signatures of Type III solar radio bursts from the solar corona [Suzuki and Dulk (1985)]. The source region of the bursts was identified using the radioheliogram obtained with the GRAPH (refer 2.10.2) at 80 MHz around the same time (Figure 5.9). The discrete source close to the east limb of the Sun corresponds to the Type III burst at 80 MHz. Its average brightness temperature [$T_{\rm b}$] is $\approx 10^8$ K. This is about three orders of magnitude lower than the peak $T_{\rm b}$ of the Type III radio bursts at 80 MHz [Suzuki and Dulk (1985)]. An inspection of the soft-X-ray emission from the “whole" Sun obtained with the GOES-15 on 4 February 2013 indicates that the X-ray activity at the time of the radio bursts mentioned above was at a low level [`www.lmsal.com/solarsoft/latest_events/`]. The corresponding energy in the 1 – 8

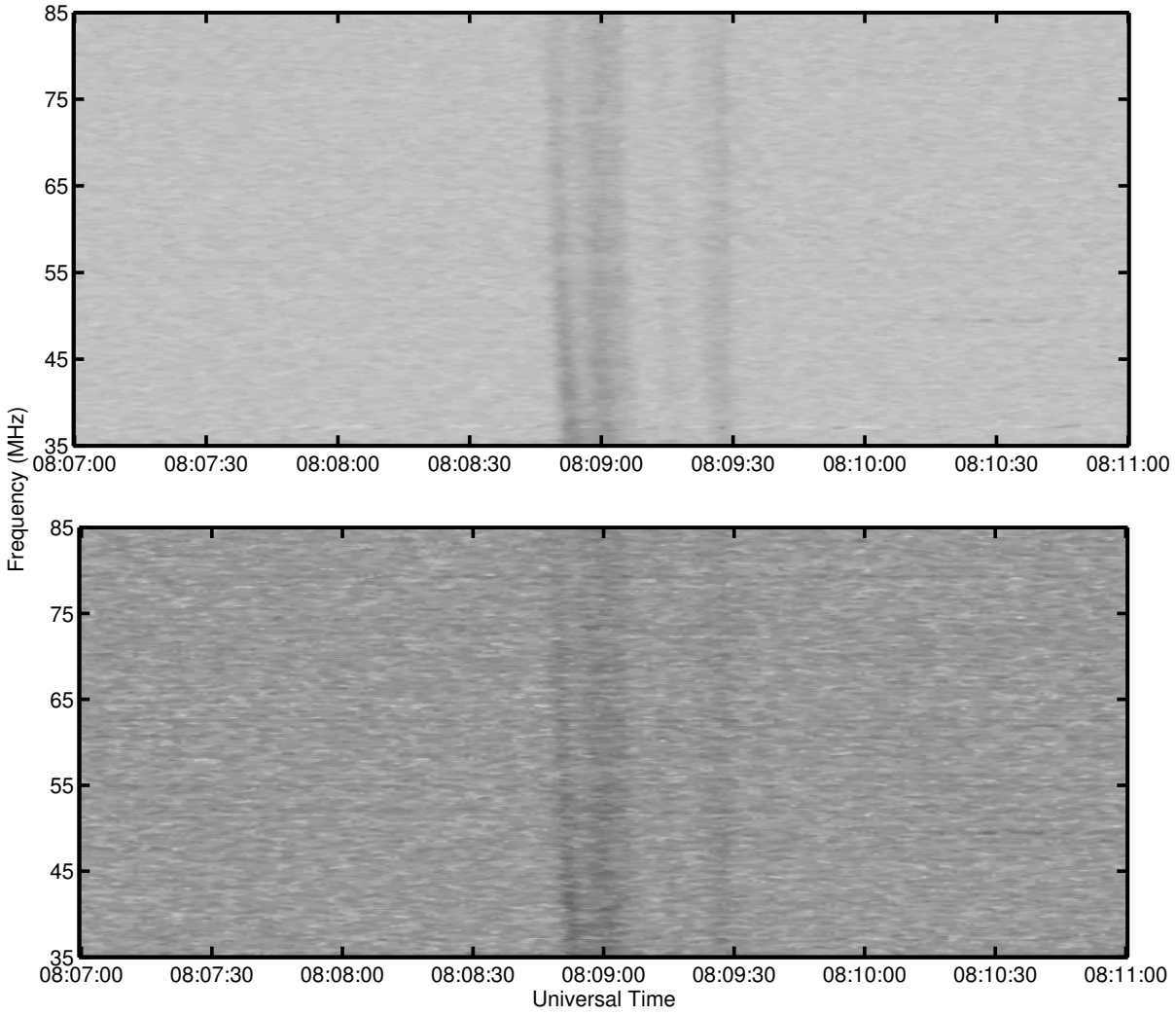

Figure 5.8: Stokes-I (upper panel) and Stokes-V (lower panel) dynamic spectra of a group of faint Type III solar radio bursts observed with the GRASP on 4 February 2013.

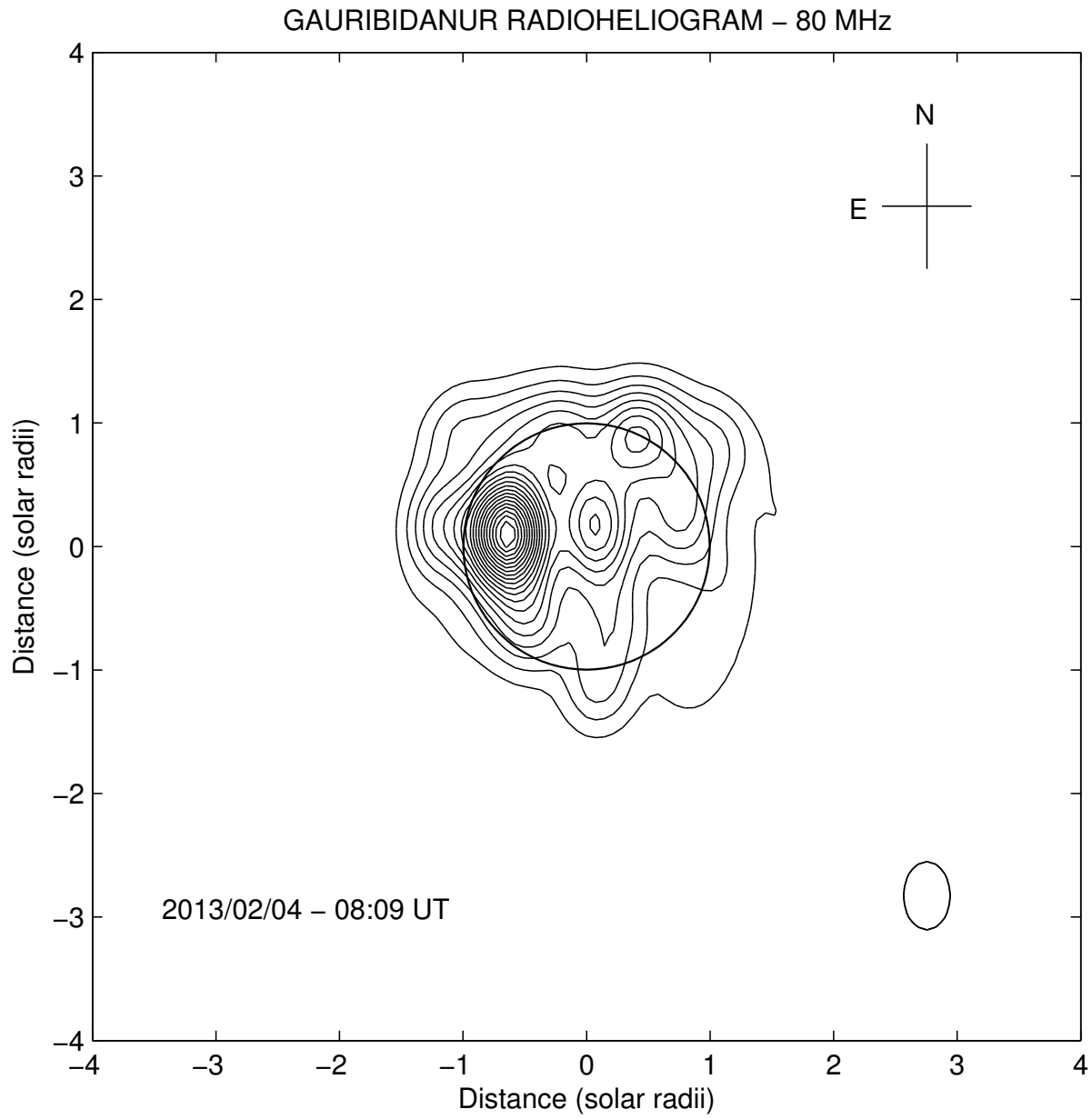

Figure 5.9: GRAPH radioheliogram obtained on 4 February 2013 around 08:09 UT at 80 MHz. The discrete source near the east limb is the location of the Type III bursts shown in Figure 5.8. Its peak $T_{\rm b}$ is $\approx 10^8$ K. The contour interval is $\approx 0.15 \times 10^8$ K. The open circle at the center represents the solar limb. The size of the GRAPH beam at 80 MHz is shown near the lower right corner.

Å wavelength range was $\approx 2 \times 10^{-7}$ Wm^{-2} (B2.0 class). No Hα flares were reported [`www.swpc.noaa.gov/`]. These indicate that the radio bursts in Figure 5.8 are probably associated with weak energy releases in the solar atmosphere [Kundu et al. (1986); White et al. (1986); Gopalswamy and Kundu (1987); Thejappa et al. (1990); Bastian (1991); Subramanian et al. (1993); Ramesh and Ebenezer (2001); Ramesh et al. (2010, 2013b)]. The close spatial correspondence between the source region of the Type III bursts in Figure 5.9 and the sunspot active region AR 11669 (N05E79) observed on that day (*i.e.,* 4 February 2013) indicates that the bursts might be associated with the latter. The above heliographic coordinates correspond to a viewing angle [θ], *i.e.,* the angle between the line-of-sight and the magnetic field direction, of $\approx 89^{\circ}$. Details related to the above Type III radio burst and the other similar events described here are listed in the columns 2 – 5 of Table 5.4.

5.5 Analysis and Results

Wild et al. (1959a) pointed out that both the fundamental [F] and the harmonic [H] Type III solar radio burst emission should generally be observable only for the events near the center of the solar disk. Elsewhere, it should be purely H-emission. This is because the F-emission is more directive compared to the H-emission. According to Caroubalos and Steinberg (1974), ground-based observations of Type III radio bursts associated with sunspot regions located $\gtrsim 70^{\circ}$ either to the east or west of the central meridian on the Sun, are primarily H-emission. Suzuki and Sheridan (1982) found that the F-component has a limiting directivity of $\pm 65^{\circ}$ from the central meridian on the Sun. A similar result was recently reported by Thejappa et al. (2012) for the very low-frequency solar Type III radio bursts observed in the interplanetary medium. This is most likely due to the larger free-free optical thickness of the overlying layer for the fundamental emission as compared to the second harmonic emission at the same frequency.

Table 5.4: Details of the Type III radio bursts

Date	Burst Time (UT)	Heliographic coordinates	Viewing angle [θ] (degrees)	Soft X-ray flux (W/m^2)	dcp 85/35	B 85/35 (G)
11 Nov 2012	05:55	N15E89	89°	6×10^{-7}	0.16/0.04	08.0/0.8
17 Nov 2012	07:52	S28W88	88°	4×10^{-7}	0.06/0.02	03.0/0.4
03 Dec 2012	04:35	N11E89	89°	2×10^{-7}	0.06/0.05	03.0/1.0
07 Dec 2012	05:14	N15W89	89°	1×10^{-7}	0.10/0.04	05.1/0.8
17 Dec 2012	05:34	N15W81	81°	4×10^{-7}	0.22/0.07	11.1/1.5
04 Feb 2013	08:09	N05E79	79°	2×10^{-7}	0.18/0.07	09.2/1.5
Col. 1	Col. 2	Col. 3	Col. 4	Col. 5	Col. 6	Col. 7

The heliographic longitude of the sunspot regions associated with the Type III radio bursts in the present case are all $\gtrsim 80°$ (column 3 in Table 5.4). The estimated dcp, particularly at 85 MHz and 35 MHz (the highest and the lowest observing frequency, respectively, in the present case), for all the events in the present work (column 6 in Table 5.4) indicates that they are consistent with the average dcp (≈ 0.11) and the range of dcp ($\approx$ 0–0.3) reported for the circularly polarized H-component of the Type III bursts in the O-mode [Suzuki and Sheridan (1977); Dulk and Suzuki (1980)]. Above arguments indicate that the Type III bursts in the present case are likely due to H-emission. Here, the sense of polarization was assumed to be the O-mode for the following reasons: i) the Type III radio bursts are due to plasma emission, and their polarization is predominantly in the O-mode for the F- and H-components [Melrose et al. (1980)]; ii) the X-mode emission experiences greater absorption than the O-mode during propagation through the solar corona [Fomichev and Chertok (1968); Thejappa et al. (2003)].

Melrose et al. (1978, 1980), Zlotnik (1981), and Willes and Melrose (1997) had shown that when the Langmuir waves are collimated in the direction of the magnetic field, weakly polarized H-radiation results with the sense of the O- mode, and the magnetic field strength [B] near the source region of a solar radio burst (H-component)

is related to the observed dcp as

$$B = \frac{f_{\rm p} \times \text{dcp}}{2.8\ a(\theta, \theta_0)} \tag{5.3}$$

where $f_{\rm p}$ is the plasma frequency of the H-component in MHz and B is the magnetic field strength in Gauss. We assumed $f_{\rm p} = f/2$, where f is the frequency of observation, since the observed emission in the 85 – 35 MHz band are most likely due to the H-component (see the previous paragraph). $a(\theta, \theta_0)$ is a slowly varying function which depends on the viewing angle θ, and the angular distribution θ_0 of the Langmuir waves. In the present case, $\theta \approx 79^\circ - 89^\circ$ (see column 4 in Table 5.4). But each event can have a range of θ values since the field lines emerging from the associated active region can diverge and/or expand non-radially [Dulk et al. (1979); Klein et al. (2008); Morosan et al. (2014)]. Reports indicate that the sizes of the Type III bursts fill a cone of angle $\theta \approx 50^\circ - 90^\circ$, particularly when the source region is near the limb as in the present case [Dulk et al. (1979); Dulk and Suzuki (1980)]. The Langmuir wave vectors can be present in a cone of angle $\theta_0 \approx 30^\circ$ with respect to the local magnetic field direction for harmonic Type III emission in the O-mode [Melrose et al. (1978); 1980; Zlotnik (1981); Dulk and Suzuki (1980); Willes and Melrose (1997); Benz (2002)]. Taking into consideration the above possible spread in the θ and θ_0 values, we find that $a(\theta, \theta_0) \approx 0.2 - 0.4$ in the present case [Suzuki and Dulk (1985)]. Assuming the average value, i.e., $a(\theta, \theta_0) \approx 0.3$, we estimated the magnetic field strengths for different Type III events listed in Table 5.4. The corresponding values, particularly at 85 MHz and 35 MHz, are listed in column 7 (Table 5.4). The minimum and the maximum B vary by a factor of ≈ 4. An inspection of column 6 in Table 5.4 indicates that this variation comes from the spread in the dcp values, which in turn could be due to differences in the sizes of the corresponding bursts. Note that smaller sources near the limb can have higher dcp than larger sources [Dulk et al. (1979)]. In such cases one need to have accurate information on the source sizes since a smaller source near the limb can also have a larger value for $a(\theta, \theta_0)$ [Suzuki

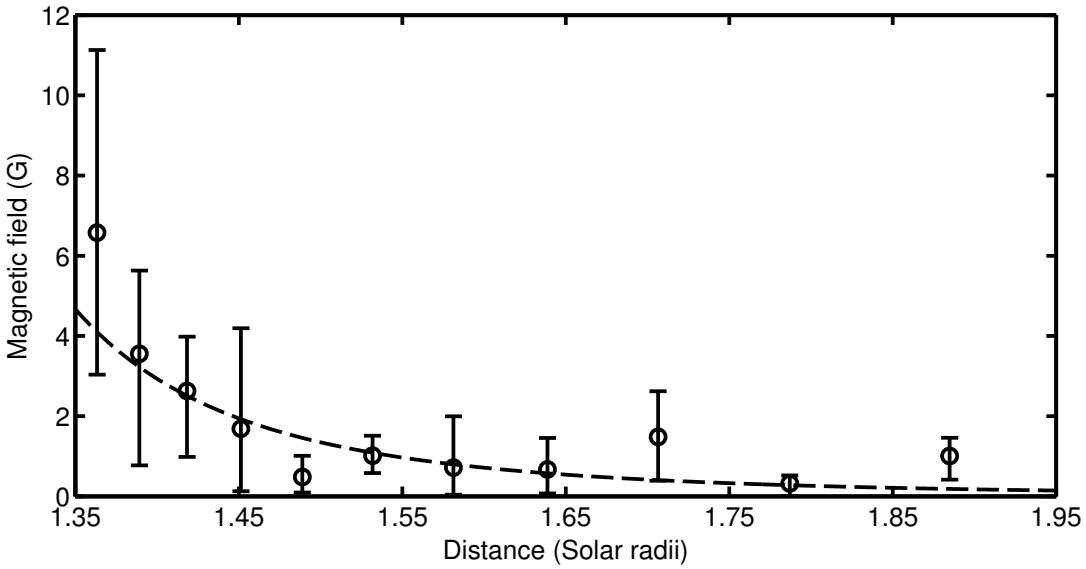

Figure 5.10: Variation of the estimated magnetic field strength (B) with radial distance in the solar atmosphere for the Type III bursts listed in Table 5.4. The vertical lines represent the range of B values at a particular frequency/radial distance estimated from the Type III bursts selected for the study. The "dashed" line is the power-law fit to the mean B (indicated by the circles) at each r.

and Dulk (1985)]. This implies that B will not vary linearly with dcp as in the present case (refer equation (5.3)). Unfortunately, the angular resolution in the present study is limited ($\approx 5' \times 7'$). However, considering the fact that the field strengths in Table 5.4 correspond to different solar active regions, they can be regarded as reasonable [Dulk and McLean (1978); Gopalswamy et al. (1986); Mercier (1990); Fineschi et al. (1999); Lin et al. (2000); Vršnak et al. (2002); Mancuso et al. (2003); Ramesh et al. (2005); Tomczyk et al. (2008); Ramesh et al. (2010); Zucca et al. (2014)]. Figure 5.10 shows the variation of B over $r \approx 1.3-2.0\ R_\odot$ for all the Type III bursts reported in the present work assuming the hybrid model of Vršnak et al. (2004) for the electron density distribution in the solar corona. Note that since the soft X-ray flare energies corresponding to all the Type III bursts in the present work are nearly the same (column 5 of Table 5.4), we may be justified in using the same density model for all the events. The power-law fit to the data points with 95% confidence bounds ("dashed" line in Figure 5.10) indicate that $B = 0.1(r-1)^{-3.5}$ in the distance range $1.3 \lesssim r \lesssim 2.0\ R_\odot$.

Chapter 6

Coronal magnetic field estimates using polarized Type V radio bursts

The contents presented in this chapter are based on the following publication

Spectropolarimeter observations of the low-frequency Type V solar radio bursts

P. Kishore, R. Ramesh, C. Kathiravan, E. Ebenezer, H. A. Srimathi, Anitha Ravishankar

Manuscript submitted to AGU.

6.1 Introduction

TYPE V bursts are relatively unusual radio transients observed in the solar corona. They appear as a diffuse continuum following particularly Type III bursts on the radio spectrograph records. The high-frequency limit of the bursts is usually $\approx$ 120 MHz, although it extends up to $\approx$ 200 MHz occasionally. On the low-frequency side, the limit seems to be $\approx$ 1 MHz. The bursts are non-directive, and have a duration of $\approx 10 - 180$ s, lasting longer at lower frequencies. The emission is widely believed to be due to plasma processes [Wild et al. (1959a); Wild et al. (1959b); Weiss and Stewart (1965); Daene and Krüger (1966); Zheleznyakov and Zaitsev (1968); Melrose (1974); Pilipp and Benz

(1977); Robinson (1977); (1978); Dulk et al. (1980)]. But there are also reports that the bursts can be explained on the basis of electron cyclotron maser action [Winglee and Dulk (1986); Tang et al. (2013)]. The Type V bursts are distinguished from the Type III bursts generally by their longer duration at any given frequency. The long duration of a Type V burst has been attributed to a spread in the velocities of associated coronal electron beams [Robinson (1978)] as compared to the Type III bursts where the beam speed is comparatively constant over the similar range of frequencies [Li et al. (2008); Cairns et al. (2009)]. But observational estimates of the drift speeds of the Type V bursts are rare. Further, the strengths of the coronal magnetic field [B] associated with the Type V bursts have also not been reported [Suzuki and Dulk (1985)]. Ground-based radio spectropolarimeter observations at low frequencies are useful in this regard since both the drift speed of the bursts and the associated B, the latter particularly in the middle corona (1.1 $R_\odot \lesssim r \lesssim$ 3 $R_\odot$) because the observed emission originates primarily there, can be obtained. Moreover, the spectral estimates of the drift speeds are also not affected by the propagation effects in the solar corona like scattering [Aubier et al. (1971); Duncan (1979)], even if they are weak [Willson et al. (1998); Ramesh et al. (1999); 2001; 2006a; 2012; Kathiravan et al. (2011); Mercier et al. (2015)]. Such a set of observations are described in this chapter. Note that the direct estimates of the coronal magnetic field strength using optical/infrared, and radio emissions are presently limited to the inner corona, i.e., $r \lesssim 1.1$ $R_\odot$ [Kuhn (1995); Lin et al. (2000); Gelfreikh (2004); White (2005)] as mentioned in the earlier chapters. In the outer corona, i.e., $r \gtrsim 3$ $R_\odot$, Faraday rotation observations are used to derive the magnetic field [Patzold et al. (1987); Spangler (2005)] as mentioned in earlier chapters.

6.2 Type V Observations

The radio data is obtained with the GRASP and the Gauribidanur Radio Interferometric Polarimeter [GRIP; Ramesh et al. (2008)] at the Gauribidanur observatory. Observations of the Sun with the above two instruments are carried out everyday during the interval $\approx 3 - 9$ UT. Polarized emission, whenever present in the GRASP and GRIP observations, corresponds mainly to the circularly polarized component (Stokes V). Linearly polarized emission, if present at the coronal source region, tends to be obliterated at low radio frequencies because of the differential Faraday rotation of the plane of polarization in the solar corona and the Earth's ionosphere within the typical observing bandwidths [Grognard and McLean (1973)] as mentioned earlier.

Fig. 6.1 shows the Stokes I and Stokes V dynamic spectra obtained from the GRASP observations on 2014 December 14 during the interval 04:27 - 04:30 UT. One can notice patches of emission drifting rapidly towards lower frequencies as a function of time in both the spectra. These are the characteristic signatures of the Type III and Type V radio bursts from the solar corona at low frequencies [Suzuki and Dulk (1985)].

The above radio events were associated with a C8.6 class soft X-ray flare from the location S10E73 on the Sun[1]. The latter corresponds to a viewing angle (θ), i.e., the angle between the line-of-sight and the magnetic field direction, of $\approx 73^{\circ}$. Figure 6.2 shows the range in duration (d) of the Type V bursts reported in the present work at different frequencies. It increases as the frequency decreases.

[1]www.lmsal.com/solarsoft/latest_events

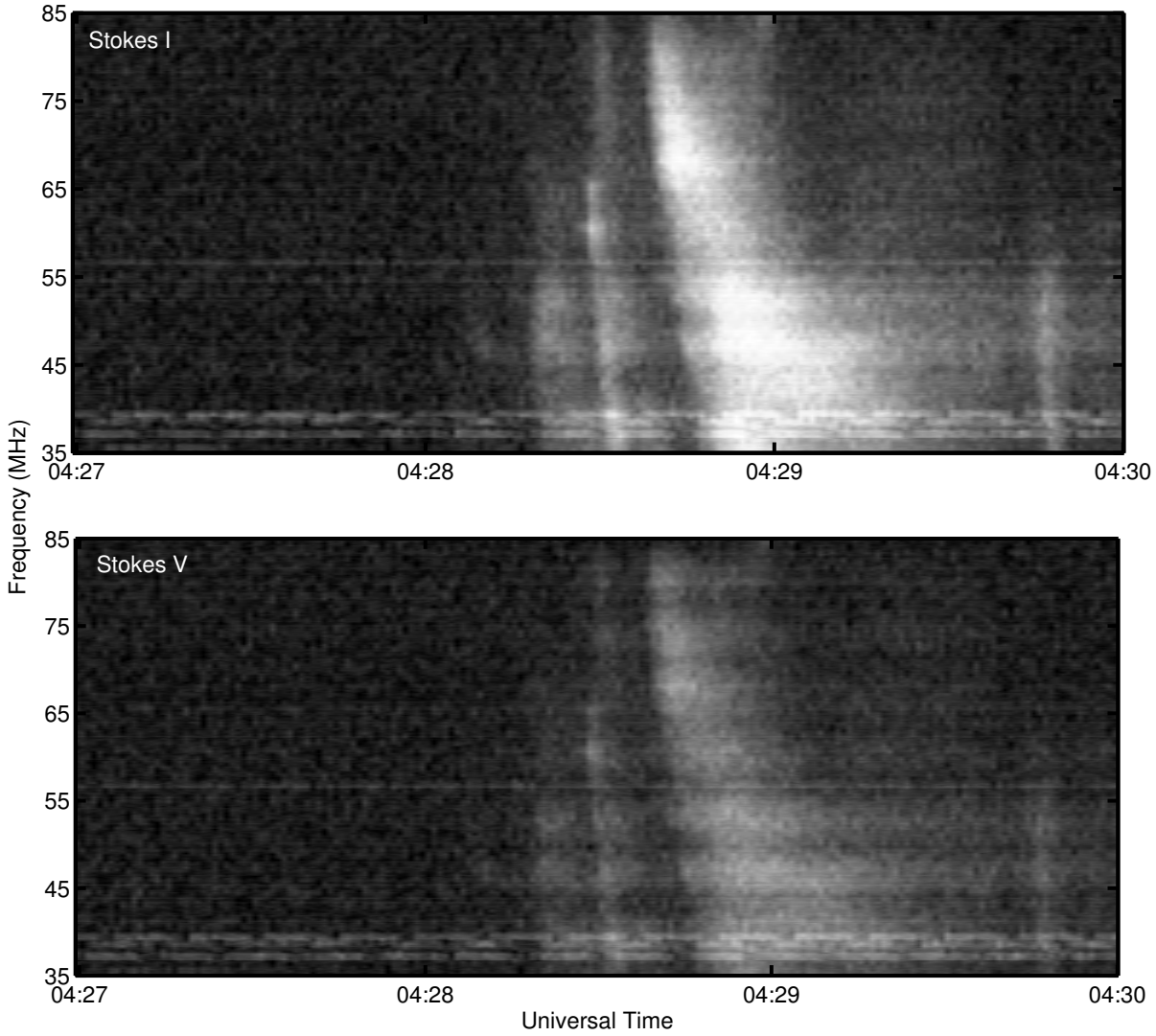

Figure 6.1: Stokes I and Stokes V dynamic spectra of the Type III and Type V bursts observed with the GRASP on 2014 December 14. The two faint events close to ≈ 04:28:30 UT and the third one close to ≈ 04:30 UT are Type III bursts. The comparatively intense event at ≈ 04:29 UT is a Type V burst. The horizontal 'white' features close to 35 MHz and 55 MHz are due to radio frequency interference (RFI).

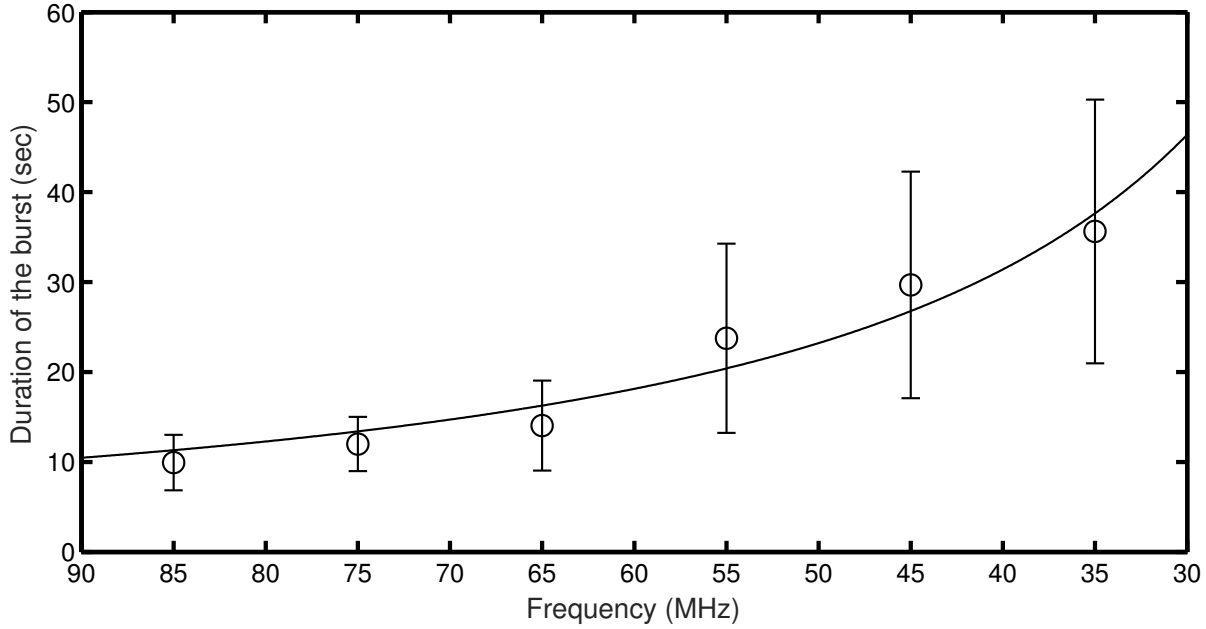

Figure 6.2: Estimated duration of Type V burst at different frequencies for the events reported in Table 6.1. The solid line is the fit to the average duration (indicated by circles) at each frequency.

We find that $d \approx 5-15$ s at 85 MHz and $\approx 20-50$ s at 35 MHz. Though these values are consistent with that reported by Daene and Krüger (1966) at 23.5 MHz ($d \approx 10-60$ s), they are smaller compared to that estimated using the $d \approx 500 f^{-1/2}$ (where f is frequency of observation in MHz) empirical relation reported by Weiss and Stewart (1965) for the average duration of the Type V bursts. It is likely that the bursts reported here may belong to the category of 'long Type IIIs', i.e., a single Type III burst followed by a small duration Type V continuum, pointed out by Stewart (1974). The observations in Figures 6.1 and 6.3 are also consistent with this.

The details related to the above radio bursts and the other similar events reported here are listed in the columns 2-5 of Table 6.1. Except for the last two Type V events (i.e., 12 April 2015 and 8 May 2015), the rest were preceded by a Type III burst within the detection limits of the GRASP. An inspection of the data obtained with the GRIP, which has better sensitivity than the GRASP, revealed that the above two Type V bursts were also preceded by single Type III bursts. We independently verified the spectral nature of

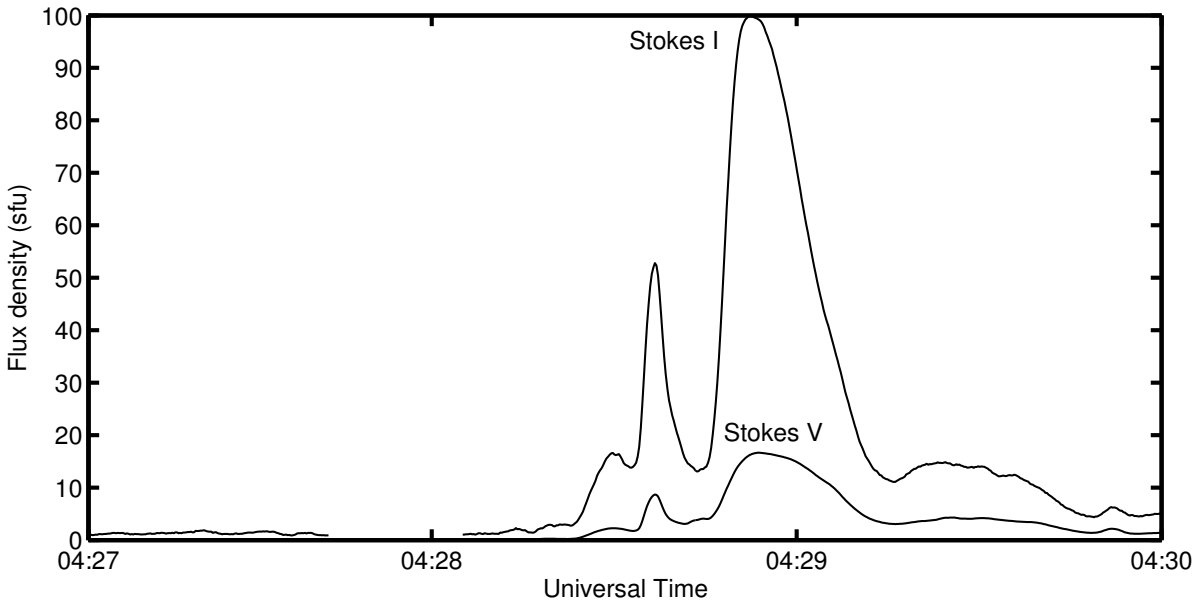

Figure 6.3: Time profile of the Type III and Type V bursts in Figure 6.1 as observed with the GRIP at 80 MHz. The better sensitivity of the GRIP over GRASP is clearly evident. While the first Type III burst close to $\approx$ 04:28:30 UT and the Type III burst close to $\approx$ 04:30 UT are too faint to be noticed in the GRASP observations at 80 MHz, here they can be seen with comparatively better contrast.

the bursts using the simultaneous total intensity observations with the GLOSS.

We calculated the dcp = V/I of the Type V bursts at different frequencies in the range $85 - 35$ MHz from the respective observed Stokes I and Stokes V amplitudes. The dcp was found to decrease with the decrease in frequency. The estimates at the highest and the lowest observing frequencies in the present case (i.e., 85 and 35 MHz, respectively) are listed in column 6 of Table 6.1.

They agree reasonably with those reported earlier [Dulk et al. (1980)]. The sense of polarization for all the events was left circular. As per the IAU definition, this implies that the rotation of the electric field vector along the direction of propagation of the incident radiation is in the counter-clockwise direction [Thompson et al. (2004)]. In the case of the preceding Type III bursts, we found that the sense of polarization was left circular for the events of 29 October 2013 and 9 July 2014, and right circular for the event of 14 December 2014. Figure 6.3 shows the Stokes I and V observations with the

Table 6.1: Details related to the Type V solar radio bursts observed with the GRASP

Date	Burst Time (UT)	Heliographic coordinates	Viewing angle [θ] (degrees)	Soft X-ray flux (W/m^2)	dcp 85/35	B 85/35 (G)
2013/10/29	04:19	N08W85	85°	3.70×10^{-6}	0.16/0.01	7.9/0.3
2014/07/09	04:38	N13W71	71°	1.70×10^{-6}	0.15/0.02	7.6/0.4
2014/12/14	04:29	S10E73	73°	8.60×10^{-6}	0.14/0.05	7.0/0.9
2015/04/12	04:05	N11E81	81°	1.00×10^{-6}	0.14/0.03	7.0/0.6
2015/05/08	07:39	N16E79	79°	8.00×10^{-7}	0.16/0.04	8.2/0.9
Col. 1	Col. 2	Col. 3	Col. 4	Col. 5	Col. 6	Col. 7

GRIP at 80 MHz around the same time as the bursts in Figure 6.1. The peak Stokes I flux density of the Type V burst is ≈ 100 sfu (1 sfu = solar flux unit = $10^{-22}\mathrm{Wm}^{-2}\mathrm{Hz}^{-1}$) and Stokes V flux density is ≈ 17 sfu. The corresponding dcp ≈ 0.17 is consistent with those estimated from the GRASP observations (see column 6 in Table 6.1). Above Stokes I flux density agrees well with the similar values reported in the literature at 80 MHz [Robinson (1977); Dulk et al. (1980)].

6.3 Analysis and Results

We calculated the drift speed of the Type III bursts and the Type V bursts in Figure 6.1 using the hybrid model proposed by Vršnak et al. (2004) for the electron density distribution in the solar corona. The values are $v \approx c/4$ and $v \approx c/10$, respectively. We used the above density model since the location of the plasma level at frequencies like 80 MHz ($r \approx 1.39$ R$_\odot$) and 43 MHz ($r \approx 1.74$ R$_\odot$) agree reasonably well with the average heliocentric distances of the Type V bursts reported earlier from two-dimensional imaging observations at the corresponding frequencies [Robinson (1977)]. Note that the time(s) at which the Type III and the Type V bursts were first noticed at the different frequencies in the range $85 - 35$ MHz were used to estimate the above drift speeds. In the case of the Type V bursts, we estimated the drift speed from

the time of occurrence of the maximum phase of the burst at each frequency as well. The drift speed in this case, based on the hybrid density model, is $v \approx c/40$. The above results indicate that the electron beams associated with the Type V burst in Figure 6.1 has a range of speeds, i.e., $v \approx c/10 - c/40$. We found that the drift speeds of the other events in Table 6.1 also exhibits a similar trend. The above range of speeds appears reasonable since there is evidence that electrons with speeds as low as $\approx 0.03c$ can excite plasma (Langmuir) waves and radio radiation, and electrons that cause the onset of the radiation travel faster than those associated with the maximum of the radiation [Dulk et al. (1987)]. We would like to point out here that the theoretical calculations by Magelssen (1976) related to the propagation of one-dimensional electron beams injected into the solar atmosphere with a velocity spread $v \approx c/2 - c/40$ indicate that the latter should give rise to bursts with a duration ≈ 18 s at a typical frequency like 58 MHz. Similar calculations by Robinson (1978) indicate that the expected duration of Type V bursts at 80 MHz and 40 MHz are $\approx$ 19 s and $\approx$ 36 s, respectively. The observational estimates of the velocity spread, and the duration of the Type V bursts reported here (see refer Figure 6.2) agree reasonably well with the above theoretical results. Therefore, the possibility that the electrons leading to Type III bursts travel along a more radial path compared to the Type V bursts could also be a reason for the longer lifetime of the latter at any given frequency [Robinson (1978)] seems less likely in the present case. Also, there is no reason why it should preferentially happen so. Further, there is an evidence that the Type III burst electrons too travel along non-radial curved magnetic field lines [Dulk et al. (1979); Klein et al. (2008); Morosan et al. (2014)]. Having said so, we would like to note that a statistical study of Type V bursts from sunspot regions close to the disk center, and near the solar limb might be useful to arrive at a more definitive conclusion since the geometry of the magnetic field lines with respect to the viewing angle can be different in the above sets.

Plasma emission in the presence of a magnetic field is split into ordinary ['O'] and the

extraordinary ['X'] modes as mentioned in the previous chapters. Due to the differential absorption of these two modes in the medium, a net dcp can be observed [Melrose and Sy (1972)]. The latter is related to the strength of the magnetic field in the source. Most of the low-frequency solar radio bursts observed from the ground originate in the 'middle' corona and their emission mechanism is due to plasma processes [McLean (1985)]. Therefore, it is possible to estimate the strength of the magnetic field in the corona from observations of the polarized radio bursts [see for eg. Dulk and Suzuki (1980); Mercier (1990); Ramesh et al. (2013b); 2013a; Sasikumar Raja et al. (2014); Hariharan et al. (2014)], and quasi-periodic Type III radio bursts [Zhao et al. (1991); Aschwanden et al. (1994); Ramesh et al. (2003a); 2005; Sasikumar Raja and Ramesh (2013)]. It has been shown earlier that the Type V solar radio bursts are usually due to second harmonic plasma emission [Zheleznyakov and Zaitsev (1968); Dulk et al. (1980)]. In such a case, the magnetic field strength (B) near the source region of the burst can be estimated using the relation [Melrose et al. (1978); 1980; Dulk and Suzuki (1980); Zlotnik (1981); Willes and Melrose (1997); Benz (2002)],

$$B = \frac{f_{\rm p} \times \rm dcp}{2.8\ a(\theta, \theta_0)} \tag{6.1}$$

where $f_p = f/2$ is the plasma frequency of the second harmonic component, and B is the magnetic field strength in Gauss (G). $a(\theta, \theta_0)$ is a slowly varying function which depends on the viewing angle θ, and the angular distribution θ_0 of the Langmuir waves. In the present case, $\theta \approx 79^\circ - 85^\circ$ (see column 4 in Table 6.1). Similarly, the Langmuir wave vectors can be present in a cone of angle $\theta_0 \approx 60^\circ$ with respect to the local magnetic field direction for the Type V bursts [Dulk et al. (1979, 1980)]. Taking into consideration the above possible range of θ and θ_0 values, and the fact that the sizes of the Type V bursts are large [Robinson (1977)], we find that $a(\theta, \theta_0) \approx 0.2 - 0.4$ [Dulk et al. (1980)]. Assuming the average value, i.e., $a(\theta, \theta_0) \approx 0.3$, we estimated the magnetic field strengths for the different Type V bursts. The corresponding values, particularly at 85 MHz and 35 MHz,

are listed in column 7 of Table 6.1. Figure 6.4 shows the variation of B with r for the Type V bursts assuming the hybrid model of Vršnak et al. (2004) for the electron density distribution in the solar corona.

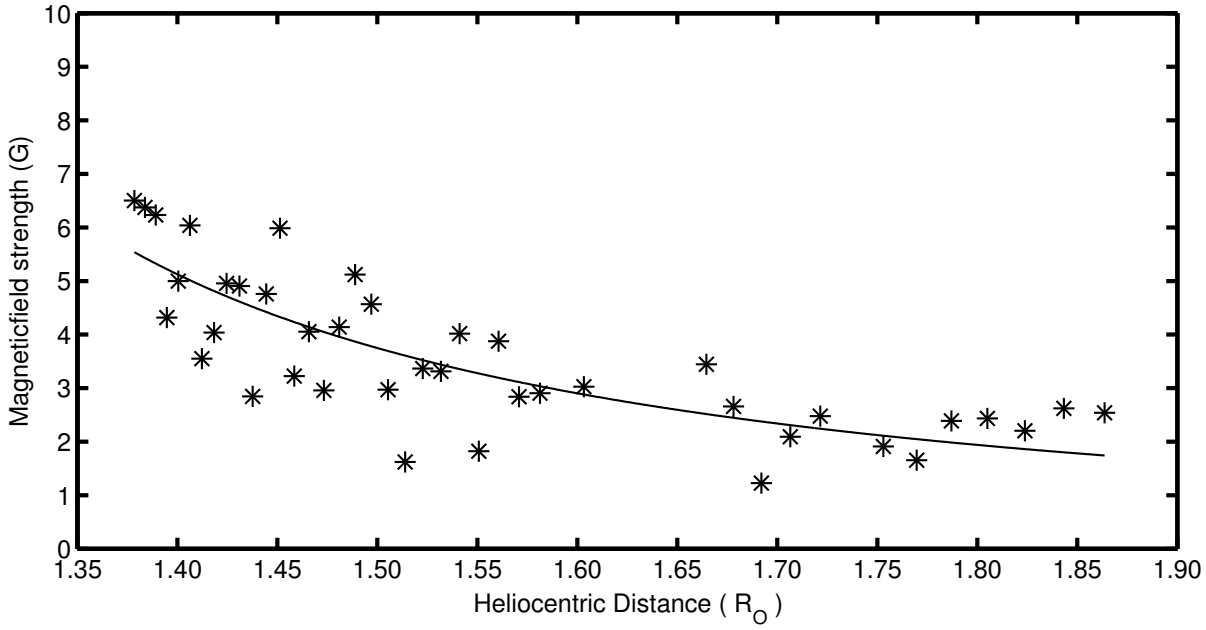

Figure 6.4: Variation of the estimated magnetic field strength [B] with heliocentric distance in the solar atmosphere for the Type V bursts listed in Table 6.1. The vertical lines represent the range of B values at a particular frequency/radial distance estimated from the different Type V bursts listed in Table 6.1. The 'dashed' line is the power-law fit ($B = 1.4(r-1)^{-1.4}$) to the average B, indicated by the circles, at each r.

Note that since the soft X-ray flare flux corresponding to all the Type V bursts considered are nearly the same (column 5 of Table 6.1). Hence, we used the same density model for all the events. A power-law fit to the data points with 95% confidence bounds ('dashed' line in Figure 6.4) indicate that $B = 1.4(r-1)^{-1.4}$ in the range 1.35 $\lesssim r \lesssim 1.90$ R$_\odot$. The above empirical relation is similar to that reported earlier from spectral observations of Type III radio bursts [Kishore et al. (2015)], Type II radio bursts [Vršnak et al. (2002); Mancuso et al. (2003)], Type I radio bursts [Gopalswamy et al. (1986); Ramesh et al. (2011)], and the combination of different types of solar radio bursts [(Dulk and McLean, 1978)]. The difference is that the present estimates are derived using direct observations of the associated circularly polarized radio

emission.

The number of electrons (N) in the Type V burst source region can be calculated as $N \approx n_n A \overline{v} d$, where n_n is the non-thermal electron density, A is the area of the source, and $\overline{v}$ is the average velocity of the electrons. Typical source sizes at 80 MHz are $\approx 2.5 \times 10^{21} \mathrm{cm}^2$ (Robinson, 1977). In the present case $d \approx$ 10 s at a typical frequency like 80 MHz (see Figure 6.2) and $\overline{v} \approx c/25$. From the above values we obtain $N \approx 3 \times 10^{31} n_n$. The electron density ($n_e$) corresponding to 80 MHz is $7.9 \times 10^7 \mathrm{cm}^{-3}$. In the case of Type III bursts, $n_n/n_e \sim 10^{-6}$ [see for eg. Raoult et al. (1990); Li et al. (2009); Ramesh et al. (2010)]. Assuming n_n/n_e for the Type V bursts to be the same as the above (Stewart, 1978), we get $N \approx 2.4 \times 10^{33}$. Compared to this, the average number of electrons producing a Type III radio burst is $\sim 3 - 5 \times 10^{33}$ [Gopalswamy and Kundu (1987)]. We also find that the average speed of $\overline{v} \approx c/25$ in the present case corresponds to an energy of ≈ 0.4 keV which is nearly the same as the energy of the electrons associated with some very low-frequency Type III bursts observed in the interplanetary medium [Dulk et al. (1987)].

Chapter 7

Conclusions & Future Scope

MOST of the coronal transients that are observed at meter wavelengths are understood to originate from the middle corona (1.2 $R_\odot < r < 3$ $R_\odot$). Currently, observations of the Sun using space-borne instruments are limited to outer ($r > 3$ $R_\odot$) and inner corona ($r \leq 1.2$ $R_\odot$) because of technical difficulties. Therefore, radio observations of the middle solar corona can effectively bridge the gap between space and ground-based observations made at other wavelengths. Also, one can study and understand several high energy processes, electron density distributions, emission mechanisms, rise, lift-off & acceleration phases of CMEs, magnetic field strength associated with different thermal and non-thermal processes, etc. in a better way because: 1) the coronal radio emission from the disk as well as off-the limb can be imaged simultaneously unlike the case of white-light observations. (2) The corona can be viewed with better contrast in radio wavelengths as compared to white-light since the former is proportional to N_e^2 whereas in the latter case it is proportional to N_e. Therefore, it was decided to commission dedicated facilities to observe the solar corona at radio wavelengths particularly in the low-frequency regime at the Gauribidanur Radio Observatory.

7.1 Summary

Right from the 1950s the dynamic spectrographs have been providing enormous volumes of data and thus greatly contributed to our present understanding of solar transient phenomena through their associated radio out-bursts. Although new insights were shed, several new questions also emerged in the recent past due to various scientific interests and reasons, which require dedicated high time and frequency resolution data of the solar corona. Therefore, it was decided to set-up such a dedicated spectral observing facility few years before at the Gauribidanur observatory. A new broad-band Log-periodic dipole antenna (LPDA) that works in the frequency range 40-440 MHz was developed for the front-end. The LPDA theory given by Carrel was followed to design the antenna; it was fabricated in-house using Aluminium material. The VSWR, radiation pattern, and other characterization tests were carried out at the observatory. The test results of the antenna were compared with the theoretical simulations using 4Nec2; they both agree reasonably well with each other. The antenna parameters such as Gain, Beam efficiency, effective aperture, sensitivity, etc. were determined. Also, a new method to reject some of the frequency bands within the wide operating band of the LPDA is described briefly, and the work may be continued further to formulate the theory on a firm footing. All the relevant details are presented in Chapter 2. Eight such LPDAs were combined in phase (adding interferometer mode) along North-South direction to form an array; it is called as the Gauribidanur Low-frequency Solar Spectrograph (abbreviated as GLOSS) array. In order to track the Sun along the Declination axis, electronically controlled delay shifter systems are used. The noise figure of GLOSS system was determined by measuring the noise level from various modules of the system; from that, the sensitivity of the system was obtained, and characterization was completed. The swept-frequency spectrum analyzer (E4401B) from Agilent Technologies is programmed to obtain the solar spectra. Each sweep takes 100 ms to cover the band, and it gives 401 intensity values. The instrument

is controlled by a PC using Agilent Veepro software. GLOSS is in continuous operation right from the day of its commission. Adopting the method suggested by Dulk et al. (2001) the GLOSS spectra were calibrated by observing the Galactic center during its local meridian transit. A Type II radio burst observed with the GLOSS on 17 November 2011 was described as an example event to show how the data can be used effectively to determine the coronal parameters; the event has both fundamental and harmonic components with a band splitting structure. The event was associated with a CME, soft x-ray and h-alpha flares. Combining the radio imaging observations of the Type II bursts and white-light observations of the CME, the spatio-temporal association between them were established. Assuming the hybrid electron density model for the background corona, the magnetic field associated with the Type II radio burst was determined to be 2.7 - 1.8 G in the radial distance range 1.4 - 1.6 $R_{\odot}$. The value is about 3 times higher than that of the undisturbed corona. This example shows how effectively the radio spectral data can be used for probing the coronal parameters by combining solar data observed at other frequencies. The present magnetic field estimates are rather crucial as there are no direct measurements possible within the above-mentioned radial distance range because of lack of observing facilities. Indirectly, they are estimated by extrapolating the line-of-sight component of the photospheric magnetic field assuming that it is force-free. Some of the other results obtained from GLOSS observations are described in Chapter 2 and Chapter 4.

GLOSS data has been used to determine the magnetic field strength of the source region responsible for Type II bursts is described elaborately in Chapter 3. Type II bursts occur as two slow drifting emission bands (as compared to Type IIIs) with a frequency ratio 1:2; they are called as the fundamental (F) and harmonic (H). Sometimes, they exhibit a split in both F and H components. They are called as the Upper (U) and Lower (L) bands which are claimed to be due to radio emission generated ahead and behind an MHD shock front. Smerd et al. (1974, 1975) showed that the split band features can

be used to estimate the magnetic field strengths along the path of the propagating MHD shocks. Considering the close spatio-temporal association between Type II bursts and CMEs as reported by Gopalswamy et al. (2013), an attempt was made to derive $B(r)$ in the corona by constraining the choice of $N_e(r)$ and the locations of the Type II bursts and the accompanying CMEs. Four Type II bursts observed during the period October, 2013 to February, 2014 with GLOSS were taken for this study because of their narrow width in order to avoid the ambiguity as whether the shock is generated at the flank or leading edge (LE) of the CME. All the Type II bursts selected belong to the split-band category; this was verified by estimating the ratio of the duration (and frequency as well) of F_L, F_U, H_L and H_U measured from the spectra.

The would-be CMEs were selected from COR1 of STEREO mission and C2 of SOHO mission; GOES data were considered for information on X-ray emission. The actual position (r_{CME}) and speed (v_{CME}) of the CME LE was determined by de-projecting the coronagraph height-time measurements. Presuming that the Type IIs are generated by the CMEs, the onset time and frequency were used to determine the velocity of the Type II bursts by choosing an appropriate electron density model satisfying the following criteria: i) the location of plasma level corresponding to a specific frequency within the Type II burst should be consistent at its time of occurrence; ii) the drift speed of the Type II burst must closely agree with v_{CME}. The electron density model given by Saito found to agree if a density enhancement factor in the range 6 - 17 (the highest value corresponds to the Halo CME) is used for the selected Type II events. In order to verify the above result, we have used the expression ($f(r) = 307.87\ r^{-3.78} - 0.14$), for the Type II onset frequency as a function of CME LE height, given by Gopalswamy et al. (2013). We could find good agreement between the two results if 2 $\times$ Gopalswamy model was used.

We have also calculated the magnetic field strength ($B(r)$) from the split band structure using the method suggested by Vršnak et al. (2002) and Cho et al. (2007).

We found B(r)=1.8 - 1.3 G in the radial distance range =1.67 - 1.97 $R_{\odot}$ for the Saito model, whereas it varies from 1.35 - 0.97 G in the range 1.68 - 1.91 $R_{\odot}$ for Gopalswamy model. The best for all the magnetic field values obtained in the present study gives $B(r) = 1.26 \times (r-1)^{-0.6}$ in the 1.6 - 2.4 $R_{\odot}$. Combing the latter with the magnetic field values obtained by other authors give $B(r) = 0.88 \times (r-1)^{-0.4}$ in the range 1.2 - 2.4 $R_{\odot}$. This is two times larger as compared to the magnetic field estimate for the non-flaring corona.

Moving Type IV radio bursts are unique with respect to the determination of CME magnetic field strength as they are observed along with them most often. It is claimed that the Type IVm bursts are due to either second harmonic plasma emission or optically thin gyro-synchrotron emission and sometimes due to both of them. In Chapter 4, we have presented three moving Type IVm events observed on January 16, 23 and 26, 2012 with GRAPH at 80 MHz and GLOSS between 85 and 35 MHz, in order to study their emission mechanism and the strength of the CME magnetic field responsible for them. We have used the LASCO white-light and GRAPH observations to establish the spatial correspondence between the location of the radio burst and the CME; the radio spectral observations are used to ascertain the type of radio emission and to select the suitable electron density model. The measured velocities of the associated CMEs using white-light observations are 1060, 2175 and 1194 Km/s, respectively. By combining the radio spectral and image data, drift speeds of the Type IVm were determined to be 162, 179 and 284 Km/s. Ten times Baumbach-Allen density model was found to be appropriate to determine the latter. The corresponding estimates obtained from the locations of the radio centroids at different instants of time from the radioheliograms are 155, 166 and 464 Km/s, respectively. The close agreement between the Type IVm drift speed, and those estimated from the radio centroids indicates that the Type IVm are not generated by the CME leading edges. Also, the locations of the radio enhancements as seen from the radioheliograms are almost co-spatial with the foot-points of the associated

CME is in support of this argument. Further, the analysis shows that the Type IVm emission are mainly due to plasma processes instead of gyro-synchrotron because: 1) the observed spectra contain radio emission at frequencies greater than two times the plasma frequency corresponding to the electron number density derived from white-light pB observations at the locations of radio enhancement implying the radio emission not to be due to gyro-synchrotron as they should have been suppressed because of Razin-Tsytovich effect; 2) past observations of Type IVm associated with the legs are due to plasma emission; 3) the derived spectral indices (-2.7 to -3.4) lie well within the range of fundamental and second harmonic plasma emission (-2 to -4) whereas it is -4.2 for the gyro-synchrotron emission. According to the theory of Type IVm bursts based on second harmonic plasma emission, energetic electrons trapped in a magnetic loop have a loss-cone distribution which excites plasma waves near the upper hybrid frequency $f_{uh}^2 = f_p^2 + f_c^2$, where f_p and f_c are electron plasma and gyro frequencies, respectively. In the absence of polarizations observations, we have assumed that Type IVm bursts are weakly polarized and estimated a limiting value for the magnetic field (4 G at a radial height of 1.6 $R_\odot$) making use of the fact that the upper hybrid frequency resonates with the fourth harmonic of gyrofrequency.

Polarization observations in the middle corona (1.2 - 3.0 $R_\odot$) are presently very rare because of lack of observational facilities. It is a general practice that the line-of-sight photospheric magnetic field is extrapolated to calculate the coronal magnetic field assuming the field is force-free. Since plasma emission is by and large responsible for the radio emission from the solar corona, and is expected to get split into ordinary and extraordinary mode in the presence of an external magnetic field, we can make use of the resultant polarized radio emission to determine the associated magnetic field strength responsible for polarization. Also, since the above radial distance range is large, one has to design a broad band radio spectro-polarimeter receiver system to cover the corresponding radio frequency range.

Chapter 5 describes one such set-up called Gauribidanur Radio Spectro-Polarimeter (GRASP) in detail. The front-end of the system consists of two LPDAs which can operate over 85 - 35 MHz and has a directional gain of 7 dBi. Placed apart of 10 m with a North-South baseline, their orientations are orthogonal to each other. This facilitates long duration (6 hours) observation as the response is broad along the RA. The declination control system enables the antenna system to target various sources that are observable. The RF signals from the antenna system are transmitted using optic fiber cables to avoid differential loss across the band which normally happens in a co-axial RF cable. All the losses attributed to the RF-to-optic signal and back are properly taken care of, and the signal is finally fed to a four port phase quadrature hybrid (QH). The QH has two i/p and two o/p ports. At each o/p port, the signal from the exactly opposite i/p port is combined with a 90° phase shifted signal from the diagonally opposite i/p port. Depending on the sense of rotation of the electric vector of the i/p signal, the output is either added or subtracted at the o/p with the noise gets cancelled out automatically. Therefore, depending on the nature of polarization, one of the output ports gives maximum and the other gives the minimum. Each one of the o/p is given to a spectrum analyzer to obtain the dynamic spectra. The sweep time is 100 ms and the instantaneous bandwidth is 125 kHz. The sensitivity of the system is < 3 sfu and < 4 sfu at the minimum and maximum observing frequency. A GPS is used for synchronizing the PCs which are controlling the observations in order to minimize the error in data acquisition. One should note that measuring the circularly polarized emission with two linearly polarized antennas with a spacing between them ensures a minimum mutual coupling and polarization cross-talk.

The system was calibrated using a broadband noise source in the lab; at first, the offset between the two back-end systems was corrected and then the difference between the two signal paths was corrected by transmitting the signal over the entire RF chains. The entire receiver set-up was tested finally with both LCP, and RCP signals generated using a standardized QH and a Circularly-Polarized Log-Periodic Antenna (CLPDA);

the signals were received using linearly-polarized LPDAs orthogonal to each other and the reproduction was satisfactory to an accuracy close to 10%. In-order to verify the calibration through observations, the radio emission from the Galactic Center(GC) was recorded as it is randomly polarized and also non-thermal in nature. The performance of the system was found to be satisfactory as it gave a degree of circular polarization (dcp) close to 2% with an error of 1% or so at 65 MHz for the radio emission from GC.

The GRASP is in regular operation since after commissioning and has observed all kinds of radio bursts both in Stokes-I and Stokes-V. Among all, we have selected 6 Type III events whose brightness temperature values were lesser ($\approx 10^8$ K) than the usual and were associated with low level of X-ray activity ($\approx 10^{-7}$ W/m^2) and no H-alpha flares. Also, their associated photospheric source regions were close to the limb (79° - 89°). Theories claim that Type IIIs whose source regions are close to the limb are due to second harmonic plasma emission and the measured dcp were also within the expected range ($\approx$ 0 - 0.3) with a mean of 0.11. The sense of polarization was assumed to be due to “O-mode" based on the arguments by Melrose et al. (1980)–Dulk et al. (1980) and the “X-mode" is absorbed more than “O-mode" during the propagation. The magnetic field strength of the source regions were calculated from the observed dcp using $B = (f_p \times dcp)/2.8a(\theta, \theta_0)$. The underlying assumption is that the weakly polarized emission was due to the collimation of Langmuir waves along the magnetic field lines. The $a(\theta, \theta_0)$ in the above expression is a slowly varying function of viewing angle θ and the direction of propagation of Langmuir waves θ_0. Assuming Type III bursts fill a cone of θ = 50 - 90° and 30° for θ_0 we found that $a(\theta, \theta_0)$ lie in the range 0.2 - 0.4. Considering a mean of 0.3 from the latter, the magnetic field strengths were calculated to be in the range 0.4 - 11.1 G. Using the hybrid model given by Vršnak et al. (2004) for the electron density distribution, the radial distance of the source regions were determined and the estimated magnetic field strength was plotted against them. The fit to those data points give an expression for the magnetic field strength as a function of radial distance (range

=1.3 - 2.0 $R_\odot$) which is $B = 0.7(r-1)^{-3.5}$ G.

Chapter 6 describes Type V radio bursts observed with the GRASP and GRIP (Gauribidanur Radio Interference Polarimeter) systems and how they can be used to estimate the parameters such as drift speed, magnetic field strength, etc. Type V bursts (120 MHz - 1 MHz) always follow Type IIIs and are non-directive; their typical lifetime is about 10 - 180 s. At any observing frequency, Type V last longer than the accompanying Type III; the widely accepted reason is that the electrons responsible for that emission have a wide range of velocity.

Five Type V events (observed during October, 2013 - May, 2015) whose associated active regions have a viewing angle (angle between the line-of-sight and magnetic field direction) of more than 70°, were selected for the study assuming that the Type Vs are due to second harmonic plasma emission. The duration of the bursts as a function of frequency was found to increase towards higher frequencies (i.e., 5 - 15 s at 85 MHz and 20 - 50 s at 35 MHz) which are more likely for long Type III bursts. The degree of circular polarization was measured from Stokes-I and Stokes-V observations of GRASP and GRIP; the values were found to be in the range 0.14 - 0.16 at 85 MHz and 0.01 - 0.05 at 35 MHz and the sense of polarization is counter-clockwise in all cases. Assuming the hybrid model given by Vršnak et al. (2004) for the coronal electron density distribution, the drift speed of Type V bursts were determined to be c/10 whereas it is c/3 for Type III. The values were determined using the start time of the burst at each frequency; but if we use the peak time of the Type V bursts, the drift speed becomes c/40 which implies that the electrons can also move at a slower rate (v = 0.03c) to produce Type V bursts; this is possible as there are evidences for slow drifting electrons exciting Langmuir waves and the subsequent radio radiation. It should also be pointed out that the propagation of one-dimensional electron beams with a velocity spread c/2 - c/40 gives a shorter duration (≈19 s at 80 MHz) for the Type V bursts as compared to the value at 40 MHz which is ≈36 s. This rules out the possibility for longer duration of Type V bursts due to

electrons travel non-radial curved paths as compared to Type III bursts.

As described earlier, a net degree of circular polarization is observed when radio waves split into “O" and “E" mode when plasma is subjected to external magnetic field. Since Type V bursts are due to second harmonic plasma emission, and the source regions are close to the solar limb, one can determine the magnetic field strength responsible for the Type V bursts using $B = (f_p \times dcp)/\ 2.8a(\theta, \theta_0)$. Assuming the Langmuir wave vectors spread over a cone of 60°, $a(\theta, \theta_0)$ having an average value of 0.3, and the electron density follows Vršnak et al. (2004) distribution, the magnetic field strengths are estimated; the values are in the range 7.0 - 8.2 G at 85 MHz and 0.3 - 0.9 G at 35 MHz. The fit for the average values of the data points gives $B = 1.4(r-1)^{-1.4}$ G over the radial distance 1.35 - 1.90 $R_\odot$. We have also estimated the number of electrons in the Type V source region using $N = n_n Avd$, where n_n is the non-thermal electron density, A is the source area, and v is the average velocity of the electrons. Considering a typical source size of $2.5 \times 10^{21}\ cm^2$, v = c/25, d = 10 s at 80 MHz and $n_n/n_e \approx 10^{-6}$, N becomes 2.4×10^{33} which is almost in the range of values for Type III bursts.

7.2 Future Scope

GLOSS and GRASP facilities can be upgraded with following improvements to their front-end and back-end receiver systems.

1. **RFI mitigation:** In Chapter 2, we described the methodology to reduce the RFI using the antenna itself by modifying its design slightly. The preliminary results, for smaller bandwidths, are promising. Therefore suitable experiments may be performed to improve this technique for large bandwidths. Empirical expressions relating the rejection-bandwidths and design parameters need to be formulated on a firm footing.

2. **RF to optical:** The signal from GLOSS antenna system is transmitted to the lab through a coaxial cable. The RF cables inherently have i) differential loss across the band of interest and ii) change in signal characteristics due to ambient temperature variation. With the rapid advancements in the technology with which RF is transmitted using optical devices and the affordability over coaxial cables in the recent times prompts us the possibility of switching over to new method of transmitting signals. In case of GRASP the individual RF signals are modulated by low power laser diodes & the conversion losses are equalized in RF to optical and vice-versa transducers (procured from M/s. Huber+Shuner technologies). Clearly, the GRASP system is therefore much better than those use the coaxial cable system. This may be implemented on the large scale array like GRAPH to minimize above losses and to have a cost effective solution to substitute RF cables with custom-made transducers developed and characterized in-house in the future.

3. **Digitization:** Both GLOSS and GRASP systems use conventional spectrum analyzers as their backend. There are a number of limitations with this type of system, viz i) fixed number of spectral points, ii) trade off between the bandwidth, resolution and sweep time, etc. iii) limitations on dynamic range iv) poor signal to noise levels, v) loss of phase information, and so on. This semi-analog system can be replaced with full digital back-end. The RF signal over the band can be digitized (at Nyquist rate) with high-speed digitizers interfaced to FPGA systems (running FFT routines) to improve the i) Signal to Noise ratio which is given as SNR = 6.02N +1.76 dB (where N is the bit resolution of Analog to Digital Converter) ii) better dynamic range which is inevitable to study weak energy releases that take place in the outer solar atmosphere. Also, the other limitations set by the former system can be overcome with state-of-the-art digital modules.

4. **Automation Software:** At present, the daily observational logs, post-processing works which include the identification of different class of bursts are carried out by observers at the Gauribidanur observatory. Intelligent processing algorithms may be developed to automate the above-mentioned processes to minimize human intervention.

5. **Digital techniques:** The conventional analog beam former circuits are used in the present observing systems. They may be changed to most efficient digital beam forming techniques. RFIs can be mitigated in real time by employing adaptive filtering methods (for example, the Recursive Least Squares method).

6. **Alternate Calibration:** The methods of calibrating GLOSS & GRASP data for i) amplitude and ii) sense of polarization using the observations of Galactic Centre (GC) are presented in Chapters 2 & 5. However, there are alternate calibration methods as given below may be tried to improve the order of accuracy in both the systems.

    - **GLOSS/GRASP flux Calibration:** The method of calibrating the absolute amplitude flux involve inaccuracies as mentioned in Section 2.9. A calibrated broad-band Noise diode may be used for this purpose. The system may be switched between Noise diode and the antenna to record the noise power with GLOSS/GRASP. Later, the obtained noise power can be converted to the equivalent noise temperature from catalogue (derived using Black body radiation laws).
    - **Calibrating the state of polarization with GRASP:** Section 5.3.3 describes calibrating the GRASP system for sensing the state of polarization using GC observations. This method also involves similar inaccuracies as mentioned above. Added to it, the ionospheric disturbances can also affect those observations. To get rid of the instrumental polarization effects, a strong

source of calibration is crucial. Since there are no strong polarized sources present in our frequency of interest ($<$ 500 MHz), polarized signals from low-Earth altitude satellites, [Weather (137 MHz), Amateur (140−145/425−440 MHz), TV transmission (171 MHz), ISS radio downlinks (140/430 MHz) and many more] which can transmit strong circularly polarized signals may be used to calibrate and to determine the sense of polarization.

7. **Full Stokes Spectropolarimeter:** Using broad band dual polarized antennas such as Cross Log-periodic Dipole Antennas as front-end and back-end with a state of art digital (as mentioned above) cross-correlation receiver, a new correlation specropolarimeter system can be developed to obtain full Stokes (I, Q, U and V) spectropolarimeter.

Statistical studies of radio bursts: Apart from instrumentation, several scientific studies may be planned to understand the physical processes responsible for different types of radio bursts including the relatively unexplored bursts like U Type, J Type, etc. The herring bone structures associated with complex class of bursts may be studied with polarization observations in order to understand them completely. Combining the radio observations (GLOSS, GRASP & GRAPH) with that of data at other wavelengths like white light, EUV, high energy X-rays can shed new light on our understanding of complex plasma phenomenon and the associated emission mechanisms (as briefed in Chapter 3). Since our knowledge of many radio bursts are limited, combined statical estimates and in-situ measurements at other wavelengths can greatly improve our present knowledge about the Solar transients.

Appendix A

Other Results of LPDA

Apart from the main antenna parameters (refer Section 2.5.2.1), the following tables show various impedances and other antenna parameters of designed LPDA at various frequencies.

1.1 Impedances & Other Antenna parameters

Table 1.1 shows the other parameters derived from various field tests and measurements. All of them are obtained from the field pattern measurements and by the laws governing the properties of transmission lines.

Frequency (MHz)	VSWR ($= \frac{V_{max}-V_{min}}{V_{max}+V_{min}}$)	Reflection Coefficient ($\|\Gamma\| = \left\|\frac{Z_L-Z_o}{Z_L+Z_o}\right\|$)	Load Impedance ($\|Z_L\|$)	Input Impedance ($\|Z_{in}(l)\|$)	Efficiency ($\%\eta = 1 - \|\Gamma\|^2$)
1.00	92.31	0.98	4615.53	0.54	4.24
3.50	88.12	0.98	4406.18	0.57	4.44
5.99	136.30	0.99	6815.19	0.37	2.89
8.49	38.36	0.95	1917.98	1.30	9.90
10.98	20.56	0.91	1027.89	2.43	17.69
13.48	18.92	0.90	946.10	2.64	19.07
15.97	20.58	0.91	1029.14	2.43	17.67
18.47	17.75	0.89	887.41	2.82	20.20
20.96	14.36	0.87	717.93	3.48	24.35
23.46	16.17	0.88	808.49	3.09	21.94

Frequency	VSWR	Reflection	Load	Input	Efficiency
(MHz)	$(= \frac{V_{max}-V_{min}}{V_{max}+V_{min}})$	Coefficient $(\lvert\Gamma\rvert = \left\lvert\frac{Z_L-Z_o}{Z_L+Z_o}\right\rvert)$	Impedance $(\lvert Z_L\rvert)$	Impedance $(\lvert Z_{in}(l)\rvert)$	$(\%\eta = 1 - \lvert\Gamma\rvert^2)$
25.95	18.81	0.90	940.55	2.66	19.17
28.45	15.45	0.88	772.71	3.24	22.83
30.94	13.88	0.87	694.19	3.60	25.07
33.44	13.75	0.86	687.44	3.64	25.28
35.93	9.99	0.82	499.69	5.00	33.07
38.43	2.68	0.46	134.10	18.64	79.13
40.92	1.72	0.26	85.81	29.14	93.05
43.42	1.29	0.13	64.73	38.62	98.35
45.91	1.87	0.30	93.59	26.71	90.78
48.41	1.60	0.23	79.89	31.29	94.71
50.90	1.64	0.24	82.15	30.43	94.08
53.40	1.76	0.27	87.81	28.47	92.47
55.89	1.35	0.15	67.26	37.17	97.83
58.39	1.61	0.24	80.73	30.97	94.48
60.88	1.66	0.25	83.14	30.07	93.80
63.38	1.47	0.19	73.34	34.09	96.42
65.87	1.57	0.22	78.56	31.82	95.06
68.37	1.74	0.27	86.82	28.79	92.76
70.86	1.58	0.22	78.76	31.74	95.01
73.36	1.47	0.19	73.36	34.08	96.41
75.85	1.71	0.26	85.71	29.17	93.08
78.35	1.66	0.25	82.84	30.18	93.89
80.84	1.50	0.20	75.07	33.30	95.98
83.34	1.42	0.17	70.95	35.24	97.00
85.83	1.54	0.21	77.14	32.41	95.44
88.33	1.75	0.27	87.26	28.65	92.63
90.82	1.78	0.28	88.81	28.15	92.18
93.32	1.63	0.24	81.40	30.71	94.29
95.81	1.58	0.23	79.15	31.58	94.90
98.31	1.68	0.25	84.03	29.75	93.55
100.80	1.70	0.26	84.95	29.43	93.29
103.30	1.41	0.17	70.55	35.44	97.09
105.79	1.48	0.19	73.87	33.84	96.29
108.29	1.46	0.19	73.11	34.20	96.48
110.78	1.57	0.22	78.62	31.80	95.05
113.28	1.73	0.27	86.74	28.82	92.78
115.77	1.80	0.29	89.86	27.82	91.88

Frequency	VSWR	Reflection	Load	Input	Efficiency
(MHz)	$(= \frac{V_{max}-V_{min}}{V_{max}+V_{min}})$	Coefficient $(\lvert\Gamma\rvert = \left\lvert\frac{Z_L-Z_o}{Z_L+Z_o}\right\rvert)$	Impedance $(\lvert Z_L\rvert)$	Impedance $(\lvert Z_{in}(l)\rvert)$	$(\%\eta = 1 - \lvert\Gamma\rvert^2)$
118.27	1.75	0.27	87.55	28.55	92.55
120.76	1.65	0.25	82.52	30.29	93.98
123.26	1.60	0.23	79.93	31.28	94.69
125.75	1.64	0.24	81.80	30.56	94.18
128.25	1.72	0.27	86.08	29.04	92.97
130.74	1.79	0.28	89.72	27.86	91.92
133.24	1.79	0.28	89.40	27.96	92.01
135.73	1.71	0.26	85.61	29.20	93.10
138.23	1.62	0.24	81.02	30.86	94.40
140.72	1.56	0.22	78.13	32.00	95.18
143.22	1.62	0.24	80.88	30.91	94.43
145.71	1.71	0.26	85.40	29.27	93.16
148.21	1.77	0.28	88.64	28.20	92.23
150.70	1.76	0.28	88.08	28.38	92.40
153.20	1.73	0.27	86.25	28.98	92.92
155.69	1.70	0.26	85.22	29.34	93.22
158.19	1.70	0.26	84.77	29.49	93.34
160.68	1.67	0.25	83.35	29.99	93.74
163.18	1.61	0.23	80.57	31.03	94.52
165.67	1.57	0.22	78.42	31.88	95.10
168.17	1.54	0.21	76.96	32.49	95.49
170.66	1.53	0.21	76.25	32.79	95.68
173.16	1.56	0.22	77.77	32.15	95.28
175.65	1.63	0.24	81.70	30.60	94.21
178.15	1.70	0.26	85.08	29.39	93.26
180.64	1.69	0.26	84.61	29.55	93.39
183.14	1.62	0.24	80.96	30.88	94.41
185.63	1.53	0.21	76.66	32.61	95.57
188.13	1.49	0.20	74.34	33.63	96.17
190.62	1.50	0.20	74.81	33.42	96.05
193.12	1.54	0.21	77.05	32.45	95.47
195.61	1.58	0.22	78.84	31.71	94.99
198.11	1.57	0.22	78.34	31.91	95.12
200.60	1.50	0.20	74.78	33.43	96.06
203.10	1.43	0.18	71.33	35.05	96.91
205.59	1.42	0.17	71.09	35.16	96.97
208.09	1.47	0.19	73.29	34.11	96.43

Frequency	VSWR	Reflection	Load	Input	Efficiency
(MHz)	$(= \frac{V_{max}-V_{min}}{V_{max}+V_{min}})$	Coefficient $(\lvert\Gamma\rvert = \left\lvert\frac{Z_L-Z_o}{Z_L+Z_o}\right\rvert)$	Impedance $(\lvert Z_L\rvert)$	Impedance $(\lvert Z_{in}(l)\rvert)$	$(\%\eta = 1 - \lvert\Gamma\rvert^2)$
210.58	1.50	0.20	74.82	33.41	96.05
213.08	1.49	0.20	74.38	33.61	96.16
215.57	1.45	0.19	72.73	34.37	96.57
218.07	1.41	0.17	70.58	35.42	97.09
220.56	1.37	0.16	68.68	36.40	97.52
223.06	1.38	0.16	69.02	36.22	97.45
225.55	1.45	0.18	72.38	34.54	96.66
228.05	1.54	0.21	76.91	32.51	95.51
230.54	1.60	0.23	79.94	31.27	94.69
233.04	1.59	0.23	79.57	31.42	94.79
235.53	1.54	0.21	77.13	32.41	95.45
238.03	1.50	0.20	75.24	33.23	95.94
240.52	1.51	0.20	75.27	33.21	95.93
243.02	1.53	0.21	76.54	32.66	95.60
245.51	1.55	0.22	77.59	32.22	95.32
248.01	1.54	0.21	77.10	32.42	95.45
250.50	1.51	0.20	75.40	33.16	95.90
253.00	1.49	0.20	74.71	33.46	96.07
255.49	1.52	0.21	76.09	32.86	95.72
257.99	1.59	0.23	79.72	31.36	94.75
260.48	1.68	0.25	83.85	29.82	93.61
262.98	1.71	0.26	85.58	29.21	93.11
265.47	1.67	0.25	83.45	29.96	93.72
267.97	1.58	0.22	78.83	31.71	94.99
270.46	1.50	0.20	75.15	33.27	95.96
272.96	1.52	0.21	75.99	32.90	95.74
275.45	1.61	0.23	80.70	30.98	94.48
277.95	1.69	0.26	84.69	29.52	93.37
280.44	1.71	0.26	85.64	29.19	93.10
282.94	1.65	0.25	82.51	30.30	93.98
285.43	1.53	0.21	76.56	32.65	95.60
287.93	1.44	0.18	71.81	34.81	96.79
290.42	1.46	0.19	73.15	34.18	96.47
292.92	1.61	0.23	80.53	31.05	94.53
295.41	1.78	0.28	89.02	28.08	92.12
297.91	1.88	0.31	94.18	26.54	90.61
300.40	1.87	0.30	93.54	26.73	90.80

Frequency	VSWR	Reflection	Load	Input	Efficiency
(MHz)	$(= \frac{V_{max}-V_{min}}{V_{max}+V_{min}})$	Coefficient $(\lvert\Gamma\rvert = \left\lvert\frac{Z_L-Z_o}{Z_L+Z_o}\right\rvert)$	Impedance $(\lvert Z_L\rvert)$	Impedance $(\lvert Z_{in}(l)\rvert)$	$(\%\eta = 1 - \lvert\Gamma\rvert^2)$
302.90	1.75	0.27	87.53	28.56	92.55
305.39	1.62	0.24	80.92	30.90	94.42
307.89	1.57	0.22	78.51	31.84	95.08
310.38	1.63	0.24	81.67	30.61	94.21
312.88	1.73	0.27	86.74	28.82	92.78
315.37	1.78	0.28	89.04	28.08	92.12
317.87	1.74	0.27	87.14	28.69	92.66
320.36	1.66	0.25	83.25	30.03	93.77
322.86	1.60	0.23	80.18	31.18	94.63
325.35	1.61	0.23	80.39	31.10	94.57
327.85	1.66	0.25	83.03	30.11	93.83
330.34	1.70	0.26	85.13	29.37	93.24
332.84	1.69	0.26	84.51	29.58	93.42
335.33	1.63	0.24	81.41	30.71	94.29
337.83	1.56	0.22	77.94	32.08	95.23
340.32	1.54	0.21	76.93	32.50	95.50
342.82	1.59	0.23	79.37	31.50	94.84
345.31	1.65	0.25	82.47	30.31	93.99
347.81	1.66	0.25	82.97	30.13	93.85
350.30	1.60	0.23	80.14	31.19	94.64
352.80	1.52	0.21	76.17	32.82	95.70
355.29	1.51	0.20	75.37	33.17	95.91
357.79	1.61	0.23	80.51	31.05	94.53
360.28	1.76	0.28	88.21	28.34	92.36
362.78	1.87	0.30	93.72	26.68	90.75
365.27	1.88	0.31	94.17	26.55	90.61
367.77	1.79	0.28	89.34	27.98	92.03
370.26	1.63	0.24	81.73	30.59	94.20
372.76	1.51	0.20	75.72	33.02	95.81
375.25	1.49	0.20	74.43	33.59	96.14
377.75	1.55	0.22	77.67	32.19	95.30
380.24	1.64	0.24	81.93	30.51	94.14
382.74	1.69	0.26	84.30	29.66	93.48
385.23	1.69	0.26	84.51	29.58	93.42
387.73	1.66	0.25	83.16	30.06	93.80
390.22	1.63	0.24	81.55	30.66	94.25
392.72	1.61	0.24	80.72	30.97	94.48

Frequency	VSWR	Reflection	Load	Input	Efficiency
(MHz)	$(= \frac{V_{max}-V_{min}}{V_{max}+V_{min}})$	Coefficient $(\lvert\Gamma\rvert = \left\lvert\frac{Z_L-Z_o}{Z_L+Z_o}\right\rvert)$	Impedance $(\lvert Z_L\rvert)$	Impedance $(\lvert Z_{in}(l)\rvert)$	$(\%\eta = 1 - \lvert\Gamma\rvert^2)$
395.21	1.61	0.23	80.43	31.08	94.56
397.71	1.59	0.23	79.54	31.43	94.80
400.20	1.56	0.22	77.96	32.07	95.22
402.70	1.55	0.22	77.46	32.27	95.36
405.19	1.59	0.23	79.73	31.36	94.75
407.69	1.70	0.26	84.84	29.47	93.32
410.18	1.82	0.29	90.85	27.52	91.59
412.68	1.88	0.31	94.03	26.59	90.65
415.17	1.86	0.30	93.20	26.82	90.90
417.67	1.79	0.28	89.26	28.01	92.05
420.16	1.70	0.26	84.82	29.47	93.33
422.66	1.67	0.25	83.58	29.91	93.68
425.15	1.73	0.27	86.65	28.85	92.81
427.65	1.83	0.29	91.49	27.33	91.40
430.14	1.90	0.31	94.95	26.33	90.38
432.64	1.90	0.31	95.17	26.27	90.32
435.13	1.85	0.30	92.45	27.04	91.12
437.63	1.78	0.28	89.05	28.07	92.11
440.12	1.75	0.27	87.40	28.60	92.59
442.62	1.77	0.28	88.35	28.30	92.32
445.11	1.81	0.29	90.37	27.66	91.73
447.61	1.83	0.29	91.49	27.33	91.40
450.10	1.81	0.29	90.60	27.60	91.66
452.60	1.77	0.28	88.66	28.20	92.23
455.09	1.77	0.28	88.64	28.20	92.23
457.59	1.83	0.29	91.56	27.31	91.38
460.08	1.92	0.32	96.01	26.04	90.07
462.58	1.99	0.33	99.54	25.12	89.03
465.07	1.99	0.33	99.44	25.14	89.06
467.57	1.93	0.32	96.73	25.85	89.86
470.06	1.89	0.31	94.56	26.44	90.50
472.56	1.91	0.31	95.53	26.17	90.21
475.05	1.99	0.33	99.50	25.12	89.04
477.55	2.08	0.35	103.79	24.09	87.77
480.04	2.07	0.35	103.60	24.13	87.82
482.54	1.95	0.32	97.54	25.63	89.62
485.03	1.79	0.28	89.49	27.94	91.99

Frequency (MHz)	VSWR ($= \frac{V_{max}-V_{min}}{V_{max}+V_{min}}$)	Reflection Coefficient ($\lvert\Gamma\rvert = \left\lvert\frac{Z_L-Z_o}{Z_L+Z_o}\right\rvert$)	Load Impedance ($\lvert Z_L\rvert$)	Input Impedance ($\lvert Z_{in}(l)\rvert$)	Efficiency ($\%\eta = 1-\lvert\Gamma\rvert^2$)
487.53	1.72	0.26	85.96	29.08	93.00
490.02	1.81	0.29	90.61	27.59	91.66
492.52	1.99	0.33	99.72	25.07	88.97
495.01	2.11	0.36	105.45	23.71	87.28
497.51	2.06	0.35	103.24	24.21	87.93
500.00	1.87	0.30	93.71	26.68	90.75

1.2 E & H-Plane Directive Gain measurement (Gain with two identical antennas)

Directive Gain of an antenna along the two principal planes (viz. E-Plane & H-plane) are measured using identical antennas: one functions as a transmitter, the other as the receiver antenna. Friss-Transmission formula in communications governed by two such antennas is given as

$$\frac{P_r}{P_t} = \left(\frac{\lambda}{4\pi R}\right)^2 G_r G_t \tag{A.1}$$

where P_r, P_t are the received and transmitted powers, G_r, G_t are the antenna directive gain of receiver & transmitter, R is the far-field distance and λ is the observing wavelength (in meters) respectively. Under the condition of identical antennas, $G_r \approx G_t \approx G$, where G is the equivalent directive gain of both antennas. Using this condition in Equation (A.1), we get the directive gain of the test antenna as

$$G = \frac{4\pi R}{\lambda}\sqrt{\frac{P_r}{P_t}} \tag{A.2}$$

From the far field measurements P_r, P_t are determined for both the principal planes.

Here far-field measurement distance is R = 90 m (refer Section 2.5.2). The directive gain thus obtained over both planes are tabulated in Table 1.2. E_{tx0}, H_{tx0}, E_{rx0}, and H_{rx0} are the powers at transmitter and receiver sides along 0° orientation (Line of Sight) of both planes.

Table 1.2: Tabulated values of Directive gains obtained from the E & H-plane radiation pattern measurements.

Frequency (MHz)	Lambda ($\lambda = \frac{300}{F(MHz)}$)m	H_{tx0} dBm	H_{rx0} dBm	Directive Gain $= \frac{4\pi R}{\lambda}\sqrt{\frac{H_{rx0}}{H_{tx0}}}$ (G_{DH} dB)	E_{tx0} dBm	E_{rx0} dBm	Directive Gain $= \frac{4\pi R}{\lambda}\sqrt{\frac{E_{rx0}}{E_{tx0}}}$ (G_{DE} dB)
40.05	7.49	0.82	-45.62	-1.43	0.30	-45.12	-0.92
41.14	7.29	0.69	-44.87	-0.88	0.37	-44.42	-0.49
42.22	7.11	0.85	-44.12	-0.47	0.46	-43.98	-0.20
43.31	6.93	0.56	-44.45	-0.38	0.47	-44.06	-0.13
44.39	6.76	0.91	-44.95	-0.70	0.52	-43.55	0.20
45.48	6.60	0.59	-45.08	-0.50	0.36	-43.76	0.28
46.56	6.44	0.62	-45.27	-0.50	0.34	-43.76	0.40
47.65	6.30	0.62	-45.36	-0.45	0.55	-43.70	0.42
48.73	6.16	0.54	-45.41	-0.34	0.14	-43.25	0.95
49.82	6.02	0.42	-45.72	-0.34	0.25	-43.74	0.74
50.90	5.89	0.56	-45.66	-0.28	0.27	-43.69	0.85
51.98	5.77	0.60	-45.68	-0.22	0.52	-44.10	0.61
53.07	5.65	0.68	-45.57	-0.12	0.22	-44.34	0.73
54.15	5.54	0.46	-45.72	0.01	0.22	-43.75	1.12
55.24	5.43	0.69	-45.77	-0.05	0.49	-43.90	0.99
56.32	5.33	0.58	-46.08	-0.06	0.41	-43.96	1.09
57.41	5.23	0.45	-46.78	-0.26	0.25	-44.00	1.23
58.49	5.13	0.49	-46.87	-0.25	0.59	-44.45	0.92
59.58	5.04	0.44	-46.87	-0.14	0.16	-44.46	1.21
60.66	4.95	0.55	-46.89	-0.13	0.40	-44.53	1.13
61.75	4.86	0.54	-46.80	0.00	0.27	-44.33	1.37
62.83	4.77	0.58	-47.05	-0.07	0.41	-43.89	1.60
63.92	4.69	0.63	-47.16	-0.08	0.42	-43.75	1.74
65.00	4.62	0.47	-47.23	0.04	0.44	-43.76	1.79
66.09	4.54	0.44	-47.05	0.22	0.08	-43.58	2.14
67.17	4.47	0.59	-47.17	0.15	0.12	-43.74	2.11
68.26	4.40	0.55	-47.52	0.07	0.24	-44.10	1.94
69.34	4.33	0.46	-47.43	0.23	0.13	-44.17	2.02

Frequency	Lambda	H_{tx0}	H_{rx0}	Directive Gain	E_{tx0}	E_{rx0}	Directive Gain
(MHz)	($\lambda = \frac{300}{F(MHz)}$)m	dBm	dBm	$= \frac{4\pi R}{\lambda}\sqrt{\frac{H_{rx0}}{H_{tx0}}}$ (G_{DH} dB)	dBm	dBm	$= \frac{4\pi R}{\lambda}\sqrt{\frac{E_{rx0}}{E_{tx0}}}$ (G_{DE} dB)
70.43	4.26	0.40	-47.45	0.31	0.25	-43.94	2.15
71.51	4.20	0.32	-47.44	0.42	0.24	-43.73	2.32
72.60	4.13	0.37	-47.93	0.22	0.26	-43.59	2.45
73.68	4.07	0.52	-49.11	-0.38	0.22	-44.47	2.09
74.77	4.01	0.32	-49.97	-0.65	0.05	-45.94	1.51
75.85	3.96	0.38	-48.36	0.19	0.05	-44.37	2.35
76.93	3.90	0.41	-48.07	0.38	0.30	-43.86	2.55
78.02	3.85	0.40	-47.97	0.50	0.00	-44.03	2.67
79.10	3.79	0.31	-48.13	0.52	-0.01	-44.76	2.37
80.19	3.74	0.60	-47.89	0.56	0.18	-44.73	2.35
81.27	3.69	0.48	-47.51	0.87	0.07	-44.57	2.54
82.36	3.64	0.49	-47.24	1.05	0.28	-44.79	2.39
83.44	3.60	0.52	-46.79	1.32	0.31	-44.05	2.80
84.53	3.55	0.49	-46.35	1.61	0.18	-43.97	2.96
85.61	3.50	0.36	-46.45	1.68	0.03	-44.24	2.96
86.70	3.46	0.34	-46.61	1.67	0.12	-43.85	3.16
87.78	3.42	0.14	-47.21	1.52	-0.05	-44.05	3.20
88.87	3.38	0.14	-47.55	1.40	0.19	-44.22	3.05
89.95	3.34	0.20	-47.66	1.37	0.40	-43.75	3.23
91.04	3.30	0.40	-47.67	1.32	0.25	-43.68	3.39
92.12	3.26	0.44	-48.04	1.16	-0.03	-43.59	3.63
93.21	3.22	0.25	-48.19	1.24	-0.13	-43.62	3.71
94.29	3.18	0.51	-48.37	1.07	0.37	-43.77	3.44
95.38	3.15	0.35	-48.48	1.14	0.23	-43.91	3.49
96.46	3.11	0.12	-48.79	1.15	0.27	-44.30	3.32
97.55	3.08	0.42	-49.04	0.92	0.36	-44.80	3.08
98.63	3.04	0.15	-49.16	1.05	0.31	-44.88	3.11
99.72	3.01	0.18	-49.44	0.94	0.16	-45.64	2.85
100.80	2.98	0.29	-49.84	0.73	0.20	-46.19	2.60
101.88	2.94	0.27	-51.03	0.19	0.15	-47.91	1.82
102.97	2.91	0.20	-50.08	0.75	0.24	-49.02	1.26
104.05	2.88	0.31	-48.73	1.41	0.25	-46.25	2.69
105.14	2.85	0.26	-48.26	1.72	0.06	-45.02	3.44
106.22	2.82	0.23	-47.89	1.96	0.20	-45.80	3.03
107.31	2.80	-0.08	-47.97	2.12	0.02	-45.51	3.31
108.39	2.77	0.22	-47.63	2.19	0.34	-45.18	3.36
109.48	2.74	0.11	-47.92	2.14	0.18	-44.52	3.81

Frequency	Lambda	H_{tx0}	H_{rx0}	Directive Gain	E_{tx0}	E_{rx0}	Directive Gain
(MHz)	($\lambda = \frac{300}{F(MHz)}$)m	dBm	dBm	$= \frac{4\pi R}{\lambda}\sqrt{\frac{H_{rx0}}{H_{tx0}}}$ (G_{DH} dB)	dBm	dBm	$= \frac{4\pi R}{\lambda}\sqrt{\frac{E_{rx0}}{E_{tx0}}}$ (G_{DE} dB)
110.56	2.71	0.20	-48.29	1.95	0.06	-44.25	4.05
111.65	2.69	0.29	-49.12	1.53	0.04	-45.02	3.71
112.73	2.66	0.14	-49.57	1.43	0.18	-45.95	3.22
113.82	2.64	0.22	-49.52	1.45	-0.12	-45.92	3.43
114.90	2.61	-0.08	-49.71	1.55	-0.02	-45.87	3.44
115.99	2.59	0.07	-49.08	1.83	0.05	-45.82	3.47
117.07	2.56	0.12	-49.24	1.77	0.05	-45.86	3.49
118.16	2.54	0.14	-49.35	1.74	-0.10	-46.00	3.54
119.24	2.52	0.05	-49.88	1.56	-0.14	-46.17	3.51
120.33	2.49	0.23	-50.09	1.40	-0.23	-46.23	3.57
121.41	2.47	0.05	-50.40	1.38	-0.26	-46.52	3.48
122.50	2.45	0.09	-50.90	1.15	-0.17	-45.71	3.88
123.58	2.43	0.11	-50.48	1.39	-0.15	-46.14	3.69
124.67	2.41	-0.09	-50.04	1.74	-0.06	-46.34	3.58
125.75	2.39	-0.10	-49.80	1.91	-0.12	-46.68	3.48
126.83	2.37	-0.08	-49.72	1.97	-0.11	-47.72	2.99
127.92	2.35	-0.27	-49.28	2.33	-0.28	-47.62	3.16
129.00	2.33	-0.26	-49.08	2.46	-0.36	-47.63	3.24
130.09	2.31	-0.15	-48.90	2.53	-0.09	-47.41	3.25
131.17	2.29	-0.31	-48.54	2.82	-0.16	-46.79	3.63
132.26	2.27	-0.25	-48.41	2.90	-0.14	-46.65	3.72
133.34	2.25	-0.32	-47.85	3.25	-0.53	-45.87	4.34
134.43	2.23	-0.29	-47.73	3.33	-0.57	-45.49	4.59
135.51	2.21	-0.56	-47.89	3.42	-0.56	-46.07	4.33
136.60	2.20	-0.18	-48.41	3.00	-0.50	-45.36	4.69
137.68	2.18	-0.41	-48.85	2.93	-0.27	-45.42	4.58
138.77	2.16	-0.11	-49.03	2.72	-0.37	-45.51	4.62
139.85	2.15	-0.32	-49.11	2.82	-0.23	-45.11	4.78
140.94	2.13	-0.10	-49.65	2.48	-0.29	-44.84	4.98
142.02	2.11	-0.30	-50.16	2.35	-0.37	-45.18	4.88
143.11	2.10	-0.44	-50.18	2.45	-0.46	-45.95	4.58
144.19	2.08	-0.37	-50.10	2.49	-0.58	-46.76	4.26
145.28	2.07	-0.52	-50.26	2.51	-0.33	-46.88	4.11
146.36	2.05	-0.30	-50.09	2.52	-0.57	-47.48	3.96
147.45	2.03	-0.28	-49.41	2.88	-0.60	-47.89	3.81
148.53	2.02	-0.41	-49.19	3.09	-0.51	-48.16	3.66
149.62	2.01	-0.46	-48.78	3.35	-0.59	-47.68	3.97

Frequency	Lambda	H_{tx0}	H_{rx0}	Directive Gain	E_{tx0}	E_{rx0}	Directive Gain
(MHz)	($\lambda = \frac{300}{F(MHz)}$)m	dBm	dBm	$= \frac{4\pi R}{\lambda}\sqrt{\frac{H_{rx0}}{H_{tx0}}}$ (G_{DH} dB)	dBm	dBm	$= \frac{4\pi R}{\lambda}\sqrt{\frac{E_{rx0}}{E_{tx0}}}$ (G_{DE} dB)
150.70	1.99	-0.37	-48.49	3.48	-0.60	-47.17	4.26
151.78	1.98	-0.34	-48.30	3.59	-0.46	-46.77	4.42
152.87	1.96	-0.45	-48.21	3.72	-0.42	-46.14	4.75
153.95	1.95	-0.39	-48.44	3.61	-0.68	-46.06	4.95
155.04	1.93	-0.65	-48.61	3.69	-0.57	-45.93	4.99
156.12	1.92	-0.77	-49.20	3.48	-0.52	-46.92	4.50
157.21	1.91	-0.58	-49.72	3.16	-0.85	-47.25	4.53
158.29	1.90	-0.57	-49.27	3.41	-0.66	-47.06	4.56
159.38	1.88	-0.46	-49.10	3.47	-0.52	-47.60	4.25
160.46	1.87	-0.58	-49.30	3.45	-0.68	-47.08	4.62
161.55	1.86	-0.83	-50.16	3.18	-0.68	-46.86	4.76
162.63	1.84	-0.91	-51.17	2.74	-0.75	-47.01	4.75
163.72	1.83	-0.96	-51.44	2.66	-0.72	-46.91	4.81
164.80	1.82	-1.09	-51.12	2.92	-0.88	-46.96	4.89
165.89	1.81	-0.78	-50.66	3.02	-0.64	-46.57	5.00
166.97	1.80	-0.94	-49.71	3.60	-0.45	-46.89	4.77
168.06	1.79	-1.02	-48.75	4.15	-0.67	-47.09	4.81
169.14	1.77	-0.76	-48.21	4.32	-0.60	-47.35	4.67
170.23	1.76	-0.87	-48.28	4.37	-0.44	-47.32	4.64
171.31	1.75	-1.07	-48.76	4.25	-0.80	-47.14	4.93
172.40	1.74	-1.06	-48.77	4.27	-0.66	-47.62	4.65
173.48	1.73	-0.89	-49.14	4.03	-0.73	-47.24	4.90
174.57	1.72	-1.14	-49.45	4.03	-0.88	-47.05	5.10
175.65	1.71	-0.93	-49.60	3.87	-0.89	-47.26	5.03
176.73	1.70	-1.07	-49.86	3.84	-1.01	-47.45	5.02
177.82	1.69	-1.07	-49.52	4.04	-1.03	-46.59	5.48
178.90	1.68	-1.04	-49.77	3.92	-1.20	-47.43	5.18
179.99	1.67	-0.94	-50.37	3.60	-1.21	-47.77	5.04
181.07	1.66	-1.18	-51.21	3.32	-1.00	-48.02	4.83
182.16	1.65	-1.27	-52.02	2.99	-1.13	-48.50	4.68
183.24	1.64	-1.51	-52.35	2.97	-1.31	-48.22	4.94
184.33	1.63	-1.40	-51.72	3.26	-1.30	-48.53	4.81
185.41	1.62	-1.47	-50.70	3.83	-1.27	-48.67	4.75
186.50	1.61	-1.19	-49.81	4.16	-1.27	-48.62	4.80
187.58	1.60	-1.27	-49.25	4.50	-1.46	-49.00	4.73
188.67	1.59	-1.31	-48.79	4.78	-1.46	-49.16	4.67
189.75	1.58	-1.40	-48.84	4.82	-1.52	-48.91	4.85

Frequency	Lambda	H_{tx0}	H_{rx0}	Directive Gain	E_{tx0}	E_{rx0}	Directive Gain
(MHz)	$(\lambda = \frac{300}{F(MHz)})$m	dBm	dBm	$=\frac{4\pi R}{\lambda}\sqrt{\frac{H_{rx0}}{H_{tx0}}}$ (G_{DH} dB)	dBm	dBm	$=\frac{4\pi R}{\lambda}\sqrt{\frac{E_{rx0}}{E_{tx0}}}$ (G_{DE} dB)
190.84	1.57	-1.47	-49.40	4.60	-1.55	-49.06	4.82
191.92	1.56	-1.55	-49.84	4.45	-1.56	-48.10	5.33
193.01	1.55	-2.05	-50.61	4.34	-1.66	-47.85	5.53
194.09	1.55	-1.64	-51.42	3.75	-1.67	-47.48	5.74
195.18	1.54	-1.54	-52.01	3.43	-1.66	-47.92	5.54
196.26	1.53	-1.53	-51.47	3.72	-1.66	-48.18	5.43
197.35	1.52	-1.33	-50.84	3.96	-1.96	-48.38	5.51
198.43	1.51	-1.53	-50.41	4.30	-1.67	-47.85	5.65
199.52	1.50	-1.68	-50.17	4.52	-1.95	-47.80	5.84
200.60	1.50	-1.66	-50.30	4.46	-2.08	-48.03	5.81
201.68	1.49	-1.79	-50.07	4.67	-2.04	-47.93	5.87
202.77	1.48	-1.74	-49.88	4.76	-1.90	-48.42	5.58
203.85	1.47	-1.76	-50.03	4.72	-2.05	-48.62	5.57
204.94	1.46	-1.68	-50.10	4.67	-1.92	-48.89	5.40
206.02	1.46	-1.71	-50.24	4.64	-2.05	-48.77	5.54
207.11	1.45	-2.09	-50.63	4.65	-2.01	-49.38	5.24
208.19	1.44	-2.07	-50.43	4.77	-2.00	-49.14	5.38
209.28	1.43	-2.03	-50.51	4.73	-1.79	-48.56	5.59
210.36	1.43	-2.10	-50.74	4.67	-2.15	-48.55	5.79
211.45	1.42	-2.14	-51.13	4.52	-1.96	-48.35	5.82
212.53	1.41	-2.23	-51.44	4.43	-1.83	-48.94	5.48
213.62	1.40	-2.19	-51.92	4.19	-2.17	-49.12	5.59
214.70	1.40	-2.17	-51.85	4.24	-2.11	-49.60	5.34
215.79	1.39	-1.94	-51.49	4.33	-1.68	-49.27	5.31
216.87	1.38	-1.99	-51.72	4.26	-2.02	-48.80	5.74
217.96	1.38	-2.16	-51.85	4.30	-1.77	-49.25	5.41
219.04	1.37	-2.09	-51.90	4.26	-1.82	-49.62	5.27
220.13	1.36	-2.29	-51.65	4.51	-1.90	-49.13	5.58
221.21	1.36	-2.23	-51.35	4.65	-2.18	-49.14	5.73
222.30	1.35	-2.14	-50.40	5.10	-1.99	-48.95	5.75
223.38	1.34	-2.20	-49.87	5.42	-1.89	-48.96	5.72
224.47	1.34	-2.24	-49.83	5.48	-1.83	-49.42	5.48
225.55	1.33	-2.08	-49.90	5.38	-1.96	-49.31	5.62
226.63	1.32	-2.46	-49.88	5.60	-1.97	-50.30	5.15
227.72	1.32	-2.49	-49.83	5.67	-2.02	-49.63	5.53
228.80	1.31	-2.75	-50.13	5.67	-2.00	-49.83	5.44
229.89	1.30	-2.80	-50.32	5.62	-2.25	-48.52	6.25

Frequency	Lambda	H_{tx0}	H_{rx0}	Directive Gain	E_{tx0}	E_{rx0}	Directive Gain
(MHz)	($\lambda = \frac{300}{F(MHz)}$)m	dBm	dBm	$= \frac{4\pi R}{\lambda}\sqrt{\frac{H_{rx0}}{H_{tx0}}}$ (G_{DH} dB)	dBm	dBm	$= \frac{4\pi R}{\lambda}\sqrt{\frac{E_{rx0}}{E_{tx0}}}$ (G_{DE} dB)
230.97	1.30	-2.89	-50.65	5.52	-2.20	-49.30	5.85
232.06	1.29	-2.70	-51.11	5.21	-2.20	-48.98	6.03
233.14	1.29	-2.51	-51.48	4.95	-2.22	-49.25	5.93
234.23	1.28	-2.66	-51.65	4.96	-2.19	-49.65	5.73
235.31	1.27	-2.83	-52.39	4.70	-2.43	-49.66	5.87
236.40	1.27	-2.45	-52.70	4.37	-2.31	-50.10	5.61
237.48	1.26	-2.57	-53.27	4.17	-2.43	-50.27	5.60
238.57	1.26	-2.85	-53.17	4.38	-2.68	-50.67	5.55
239.65	1.25	-2.79	-52.92	4.49	-2.38	-50.58	5.46
240.74	1.25	-2.69	-52.66	4.59	-2.44	-50.30	5.65
241.82	1.24	-2.69	-52.32	4.78	-2.60	-50.84	5.48
242.91	1.24	-3.03	-52.30	4.98	-2.94	-50.89	5.64
243.99	1.23	-2.65	-51.97	4.97	-2.58	-51.20	5.33
245.08	1.22	-2.75	-51.53	5.26	-2.66	-51.51	5.23
246.16	1.22	-2.86	-51.63	5.29	-2.67	-51.61	5.21
247.25	1.21	-2.82	-51.53	5.34	-2.83	-51.30	5.46
248.33	1.21	-2.76	-51.38	5.40	-2.87	-50.78	5.76
249.42	1.20	-3.01	-52.01	5.23	-2.95	-50.72	5.85
250.50	1.20	-2.87	-52.11	5.13	-2.89	-51.09	5.65
251.58	1.19	-3.08	-52.86	4.88	-2.95	-50.90	5.80
252.67	1.19	-2.99	-52.97	4.80	-2.84	-51.20	5.61
253.75	1.18	-2.91	-53.19	4.67	-2.86	-51.33	5.57
254.84	1.18	-2.98	-53.42	4.60	-3.01	-51.40	5.63
255.92	1.17	-3.03	-53.86	4.43	-2.74	-50.92	5.76
257.01	1.17	-3.19	-53.86	4.53	-3.17	-51.41	5.74
258.09	1.16	-3.05	-53.67	4.57	-2.93	-51.21	5.74
259.18	1.16	-3.18	-53.31	4.83	-2.91	-51.91	5.40
260.26	1.15	-3.33	-52.96	5.10	-3.20	-51.35	5.84
261.35	1.15	-3.25	-52.39	5.36	-3.20	-51.13	5.97
262.43	1.14	-3.01	-52.44	5.24	-2.86	-50.82	5.98
263.52	1.14	-3.20	-52.29	5.42	-2.95	-50.98	5.96
264.60	1.13	-3.28	-52.48	5.39	-2.97	-51.69	5.63
265.69	1.13	-3.09	-52.05	5.52	-2.99	-51.21	5.90
266.77	1.12	-3.37	-51.90	5.76	-2.91	-50.80	6.08
267.86	1.12	-3.25	-51.91	5.71	-2.90	-50.60	6.19
268.94	1.12	-3.37	-52.19	5.65	-2.96	-50.95	6.07
270.03	1.11	-3.38	-52.40	5.57	-3.01	-51.38	5.89

Frequency	Lambda	H_{tx0}	H_{rx0}	Directive Gain	E_{tx0}	E_{rx0}	Directive Gain
(MHz)	($\lambda = \frac{300}{F(MHz)}$)m	dBm	dBm	$= \frac{4\pi R}{\lambda}\sqrt{\frac{H_{rx0}}{H_{tx0}}}$ (G_{DH} dB)	dBm	dBm	$= \frac{4\pi R}{\lambda}\sqrt{\frac{E_{rx0}}{E_{tx0}}}$ (G_{DE} dB)
271.11	1.11	-3.51	-52.00	5.85	-3.25	-51.24	6.10
272.20	1.10	-3.31	-51.40	6.06	-3.23	-51.41	6.02
273.28	1.10	-3.45	-51.47	6.12	-3.19	-51.14	6.16
274.37	1.09	-3.39	-52.25	5.71	-3.20	-51.63	5.93
275.45	1.09	-3.50	-52.54	5.64	-3.01	-51.93	5.71
276.53	1.08	-3.55	-53.34	5.28	-3.03	-51.95	5.72
277.62	1.08	-3.42	-53.73	5.04	-3.13	-52.32	5.60
278.70	1.08	-3.54	-53.94	5.01	-3.45	-52.39	5.75
279.79	1.07	-3.33	-53.97	4.91	-3.30	-51.96	5.90
280.87	1.07	-3.45	-54.30	4.82	-3.18	-51.83	5.93
281.96	1.06	-3.41	-54.11	4.91	-3.18	-52.17	5.77
283.04	1.06	-3.50	-54.32	4.87	-3.21	-52.15	5.81
284.13	1.06	-3.64	-54.45	4.89	-3.38	-52.73	5.63
285.21	1.05	-3.47	-54.52	4.79	-3.48	-52.49	5.81
286.30	1.05	-3.43	-54.61	4.74	-3.39	-52.48	5.79
287.38	1.04	-3.58	-53.89	5.19	-3.39	-52.22	5.93
288.47	1.04	-3.68	-53.37	5.52	-3.34	-52.64	5.72
289.55	1.04	-3.63	-52.64	5.87	-3.26	-52.30	5.86
290.64	1.03	-3.96	-52.20	6.27	-3.27	-52.22	5.92
291.72	1.03	-3.71	-51.51	6.51	-3.55	-51.85	6.26
292.81	1.02	-3.95	-51.44	6.68	-3.63	-51.71	6.39
293.89	1.02	-3.67	-51.60	6.48	-3.45	-51.74	6.30
294.98	1.02	-3.72	-52.37	6.13	-3.58	-51.65	6.43
296.06	1.01	-3.77	-52.58	6.07	-3.50	-51.69	6.38
297.15	1.01	-3.73	-53.10	5.81	-3.46	-51.94	6.25
298.23	1.01	-3.70	-53.62	5.55	-3.47	-51.56	6.47
299.32	1.00	-3.83	-54.13	5.37	-3.75	-51.86	6.47
300.40	1.00	-3.75	-54.77	5.03	-3.50	-52.03	6.28
301.48	1.00	-3.85	-55.02	4.97	-3.42	-52.26	6.14
302.57	0.99	-3.90	-54.69	5.17	-3.42	-52.75	5.91
303.65	0.99	-3.83	-54.37	5.31	-3.25	-53.16	5.63
304.74	0.98	-4.05	-53.55	5.85	-3.46	-52.58	6.04
305.82	0.98	-3.96	-53.39	5.90	-3.37	-52.50	6.05
306.91	0.98	-4.03	-53.10	6.10	-3.53	-52.69	6.06
307.99	0.97	-4.03	-52.60	6.36	-3.60	-52.47	6.22
309.08	0.97	-4.10	-52.52	6.45	-3.36	-52.49	6.10
310.16	0.97	-4.04	-52.59	6.40	-3.47	-52.35	6.24

Frequency	Lambda	H_{tx0}	H_{rx0}	Directive Gain	E_{tx0}	E_{rx0}	Directive Gain
(MHz)	($\lambda = \frac{300}{F(MHz)}$)m	dBm	dBm	$= \frac{4\pi R}{\lambda}\sqrt{\frac{H_{rx0}}{H_{tx0}}}$ (G_{DH} dB)	dBm	dBm	$= \frac{4\pi R}{\lambda}\sqrt{\frac{E_{rx0}}{E_{tx0}}}$ (G_{DE} dB)
311.25	0.96	-4.17	-52.93	6.31	-3.33	-51.89	6.42
312.33	0.96	-4.09	-53.17	6.17	-3.31	-52.04	6.35
313.42	0.96	-4.10	-53.55	6.00	-3.20	-52.39	6.13
314.50	0.95	-3.98	-54.03	5.71	-3.74	-52.66	6.28
315.59	0.95	-3.99	-53.76	5.87	-3.32	-52.08	6.38
316.67	0.95	-3.96	-53.86	5.82	-3.42	-52.69	6.14
317.76	0.94	-3.95	-53.51	6.00	-3.34	-52.59	6.16
318.84	0.94	-3.81	-53.43	5.99	-3.34	-52.98	5.98
319.93	0.94	-3.87	-53.51	5.99	-3.62	-53.12	6.07
321.01	0.93	-4.02	-53.81	5.93	-3.59	-53.64	5.81
322.10	0.93	-4.03	-53.91	5.90	-3.12	-53.29	5.76
323.18	0.93	-3.96	-54.22	5.73	-3.58	-53.52	5.89
324.27	0.93	-4.02	-54.55	5.61	-3.24	-53.18	5.90
325.35	0.92	-3.98	-55.31	5.22	-3.33	-53.34	5.88
326.43	0.92	-3.86	-55.25	5.20	-3.44	-53.25	6.00
327.52	0.92	-3.76	-55.15	5.22	-3.45	-53.49	5.90
328.60	0.91	-4.34	-55.10	5.55	-3.42	-53.18	6.05
329.69	0.91	-3.97	-54.94	5.46	-3.59	-53.22	6.13
330.77	0.91	-4.07	-54.88	5.55	-3.45	-53.04	6.17
331.86	0.90	-3.95	-54.81	5.54	-3.55	-53.39	6.05
332.94	0.90	-4.12	-54.69	5.70	-3.63	-53.51	6.05
334.03	0.90	-3.84	-54.10	5.87	-3.63	-52.84	6.40
335.11	0.90	-4.02	-53.74	6.15	-3.78	-52.84	6.49
336.20	0.89	-3.81	-53.52	6.17	-3.79	-53.30	6.28
337.28	0.89	-3.78	-53.66	6.10	-3.83	-53.54	6.19
338.37	0.89	-3.75	-53.36	6.25	-3.53	-53.10	6.27
339.45	0.88	-3.99	-53.56	6.28	-3.73	-52.85	6.51
340.54	0.88	-3.69	-53.43	6.21	-3.78	-53.67	6.14
341.62	0.88	-3.86	-53.98	6.04	-3.64	-52.99	6.43
342.71	0.88	-3.93	-53.95	6.10	-3.64	-53.54	6.16
343.79	0.87	-3.71	-54.01	5.97	-3.86	-53.20	6.46
344.88	0.87	-3.58	-54.45	5.70	-3.84	-53.40	6.36
345.96	0.87	-3.94	-54.48	5.88	-3.66	-53.81	6.08
347.05	0.86	-3.90	-54.79	5.72	-3.77	-53.46	6.32
348.13	0.86	-4.01	-54.98	5.69	-3.44	-53.54	6.13
349.22	0.86	-3.94	-55.59	5.37	-3.73	-53.89	6.12
350.30	0.86	-3.83	-56.20	5.02	-3.68	-54.45	5.82

Frequency	Lambda	H_{tx0}	H_{rx0}	Directive Gain	E_{tx0}	E_{rx0}	Directive Gain
(MHz)	($\lambda = \frac{300}{F(MHz)}$)m	dBm	dBm	$= \frac{4\pi R}{\lambda}\sqrt{\frac{H_{rx0}}{H_{tx0}}}$ (G_{DH} dB)	dBm	dBm	$= \frac{4\pi R}{\lambda}\sqrt{\frac{E_{rx0}}{E_{tx0}}}$ (G_{DE} dB)
351.38	0.85	-3.99	-56.65	4.89	-3.54	-54.39	5.80
352.47	0.85	-3.72	-56.40	4.89	-3.72	-54.27	5.96
353.55	0.85	-3.72	-55.81	5.20	-3.49	-54.36	5.81
354.64	0.85	-3.89	-55.12	5.64	-3.52	-54.46	5.79
355.72	0.84	-3.60	-54.43	5.86	-3.45	-54.12	5.94
356.81	0.84	-3.76	-54.45	5.94	-3.69	-54.12	6.07
357.89	0.84	-3.61	-54.51	5.85	-3.49	-54.16	5.97
358.98	0.84	-3.65	-54.41	5.93	-3.29	-54.55	5.69
360.06	0.83	-3.82	-54.65	5.91	-3.51	-54.43	5.87
361.15	0.83	-3.80	-54.56	5.96	-3.31	-54.43	5.78
362.23	0.83	-3.70	-54.69	5.86	-3.44	-53.83	6.16
363.32	0.83	-3.56	-54.82	5.73	-3.42	-54.00	6.08
364.40	0.82	-3.85	-55.17	5.72	-3.41	-54.23	5.97
365.49	0.82	-3.57	-55.13	5.61	-3.40	-54.23	5.98
366.57	0.82	-3.72	-55.31	5.61	-3.35	-54.07	6.05
367.66	0.82	-3.79	-55.62	5.50	-3.48	-53.86	6.23
368.74	0.81	-3.74	-55.83	5.38	-3.36	-53.86	6.18
369.83	0.81	-3.53	-56.39	5.01	-3.33	-54.56	5.83
370.91	0.81	-3.62	-56.62	4.95	-3.35	-55.05	5.61
372.00	0.81	-3.38	-55.99	5.16	-3.10	-54.66	5.69
373.08	0.80	-3.39	-55.64	5.35	-3.13	-54.22	5.94
374.17	0.80	-3.30	-55.00	5.64	-3.10	-53.89	6.10
375.25	0.80	-3.49	-54.62	5.94	-3.03	-54.13	5.96
376.33	0.80	-3.46	-54.48	6.01	-3.26	-54.02	6.14
377.42	0.79	-3.65	-54.20	6.25	-3.39	-53.66	6.40
378.50	0.79	-3.69	-54.01	6.38	-3.32	-53.50	6.46
379.59	0.79	-3.75	-53.54	6.66	-3.33	-53.34	6.55
380.67	0.79	-3.46	-53.60	6.50	-3.34	-53.12	6.68
381.76	0.79	-3.63	-53.79	6.50	-3.27	-53.26	6.59
382.84	0.78	-3.56	-54.13	6.31	-3.30	-53.47	6.51
383.93	0.78	-3.86	-54.44	6.31	-3.40	-53.69	6.46
385.01	0.78	-3.86	-54.86	6.12	-3.48	-53.59	6.56
386.10	0.78	-3.86	-55.12	6.00	-3.39	-53.51	6.57
387.18	0.77	-3.87	-55.10	6.03	-3.34	-54.21	6.21
388.27	0.77	-3.99	-55.15	6.07	-3.32	-54.07	6.28
389.35	0.77	-3.82	-55.23	5.96	-3.27	-54.25	6.18
390.44	0.77	-3.63	-54.85	6.07	-3.44	-54.36	6.22

Frequency	Lambda	H_{tx0}	H_{rx0}	Directive Gain	E_{tx0}	E_{rx0}	Directive Gain
(MHz)	($\lambda = \frac{300}{F(MHz)}$)m	dBm	dBm	$= \frac{4\pi R}{\lambda}\sqrt{\frac{H_{rx0}}{H_{tx0}}}$ (G_{DH} dB)	dBm	dBm	$= \frac{4\pi R}{\lambda}\sqrt{\frac{E_{rx0}}{E_{tx0}}}$ (G_{DE} dB)
391.52	0.77	-3.59	-54.83	6.07	-3.27	-54.16	6.25
392.61	0.76	-3.56	-55.09	5.94	-3.56	-54.25	6.36
393.69	0.76	-3.52	-55.14	5.90	-3.35	-54.80	5.99
394.78	0.76	-3.45	-55.29	5.80	-3.44	-54.36	6.27
395.86	0.76	-3.70	-55.53	5.82	-3.43	-54.29	6.31
396.95	0.76	-3.56	-55.45	5.80	-3.48	-54.63	6.18
398.03	0.75	-3.52	-55.43	5.81	-3.41	-54.23	6.35
399.12	0.75	-3.68	-55.40	5.91	-3.79	-54.5	6.40
400.20	0.75	-3.56	-55.40	5.86	-3.53	-54.72	6.19
401.28	0.75	-3.57	-55.39	5.89	-3.22	-54.78	6.02
402.37	0.75	-3.63	-55.34	5.95	-3.33	-54.86	6.05
403.45	0.74	-3.78	-55.19	6.11	-3.46	-54.48	6.31
404.54	0.74	-3.76	-55.10	6.16	-3.50	-54.80	6.18
405.62	0.74	-3.52	-55.23	5.99	-3.23	-54.54	6.19
406.71	0.74	-3.91	-55.75	5.93	-3.56	-54.98	6.15
407.79	0.74	-3.76	-55.68	5.91	-3.31	-55.32	5.86
408.88	0.73	-3.49	-55.70	5.77	-3.18	-55.16	5.89
409.96	0.73	-3.75	-55.39	6.07	-3.13	-55.40	5.76
411.05	0.73	-3.75	-55.33	6.11	-3.22	-55.20	5.91
412.13	0.73	-3.83	-55.76	5.95	-3.16	-55.57	5.71
413.22	0.73	-3.87	-55.88	5.92	-3.34	-55.70	5.75
414.30	0.72	-4.00	-56.17	5.85	-3.51	-56.15	5.62
415.39	0.72	-4.07	-56.00	5.98	-3.27	-55.19	5.99
416.47	0.72	-3.80	-55.76	5.98	-3.17	-55.64	5.73
417.56	0.72	-3.78	-55.84	5.94	-3.28	-55.14	6.04
418.64	0.72	-3.82	-55.98	5.90	-3.00	-55.12	5.92
419.73	0.71	-3.92	-55.99	5.96	-3.10	-55.02	6.03
420.81	0.71	-4.06	-56.22	5.92	-3.33	-55.45	5.95
421.90	0.71	-4.03	-55.73	6.16	-3.43	-55.54	5.96
422.98	0.71	-4.04	-55.23	6.43	-3.28	-55.44	5.95
424.07	0.71	-3.97	-55.20	6.42	-3.47	-55.40	6.07
425.15	0.71	-3.90	-55.62	6.19	-3.62	-55.39	6.17
426.23	0.70	-3.76	-55.74	6.07	-3.52	-55.33	6.16
427.32	0.70	-3.89	-55.92	6.05	-3.52	-55.91	5.88
428.40	0.70	-3.96	-55.79	6.16	-3.75	-56.03	5.94
429.49	0.70	-3.95	-55.80	6.17	-3.49	-55.89	5.89
430.57	0.70	-4.07	-55.88	6.20	-3.75	-55.87	6.05

Frequency	Lambda	H_{tx0}	H_{rx0}	Directive Gain	E_{tx0}	E_{rx0}	Directive Gain
(MHz)	($\lambda = \frac{300}{F(MHz)}$)m	dBm	dBm	$= \frac{4\pi R}{\lambda}\sqrt{\frac{H_{rx0}}{H_{tx0}}}$ (G_{DH} dB)	dBm	dBm	$= \frac{4\pi R}{\lambda}\sqrt{\frac{E_{rx0}}{E_{tx0}}}$ (G_{DE} dB)
431.66	0.69	-4.19	-56.37	6.02	-3.97	-55.57	6.32
432.74	0.69	-3.99	-56.62	5.81	-3.83	-56.02	6.03
433.83	0.69	-4.14	-56.49	5.96	-3.94	-56.07	6.07
434.91	0.69	-4.09	-56.28	6.05	-4.28	-55.83	6.37
436.00	0.69	-4.08	-55.75	6.32	-3.93	-55.84	6.20
437.08	0.69	-4.14	-55.55	6.46	-4.16	-55.79	6.36
438.17	0.68	-4.24	-55.75	6.42	-4.32	-56.66	6.01
439.25	0.68	-4.36	-56.24	6.25	-4.22	-57.32	5.64
440.34	0.68	-4.37	-56.45	6.16	-4.13	-57.55	5.49
441.42	0.68	-4.44	-56.66	6.10	-4.05	-57.31	5.58
442.51	0.68	-4.39	-56.84	6.00	-4.45	-57.30	5.80
443.59	0.68	-4.50	-56.92	6.02	-4.22	-57.08	5.80
444.68	0.67	-4.36	-56.99	5.93	-4.02	-57.05	5.73
445.76	0.67	-4.51	-57.07	5.97	-4.35	-56.64	6.11
446.85	0.67	-4.71	-57.09	6.07	-4.23	-56.33	6.22
447.93	0.67	-4.63	-56.58	6.30	-4.32	-55.85	6.51
449.02	0.67	-5.07	-56.41	6.61	-4.41	-55.82	6.58
450.10	0.67	-4.95	-56.37	6.58	-4.35	-56.35	6.30
451.18	0.66	-5.18	-56.09	6.85	-4.40	-56.24	6.39
452.27	0.66	-5.25	-56.00	6.94	-4.40	-56.61	6.21
453.35	0.66	-5.11	-55.96	6.90	-4.37	-56.96	6.03
454.44	0.66	-5.05	-56.01	6.86	-4.12	-56.88	5.96
455.52	0.66	-5.11	-56.66	6.57	-4.16	-56.90	5.98
456.61	0.66	-5.30	-57.50	6.26	-4.32	-57.92	5.56
457.69	0.66	-5.25	-57.90	6.04	-4.12	-58.29	5.29
458.78	0.65	-5.26	-58.13	5.94	-4.25	-58.21	5.40
459.86	0.65	-5.27	-58.33	5.86	-4.31	-58.14	5.48
460.95	0.65	-5.19	-58.16	5.91	-4.50	-58.39	5.46
462.03	0.65	-5.07	-58.12	5.88	-4.52	-58.12	5.61
463.12	0.65	-5.14	-58.10	5.94	-4.80	-58.41	5.62
464.20	0.65	-5.23	-58.36	5.86	-4.79	-58.74	5.46
465.29	0.64	-5.12	-58.03	5.98	-4.47	-58.28	5.54
466.37	0.64	-5.17	-57.96	6.05	-4.68	-58.44	5.57
467.46	0.64	-5.32	-57.96	6.14	-4.69	-58.06	5.78
468.54	0.64	-5.46	-58.05	6.17	-4.79	-58.46	5.64
469.63	0.64	-5.72	-58.14	6.27	-4.76	-58.43	5.65
470.71	0.64	-5.73	-58.40	6.15	-4.96	-59.32	5.31

Frequency	Lambda	H_{tx0}	H_{rx0}	Directive Gain	E_{tx0}	E_{rx0}	Directive Gain
(MHz)	($\lambda = \frac{300}{F(MHz)}$)m	dBm	dBm	$= \frac{4\pi R}{\lambda}\sqrt{\frac{H_{rx0}}{H_{tx0}}}$ (G_{DH} dB)	dBm	dBm	$= \frac{4\pi R}{\lambda}\sqrt{\frac{E_{rx0}}{E_{tx0}}}$ (G_{DE} dB)
471.80	0.64	-5.65	-58.41	6.12	-4.99	-59.29	5.35
472.88	0.63	-5.62	-58.21	6.21	-5.27	-59.39	5.45
473.97	0.63	-5.97	-58.20	6.40	-5.20	-59.25	5.50
475.05	0.63	-5.88	-58.49	6.22	-5.37	-59.72	5.36
476.13	0.63	-6.11	-58.67	6.26	-5.27	-60.24	5.06
477.22	0.63	-6.23	-58.96	6.18	-5.29	-60.47	4.96
478.30	0.63	-6.30	-59.28	6.07	-5.32	-60.70	4.87
479.39	0.63	-6.21	-59.25	6.05	-5.28	-60.44	4.99
480.47	0.62	-6.23	-59.37	6.01	-5.36	-60.37	5.08
481.56	0.62	-6.11	-59.34	5.97	-5.52	-60.92	4.89
482.64	0.62	-6.29	-59.41	6.04	-5.64	-61.09	4.88
483.73	0.62	-6.36	-59.20	6.19	-5.61	-60.84	5.00
484.81	0.62	-6.46	-59.69	6.00	-5.82	-61.51	4.78
485.90	0.62	-6.53	-59.21	6.29	-5.82	-61.00	5.04
486.98	0.62	-6.42	-59.32	6.19	-5.73	-61.31	4.85
488.07	0.61	-6.42	-59.76	5.98	-5.89	-61.79	4.70
489.15	0.61	-6.56	-59.80	6.04	-6.25	-62.57	4.50
490.24	0.61	-6.63	-59.88	6.04	-6.13	-62.53	4.47
491.32	0.61	-6.83	-59.89	6.14	-6.65	-62.41	4.80
492.41	0.61	-6.69	-60.00	6.03	-6.53	-62.05	4.93
493.49	0.61	-7.19	-59.83	6.37	-6.50	-62.27	4.81
494.58	0.61	-7.18	-59.67	6.46	-6.64	-62.06	5.00
495.66	0.61	-7.25	-59.64	6.52	-6.60	-62.34	4.85
496.75	0.60	-7.15	-59.51	6.54	-6.54	-61.81	5.09
497.83	0.60	-7.27	-59.33	6.70	-6.36	-61.85	4.99
498.92	0.60	-7.47	-59.37	6.79	-7.03	-61.61	5.46
500.00	0.60	-7.30	-59.36	6.72	-6.95	-61.94	5.26

1.3 Grating Lobes of GRASP & GLOSS

To know the theoretical response of grating lobes, their angular separation with main lobe as well as the half power beam-widths of GRASP and GLOSS systems a simulation is performed. Both GLOSS and GRASP systems resemble the linear phased arrays. For GRASP system, the power is combined along the single antenna E & H-plane beam response of LPDA, whereas it is combined along the H-plane response (along North-

South) for GLOSS. As the separation between the antennas are comparable to the observing wavelength, grating lobes are expected to appear. The theoretical adding interferometric response of GLOSS system is treated herewith; the same can be extended to GRASP system as well.

A uniform linear phased array like GLOSS (refer Figure A.1), inter-elements separated by a distance of 'd' m, is properly phased ($\psi = \psi_1 + \psi_2$) and combined to give an equivalent system response given as in Jordan and Balmain (1968)

$$E_{res} = E_o(1 + e^{j\psi} + e^{2j\psi} + ... + e^{(n-1)j\psi}) \tag{A.3}$$

Here E_{res} is the resultant response of entire array, E_o is the response of LPDA in N-S direction which is ≈110° (refer Figure A.2). The phase difference between the adjacent antennas ψ_1 & ψ_2 are due to their individual separation ('1d', '2d', etc.) as well as due to the source position (angle 'θ') with respect to the array baseline (geometric phase). This is given as $\psi = \frac{2\pi}{\lambda} dsin(\theta)$. To know the resultant group beam profiles of GLOSS and GRASP, equation (A.3) is used. Figure A.3, Left: top & bottom as well as Right: top & bottom shows the rectangular plot of combined 'group' and 'grating beam' responses of GRASP and GLOSS systems. Also, Figures A.4, A.5 are the polar plots obtained for both GLOSS & GRASP near their observing frequency limits.

As we are particularly interested in low-frequency solar observations, the radio Sun, which subtends $< 1°$ or even less in the frequency of interest of GLOSS & GRASP. This is minimal compared to the group as well as the any grating lobe beam-widths. Also, the quite Sun flux estimates are higher when compared to the other weak radio sources; therefore the effects of grating lobe contribution will be minimal on both receivers.

Figure A.1: 8 equispaced identical LPDAs of GLOSS in adding interferometer mode. Here ψ_1, ψ_2 are the individual stage phase and ψ is the overall phase difference ($\psi = \psi_1 + \psi_2$) of arriving signals due to the geometrical position of the antennas with respect to the source. The source angle 'θ' is an angular measure with respect to the normal to the baseline of LPDAs.

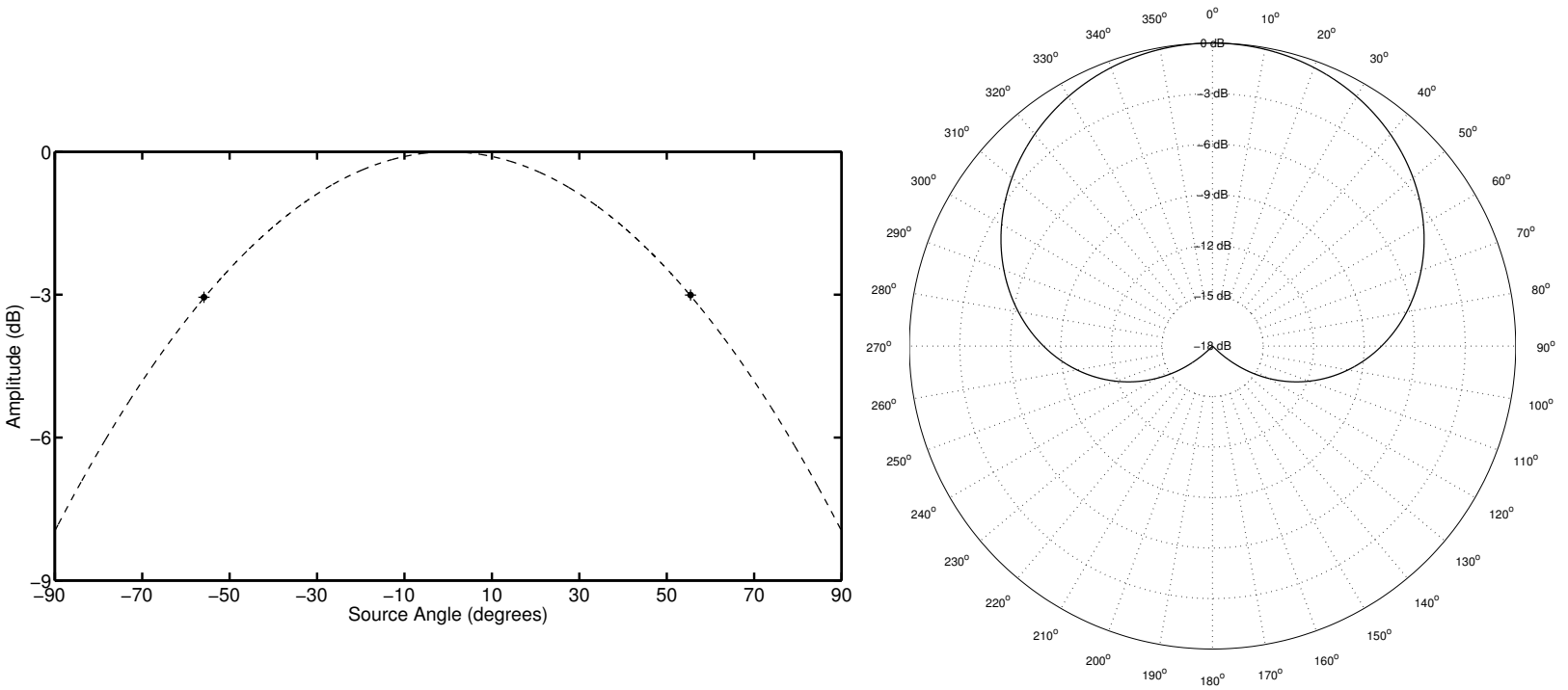

Figure A.2: Left plot: shows the modelled single antenna beam of LPDA in North-South direction. The beam profile is approximated with Gaussian distribution; having zero mean and half power beam-width (1σ) corresponds to 110° (refer 2.3). The 'star mark' represents the half power points or -3 dB level. Right plot: same as left plot but in polar form. One can notice the HPBW $\approx$ 110° from -3 dB levels from either of the plots. According to the property of LPDA (refer Section 2.5.2) this beam profile and HPBW are identical and independent of working range of frequencies of LPDA.

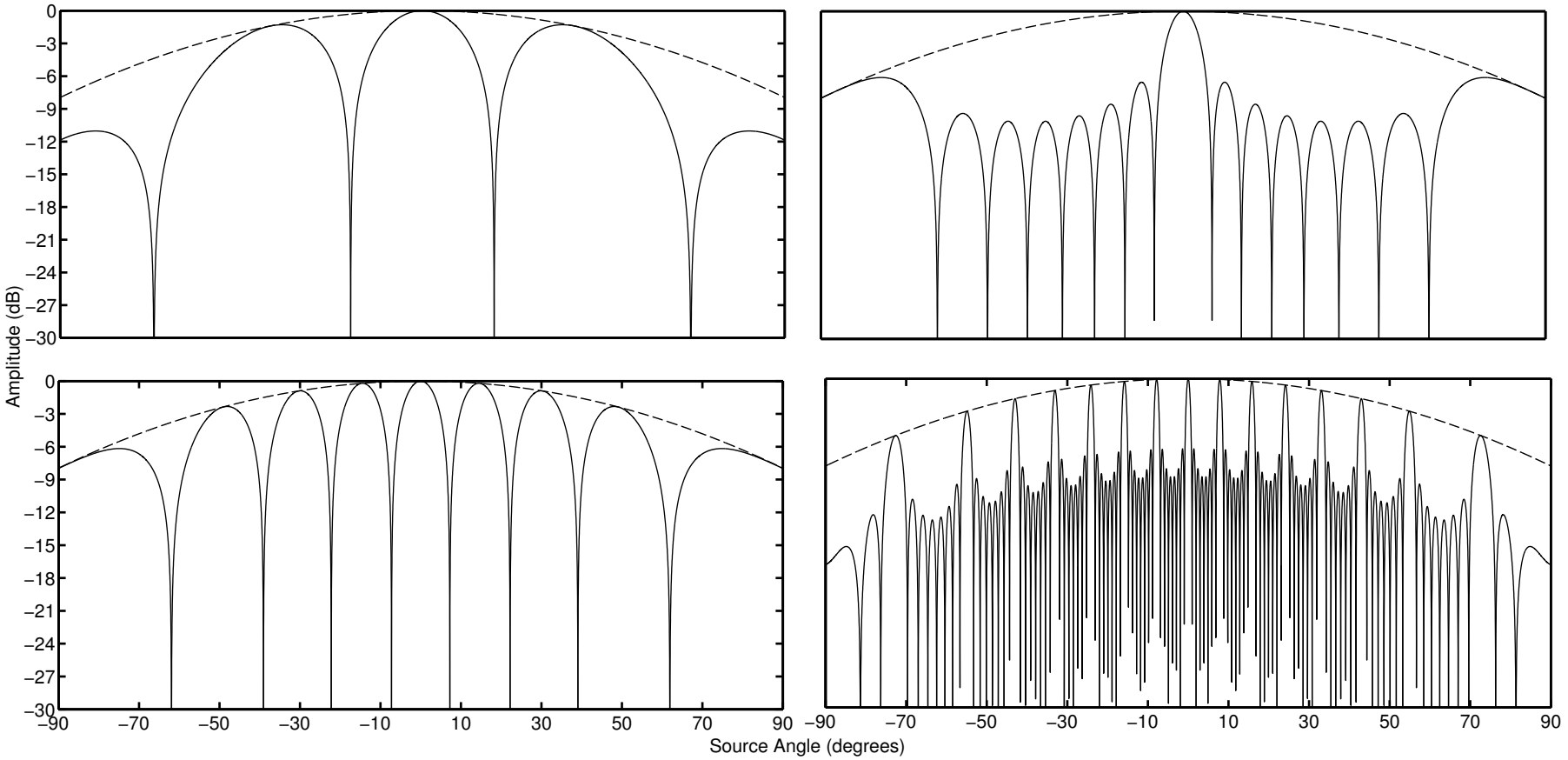

Figure A.3: Left top and bottom panels: superposed GRASP Group Beam (‘solid line’) and single antenna beam (‘dashed line’) in North-South direction. The top left panel corresponds to lowest frequency, i.e., 35 MHz whereas the bottom left panel is the plot obtained at 85 MHz respectively. Right top and bottom panels: These plots are of similar kind obtained for GLOSS at working frequencies of 60 MHz & 440 MHz respectively.

Figure A.4: Left panel: Simulated GRASP group beam at 35 MHz, Right Panel: Similar profile simulated for 85 MHz. One can notice the grating lobes are almost on par to the main lobe, and their amplitudes are modulated by the single antenna beam profile. The concentric circles are the expected power levels with respect to maximum value, when the source transits over the respective beams.

Figure A.5: Similar to the Figure A.4, but simulated to know the group beam response of GLOSS. The theoretical half-power beam widths at the lowest (60 MHz) and highest (440 MHz) frequencies are $\approx 8^\circ$ and $\approx 1^\circ$ respectively. The separation between the main lobe and grating lobe is $\approx 90^\circ$ at 60 MHz and $\approx 9^\circ$ at440 MHz respectively (refer equation(2.10)).

References

Akmal, A., Raymond, J. C., Vourlidas, A., et al. *Astrophys. J.*, 553:922–934, June 2001.

Allen, C. W. *Mon. Not. Roy. Astron. Soc.*, 107:426, 1947.

Aschwanden, M. J. and Acton, L. W. *Astrophys. J.*, 550(1):475, 2001.

Aschwanden, M. J., Benz, A. O., and Montello, M. L. *Astrophys. J.*, 431:432–449, August 1994.

Aubier, M., Leblanc, Y., and Boischot, A. *Astron. Astrophys.*, 12:435, June 1971.

Aurass, H., Rausche, G., Mann, G., and Hofmann, A. *Astron. Astrophys.*, 435:1137–1148, June 2005.

Avignon, Y., Lantos, P., Palagi, F., and Patriarchi, P. *Solar Phys.*, 45(1):141–145, 1975.

Babcock, W., Horace. *Astrophys. J.*, 133:572, 1961.

Balanis, C. A. *New Jersey: John Wiley & Sons, Inc*, 8:21–31, 2005.

Bastian, T. S. *Astrophys. J.*, 370:L49–L52, 1991.

Bastian, T. S. *Planet. Space Sci.*, 52:1381–1389, December 2004.

Bastian, T. S. and Gary, D. E. *J. Geophys. Res.*, 102:14031–14040, July 1997.

Bastian, T. S., Pick, M., Kerdraon, A., Maia, D., and Vourlidas, A. *Astrophys. J. Lett.*, 558:L65–L69, September 2001.

Baumback, S. *Astronomische Nachrichten*, 263:121, July 1937.

Bemporad, A., Raymond, J., Poletto, G., and Romoli, M. *Astrophys. J.*, 655:576–590, January 2007.

Benz, A. O., editor. *Plasma astrophysics: Kinetic processes in solar and stellar coronae*, volume 184 of *Astrophysics and Space Science Library*, 1993.

Benz, A. O., editor. *Plasma Astrophysics, second edition*, volume 279 of *Astrophysics and Space Science Library*, June 2002.

Benz, A. O., Monstein, C., Meyer, H., et al. *Earth, Moon & Planets*, 104:277–285, April 2009.

Boischot, A. *Sci., Paris*, 245:2194, 1957.

Bower, G. C., Falcke, H., and Backer, D. C. *Astrophys. J. Lett.*, 523(1):L29, 1999.

Brueckner, G. E., Howard, R. A., Koomen, M. J., et al. *Solar Phys.*, 162(1-2):357–402, 1995.

Cairns, I. H., Lobzin, V. V., Warmuth, A., et al. *Astrophys. J. Lett.*, 706:L265–L269, December 2009.

Cane, H. V. *Non-thermal galactic background radiation*. PhD thesis, University of Tasmania, 1977.

Cane, H. V. *Australian Journal of Physics*, 31(6):561–566, 1978.

Cane, H. V. and Whitham, P. S. *Monthly Notices of the Royal Astronomical Society*, 179(1):21–29, 1977.

Caroubalos, C. and Steinberg, J. L. Direct Measurements of the Directivity of Type i and Type III Radiation at 169 MHZ (presented by C. Caroubalos). In *Coronal Disturbances*, volume 57, page 239, 1974.

Carrel, R. L. The design of log-periodic dipole antennas. In *1958 IRE International Convention Record*, volume 9, pages 61–75, March 1961.

Carrell, R. L. Analysis and design of the log-periodic dipole antenna. Technical report, DTIC Document, 1961.

Carrell, R. L. The design of log-periodic dipole antennas. In *IRE International Convention Record*, volume 9, pages 61–75. IEEE, 1966.

Cho, K.-S., Lee, J., Gary, D. E., Moon, Y.-J., and Park, Y. D. *Astrophys. J.*, 665(1):799, 2007.

Cho, K.-S., Bong, S.-C., Kim, Y.-H., et al. *Astronomy & Astrophysics*, 491(3):873–882, 2008.

Cho, K.-S., Gopalswamy, N., Kwon, R.-Y., Kim, R.-S., and Yashiro, S. *Astrophys. J.*, 765(2):148, 2013.

Christensen-Dalsgaard, J., Däppen, W., Ajukov, S. V., et al. *Science*, 272(5266):1286–1292, 1996.

Ciaravella, A., Raymond, J. C., Reale, F., Strachan, L., and Peres, G. *Astrophys. J.*, 557:351–365, August 2001.

Daene, H. and Krüger, A. *Astronomische Nachrichten*, 289:117, April 1966.

DuHamel, R. and Isbell, D. E. Broadband logarithmically periodic antenna structures. In *1958 IRE International Convention Record*, volume 5, pages 119–128. IEEE, 1966.

Dulk, G. A. *Solar Phys.*, 32:491–503, October 1973.

Dulk, G. A. *Annual Review of Astronomy & Astrophysics*, 23:169–224, 1985.

Dulk, G. A. and McLean, D. J. *Solar Phys.*, 57:279–295, April 1978.

Dulk, G. A. and Suzuki, S. *Astron. Astrophys.*, 88:203–217, August 1980.

Dulk, G. A., Melrose, D. B., and Suzuki, S. *Proceedings of the Astronomical Society of Australia*, 3:375–379, 1979.

Dulk, G. A., Gary, D. E., and Suzuki, S. A&A, 88:218–229, August 1980.

Dulk, G. A., Goldman, M. V., Steinberg, J. L., and Hoang, S. *Astron. Astrophys.*, 173:366–374, February 1987.

Dulk, G. A., Erickson, W. C., Manning, R., and Bougeret, J.-L. *Astron. Astrophys.*, 365:294–300, January 2001.

Duncan, R. A. *Proceedings of the Astronomical Society of Australia*, 3:253–256, 1978.

Duncan, R. A. *Solar Phys.*, 63:389–398, September 1979.

Duncan, R. A. *Solar Phys.*, 73:191–204, September 1981.

Ebenezer, E., Subramanian, K. R., Ramesh, R., Sundararajan, M. S., and Kathiravan, C. *Bulletin of the Astronomical Society of India*, 35:111–119, June 2007.

Erickson, W. C. *Proc. Astron. Soc. Aust.*, 14:278–282, November 1997.

Fineschi, S., van Ballegoijen, A., and Kohl, J. L. Coronal Magnetic Field Diagnostics with UV Spectropolarimetry. In *8th SOHO Workshop: Plasma Dynamics and Diagnostics in the Solar Transition Region and Corona*, volume 446, page 317, 1999.

Fludra, A., Del Zanna, G., Alexander, D., and Bromage, B. J. I. J. Geophys. Res., 104:9709–9720, May 1999. doi: 10.1029/1998JA900033.

Fomichev, V. V. and Chertok, I. M. *Soviet Astronomy*, 12:21, 1968.

Friis, H. T. *Proceedings of the IRE,* 32(7):419–422, 1944.

Gary, D. E., Dulk, G. A., House, L. L., Illing, R., and Wagner, W. J. *Astron. Astrophys.*, 152:42–50, November 1985.

Gelfreikh, G. B. Coronal Magnetic Field Measurements Through Bremsstrahlung Emission. In Gary, D. E. and Keller, C. U., editors, *Astrophysics and Space Science Library*, volume 314 of *Astrophysics and Space Science Library*, page 115, September 2004.

Golub, L., Deluca, E., Austin, G., et al. Sol. Phys., 243:63–86, June 2007. doi: 10.1007/s11207-007-0182-1.

Gopalswamy, N. and Kundu, M. R. *Solar Phys.*, 111:347–363, September 1987.

Gopalswamy, N. and Kundu, M. R. *Solar Phys.*, 122:91–110, March 1989a.

Gopalswamy, N. and Kundu, M. R. *Solar Phys.*, 122:145–173, March 1989b.

Gopalswamy, N. and Kundu, M. R. *Astrophys. J. Lett.*, 390:L37–L39, May 1992.

Gopalswamy, N. and Kundu, M. R. Surprises in the Radio Signatures of CMEs. In Benz, A. O. and Krüger, A., editors, *Coronal Magnetic Energy Releases*, volume 444 of *Lecture Notes in Physics, Berlin Springer Verlag*, page 223, 1995.

Gopalswamy, N., Thejappa, G., Sastry, C. V., and Tlamicha, A. *Bulletin of the Astronomical Institutes of Czechoslovakia*, 37:115–120, March 1986.

Gopalswamy, N., Lara, A., Lepping, R. P., et al. Geophys. Res. Lett., 27:145–148, January 2000.

Gopalswamy, N., Aguilar-Rodriguez, E., Yashiro, S., et al. *Journal of Geophysical Research: Space Physics*, 110(A12), 2005.

Gopalswamy, N., Thompson, W. T., Davila, J. M., et al. *Solar Phys.*, 259(1-2):227–254, 2009.

Gopalswamy, N., Nitta, N., Akiyama, S., Mäkelä, P., and Yashiro, S. *Astrophys. J.*, 744(1):72, 2011.

Gopalswamy, N., Makela, P., Yashiro, S., and Davila, J. M. *Sun and Geosphere*, 7:7–11, August 2012.

Gopalswamy, N., Xie, H., Mäkelä, P., et al. *Advances in Space Research*, 51(11):1981–1989, 2013.

Gough, D. O. and McIntyre, M. E. *Nature*, 394(6695):755–757, 1998.

Grognard, R. J. M. and McLean, D. J. *Solar Phys.*, 29:149–161, March 1973.

Hariharan, K., Ramesh, R., Kishore, P., Kathiravan, C., and Gopalswamy, N. *Astrophys. J.*, 795:14, November 2014.

Hariharan, K., Ramesh, R., and Kathiravan, C. *Solar Phys.*, 290(9):2479–2489, 2015.

Hariharan, K., Ramesh, R., Kathiravan, C., Abhilash, H. N., and Rajalingam, M. *Astrophys. J. Suppl.*, 222 (2):21, 2016.

Howard, R. A., Moses, J. D., Vourlidas, A., et al. *Space Sci. Rev.*, 136:67–115, April 2008.

Hutira, F., Bezek, J., and Bilik, V. Design and investigation of a log-periodic antenna for DCS, PCS and UMTS mobile communications bands. In *RF and Microwave Conference, Malaysia October*, 2004.

Isbell, D. E. *Antennas and Propagation, IRE Transactions on*, 8(3):260–267, 1960.

Iwai, K. and Shibasaki, K. *Publications of the Astronomical Society of Japan*, 65(sp1):S14, 2013.

Jackson, B. V. and Howard, R. A. Sol. Phys., 148:359–370, December 1993.

Jordan, E. C. and Balmain, K. G. Electromagnetic Waves and Radiating Systems, Prentice Hall, 1968.

Kai, K., Melrose, D., and Suzuki, S. Solar Radio Physics, ed, 1985.

Kathiravan, C. and Ramesh, R. *Astrophys. J.*, 610(1):532, 2004.

Kathiravan, C. and Ramesh, R. *Astrophys. J. Lett.*, 627:L77–L80, July 2005.

Kathiravan, C., Ramesh, R., and Subramanian, K. R. *Astrophys. J. Lett.*, 567(1):L93, 2002.

Kathiravan, C., Ramesh, R., Barve, I. V., and Rajalingam, M. *Astrophys. J.*, 730:91, April 2011.

Kerdraon, A. *Astron. Astrophys.*, 71:266–268, January 1979.

Kishore, P. and Kathiravan, C. A preliminary scheme to modify the reception characteristics of a log-periodic antenna within its operating bandwidth. In *Astronomical Society of India Conference Series*, volume 9 of *Astronomical Society of India Conference Series*, 2013.

Kishore, P., Kathiravan, C., Ramesh, R., Rajalingam, M., and Barve, I. V. *Solar Phys.*, 289:3995–4005, October 2014.

Kishore, P., Ramesh, R., Kathiravan, C., and Rajalingam, M. *Solar Phys.*, pages 1–14, 2015. ISSN 0038-0938.

Klein, K.-L., Krucker, S., Lointier, G., and Kerdraon, A. *Astron. Astrophys.*, 486:589–596, August 2008.

Kouloumvakos, A., Patsourakos, S., Hillaris, A., et al. *Solar Phys.*, 289(6):2123–2139, 2014.

Kraus, J. D. *New York: McGraw-Hill, 1966*, 1, 1966.

Kraus, J. D. and Marhefka, R. J. *Antennas for all Applications*, 2001.

Kraus, J. D. and Moffet, A. T. *American Journal of Physics*, 35(5):450–450, 1967.

Kraus, J. D., Marhefka, R. J., and Khan, A. S. *Antennas and Wave Propagation*. Tata McGraw-Hill Education, 2006.

Krüger, A. *Introduction to solar radio astronomy and radio physics*, volume 16. Springer Science & Business Media, 2012.

Kuhn, J. R. Infrared Coronal Magnetic Field Measurements. In Kuhn, J. R. and Penn, M. J., editors, *Infrared tools for solar astrophysics: What's next?*, page 89, 1995.

Kundu, M. R., Gergely, T. E., Szabo, A., Loiacono, R., and White, S. M. *Astrophys. J.*, 308:436–442, 1986.

Kundu, M. R., Schmahl, E. J., Gopalswamy, N., and White, S. M. *Advances in Space Research*, 9:41–45, 1989.

Kwon, R.-Y., Ofman, L., Olmedo, O., et al. *Astrophys. J.*, 766(1):55, 2013.

Lang, K. R. and Willson, R. F. *Astrophys. J.*, 319:514–519, August 1987.

Lantos, P., Alissandrakis, C. E., Gergely, T., and Kundu, M. R. *Solar Phys.*, 112(2):325–340, 1987.

Leblanc, Y., Dulk, G. A., and Bougeret, J.-L. *Solar Phys.*, 183(1):165–180, 1998.

Lee, J. *Space Science Reviews*, 133(1-4):73–102, 2007.

Lemen, J. R., Title, A. M., Akin, D. J., et al. *Solar Phys.*, 275:17–40, January 2012.

Li, B., Cairns, I. H., and Robinson, P. A. *Journal of Geophysical Research (Space Physics)*, 113:A06105, June 2008.

Li, B., Cairns, I. H., and Robinson, P. A. *Journal of Geophysical Research (Space Physics)*, 114:A02104, February 2009.

Lin, H., Kuhn, J. R., and Coulter, R. *Astrophys. J. Lett.*, 613:L177–L180, October 2004a.

Lin, H., Penn, M. J., and Tomczyk, S. *Astrophys. J. Lett.*, 541(2):L83, 2000.

Lin, J., Mancuso, S., and Vourlidas, A. *Astrophys. J.*, 649(2):1110, 2006.

Lin, R. P., Dennis, B., Hurford, G., Smith, D. M., and Zehnder, A. The Reuven Ramaty high-energy solar spectroscopic imager (RHESSI) mission. In Fineschi, S. and Gummin, M. A., editors, *Telescopes and Instrumentation for Solar Astrophysics*, volume 5171 of Proc. SPIE, pages 38–52, February 2004b. doi: 10.1117/12.506649.

Liu, Y., Luhmann, J. G., Bale, S. D., and Lin, R. P. *Astrophys. J. Lett.*, 691(2):L151, 2009.

Ma, S., Raymond, C., John, Golub, L., et al. *Astrophys. J.*, 738(2):160, 2011.

Magelssen, G. R. *Nonrelativistic electron stream propagation in the solar atmosphere and solar wind: Type III bursts*. PhD thesis, National Center for Atmospheric Research, Boulder, CO., December 1976.

Mancuso, S. and Garzelli, M. V. *Astronomy & Astrophysics*, 553:A100, 2013.

Mancuso, S. and Raymond, J. C. *Astronomy & Astrophysics*, 413(1):363–371, 2004.

Mancuso, S., Raymond, J. C., Kohl, J., et al. *Astron. Astrophys.*, 400:347–353, March 2003.

Mann, G., Klassen, A., Classen, H.-T., et al. *Astronomy and Astrophysics Supplement Series*, 119(3):489–498, 1996.

McLean, D. J. *Metrewave solar radio bursts*, pages 37–52. 1985.

McLean, D. J. and Labrum, N. R. *Solar radiophysics: Studies of emission from the sun at metre wavelengths*. 1985.

Melrose, D. B. *Proceedings of the Astronomical Society of Australia*, 2:261–263, September 1974.

Melrose, D. B. *Solar Phys.*, 43:211–236, July 1975.

Melrose, D. B. Solar Radio Physics, ed, 1985.

Melrose, D. B. and Sy, W. N. *Australian Journal of Physics*, 25:387, August 1972.

Melrose, D. B., Dulk, G. A., and Smerd, S. F. *Astron. Astrophys.*, 66:315–324, June 1978.

Melrose, D. B., Dulk, G. A., and Gary, D. E. *Proceedings of the Astronomical Society of Australia*, 4:50–53, 1980.

Mercier, C. *Solar Phys.*, 130:119–129, December 1990.

Mercier, C., Subramanian, P., Kerdraon, A., et al. *Astron. Astrophys.*, 447:1189–1201, March 2006.

Mercier, C., Subramanian, P., Chambe, G., and Janardhan, P. *Astron. Astrophys.*, 576:A136, April 2015.

Monstein, C., Ramesh, R., and Kathiravan, C. 2007.

Morosan, D. E., Gallagher, P. T., Zucca, P., et al. *Astron. Astrophys.*, 568:A67, August 2014.

Morris, D., Radhakrishnan, V., and Seielstad, G. A. *Astrophys. J.*, 139:551, 1964.

Nelson, G. J. *Proceedings of the Astronomical Society of Australia*, 3:159–162, September 1977.

Nelson, G. J. and Melrose, D. B. Type II bursts, Solar Radiophysics DJ McLean, NR Labrum, 333–359, 1985.

Nelson, G. J., Sheridan, K. V., and Suzuki, S. *Solar Radiophysics: Studies of emission from the sun at metre wavelengths*, 1:113–154, 1985.

Newkirk Jr, G. *Astrophys. J.*, 133:983, 1961.

Ontiveros, V. and Vourlidas, A. *Astrophys. J.*, 693(1):267, 2009.

Parker, E. N. *Astrophys. J.*, 122:293, 1955.

Patzold, M., Bird, M. K., Volland, H., et al. *Solar Phys.*, 109:91–105, September 1987.

Pierce, A. K. and Slaughter, C. D. Sol. Phys., 51:25–41, February 1977. doi: 10.1007/BF00240442.

Pilipp, W. G. and Benz, A. O. *Astron. Astrophys.*, 56:39–51, April 1977.

Raja, K. S. and Ramesh, R. *Astrophys. J.*, 775(1):38, 2013.

Raja, K. S., Kathiravan, C., Ramesh, R., Rajalingam, M., and Barve, I. V. *Astrophys. J. Suppl.*, 207(1):2, 2013.

Ramesh, R. and Ebenezer, E. *Astrophys. J. Lett.*, 558:L141–L143, September 2001.

Ramesh, R. and Sastry, C. V. *Astron. Astrophys.*, 358:749–752, June 2000.

Ramesh, R., Subramanian, K. R., Sundararajan, M. S., and Sastry, C. V. *Solar Phys.*, 181:439–453, August 1998.

Ramesh, R., Subramanian, K. R., and Sastry, C. V. *Solar Phys.*, 185:77–85, March 1999.

Ramesh, R., Subramanian, K. R., and Sastry, C. V. *Astronomy and Astrophysics Supplement Series*, 139(1): 179–181, 1999.

Ramesh, R., Kathiravan, C., and Sastry, C. V. *Astrophys. J. Lett.*, 548(2):L229, 2001.

Ramesh, R., Kathiravan, C., Narayanan, A. S., and Ebenezer, E. *Astron. Astrophys.*, 400:753–758, March 2003a.

Ramesh, R., Kathiravan, C., and Sastry, C. V. *Astrophys. J. Lett.*, 591:L163–L166, July 2003b.

Ramesh, R., Narayanan, A. S., Kathiravan, C., Sastry, C. V., and Shankar, N. U. *Astron. Astrophys.*, 431: 353–357, February 2005.

Ramesh, R., Nataraj, H. S., Kathiravan, C., and Sastry, C. V. *Astrophys. J.*, 648:707–711, September 2006a.

Ramesh, R., Rajan, M. S. S., and Sastry, C. V. *Experimental Astronomy*, 21:31–40, February 2006b.

Ramesh, R., Kathiravan, C., Sundararajan, M. S., Barve, I. V., and Sastry, C. V. *Solar Phys.*, 253:319–327, December 2008.

Ramesh, R., Kathiravan, C., Barve, I. V., Beeharry, G. K., and Rajasekara, G. N. *Astrophys. J. Lett.*, 719: L41–L44, August 2010.

Ramesh, R., Kathiravan, C., Kartha, S. S., and Gopalswamy, N. *Astrophys. J.*, 712(1):188, 2010.

Ramesh, R., Kathiravan, C., and Sastry, C. V. *Astrophys. J.*, 711:1029–1032, March 2010.

Ramesh, R., Kathiravan, C., and Narayanan, A. S. *Astrophys. J.*, 734(1):39, 2011.

Ramesh, R., Kathiravan, C., Barve, I. V., and Rajalingam, M. *Astrophys. J.*, 744:165, January 2012.

Ramesh, R., Lakshmi, M. A., Kathiravan, C., Gopalswamy, N., and Umapathy, S. *Astrophys. J.*, 752(2):107, 2012.

Ramesh, R., Kishore, P., Mulay, S. M., et al. *Astrophys. J.*, 778:30, November 2013a.

Ramesh, R., Sasikumar Raja, K., Kathiravan, C., and Narayanan, A. S. *Astrophys. J.*, 762:89, January 2013b.

Raoult, A., Mangeney, A., and Vlahos, L. *Astron. Astrophys.*, 233:229–234, July 1990.

Riddle, A. C. *Solar Phys.*, 35:153–169, March 1974.

Roberts, J. A. *Phys*, 12:327, 1959.

Robinson, R. D. *Solar Phys.*, 55:459–472, December 1977.

Robinson, R. D. *Solar Phys.*, 56:405–416, February 1978.

Rumsey, V. H. *Part*, 1:114, 1957.

Saito, K., Poland, A. I., and Munro, H., Richard. *Solar Phys.*, 55(1):121–134, 1977.

Sasikumar Raja, K. and Ramesh, R. *Astrophys. J.*, 775:38, September 2013.

Sasikumar Raja, K., Ramesh, R., Hariharan, K., Kathiravan, C., and Wang, T. J. *Astrophys. J.*, 796:56, November 2014.

Sastry, C. V., Dwarkanath, K. S., Shevgaonkar, R. K., and Krishan, V. *Solar Phys.*, 73(2):363–377, 1981.

Sastry, C. V., Shevgaonkar, R. K., and Ramanuja, M. N. *Solar Phys.*, 87(2):391–399, 1983.

Schatten, H., Kenneth, Wilcox, M., John, and Ness, N. F. *Solar Phys.*, 6(3):442–455, 1969.

Schmahl, E. J., Gopalswamy, N., and Kundu, M. R. *Solar Phys.*, 150(1-2):325–337, 1994.

Schrijver, J., Carolus and DeRosa, M. L. *Solar Phys.*, 212(1):165–200, 2003.

Schwenn, R. *Living Reviews in Solar Phys.*, 3(2):1–72, 2006.

Sheridan, K. V. and McLean, D. J. Solar Radio Physics, ed, 1985.

Sheridan, K. V., Jackson, B. V., McLear, D. J., and Dulk, G. A. *Proceedings of the Astronomical Society of Australia*, 3, 1978.

Smerd, S. F. *Australian Journal of Chemistry*, 3(1):34–59, 1950.

Smerd, S. F. and Dulk, G. A. In Howard, R., editor, *Solar Magnetic Fields*, volume 43 of *IAU Symposium*, page 616, 1971.

Smerd, S. F., Sheridan, K. V., and Stewart, R. T. *GA Newkirk (Dordrecht: Reidel)*, 389, 1974.

Smerd, S. F., Sheridan, K. V., and Stewart, R. T. *Astrophysical Letters*, 16:23–28, 1975.

Spangler, S. R. *Space Sci. Rev.*, 121:189–200, November 2005.

Stepanov, A. V. *Soviet Astronomy*, 17:781, 1974.

Stewart, R. T. Ground-Based Observations of Type III Bursts. In Newkirk, G. A., editor, *Coronal Disturbances*, volume 57 of *IAU Symposium*, page 161, 1974.

Stewart, R. T. *Solar Phys.*, 58:121–126, June 1978.

Stewart, R. T. Solar Radio Physics, ed, 1985.

Stewart, R. T. and McLean, D. J. *Proceedings of the Astronomical Society of Australia*, 4:386–389, 1982.

Stewart, R. T., McCabe, M. K., Koomen, M. J., Hansen, R. T., and Dulk, G. A. *Solar Phys.*, 36(1):203–217, 1974.

Stewart, R. T., Dulk, G. A., Sheridan, K. V., et al. *Astron. Astrophys.*, 116:217–223, December 1982.

Subramanian, K. R. *Astronomy & Astrophysics*, 426(1):329–331, 2004.

Subramanian, K. R., Gopalswamy, N., and Sastry, C. V. *Solar Phys.*, 143:301–316, February 1993.

Susino, R., Bemporad, A., and Mancuso, S. *Astrophys. J.*, 812(2):119, 2015.

Suzuki, S. *Solar Phys.*, 38(1):3–7, 1974.

Suzuki, S. and Dulk, G. A. *Bursts of Type III and Type V*, pages 289–332. 1985.

Suzuki, S. and Sheridan, K. V. *Radiophysics and Quantum Electronics*, 20(9):989–996, 1977.

Suzuki, S. and Sheridan, K. V. On the fundamental and harmonic components of low-frequency type III solar radio bursts. In *Proceedings of the Astronomical Society of Australia*, volume 4, pages 382–386, 1982.

Tang, J. F., Wu, D. J., and Tan, C. M. *Astrophys. J.*, 779:83, December 2013.

Thejappa, G. and MacDowall, R. J. *Astrophys. J.*, 676:1338-1345, April 2008.

Thejappa, G., Gopalswamy, N., and Kundu, M. R. *Solar Phys.*, 127:165–183, May 1990.

Thejappa, G., Zlobec, P., and MacDowall, R. J. *Astrophys. J.*, 592(2):1234, 2003.

Thejappa, G., MacDowall, R. J., and Bergamo, M. *Astrophys. J.*, 745(2):187, 2012.

Thompson, A. R., Moran, J. M., and Swenson, G. W. *Interferometry and Synthesis in Radio Astronomy, John Wiley & Sons, 2004*. 2004.

Tidman, D. A., Birmingham, T. J., and Stainer, H. M. *Astrophys. J.*, 146:207, 1966.

Tomczyk, S., Card, G. L., Darnell, T., et al. *Solar Phys.*, 247:411–428, February 2008.

Tonks, L. and Langmuir, I. *Physical review*, 34(6):876, 1929.

Tun, S. D. and Vourlidas, A. *Astrophys. J.*, 766:130, April 2013.

Vasanth, V., Umapathy, S., Vršnak, B., Žic, T., and Prakash, O. *Solar Phys.*, 289(1):251–261, 2014.

Vourlidas, A., Wu, S. T., Wang, A. H., Subramanian, P., and Howard, R. A. *Astrophys. J.*, 598(2):1392, 2003.

Vršnak, B., Aurass, H., Magdalenić, J., and Gopalswamy, N. *Astronomy & Astrophysics*, 377(1):321–329, 2001.

Vršnak, B., Magdalenić, J., and Zlobec, P. *Astronomy & Astrophysics*, 413(2):753–763, 2004.

Vršnak, B., Magdalenić, J., Aurass, H., and Mann, G. *Astron. Astrophys.*, 396:673–682, December 2002.

Vršnak, B., Magdalenić, J., and Zlobec, P. *Astron. Astrophys.*, 413:753–763, January 2004.

Weiler, K. W. and De Pater, I. *Astrophys. J. Suppl.*, 52:293–327, 1983.

Weiler, K. W. and Raimond, E. *Astronomy and Astrophysics*, 52:397–402, 1976.

Weiss, L. A. A. and Stewart, R. T. *Australian Journal of Physics*, 18:143, April 1965.

West, M. J., Zhukov, A. N., Dolla, L., and Rodriguez, L. *Astrophys. J.*, 730(2):122, 2011.

White, S. M. Radio Measurements of Coronal Magnetic Fields. In Innes, D. E., Lagg, A., and Solanki, S. A., editors, *Chromospheric and Coronal Magnetic Fields*, volume 596 of *ESA Special Publication*, page 10, November 2005.

White, S. M., Kundu, M. R., and Szabo, A. *Solar Phys.*, 107:135–157, March 1986.

White, S. M. *Asian Journal of Physics*, 16:189–207, 2007.

Wild, J. P. *Solar Phys.*, 9:260–264, October 1969.

Wild, J. P. and Smerd, S. F. *Annual Review of Astronomy & Astrophysics*, 10:159, 1972.

Wild, J. P., Murray, J. D., and Rowe, W. C. *Australian Journal of Physics*, 7(3):439–459, 1954.

Wild, J. P., Sheridan, K. V., and Neylan, A. A. *Australian Journal of Physics*, 12:369, December 1959a.

Wild, J. P., Sheridan, K. V., and Trent, G. H. The transverse motions of the sources of solar radio bursts. In Bracewell, R. N., editor, *URSI Symp. 1: Paris Symposium on Radio Astronomy*, volume 9 of *IAU Symposium*, page 176, 1959b.

Wild, J. P., Smerd, S. F., and Weiss, A. A. *Annual Review of Astronomy and Astrophysics*, 1:291, 1963.

Willes, A. J. and Melrose, D. B. *Solar Phys.*, 171:393–418, April 1997.

Willson, R. F., Redfield, S. L., Lang, K. R., Thompson, B. J., and St. Cyr, O. C. *Astrophys. J. Lett.*, 504: L117–L121, September 1998.

Winglee, R. M. and Dulk, G. A. *Astrophys. J.*, 310:432–443, November 1986.

Zhao, R.-Y., Mangeney, A., and Pick, M. *Astron. Astrophys.*, 241:183–186, January 1991.

Zheleznyakov, V. V. and Zaitsev, V. V. *Soviet Astron.*, 12:14, August 1968.

Zimovets, I., Vilmer, N., Chian, A.-L., Sharykin, I., and Struminsky, A. *Astronomy & Astrophysics*, 547:A6, 2012.

Zlotnik, E. I. *Astron. Astrophys.*, 101:250–258, August 1981.

Zucca, P., Carley, P., Eoin, Bloomfield, D. S., and Gallagher, T., Peter. *Astronomy & Astrophysics*, 564:A47, 2014.